Dissertation

Numerical Investigations of the Ignition Characteristics and Flame Morphology of Polyoxymethylene Dimethyl Ether

carried out for the purpose of obtaining the degree of

Doctor technicae (Dr. techn.)

submitted at

TU Wien
Faculty of Mechanical and Industrial Engineering

by

Dipl.-Ing. Frederik Alexander WIESMANN
Mat. No.: 12038085

Vienna, May 2024

Dissertation

Numerical Investigations of the Ignition Characteristics and Flame Morphology of Polyoxymethylene Dimethyl Ether

carried out for the purpose of obtaining the degree of
Doctor technicae (Dr. techn.),

submitted at TU Wien
Faculty of Mechanical and Industrial Engineering

by

Dipl.-Ing. Frederik Alexander WIESMANN
Mat. No.: 12038085

under the supervision of
Assoc. Prof. Dr. techn. Thomas Lauer
Institute of Powertrains and Automotive Technology, E315

Reviewed by
Lyle M. Pickett, PhD
Sandia National Laboratories, Combustion Research Facility,
7011 East Ave., Livermore, 94551, CA, USA
and
Prof. José María García Oliver, PhD
CMT - Clean Mobility & Thermofluids, Universitat Politècnica de València,
Camino de Vera, s/n, 46022 Valencia, Spain

Vienna, May 2024

Signature

Funding

This work was supported by the Austrian Research Promotion Agency (FFG), grant number 874418, and the Federal Ministry of Climate Action, Environment, Energy, Mobility, Innovation and Technology within the framework of the collective research networking program (CORNET) project “eSpray”.

The presented computational results were achieved using the Vienna Scientific Cluster (VSC) via the funded project No. 71485.

I confirm, that the printing of this thesis requires the approval of the examination board.

Affidavit

I declare in lieu of oath, that I wrote this thesis and carried out the associated research myself, using only the literature cited in this volume. If text passages from sources are used literally, they are marked as such.

I confirm that this work is original and has not been submitted for examination elsewhere, nor is it currently under consideration for a thesis elsewhere.

I acknowledge that the submitted work will be checked electronically-technically using suitable and state-of-the-art means (plagiarism detection software). On the one hand, this ensures that the submitted work was prepared according to the high-quality standards within the applicable rules to ensure good scientific practice “Code of Conduct” at the TU Wien. On the other hand, a comparison with other student theses avoids violations of my personal copyright.

Vienna, May 2024

Signature

Danksagung

Die vorliegende Arbeit entstand während meiner Tätigkeit als Projektassistent am Institut für Fahrzeugantriebe und Automobiltechnik der Technischen Universität Wien.

Zuallererst möchte ich mich herzlich bei Prof. Dr. Thomas Lauer für die wissenschaftliche Betreuung meiner Arbeit bedanken. Die fachliche Unterstützung war immer hevorragend und ich habe vor Allem das große Vertrauen in meine Arbeit sowie die mir entgegengebrachte Freiheit stets sehr wertgeschätzt. Auch bedanke ich mich bei dem ehemaligen Institutsvorstand Prof. Dr. Bernhard Geringer für die stete Unterstützung sowie für die Möglichkeit, spannende internationale Konferenzen zu besuchen.

Ein weiterer Dank geht an Lyle M. Pickett sowie José María García Oliver für die übernahme der Gutachten der vorliegenden Arbeit.

Ich möchte mich auch bei allen Mitarbeiterinnen und Mitarbeiter des Instituts im Sekretariat bedanken, die mir immer äußerst hilfsbereit bei allen organisatorische Fragen geholfen haben.

Ein großer Dank geht auch an alle meine Kollegen am Institut. Insbesondere bei Norbert Zöbinger und Jens Frühhaber bedanke ich mich für die vielen fachlichen Diskussionen und für ihre Hilfe. Außerdem möchte ich mich bei Max Quissek, Maximilian Haslinger, Wladimir Budenkow, Christoph Schwella, Lukas Acker und Chistroph Steindl für die tolle Arbeitsatmosphäre und das freundschaftliche Umfeld bedanken.

Auch möchte ich mich bei meinen Eltern und meinen Geschwistern bedanken. Ich wäre nicht an diesem Punkt in meinem Leben angekommen, ohne Eure immerwährende Unterstützung und Motivation. Meinen Eltern bin ich sehr dankbar, dass sie immer eine Stütze für mich waren und mich nie zu irgendetwas gedrängt haben, sondern immer nur in meinen Absichten gestärkt.

Allerdings wäre diese Doktorarbeit unmöglich gewesen ohne das Vertrauen, die Unterstützung und das Verständnis von meiner Ehefrau Anke. Ich bin Dir für immer dankbar dafür. Diese Arbeit ist für Dich, für Nora und für Olivia.

May 2024 *B24005*

Contents

Abstract

Climate-neutral synthetic fuels based on renewable energy sources, the so-called e-fuels, are a controversial topic regarding future individual mobility scenarios. Besides the ability to provide chemical storage for volatile excess renewable energy, e-fuels have a significant potential to deliver controlled, clean, and efficient combustion for future vehicles with internal combustion engines (ICE). One promising group of liquid energy carriers are oxygenated e-fuels, which contain oxygen within their chemical structure and potentially burn without soot emission in compression-ignition (CI) engines. Especially, polyoxymethylene dimethyl ethers (PODE or OME) effectively avoid the formation of soot precursors like acetylene C_2H_2 due to the lack of carbon-carbon bonds. This characteristic alleviates the typical soot-NO_x trade-off for diesel engines. However, OME's different chemical composition and physical-chemical behavior need to be understood in depth to achieve combustion that provides the highest thermal efficiencies and lowest pollutant formation. Identifying the deviations in mixing, ignition behavior, flame morphology, and emission characteristics from conventional diesel-like fuels necessitates applying basic experimental and numerical research to characterize this group of fuels fully.

In the course of this thesis, the spray combustion characteristics of OME_{3-5} fuel were analyzed. Using a commercial CFD code, the numerical results were validated with free-jet experiments in a constant-pressure vessel at diesel engine-relevant conditions and with a single-cylinder research engine with an optically accessible piston crown. The liquid penetration length was measured via Mie-scattering and diffused back-illumination (DBI). Air entrainment and mixing were determined using Rayleigh scattering and schlieren measurements. Ignition was detected with formaldehyde (CH_2O) planar laser-induced fluorescence (PLIF) for the low-temperature flame and OH*-chemiluminescence for the high-temperature ignition.

The aim of the present research was to gather the experimental data to validate a CFD model and generate additional insight into the OME combustion process that is otherwise impossible to obtain via experimental techniques. At first, the OME fuel's inert and reactive spray characteristics compared to diesel-like n-dodecane were studied. A coherent liquid injection and spray breakup model was developed. A new chemical kinetic mechanism for OME_{1-6} spray combustion was derived as input to the CFD setup. The CFD model was then applied to the combustion process of the single-cylinder research engine. A systematic approach was developed to incorporate the significant losses caused by piston ring leakages (blow-by).

The ignition behavior for the OME fuel was demonstrated to differ significantly from that of n-dodecane, showing highly elevated levels of reaction activity for OME in regions where non-oxygenated fuels like n-dodecane cannot form an ignitable mixture. The entire OME combustion process was proven to occur within a mixing regime that effectively prohibits soot formation.

Additionally, an in-depth comparison of the cold-stage and hot-stage ignition for OME and n-dodecane, simulated employing Reynolds-Averaged Navier-Stokes (RANS) and Large Eddy Simulation (LES) turbulence modeling approaches, was conducted. The overall validity of the RANS approach was proven with remarkable concordance to the *OH**-chemiluminescence experiments at high ambient temperatures. At the same time, the advantages of LES were carved out by demonstrating its ability to capture small-scale fluctuations in the combustion process.

In summary, the in-depth numerical analysis delivered valuable insights into the combustion characteristics of OME. The identified deviations for OME regarding ignition behavior, flame morphology, and transient operation compared to diesel-like fuels will help guide future applications of OME fuel in ICEs and elsewhere.

Kurzfassung

Klimaneutrale synthetische Kraftstoffe auf Basis erneuerbarer Energiequellen, die sogenannten E-Fuels, sind ein kontroverses Thema für zukünftige individuelle Mobilitätsszenarien. Neben der Fähigkeit, flüchtige überschüssige erneuerbare Energie chemisch zu speichern, haben E-Fuels ein erhebliches Potenzial für eine kontrollierte, saubere und effiziente Verbrennung künftiger Fahrzeuge mit Verbrennungsmotoren. Eine vielversprechende Gruppe von flüssiger Energieträger sind oxygenierte E-Fuels, die Sauerstoff in ihrer chemischen Struktur enthalten und möglicherweise ohne Rußemission in Selbstzündungsmotoren verbrennen. Insbesondere Polyoxymethylendimethylether (PODE oder OME) verhindern effektiv die Produktion von Rußvorläufern wie Acetylen C_2H_2 aufgrund des Fehlens von Kohlenstoff-Kohlenstoff-Bindungen. Diese Eigenschaft mildert den typischen Ruß-NO_x-Kompromiss für Dieselmotoren. Allerdings müssen die unterschiedliche chemische Zusammensetzung und das physikalisch-chemische Verhalten von OME eingehend verstanden werden, um eine Verbrennung zu erreichen, die die höchsten thermischen Wirkungsgrade und die geringste Schadstoffbildung bietet. Um die Abweichungen bei der Mischung, dem Zündverhalten, der Flammenmorphologie und den Emissionseigenschaften von herkömmlichen dieselähnlichen Kraftstoffen zu identifizieren, ist die Anwendung grundlegender experimenteller und numerischer Forschung nötig, um diese Gruppe von Kraftstoffen vollständig zu charakterisieren.

Im Rahmen dieser Arbeit wurden die Freistrahl- sowie Verbrennungseigenschaften eines OME_{3-5} Kraftstoffs analysiert. Unter Verwendung eines kommerziellen CFD-Codes wurden die numerischen Ergebnisse mit Freistrahlexperimenten in einem optischen Verbrennungsprüfstand mit konstantem Druck unter dieselmotorrelevanten Bedingungen und mit einem Einzylinder-Forschungsmotor mit optisch zugänglichem Kolbenboden validiert. Die Flüssigkeitseindringtiefe wurde mittels Mie-Streuung und diffuser Rückbeleuchtung (DBI) gemessen. Die Durchmischung der Kraftsoffe mit der Umgebungsluft wurde mittels Rayleigh-Streuung und Schlierenmessungen bestimmt. Die Zündung wurde mit planarer laserinduzierter Fluoreszenz von Formaldehyd (CH_2O) für die Niedertemperaturflamme und OH*-Chemilumineszenz für die Hochtemperaturzündung nachgewiesen.

Ziel der vorliegenden Forschung war es, experimentelle Daten zu sammeln, um ein CFD-Modell zu validieren und zusätzliche Einblicke in den OME-Verbrennungsprozess zu gewinnen, die sonst mit experimentellen Techniken nicht möglich wären. Zunächst wurden die inerten und reaktiven Freistrahleigenschaften von OME im Vergleich zu dieselähnlichem n-Dodekan unter

dieselmotorrelevanten Bedingungen mithilfe eines kommerziellen CFD-Codes untersucht. Es wurde ein kohärentes Modell zur Einspritzung und sowie zum Tropfenaufbruch entwickelt. Ein neuer kinetischer Reaktionsmechanismus für die Verbrennung von OME wurde als Input für das CFD-Modell abgeleitet. Anschließend wurde das CFD-Modell auf den Verbrennungsprozess eines Einzylinder-Forschungsmotors mit optisch zugänglichem Kolbenboden angewendet. Im Zuge dessen wurde ein systematischer Ansatz zur Einbeziehung der signifikaten Verluste durch Kolbenringleckagen entwickelt.

Es konnte gezeigt werden, dass sich das Zündverhalten des OME Kraftstoffs maßgeblich von dem von n-Dodekan unterscheidet und eine stark erhöhte Reaktionsaktivität von OME in Regionen vorliegt, in denen nicht sauerstoffhaltige Kraftstoffe wie n-Dodekan kein zündfähiges Gemisch bilden können. Der gesamte Verbrennungsprozess von OME konnete innerhalb eines Mischungszustandes beschrieben werden, der die Rußbildung wirksam verhindert.

Außerdem wurde ein ausführlicher Vergleich der Kalt- und Heißphasenzündung für OME und n-Dodekan durchgeführt, der mithilfe der Turbulenzmodellierungsansätze Reynolds-Averaged Navier-Stokes (RANS) und Large Eddy Simulation (LES) simuliert wurde. Die allgemeine Gültigkeit des RANS-Ansatzes wurde durch bemerkenswerter Übereinstimmung mit den OH^*-Chemilumineszenz Messungen bei hohen Umgebungstemperaturen nachgewiesen. Gleichzeitig wurden die Vorteile von LES herausgearbeitet, indem seine Fähigkeit demonstriert wurde, kleinskalige Schwankungen im Verbrennungsprozess zu erfassen.

Zusammenfassend lieferte die eingehende numerische Analyse wertvolle Erkenntnisse über die Verbrennungseigenschaften von OME. Die identifizierten Abweichungen für OME hinsichtlich Zündverhalten, Flammenmorphologie und transientem Betrieb im Vergleich zu dieselähnlichen Kraftstoffen werden als Orientierung für zukünftige Anwendungen von OME-Kraftstoffen in Verbrennungsmotoren und anderswo dienen.

List of Abbreviations and Symbols

Latin Symbols

a	-	Number of Fuel Species Moles; Spray Cone Angle Constant
a_{KH}	m	Radius of Parent Droplet for Kelvin-Helmholtz Breakup Model
B	-	Coefficient of Kelvin-Helmholtz-Rayleigh-Taylor Breakup Model
B_M	-	Spalding Mass Transfer Number
B_T		Heat Transfer Number
C_{ext}	m^2	Extinction Coefficient
d	m	Diameter
f	s^{-1}	Elliptic Relaxation Function
ΔH_{vap}	J/kg	Latent Heat of Evaporation
k	m^2/s^2	Turbulent Kinetic Energy
m	kg	Mass
n	-	Number of Atoms
Nu	-	Nusselt Number
Oh	-	Ohnesorge Number
p	Pa	Pressure
Pr	-	Prandtl Number
r	m	Radius
Re	-	Reynolds Number
Sc	-	Schmidt Number
Sh	-	Sherwood Number
t	s	Time
T	K	Temperature
v	m/s	Velocity
$\overline{v^2}$	m^2/s^2	Velocity Scale (wall-normal)
w	-	Mass Fraction
We	-	Weber Number
x,y,z	-	Space Coordinate
Z	-	Mixture Fraction

Greek Symbols

β	m^2/s	Binary Diffusion Coefficient
ε	m^2/s^3	Turbulent Dissipation Rate
ζ	-	Velocity Scales Ratio
Λ	m	Wave Length
μ	kg/ms	Dynamic Viscosity
ν	m^2/s	Kinematic Viscosity
ϕ	-	Equivalence Ratio
ϕ_Ω	-	Oxygen Equivalence Ratio
ρ	kg^3/m	Density
σ	N/m	Surface Tension
τ	s	Characteristic Breakup Time
τ_{opt}	-	Optical Thickness
χ	s^{-1}	Scalar Dissipation Rate
Ω	-	Oxygen Ratio; Growth Rate

Subscripts and Superscripts

d	Droplet
ext	Extinction
f	Fuel
g	Gaseous
i	Species; Element
inj	Injection
KH	Kelvin-Helmholtz
l	Liquid
noz	Nozzle
opt	Optical
ox	Oxidizer
RT	Rayleigh-Taylor
S	Droplet Surface
st	Stoichiometric
∞	Ambient Conditions

Abbreviations

CCUS	Carbon Capture Utilization and Storage
CFD	Computational Fluid Dynamics
CN	Cetane Number
CRF	Combustion Research Facility
DAC	Direct Air Capture
DBI	Diffuse Back Illuminated Imaging
DI	Direct Injection
DNS	Direct Numerical Simulation
ECN	Engine Combustion Network
EOI	End of Injection
FST	Institute of Fluid System Technology
GHG	Greenhouse Gas
ID	Ignition Delay
IEA	International Energy Agency
ICE	Internal Combustion Engine
IVG	Institute for Combustion and Gas Dynamics - Reactive Fluids
JSR	Jet-Stirred Reactor
KH	Kelvin-Helmholtz
KH-RT	Kelvin-Helmholtz-Rayleigh-Taylor Breakup Model
LES	Large Eddy Simulation
LHV	Lower Heating Value
LLNL	Lawrence Livermore National Laboratories
LOL	Flame Lift-Off Length
LVF	Liquid Volume Fraction
NO_x	Nitrogen Oxides
OME/PODE	Polyoxymethylene Dimethyl Ethers
PAH	Polycyclic Aromatic Hydrocarbons
PLIF	Planar Laser-Induced Fluorescence
PLV	Projected Liquid Volume
PtL	Power-to-Liquid
PtG	Power-to-Gas
RANS	Reynolds Averaged Navier Stokes (Equation)
RT	Rayleigh-Taylor
SJTU	Shanghai Jiao Tong University
SNL	Sandia National Laboratories
SOC	Start of Combustion

SOI	Start of Injection
ST	Shock Tube
TCI	Turbulence Chemistry Interaction
TKE	Turbulence Kinetic Energy
UDE	University of Duisburg-Essen

Part I

Introduction

1 Motivation

Achieving global climate neutrality by the middle of the 21st century is an imperative to leave future generations a habitable planet. As all significant international players officially agree to this goal, the means and ways to get there are highly disputed.

Individual mobility is undergoing rapid changes worldwide due to the transition away from fossil fuels. Besides the strong and obvious push towards electrification of passenger cars' powertrains in the European Union (EU) and the United States of America, a steady and growing recognition of the importance of sustainable liquid energy carriers for the future global transportation system is undeniable. In this context, e-fuels present a possibility to achieve CO_2-neutrality in even hard-to-decarbonize applications. The term "e-fuels" describes fuels, liquid or gaseous, based on electrolytic hydrogen, which itself is an e-fuel. Figure 1 visualizes the different pathways of e-fuel production, which encompasses a whole range of different types of fuels if the hydrogen is synthesized with carbon. The synthesis procedure is usually referenced as Power-to-Liquid (PtL) for liquid fuels or Power-to-Gas (PtG) for gaseous fuels. Drop-in e-fuels are available via a Fischer-Tropsch synthesis. Alternative e-fuels containing carbon, like polyoxymethylene dimethyl ethers (PODE_n or OME_n), require methanol (CH_3OH) as an intermediate product, which can also be produced with a direct methanol synthesis. In case the electrolysis was conducted with renewable energy sources, and the CO_2 needed for the synthesis was derived through direct air capture (DAC), the obtained e-fuels can be labeled as CO_2-neutral.

The greatest potential of CO_2-neutral e-fuels in the future is seen in aviation and marine applications [1]. They are expected to remain significantly more expensive than fossil fuels and to rather compete with other low-emission options like biofuels in the medium term. However, even in an optimistic transition scenario, the International Energy Agency (IEA) predicts that diesel trucks will still represent a significant share of heavy-duty transportation in 2050 [2]. Currently, global transport emission reduction efforts are insufficient to achieve net zero greenhouse gas (GHG) emissions by 2050. Hence, an accelerated deployment of CO_2-neutral e-fuels in the near future is mandatory for staying aligned with the net zero trajectory and will also be conducive to diversifying decarbonization options available for transport [1]. The Paris Climate Accord to limit

petroleum-derived counterparts. By contrast, alternative e-fuels such as e-ammonia and e-methanol require investments in distribution infrastructure and end-use equipment to enable their use in the transport sector.

Figure 3.1 E-fuels and production routes considered in this report

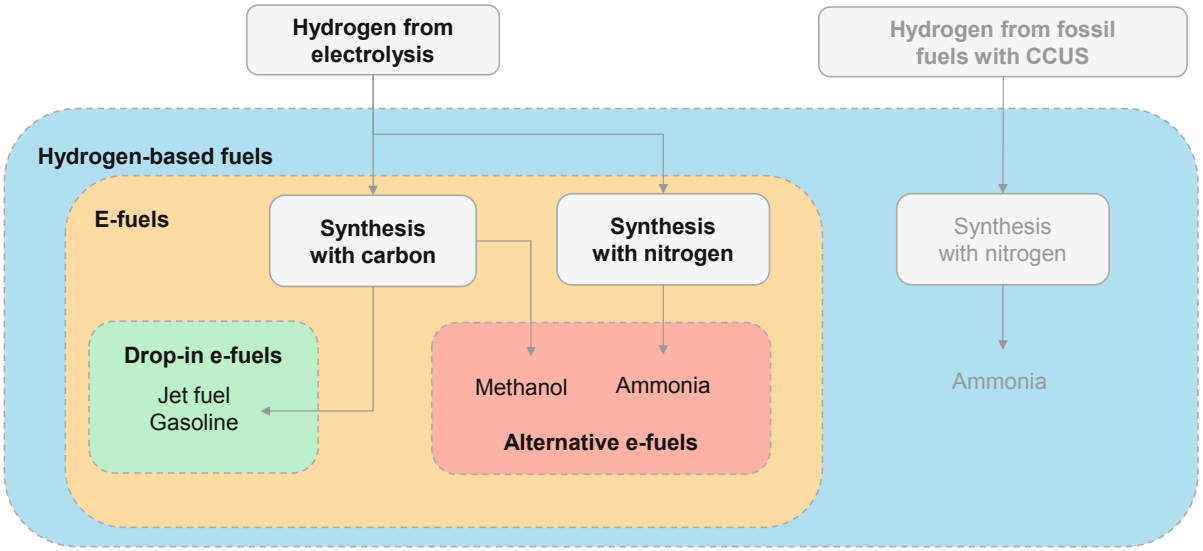

Figure 1: E-fuels production routes and classification, taken from [1].

Note: E-fuels represent a subset of hydrogen-based fuels, a category that also includes fuels obtained from hydrogen produced from fossil fuels with CCUS.

global warming to less than 2 °C, compared to pre-industrial levels, is only achievable when the current global vehicle fleet will be fueled with increasingly CO_2-neutral blends, using synthetic "drop-in" e-fuels. Overall, it is expected that by 2050, more than 70 % of the final energy demand of all transport modes, including aviation and marine applications, in the EU will be met by PtL or PtG e-fuels [3], see Figure 2. Independent of which future scenario is considered, even assuming an optimistic target of 70 % for the share of battery electric vehicles (BEV) of all passenger cars' powertrains in 2050 in the *More-electric-eDrives* scenario, renewable liquid (e-)fuels will dominate the final energy demand when all transport modes are taken into account.

Besides the apparent advantages of storing volatile renewable energy sources in transportable liquids via well-established industry processes, oxygenated fuels that do not contain carbon-carbon bonds combine low pollutant formation during combustion with a long vehicle driving range. OME_n, in particular, OME_{3-5}, was proven in various studies to be suited as a fuel blended into diesel [4–7] or used neatly in diesel engines [8], always showing a drastically reduction in soot emissions, effectively solving the soot-NO_x trade-off for diesel engines.

The injection process and the fuel properties primarily characterize the combustion in modern diesel engines. The main challenges in describing the combustion process are spray propagation, liquid spray breakup into ligaments and droplets and their subsequent evaporation, auto-ignition, heat release, and heat transfer to the cylinder walls and formation of pollutants [9]. Characteristic fuel properties drive these processes. The fuels' viscosity, density, and surface tension strongly influence the liquid breakup. The vapor pressure and heat of evaporation determines the evaporation of fuel droplets. The auto-ignition of the fuel spray is a function of the ignitability, measured by the fuels' cetane number (CN). The heat release of the combustion is limited by the lower heating value (LHV). The chemical composition of the fuel determines which pollutants are formed at certain temperatures and mixing regimes.

Figure 20 shows the final fuel consumption in transport by fuel in the four scenarios modelled in this study.

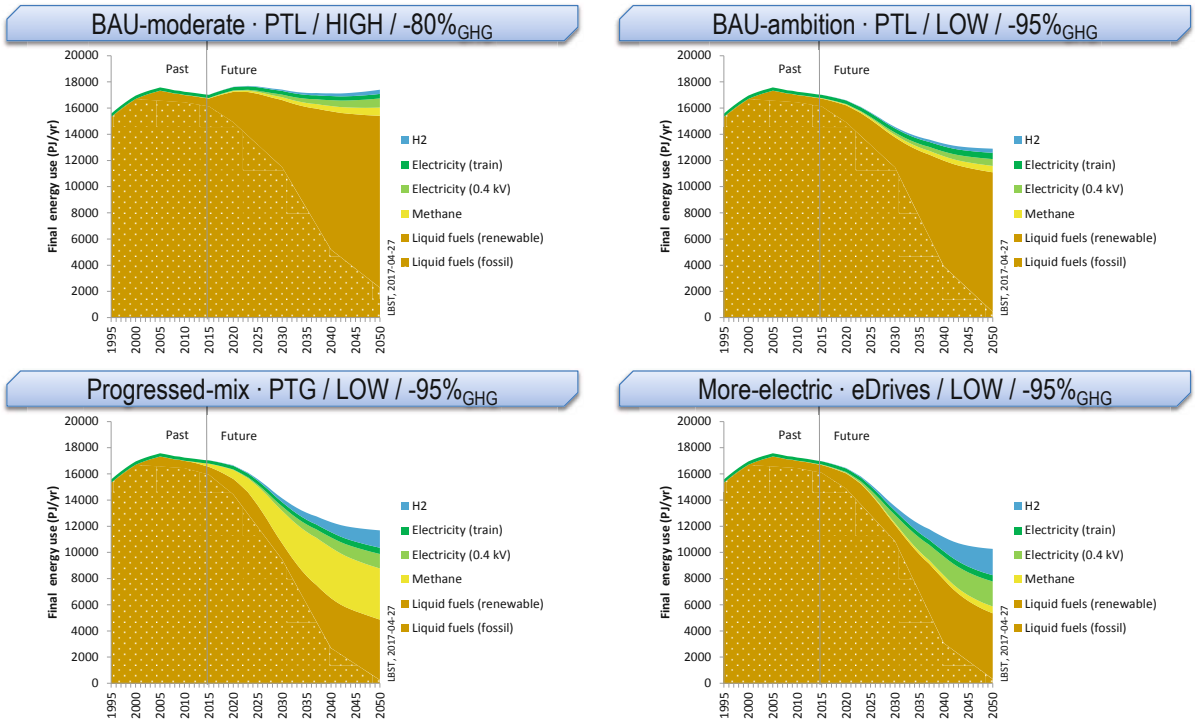

Figure 20: Final energy demand in EU transport from 1995 to 2050 by fuel

Figure 2: Final energy demand in EU transport from 1995 to 2050 by fuel for four different development routes with -80 % to -95 % GHG emissions in 2050 compared to 1990 levels: *BAU-moderate*: PtL dominated scenario combined with high transport demand; *BAU-ambition*: PtL dominated scenario combined with low transport demand; *Progressed mix*: PtG dominated scenario combined with low transport demand; *More electric*: eDrive dominated scenario combined with low transport demand [3].

The final fuel consumption strongly depends on the transport demand. Although the energy efficiency of the ICE vehicles increases in both business-as-usual scenario due to internal combustion engines that are embedded in successively more electrified (hybrid) powertrains (by 2050 predominantly in range extender configurations), the overall final fuel demand remains approximately at today's level in the scenario BAU-moderate. In the BAU-moderate scenario route, the increasing transportation demand compensates the improvements in powertrain efficiencies. In contrast to that, the BAU-ambition scenario route leads to a decrease of final fuel demand despite the dominant use of vehicles using internal combustion engines (ICE) because of LOW growth in BAU-ambition versus HIGH growth in BAU-moderate.

The final energy demand for the direct use of electricity (e.g. for BEVs and range extender electric vehicles (REEVs) operated in the electricity mode) is low because the electric powertrain is so efficient. However, even in the eDrives scenario, the demand for liquid fuels is still high in 2050. The reason is the high fuel demand from international navigation (both in the high and low transport fuel demand case). Furthermore, even by 2050, a significant number of legacy ICE vehicles are still operating throughout all scenarios.

Acknowledging the necessity for ramping up e-fuel production significantly and the advantages gained by using oxygenated synthetic fuels like OME, further research to characterize oxygenated e-fuels will likely impact future propulsion technology. However, due to the influence of the fuel properties on the overall diesel combustion process, any future sustainable diesel-fuel alternative has to be analyzed in detail to identify its potential and deficiencies.

In summary, the investigation of the spray combustion for OME fuels is needed to accurately determine its potential as a CO_2-neutral alternative for fossil diesel in the future transport system.

2 Problem Definition and Research Objective

2.1 Problem Definition

The high-pressure fuel injection and subsequent autoignition characterize the compression-ignition combustion process within modern diesel engines. The direct injection (DI) typically starts shortly before the top dead center in the compression stroke at ambient conditions above 800 K and 60 bar. Injection pressures of 2500 bar and above result in injection velocities of the liquid fuel penetrating the ambient air of about 500 m/s.

After the start of injection (SOI), the liquid phase of the fuel reaches a maximum penetration length (i.e., liquid length) that is almost constant during the steady period of the injection process. The liquid fuel has to evaporate entirely for diesel engines before hitting the piston bowl wall or cylinder liner. Over-penetration and dilution of fuel into the cylinder wall oil film from late-cycle post-injections can increase the component wear [10–12]. Wall-wetting for early SOI strategies also causes higher emissions of unburned hydrocarbons (UHC) and carbon monoxide (*CO*), thus reducing the combustion efficiency [13, 14].

The period between the SOI and the start of combustion (SOC) is referred to as the ignition delay (ID). During this process, the injected liquid fuel atomizes, evaporates, and mixes with the ambient air in the combustion chamber, generating an ignitable mixture. The most-cited indicator to characterize a fuel's ignition delay is the cetane number (CN), with higher cetane numbers resulting in shorter ignition delays. The ignition delay controls the diesel combustion process and alters the engine performance and emissions. A strong positive correlation was reported in [15] between ignition delay duration and *CO* emissions due to resulting over-lean mixtures and quenching of the mixtures at the cylinder walls with increased ignition delay. However, it was also shown that the CN and ignition delay are not necessarily the dominant factors for the production of NO_x and particulates, arguing that the fuel's physical properties and molecular structure also excite a significant influence.

After the SOC, the typical diesel combustion can be grouped into three phases: Initial premixed combustion, mixing-controlled combustion, and kinetically controlled combustion [16]. The first

phase occurs immediately after the self-ignition of the fuel-air mixture. The heat release rate in this phase is mainly controlled by the amount of ignitable fuel-air mixture and the rates of the chemical reactions. This phase's time scales are much smaller than the other phases, causing a sharp rise in pressure.

In the second and main phase of diesel combustion, the heat release is determined by the turbulent mixing of fuel spray and entrained ambient air. Fuel injection, atomization, evaporation, mixing, combustion, and formation of particulates all co-occur. This phase is referred to as quasi-steady and is conceptually described by the model of Dec [17] and Flynn et al. [18] in Figure 3. A fuel-rich mixing region is formed downstream of the liquid length with temperatures of about 1600 K, releasing approximately 15 % of the overall heat [18]. According to Dec [17] and Chomiak and Karlsson [19], this region is referred to as rich central reaction zone. Further downstream, an accumulation of particulates can be observed in the jet center. These particulates are formed from precursor species generated in the premixed combustion phase. The diffusion flame encapsulates the fuel spray along an isosurface of stoichiometric conditions reaching up to 2700 K, where partially oxidized products and formed particles oxidize completely to CO_2 and water vapor. The high temperatures lead to the formation of NO_x on the fuel-lean side of the diffusion flame.

The axial distance from the injector tip to the diffusion flame is called lift-off length (LOL). It is mainly influenced by the fuel spray atomization and evaporation processes near the injector tip and by the chemical reaction occurring in the fuel jet. The lift-off length is an essential characteristic of the diesel diffusion flame, especially regarding soot formation. Higher injector pressures and smaller nozzle orifices increase the lift-off length and fuel-air mixing occurring by the lift-off length [20]. This results in a more intense rich central reaction zone with less soot formed, as visualized in Figure 4. Besides ambient conditions and the injection system, the used fuel itself has a significant impact on the flame stabilization process, with oxygenated fuels showing different dependencies of their lift-off lengths on temperature and oxygen content [21–23]. In general, fuels with shorter ignition delays due to higher cetane numbers have shorter lift-off lengths. Picket et al. [24] detected a cool flame via excited $HCHO$*-chemiluminescence upstream of the lift-off location before autoignition and during quasi-steady combustion, showing that the first-stage (low temperature) ignition affects lift-off and that flame stabilization is by ignition rather than flame propagation.

The third and final phase of diesel combustion occurs after the end of injection (EOI). No additional momentum is introduced into the jet, and the diffusion flame surrounds a region of partially oxidized products of the fuel-rich premixed combustion [16]. Soot formation and oxidation in this phase strongly depend on the speed of the closing movement of the injector needle. A slow closure of the needle results in a smaller momentum of the last liquid fuel entering the combustion chamber, which diminishes the air entrainment and mixing process, yielding higher soot concentrations. During the expansion stroke, the in-cylinder temperature,

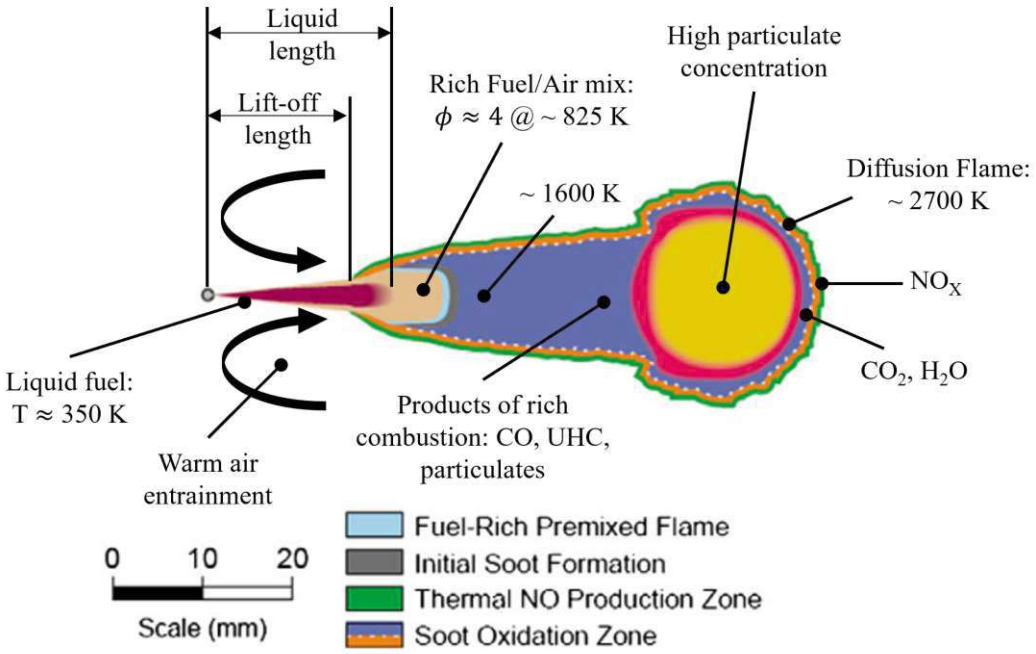

Figure 3: Phenomenological description of a diffusion flame with diesel fuel according to Dec [17] and Flynn et al. [18], adapted from [25].

and hence the reaction rates, falls so that the combustion is chemically or kinetically controlled.

Conventional diesel-like fuel sprays were shown to behave like gas jets due to the rapid air entrainment resulting from the high injection pressures and velocities. The entrained air quickly dominates the flow characteristics of the jet and renders its mass distribution independent of the used fuel [26, 27]. However, the quality of the mixture, ignition, and combustion is dependent on the chemical composition of the fuel [26]. Different fuels' locally equal mass distributions have to be transferred to equivalence ratios (Equation 1) to determine the actual mixing regime. Oxygenated fuels achieve leaner mixtures because of their lower stoichiometric air requirements. The interesting aspect is that the fuel mass distribution can be designed solely by the parameters of the injection system. At the same time, the combustion characteristics are determined by applying a fuel with appropriate chemical properties for a specific combustion concept [27].

$$\phi = \frac{m_f/m_{ox}}{(m_f/m_{ox})_{st}} \tag{1}$$

Polyoxymethylene dimethyl ethers (PODE$_n$ or OME$_n$) is a homologous range of oligomeric polyethers. They are characterized by a so-called C1 structure, indicating the lack of carbon-carbon bonds, with the chemical structural formula $H_3C\text{-}O(\text{-}CH_2O)_n\text{-}CH_3$. They are denoted by the number (n) of oxymethylene ether groups ($\text{-}CH_2O$).

Figure 5 shows the process chain of the OME$_n$ production with methanol as a starting product. The synthesis of OME$_n$, labeled as POMDME in Figure 5, occurs in an anhydrous environment from the intermediates trioxane and methylal ($C_3H_8O_2$, also called Dimethoxymethane or

Also other routes for the POMDME synthesis are feasible. DME can be used instead of methylal to react with trioxane over an acidic catalyst to POMDMEs [19]. Another possibility is to integrate the methylal process and the POMDME process [20]. In a first step methanol and formaldehyde react to methylal. In a second step over the same acidic catalyst formaldehyde is added to methylal to form POMDMEs. During the formation of methylal, water is produced which is the drawback of this integrated process. Water reacts with formaldehyde to methylene glycol and poly(oxymethylene)glycols, which reduce the selectivity of POMDMEs and are difficult to remove.

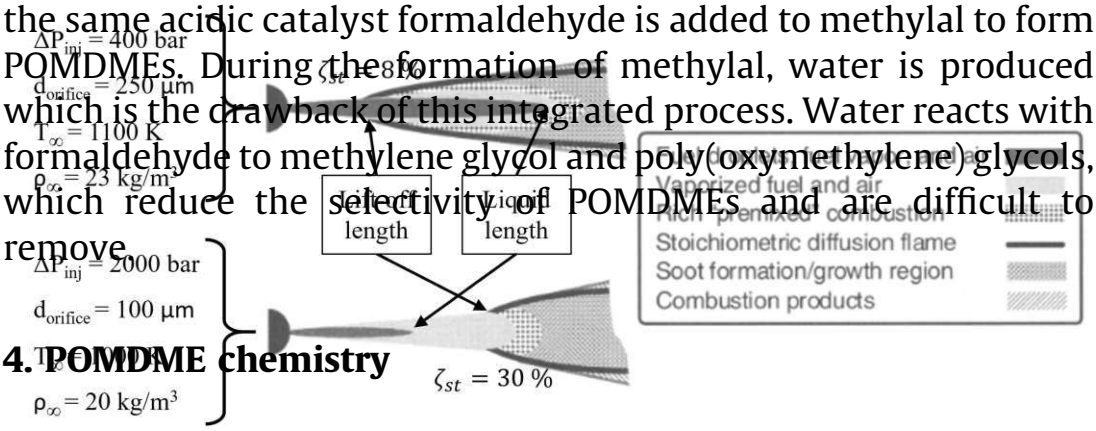

Figure 3: Experimental data of lift-off length for two different injection conditions published in [20]. The term ζ_{st} indicates the ratio of air entrained up to the position of the lift-off length in relation to the stoichiometric amount.

4. POMDME chemistry

In the present section the chemistry of the formation of POMDMEs from methylal and trioxane is considered in more detail. The POMDME with n CH_2O segments is labeled as POMDME n in the

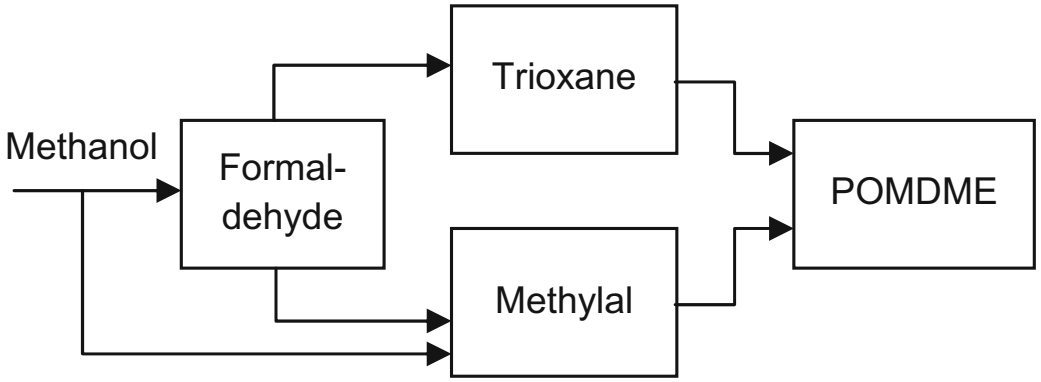

Figure 4: Process chain diagram for POMDME synthesis, based on [28].

Fig. 1: Block flow diagram of the POMDME process chain.

OME_1). Trioxane is used for chain extension and methylal for chain termination [28]. At first, the trioxane is converted to formaldehyde (CH_2O) over an acidic catalyst according, which in turn reacts with OME_1 to produce OME_2 [28]. Further addition of CH_2O to OME_n leads to OME_{n+1}.

With increasing n, as can be seen in Table 2.1, the boiling point, density, cetane number, and oxygen content increase while the lower heating value (LHV) decreases slightly. Comparing OME's properties to standard B7 diesel (diesel blended with seven % of FAME-type biodiesel), it can be seen that OME_n fuel with a chain length greater than one ($n > 1$) consists of an LHV which is not even half that of B7 diesel. This effect is slightly compensated by the higher density of OME_n, which leads to a volumetric diesel equivalent ratio (Equation 2) of approximately 1.7-1.8. Therefore, 70-80 % more fuel volume must be injected in every engine cycle when replacing diesel fuel with OME_n.

$$\frac{LHV_{B7,Diesel}}{LHV_{OME_n}} \cdot \frac{\rho_{B7,Diesel}}{\rho_{OME_n}} \approx 1.7 - 1.8 \tag{2}$$

Table 2.1: Fuel properties for diesel (EN590 and B7) and different OMEs. [5, 8, 31, 32]

Property	Unit	EN 590	B7 Diesel	OME_1	OME_2	OME_3	OME_4	OME_5	OME_6
Density (T=15 °C)	[kg/m^3]	820-845	832.6	860	980	1030	1070	1110	1140
Kinematic Viscosity (T=40 °C)	[mm^2/s]	2-4.5	3.1	0.37	0.559	0.866	1.33	1.96	n.a.
Surface tension ISO 6295	[mN/m]	26	-	20.6	24.3	25.0	28.2	-	-
Cetane number (CN)	[-]	>51	57.5	28	68	72	84	93	104
Lubricity (T=60 °C)	[µm]	-	<460	759	576	534	465	437	n.a.
Flashpoint	[°C]	>55	77	<0	16	20	77	103	169
Lower heating value (LHV)	[MJ/kg]	-	42.8	22.44	20.32	19.14	18.38	17.86	17.47
Boiling point	[°C]	-	180-390	42	105	156	202	242	280
Oxygen content	[wt. %]	-	0.8	42.1	45.3	47.1	48.2	48.9	49.6

However, the oxygen content of OME_n is significant, reaching nearly 50 % for OME_6, which lowers the LHV accordingly. This means that, assuming unchanged displacement volume, switching from diesel to OME_n would not change the maximum power density, as OME_n has a substantially lower air requirement and releases the same amount of energy with the same airflow and air-to-fuel ratio [29].

Another important aspect regarding the fuel properties of OME_n is the deviation from the EN 590 diesel norm. Table 2.1 shows that the requirements set by EN 590 regarding cetane number are only met by OMEs with $n > 2$. The density and kinematic viscosity are not within the required range for any OME_n. However, OME_5 is almost within the range of allowed viscosities according to EN 590. It can also be seen that the lubricity comes close to diesel-like values for OME with $n \geq 3$, which is vital for high-pressure diesel injector operation as the fuel itself primarily lubricates the injection pumps. The boiling point also falls within the boiling range of diesel fuel for higher OME_n with $n > 3$. Summarizing the properties of the different OME_n, it can be deduced that a mixture of longer-chained OMEs, especially OME_{3-5}, is more suited to be applied in diesel engines than single-component OME fuels [30].

In addition to the different fluid properties for OME_n and standard diesel fuel shown in Table 2.1, Lautenschütz et al. [32] reported that the surface tension for OME_n is higher compared to n-alkanes of the same molecular chain length (number of carbon plus oxygen atoms in chemical structure) and exceeds that of EN 590 diesel starting from OME_4. The authors in [33] demonstrated a decreasing vapor pressure and a higher heat of evaporation with increasing length

(n) of OME_n fuels. These characteristics of OME_n, compared to diesel-like fuels, lead to a different liquid fuel breakup, evaporation, and autoignition process.

The liquid length was observed in typical diesel sprays to depend on ambient and fuel injection conditions [34–36]. However, the fluid properties of the used fuel were also demonstrated to play a significant role. Besides the positive correlation between fuel boiling-point and liquid length [37–39], experimental investigations by Kook and Picket [40] pointed out that higher liquid fuel densities lead to an increased liquid penetration length as the ratio of ambient hot air mass entrainment per liquid fuel mass decreases. The higher density, in combination with the other characteristics of OME_n, points to a greater liquid penetration length the higher the number (n) of oxymethylene ether groups (-CH_2O), which was experimentally proven under diesel engine relevant conditions in a constant-volume chamber in [41]. It was also demonstrated in [41] that the liquid of an OME_{3-5} fuel mixture penetrates further than n-dodecane but is shorter than standard diesel fuel.

The mixture formation of an OME_{3-5} fuel composition, identical to the one used in the present research, was analyzed in an oxygen-free environment in [42]. Consistent with previous studies, the mass distribution within the spray was determined to be independent of the actual fuel used. However, local equivalence ratios differed significantly due to the different stoichiometric air requirements, with OME_{3-5} showing a highly elevated air-fuel ratio along the jet center axis. The combustion concepts of diesel spray presented in Figures 3 and 4 only partially apply for oxygenated fuels, like OME_{3-5}. The distinct and separated zones of fuel, air, and fuel-air mixtures are composed differently, especially close to the jet center. Depending on the chemically bound oxygen content and stoichiometric air requirement of an oxygenated fuel, oxygen, and hence ignitable mixtures, were shown in [42] to be present at locations virtually impossible to reach for conventional non-oxygenated fuels.

The different properties for the OME_n fuels yield a diffusion flame with distinct characteristics that differ from non-oxygenated fuels but also for various mixtures of OME_n components. Pastor et al. [41] showed that the lift-off length stabilized farther away from the injector tip for OME_1 compared to a mixture of OME_{3-5}, with a significantly longer ignition delay, indicating the influence of the different reactivities (cetane numbers) of the two fuels. Neither fuel showed any soot production. OME_{3-5} was shown to ignite earlier than n-dodecane, diesel, and hydrotreated vegetable oil (HVO), even though its cetane number was not the highest of the tested fuels. This observation indicates the different ignition behavior for OME_n fuels compared to standard diesel-like fuels.

The transition from the cool flame, indicated by the production of formaldehyde (CH_2O), to the high-temperature reactions, highlighted by the rise of excited OH^* or ground state OH radical concentration, is an essential characteristic of the compression-ignition combustion process. It was shown to play a significant role in the flame lift-off stabilization process [24], which was recently confirmed with advanced CH_2O planar laser-induced fluorescence (PLIF) measurements

and Large Eddy Simulations (LES) calculations for n-dodecane [43]. Apart from the previously mentioned three global phases of diesel combustion, the authors in [43] identified several distinct stages of combustion, the first being the initial detection of CH_2O at the periphery of the jet, which is then consumed to form OH radicals signaling the second stage, or high-temperature, ignition. The transient behavior and the locations of these ignition stages are not yet known for OME combustion. Furthermore, the mixture paired with the formation and consumption of CH_2O and OH was shown in [43] to only yield equivalence ratios of $\phi < 3$ before the high-temperature ignition starts. This process, identified as the "cool-flame wave", which describes the propagation of elevated CH_2O concentrations from lean to fuel-rich mixtures prior to the high-temperature ignition, has not yet been studied for OME fuel mixtures.

The influence of short pilot injections on the overall combustion process of compression ignition engines is significant. The unburned hydrocarbon (UHC) and carbon monoxide (CO) emissions are reduced since, for each injection pulse, the in-cylinder charge is more fuel lean, which results in a more complete combustion [44]. From a modeling point of view, short pilot injections pose a significant challenge because of their highly transient behavior and the small and hard-to-quantify amount of fuel introduced into the combustion chamber. The injector is forced into a ballistic working regime. The coil energizing time and the amount of injected fuel are not correlated linearly, and the entire injection process is dominated by ramping-up and down phases. Flowmeter measurements with long-tube type instruments (HDA) were reported in [45] to deliver unrealistic results for short pilot injections for the standardized Spray A injector used by the Engine Combustion Network (ECN) [46]. Therefore, the authors in [47] pursued an approach to model the injection profile based on the conservation of momentum along the spray axis. The fluid properties also have to be considered for pilot injections. Strauß et al. [42] showed that the low viscosity and high density of the used OME_{3-5} fuel strongly influenced the opening and closing behavior of the nozzle. The opening process needed more time than for n-dodecane and 1-octanol, and the injector did not even open completely when injecting OME_{3-5}. The impact of those characteristics for OME on the combustion process with a multiple-injection scheme using short pilot injections is yet to be thoroughly analyzed.

Computational Fluid Dynamics (CFD) tools are essential for an in-depth understanding of the processes dominating diesel combustion. To correctly represent the low- and high-temperature ignition stages and the subsequent diffusion flame, chemical reaction mechanisms are used as a direct input to the CFD code. These mechanisms model the most significant reaction steps in the oxidation scheme of the respective fuel. The detailed reaction kinetics of diesel fuels and their surrogates encompass thousands of species and reactions. For instance, the detailed mechanism developed by Westbrook et al. [48] for n-alkanes from n-octane to n-hexadecane consists of 2775 species and 11173 reactions. Hence, the mechanisms must be reduced for utilization in CFD applications. For OME_n fuels, several reaction mechanisms were developed recently for different OME_n component fuels. Sun et al. [49] developed a reaction mechanism for OME_3

including only high-temperature reactions with rate constants analog to dimethyl ether (DME: CH_3OCH_3) and diethyl ether (DEE: $C_2H_5OC_2H_5$). He et al. [50] extended this mechanism to incorporate low-temperature reactions based on theoretical "ab initio/density functional theory" calculations for OME_1. It contains 225 species and 1082 reactions. Cai et al. [51] provided a reaction mechanism for OME_{2-4} consisting of 322 species by applying an automatic generator for the base reaction classes of the OME_1 mechanism published in [52]. The calculated ignition delays showed improved behavior compared to the mechanism of He et al. [50] when validated against shock tube (ST) experiments over a range of pressures (10 bar and 20 bar), equivalence ratios (0.5, 1.0, and 2.0) and temperatures (663-1137 K). Niu et al. [53] created a reaction mechanism for the combustion of OME_{1-6}, suitable for simulating various mixtures of OME components. It was developed in two steps, first a sub-mechanism for OME_{1-2} is formed using a decoupling methodology [54] on the mechanism of Cai et al. [51]. The reaction paths for OME_{3-6} are deduced by postulating that the bond dissociation energies of all *C-O* and *C-H* bonds of the same type are similar in different OME_n [49]. The final mechanism only consists of 92 species and 389 reactions, making it an efficient choice for CFD simulations of internal combustion engines. The capability to predict the ignition delay was shown to be at least the same quality as for the detailed mechanism by Cai et al. [51]. However, it was noted that both mechanisms, reduced [53] and detailed [51], showed deviations from experimental data when calculating the ignition delay at lean and stoichiometric conditions, suggesting that possible improvements are needed for the high-temperature chemistry. Using the measured laminar flame speeds for OME_1 in [55] and OME_3 in [49], the proposed reduced mechanism proved to predict the experimental data satisfactorily. However, the lack of concentration profiles of key species, i.e., CO, CO_2 or CH_4, for the combustion of OME_n at different ambient conditions obtained with jet-stirred reactor (JSR) measurements, was also highlighted in [53].

2.2 Research Objective

This thesis aims to extend the knowledge on the spray atomization and ignition characteristics of an OME_{3-5} fuel compared to diesel-like fuels, including the influence of multiple injection patterns. Experimental data received from research institutions in an international network project was used to validate a numerical spray combustion model that does not only cover the physical and chemical characteristics of conventional fuels but also those of oxygenated e-fuels like OME_{3-5}. In particular, the following key questions drove the research:

1. What are the differences of OME_{3-5} and conventional diesel-like fuels for the inert spray? The basis of understanding the combustion process of any fuel is to fully understand the spray characteristics, i.e., atomization, evaporation, and turbulent mixing, first. A goal of the research was to analyze the liquid and gaseous phase of the OME_{3-5} spray in an oxygen-free environment

to determine the differences to diesel-like fuel sprays caused by the different chemical and physical properties of OME_{3-5}.

2. How does OME_{3-5} differ from conventional fossil fuels in terms of its spatio-temporal behavior of ignition?
Key parameters of the compression-ignition combustion process, like ignition delay and flame lift-off length, needed to be investigated for various ambient conditions to yield a detailed picture of the global ignition characteristics of OME_{3-5}. The influence of changing ambient temperatures and oxygen content in the atmosphere was of interest to determine possible deviations from conventional diesel-like fuels.

3. How does the chemically-bound oxygen in OME_{3-5} influence the mixing and the subsequent flame morphology?
Conventional diesel-like fuels do not contain any oxygen, whereas OME_3 consists of 47 wt.% oxygen, which even increases to 48.9 wt.% for OME_5. The exact manner and intensity of how the significant amount of oxygen affects the flame shape, as well as the flame's low- and high-temperature reaction distribution, signaled by the rise of CH_2O and OH-radical concentrations respectively, was another research objective.

4. How do the fluid properties for OME_{3-5} influence the compression-ignition combustion with multiple-injection patterns?
Multiple injection strategies are common in real engine applications and are needed for advanced combustion control. The differences in the fluid properties for OME_{3-5} compared to conventional diesel-like fuels, especially the significantly lower LHV, are likely to cause a different characteristic transient behavior of the combustion process. In particular, short pilot injections deliver a complex mixture formation and ignition process and pose a challenge to CFD modeling approaches [47]. The interaction of the main fuel injection with the burned and unburned species resulting from the pilot injection was not yet studied for OME_{3-5}. The aim was to identify differences in the transient ignition behavior of OME_{3-5} and diesel-like fuels.

5. How does the compression-ignition engine cycle of OME_{3-5} differ from diesel-like fuels?
A major aspect of this research was transforming the free-jet CFD model to a single-cylinder engine model, intending to gain further insights into the OME_{3-5} combustion in a more application-oriented approach. The experimentally demonstrated nearly soot-free engine combustion for OME_n fuels found in the literature [4–8] drove the investigation into the mixing regime of the OME_{3-5} engine combustion. The analysis of the potential of OME_{3-5}, compared to diesel-like fuels, to form soot-precursors was a key point of this research.

6. What is the influence of the turbulence modeling approach in characterizing the differences in turbulent mixing and autoignition for OME_{3-5} and diesel-like fuels?
The compression-ignition process is characterized by turbulent mixing. The different phases of the diesel combustion process for conventional, diesel-like fuel prior to and after high-temperature ignition are well-characterized conceptually [17, 18], and more detailed by thorough experimental and numerical investigations [43]. An objective of the present research was to describe the transition from the cool flame, indicated by the formation of formaldehyde (CH_2O), to the high-temperature ignition, signaled by the rise of OH-radicals, for OME_{3-5}. Comparing the combustion stages of diesel-like fuels identified in [43] to OME_{3-5}, an emphasis was set to understand the effect of different turbulence modeling approaches, Reynolds-Averaged Navier-Stokes (RANS) and Large Eddy Simulations (LES).

7. What is the impact of the reaction mechanisms on the simulated flame morphology and the quality of predicting the combustion characteristics of OME_{3-5}?
Reaction kinetics for OME_n fuels as input for CFD codes were developed only recently with a clear focus on describing the combustion of OME_3. As this research used an OME mixture with significant shares of OME_4 and OME_5, see Table 3.1, most developed reaction mechanisms would introduce intrinsic errors into the simulation by neglecting the different fuel properties of different OME components. As only the mechanism of Niu et al. [53] incorporated OME components up to OME_6, a research objective of this thesis was to determine the potential of this reaction mechanism and to highlight possible areas of improvements to better match the ignition characteristics and flame morphology of OME_{3-5}.

3 Methodology

This thesis's research is based on numerical investigations validated by experiments conducted by several partner institutes within an international research project. Various experimental techniques were applied to generate an appropriate database to focus the numerical model validation. The injection system and ambient conditions to be studied were chosen to represent realistic diesel engine operating points for passenger vehicles based on the guidelines published by the Engine Combustion Network (ECN) [46]. The standardized operating point of *Spray A conditions* was set as a baseline for the present research. It represents ambient conditions at the start of injection (SOI) of $T_\infty = 900$ K and $\rho_\infty = 22.8$ kg/m^3. Depending on the ambient gas composition, this results in an ambient pressure of approximately $p_\infty \approx 60$ bar. The injector conditions are set to an injection pressure of $p_{inj} = 1500$ bar and a fuel temperature of $T_f = 363$ K. The investigation of different ambient conditions focused on varying the ambient temperature and the oxygen content at SOI while keeping a constant ambient density of 22.8 kg/m^3. An oxygen content of the ambient gas of 0 Vol.-% was used to study the inert spray, while reactive conditions were analyzed at 15 Vol.-% and 21 Vol.-% oxygen. The investigated injection patterns were differentiated as single and multiple injections. The single injection consisted of an injection duration of $t_{inj,single} = 1.5$ ms. The multiple injection pattern was realized with a timing of 0.3 ms for the pilot injection, 0.5 ms for the dwell phase, and 1.2 ms for the main injection duration ($t_{inj,multi} = 0.3/0.5/1.2$ ms).

Two different fuels were investigated: n-dodecane as a diesel-like n-paraffinic reference fuel and an OME$_n$ fuel consisting of components with $n = 3,4,5,6$, see Table 2.1. The composition of the used OME$_n$ fuel and its different oxymethylene ether groups is displayed in Table 3.1, taken from a batch analysis conducted by Analytik Service Gesellschaft (ASG) [56]. It can be seen that OME$_3$ dominates the chosen fuel with only traces of OME$_6$. Hence, from now on, the fuel is referenced by its major contributing components, OME$_{3-5}$. The physical and chemical properties of the OME$_{3-5}$ fuel are shown in Table 3.2 together with those of n-dodecane. The values are extracted from the batch report of ASG [56] and from [41].

Table 3.2: Fuel properties for n-dodecane and OME_{3-5} [41, 56].

Property	**Unit**	**n-dodecane**	**OME_{3-5}**
Density	kg/m^3 (T=15°C)	751.20	1057.10
Viscosity	mm^2/s (T=40°C)	1.44	1.08
Cetane number	-	74	68.6
Lubricity	µm	563	320
Flashpoint	°C	83	65
Lower heating value	MJ/kg	44.20	19.26
Initial boiling point	°C	214.00	144.40
Final boiling point	°C	218	242.4
Total contaminations	mg/kg	-	< 1
Carbon content	% [m/m]	84	43
Hydrogen content	% [m/m]	16	8.53
Oxygen content	% [m/m]	0	46.4
$(A/F)_{st}$ at 21% of O_2	-	14.92:1	5.89:1
$(A/F)_{st}$ at 15% of O_2	-	20.72:1	8.18:1
Heat of Vaporization (T=90°C)	kJ/mol	62.80*	52.23*

* Taken from internal AVL FIRE database

Table 3.1: OME fuel components.

Molecule	**Content [wt. %]**
OME_1	0.01
OME_2	< 0.01
OME_3	57.90
OME_4	28.87
OME_5	10.07
OME_6	1.91

This thesis utilizes three different injectors as part of the research: The Continental 3 Hole injector (Conti3L), the Spray A3 injector, and the Spray B injector. The investigations with constant-volume chambers (CVC), publications [57–59], were conducted with the Spray A3 and the Conti3L injector. The engine simulations and optical experiments in [60] were achieved with the Spray B injector. Table 3.3 lists the characteristics of the different injectors. The Spray A3 injector used in this study is a piezo-actuated injector with a highly convergent single-hole orifice nozzle. It is a standardized injector of the ECN with more details described in [61]. The Conti3L injector is also piezo-driven but has three holes based on a common rail high-pressure diesel injector unit PCRs2. Its orifices are oriented at 45° elevation from the injector axis and with a constant angle of 120° between orifices. The Spray B injector is a three-hole injector with an elevation angle of 72.5° for usage in diesel engines. As a standard injector of the ECN, more details can be found in [46, 62]. The contraction coefficient (C_A) of all injectors considers the

reduction of free flow area caused by non-uniform velocity profiles, hydraulic flip, or cavitation.

Table 3.3: Injector properties.

	Conti3L	Spray A3	Spray B
Orifice exit diameter (d_{noz}) [µm]	115	97	90
Contraction coefficient (C_A) [-]	0.98	0.98	0.98
Number of holes [-]	3	1	3
Elevation angle [°]	45	0	72.5

3.1 Numerical Methodology

All simulations carried out at the TU Wien were set up using the commercial CFD code AVL FIRE™ version 2020 R1. However, the described models and their scientific approach are not designated to this software and can be implemented in any other comparable software. They were based upon the Reynolds-Averaged Navier-Stokes (RANS) approach to model the turbulent flow field.

Additional CFD calculations were conducted at Sandia National Laboratories (SNL), employing Large Eddy Simulations (LES) to compare the influence of the turbulence modeling. This simulation setup was validated previously and can be studied in the literature [43, 63]. A detailed comparison of the two turbulence models (LES and RANS) can be found in [59].

Thus, the following paragraphs describe the development and setup of the RANS simulation model, which was the main focus of this research.

3.1.1 General Simulation Environment

The basis of the numerical methodology of the research is the Euler-Lagrange approach, where the gaseous phase is simulated within an Eulerian framework. On the other hand, the liquid phase is modeled by discrete droplets, which are collected by their respective properties within so-called parcels. These parcels are then tracked throughout the computational domain in a Lagrangian manner.

As part of the research project that led to this thesis, a large number of CFD simulations for a constant-volume chamber and a research engine were intended from the beginning. Therefore, the decision was made to use a RANS turbulence modeling setup because LES were assessed as computationally too expensive. The well-established $k-\zeta-f$ turbulence model, proposed in [64], was chosen to model the turbulent flow field for the free-jet investigations [57] as well as for engine cycle simulations [60]. This approach applies to all relevant models described in this chapter. The detailed investigation of the free-jet combustion for n-dodecane and OME_{3-5} delivered comprehensive and validated models for the fuel spray injection and the combustion,

which were then imposed on a single-cylinder engine model. This methodology was chosen to guarantee that the different models used in the setup are validated.

The standards and methodologies published by the ECN [46] were an essential reference for this thesis. Besides establishing methods for standardized analysis of spray combustion simulation, see Chapter 3.1.4, a reference for well-resolved RANS calculations for diesel-like sprays is set with a maximum resolution of 250 µm in cell size. Based on this recommendation, a grid dependence analysis for the spray simulations for this research was concluded with the generation of spray refinements for all used meshes with a minimum cell size of 125 µm.

3.1.2 Spray Model

In general, liquid spray breakup can be characterized by two consecutive processes. At first, the intact liquid core disintegrates into ligaments. This process is usually referred to as spray atomization or primary breakup. It is mainly driven by turbulence and cavitation of the liquid jet, originating inside the nozzle and reaching the nozzle exit [25]. The subsequent breakup of the ligaments into smaller droplets is classified as secondary breakup. Reitz and Bracco [65] defined four regimes for the primary breakup: Rayleigh, First Wind Induced, Second Wind Induced, and Atomization. The regimes can be classified by the dimensionless Reynolds (Equation 3), Weber (Equation 4), and Ohnesorge (Equation 5) numbers, referencing injection velocity (v_{inj}) and nozzle orifice diameter (d_{noz}). The subscripts l and g denote the properties of the liquid and gaseous phases, respectively. The Rayleigh regime describes liquid fuel breakup with small Reynolds numbers and low relative velocities between the fuel spray and the ambient atmosphere. On the other end of the spectrum, the atomization regime describes the rapid liquid core disintegration of fuel sprays due to high injection pressures and velocities, resulting in high Reynolds and Ohnesorge numbers accordingly. The injection process in diesel engines almost entirely falls within this regime. The other regimes only play a minor role at the beginning and end of the injection, when low relative spray velocities occur due to the throttling of the flow in the needle seat area [66].

$$Re = \frac{\rho_l v_{inj} d_{noz}}{\mu_l} \tag{3}$$

$$We = \frac{\rho_g v_{inj}^2 d_{noz}}{\sigma_l} \tag{4}$$

$$Oh = \frac{\mu_l}{\sqrt{\rho_l \sigma_l d_{noz}}} \tag{5}$$

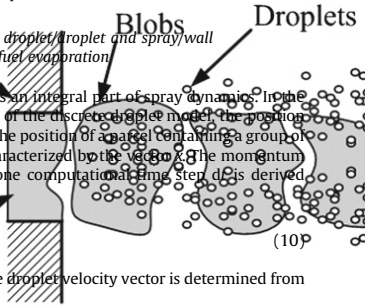

Fig. 2. (a) Schematic of the *Blob*-injection model [67], taken from [68].

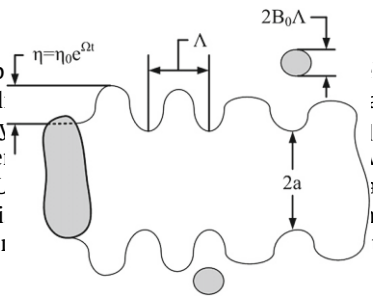

Fig. 3. Schematic diagram showing surface waves and breakup of a "blob".

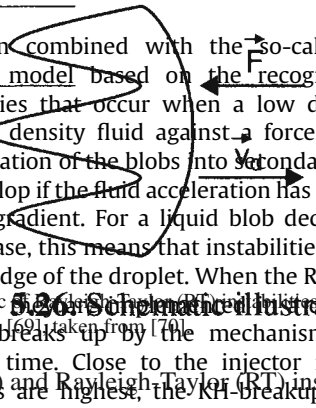

Fig. 4. Schematic illustration of Rayleigh–Taylor (RT) instabilities acting on a *Blob* [69], taken from [70].

Figure 6: *Blob*-injection model with Kelvin-Helmholtz (KH) and Rayleigh-Taylor (RT) instabilities.

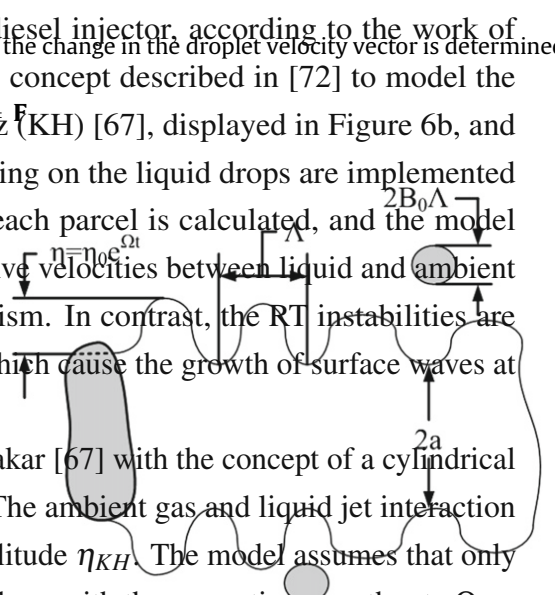

Fig. 3. Schematic diagram showing surface waves and breakup of a "blob".

and wavelength Λ_{KH}. The calculation of the resulting droplet radii ($r_{d,KH}$) of the breakup process is described with Equation 6. This successive breakup of liquid droplets leads to a reduction in the size of the injected blobs. The radius of each parent drop (a_{KH}) is changing in time according to Equation 7 with the characteristic breakup time τ_{KH} (Equation 8).

$$r_{d,KH} = B_0 \Lambda_{KH} \tag{6}$$

$$\frac{da_{KH}}{dt} = -\frac{a_{KH} - r_{d,KH}}{\tau_{KH}} \tag{7}$$

$$\tau_{KH} = 3.726\, B_1 \frac{a_{KH}}{\Lambda_{KH}\Omega_{KH}} \tag{8}$$

B_0 is generally set to 0.61 following the original findings of Reitz [67]. However, the model parameter B_1 is the primary fitting parameter for the KH breakup. The values can vary widely, with AVL FIRE™ allowing for a range of 5-60. The authors of [73] chose a value of $B_1 = 1.73$, whereas Patterson and Reitz [74] used a value of $B_1 = 30$. This indicates the influence of the cavitation structures and turbulent eddies of the inner nozzle flow on the primary breakup that is attempted to be captured by this parameter. As the liquid length and, hence, the mixing process is affected significantly by B_1, the present research aimed to limit the range of values used for this parameter to ensure the model's predictivity. All RANS calculation results in this thesis were achieved with a range of values of $B_1 = 8.5 - 10$. Using these relatively small values, the liquid breakup process of the injected blobs could be modeled fast enough to represent the experimentally determined liquid length adequately.

The RT instabilities are caused when a liquid-gas interface is accelerated opposite the density gradient. When a liquid droplet decelerates due to drag forces, the RT instabilities grow at the trailing edge (Figure 6c). The acceleration, i.e., the drag forces, is the primary driver of the rapid growth of RT instabilities, whereas the surface tension (σ) counteracts the droplet breakup. The characteristic breakup time (Equation 9) is derived with the frequency (Ω_{RT}) of the fastest growing wave describing the RT instabilities and is only valid in case the respective wavelength is smaller than the diameter of the parent droplet ($\Lambda_{RT} < 2a_{RT}$).

$$\tau_{RT} = \frac{1}{\Omega_{RT}} \tag{9}$$

The droplet velocities and accelerations are highest near the injector nozzle, making the RT breakup dominant in the near nozzle regions. The KH breakup becomes the governing model further downstream [70]. However, the KH-RT model enforces one constraint to model the intact liquid core. It defines a certain length downstream of the nozzle where the liquid phase only undergoes KH breakup according to Equation 10. Otherwise, the RT breakup model would predict a too rapid breakup at the nozzle exit. This thesis utilized a value of $C_{KHRT} = 10$

throughout all simulations, based on the findings in [72].

$$L_{KH,breakup} = C_{KHRT} \sqrt{\frac{\rho_l}{\rho_g}}\, d_{noz} \tag{10}$$

Picket et al. [45] highlighted the weaknesses of measuring the mass flow rate of injection (ROI) using a standard long-tube instrument where the fuel is injected into a column of the same fuel at a certain back pressure. The detected change in pressure in the column is directly related to the ROI [75]. Especially during injection startup, the experiments were shown to underestimate the actual ROI, with significant fluctuations during the first 200 µs of injection. As the injection rate represents an input boundary condition to the CFD model, these uncertainties are critical to adequately modeling the processes within a diesel spray. A model ROI called *Virtual Injection Rate Generator'* [76] correctly predicted the measured spray penetration of the standardized Spray A injector of the ECN. It was developed by the CMT-Motores Térmicos of the Universidad Politécnica de Valencia, considering expected hydraulic pressure fluctuations but rejecting fluctuations considered experimental noise artifacts. Following the recommendations of the ECN [46], the proposed model ROI for the standardized injectors Spray A3 [76] and Spray B [62], from now on called virtual rate of injection (VROI), was used in the present research. The VROI for the Conti3L injector was determined in close approximation to the model proposed by CMT. Figure 7 displays the virtual ROI used as CFD input in contrast to the measured mass flow rate with the standard long-tube device (HDA) at the Institute of Fluid System Technology (FST) at the University of Erlangen-Nuremberg for n-dodecane (DOD) and OME_{3-5}. The ambient and injector conditions were nominal *Spray A conditions'* ($T_\infty = 900$ K, $\rho_\infty = 22.8$ kg/m^3, $p_{inj} = 1500$ bar). The calculated (VROI) and measured (HDA ROI) rates of injection for the Conti3L injector are seen in Figure 7a. The ramping-up and ramping-down phases are modeled significantly faster compared to the measurements. The quasi-steady phase, approximately 250 µs after SOI, likely shows no fluctuations since the results are averaged for all three nozzle holes. Therefore, the modeled VROI follows the measurements of the Conti3L injector for the quasi-steady phase.

As described in chapter 2.1, short pilot injections are challenging to model because of the highly transient behavior. This magnifies the problems identified in the previous paragraph for correctly determining the mass flow rates. The method to model the pilot injection in this thesis was based upon the findings in [47]. The initial velocity at the nozzle exit for the pilot injections was calculated according to Equation 11, derived from the conservation of momentum along the spray axis. In Equation 11, the conservation of momentum is evaluated at the location of the fuel vapor penetration (S) with the respective vapor cone angle (Θ). Both parameters are experimentally determined. The constant a was described by Naber and Siebers [77] to establish a relation between the measured cone angle (Θ) and the theoretical spray dispersion angle (α), which showed the best agreement with experiments for a value of 0.66. The contraction

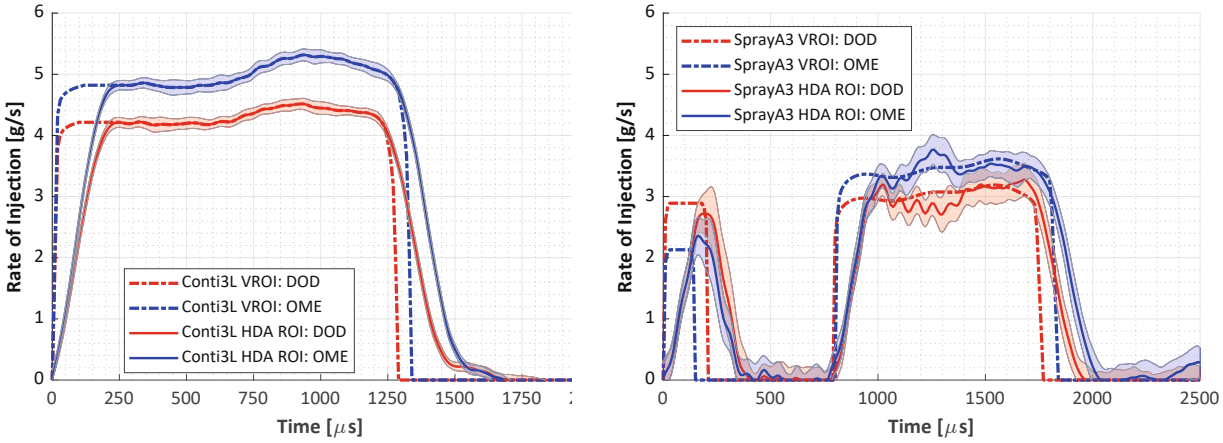

(a) Conti3L injector with single injection scheme.

(b) SprayA3 injector with multiple injection scheme.

Figure 7: Rate of injection (ROI) at standard *Spray A conditions*: Measured with HDA instrument and virtual ROI for CFD input.

coefficient of the injector nozzle is denoted as C_A in Equation 11, see table 3.3. The terms ρ_l and ρ_M describe the density of the liquid fuel and the mixture of fuel and ambient gas, respectively.

$$v_{0,pilot} = \frac{S^2}{t} \cdot a \cdot \tan\left(\frac{\Theta}{2}\right) \cdot \sqrt{\frac{\rho_M}{\rho_l \cdot d_{noz}^2 \cdot \sqrt{C_A}}} \tag{11}$$

In Figure 7b, the modeled and measured rate of injection is shown for the Spray A3 injector with an injection timing following the pattern of $t_{inj,multi} = 0.3/0.5/1.2$ ms for the pilot/dwell/main phases. The vapor penetration and cone angle were taken from the schlieren experiments conducted at FST to calculate the injection rate for the pilot injection. The fluctuations described in [45] are clearly visible for the HDA experiments during the initial phase of the main injection. Furthermore, the incomplete opening of the injector during the pilot injection can also be seen in Figure 7b. The maximum ROI is not reached for either fuel. Especially for OME, the difference in maximum ROI during pilot and main injection is significant, indicating the influence of the fuel's viscosity and density for the injector opening process identified in [42]. The faster ramp-up and ramp-down of the mass flow rates delivered as input to the CFD model was essential to correctly predict the spray penetration and, thus, to model the turbulent mixing process adequately.

The influence of the turbulent flow field on the trajectories of the liquid parcels was considered with the model established by O'Rourke [78]. The turbulent dispersion model takes into account that the instantaneous velocity of turbulent eddies deflects the liquid particles as they pass through them, which cannot be resolved in detail by the flow field. A fluctuating velocity (u_i') is added to the particles based on the gaseous phase's turbulence kinetic energy (TKE). The model by O'Rourke [78] hereby enables the particles to cross multiple turbulent eddies during one calculation step by updating u_i' and the location of the particles for each new eddies that is traversed. This procedure is beneficial in case the turbulent eddy break-up time or the time for a

droplet to pass the eddy is small since the spray calculation time step is not reduced, as would be necessary for other models, i.e. [79].

The evaporation of droplets had to consider the multi-component character of the OME_{3-5} fuel. This was accomplished by utilizing the model of Brenn et al. [80], which is a multiple-component extension of the classic evaporation model by Abramzon and Sirignano [81]. The only difference to the single-component model is that the mass transfer of every component is considered separately. The heat transfer, however, is still modeled as a global quantity as in the original model. The different components in the liquid droplet are assumed to be distributed homogeneously. The basis of this model are fictional gas films surrounding the evaporating droplet, which resist the heat and mass transfer with the respective thicknesses δ_T and δ_m. It is an iterative procedure based on calculating the mass transfer rates for each component (i) over the concentration boundary layer (δ_m) using the modified Sherwood number (Sh^* in Equation 12) as well as globally with averaged properties over the thermal film (δ_T) using the modified Nusselt number (Nu^* in Equation 13). In Equation 12, B_M denotes the Spalding mass transfer number and β the binary diffusion coefficient of fuel vapor in gas It should be noted that the implementation in AVL FIRE™, in contrast to [80], uses the total droplet diameter (D_d) instead of the volume equivalent partial diameter in Equation 12 and 13 to assure consistency in case of all components belong to the same fuel.

$$\dot{m}_i = \pi \left(\overline{\rho\beta}\right)_{i,g} D_d Sh_i^* \ln(1+B_{M,i}) \tag{12}$$

$$\dot{m} = \pi \frac{\overline{k}_g}{\overline{c}_{p,F}} D_d Nu^* \ln(1+B_T) \tag{13}$$

The global heat transferred to the droplet for evaporation is calculated with Equation 14, with the latent heat of evaporation (ΔH_{vap}) evaluated at the temperature of the droplet surface (T_S). The energy balance yields the new temperature of the droplet. Further explanation of the terms and the iterative procedure can be found in [80, 81].

$$\dot{Q} = \dot{m}\left(\frac{\overline{c}_{p,F}\cdot(T_\infty - T_S)}{B_T} - \Delta H_{vap}(T_S)\right) \tag{14}$$

The drag-law coefficient to calculate the main force (drag force) acting upon the liquid parcels was calculated with the correlation developed by Schiller and Naumann [82].

3.1.3 Combustion Model

The fuel spray combustion was simulated using direct chemical kinetic solver methods, where chemical reaction mechanisms describing the oxidation of the respective fuels are solved during run-time. Each computational cell is treated as a zero-dimension reactor model and calculates the source terms for each species transport and enthalpy equation at the beginning of each time

step. The chemical reaction mechanisms detail specific reaction rates for the production and destruction of the involved species based on the respective concentration and the temperature within the grid cell.

The chemical reaction mechanism is a crucial driver of the prediction quality of the numerical setup. Novella et al. [83] compared several reduced and skeletal reaction mechanisms, ranging in complexity from 110 to 29 species, under *Spray A conditions*. The 2D RANS calculations confirmed the importance of adequate reaction mechanisms to correctly predict the ignition delay, the ignition sites, and the spatial configuration of the flame, especially the lift-off length.

The kinetic models used in the present research are the mechanisms developed by Yao et al. [84] for the combustion of n-dodecane and the oxidation mechanism constructed by Niu et al. [53], described in chapter 2.1. The ECN recommends the oxidation scheme by Yao et al. for the spray combustion simulation of n-dodecane. It is a skeletal mechanism with 54 species and 269 reactions and involves sub-mechanisms for high-temperature and low-temperature chemistry. The starting point of its development was the semi-detailed mechanism developed by You et al. [85] with 171 species and 1306 reactions, which was extensively validated for high-temperature conditions. The low-temperature reaction rates were tuned against a detailed mechanism by the Lawrence Livermore National Laboratory (LLNL) [86], consisting of approximately 7200 species and 31400 reactions, and experimental data at *Spray A conditions*. It was validated regarding ignition delay against shock tube experimental data and the conversion rate of n-dodecane and species mole fraction profiles against jet-stirred reactor (JSR) measurements. Additionally, laminar flame speeds calculated with one-dimensional simulations were compared against experiments. The mechanism performed well over a wide range of ambient conditions, even compared to the detailed LLNL mechanism.

In addition, the LES and RANS calculations for n-dodecane in [59] were conducted with a mechanism recently developed by the LLNL and described in the supplementary material in [43]. It consists of 251 species and 1484 reactions. It was derived by isomer and reaction lumping along the essential reaction pathways of the current state-of-the-art detailed kinetic mechanism for n-dodecane [87]. The ignition behavior of the detailed kinetics mechanism [87] was validated intensively by employing a rapid compression machine (RCM). The 0D-simulated ignition delay of the reduced mechanism presented in [43] was compared to the detailed mechanism across a wide range of pressure, temperature, and equivalence ratios.

As described in chapter 2.1, the mechanism of Niu et al. for the oxidation of OME_{1-6} consists of 92 species and 389 reactions and is, so far, the only publicly available OME_n reaction mechanism that incorporates all components of the OME fuel mix (Table 3.1) used in this thesis. The compact structure of this mechanism ensures time-efficient computation of in-cylinder combustion. However, the authors of [53] suggested adjustments to the high-temperature chemistry. Also, they pointed to the lack of jet-stirred reactor (JSR) measurements to validate the production and destruction of key species, i.e., CO, CO_2 or CH_4, for changing ambient

conditions. These considerations were the starting point of the research to create a new reaction scheme for the OME_{3-5} combustion. The investigation of the Shanghai Jiao Tong University (SJTU) resulted in a modified reaction, based on [53], with improved ignition characteristics at diesel engine relevant conditions and was published in [58].

Typically, a CFD simulation's kinetics solver treats every cell as a well-mixed homogenous reactor. This assumption does not consider fluctuations in the mixture composition and thermodynamic condition on a sub-grid scale. The influence of turbulence on the reaction kinetics in CFD simulations is referenced as turbulence chemistry interaction (TCI). Figure 8 illustrates fluctuations caused by turbulent eddies that deliver ambient air into the boundary shear layer of a diffusion flame. This process is called intermittency. The positions "1" in Figure 8a experience high fluctuations of their mixing and thermodynamic state, i.e., fuel or oxygen mass fraction and temperature. The transient development of the fuel mass fraction of these positions labeled "1" in Figure 8a is displayed qualitatively on the left in Figure 8b. It can be seen that almost always, there is either only fuel or ambient oxygen at these positions, but not a state of fuel and oxygen mixed. Simply averaging this location's fuel and oxygen mass fractions would generate an ignitable well-mixed mixture [88]. Probability density functions (PDF) can solve this problem by adequately weighing the different mixing states at different locations in the flame. The respective PDF of the fuel mass fraction in Figure 8b is displayed on the right, correctly emphasizing pure fuel or oxygen mixing states. To ensure time-efficient computation, an adequate shape of the PDF is presumed *a priori*, hence the naming convention *presumed* probability density function (pPDF). Mostly *Gauß*- and β-distributions are chosen [9, 88]. The β-distribution is widely used in the case of tabulated kinetics. For this approach, the reaction mechanisms are tabulated, generally using the mixture fraction, see Equation 17, and temperature as variables, and the β-pPDF is constructed using the mixture fraction and its variance.

The TCI implementation in AVL FIRE™ is realized with a *Gauß*-pPDF applied on the local instantaneous temperature (Equation 15), which acts as the random variable satisfying the Gaussian distribution. This way, the pPDF implementation affects any non-linear function of the temperature [89].

$$\overline{f(T)} = \int_{-\infty}^{+\infty} f\left(\overline{T} + \sqrt{\overline{T'T'}} \cdot x\right) \cdot \frac{1}{\sqrt{2\pi}} exp\left(-\frac{x^2}{2}\right) \, dx \tag{15}$$

Kundu et al. [90] investigated the influence of TCI in a more general sense by solving 1D flamelet equations with a stoichiometric scalar dissipation rate (χ_{st}) of zero and $\chi_{st} = 2\ s^{-1}$. The case with $\chi_{st} = 0$ represents a homogeneous reactor. The value of $\chi_{st} = 2\ s^{-1}$ was calculated previously at ignition with CFD simulations using tabulated kinetics coupled with LES. It was reported that the first-stage ignition was not influenced by turbulence. On the other hand, scalar dissipation causes the low-temperature radicals to diffuse toward the relatively richer regions. It was observed that this diffusion process plays a significant role for the main ignition.

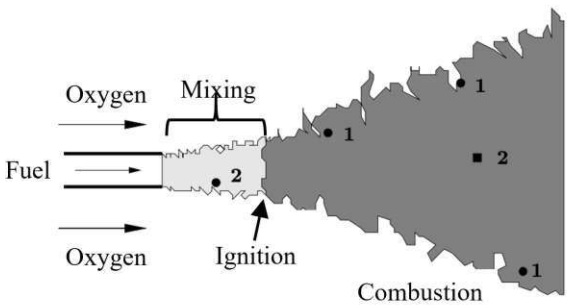

(a) Turbulent diffusion flame illustrating intermittency, adapted from [88].

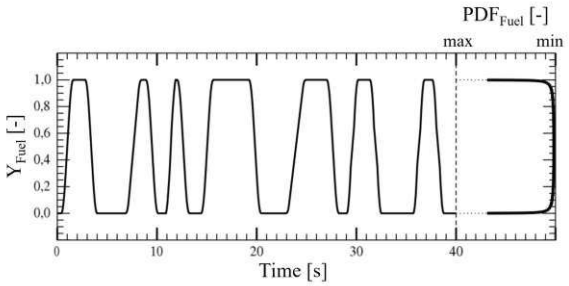

(b) Transient development of fuel mass fraction (left) at highly intermittent point ("1") with respective probability density function (right), adapted from [88].

Figure 8: Illustration of turbulent intermittency and its modeling via presumed probability density functions (pPDF).

However, in the course of the present research, it was found that the method of clustering the numerical cells based on their thermodynamic conditions, e.g., temperature, equivalence ratio, etc., to speed up the calculations of the chemistry solver did not alter the results in any significant way. With this so-called multi-zone speed-up method the chemical reactions are solved only for the mean of the clusters and the results are mapped back to the original cells. In AVL FIRE® the clustering and mapping-back processes follow the principles published in [91] and the clustering occurs within temperature ranges of $\Delta T = 5$ K and equivalence ratio zones of $\Delta\phi = 0.05$ [92]. The multi-zone speed-up is not possible to use if TCI is enabled for the simulation. Imposing a stochastic distribution on the instantaneous temperature is not compatible with the clustering procedure needed for the multi-zone method. However, only minor differences in ignition delay were monitored when using the multi-zone approach compared to simulations with activated TCI. The flame morphology was not observed to alter at all. The absence of significant influence when imposing the stochastic character of turbulence on the combustion model hints at an already well-resolved turbulent flow field. The high grid resolution was therefore assessed to be responsible for this behavior. Hence, the multi-zone approach was utilized to simulate the single-cylinder engine in [60]. The same applies when comparing the RANS calculations to the LES conducted by Sandia [59]. Because of the vast number of cells necessary to resolve the flow field sufficiently, enabling TCI for LES calculations was impossible without exceeding feasible time constraints.

The RANS calculations simulating the constant volume vessel published in [57,58] considered TCI via Equation 15 as the additional time needed to incorporate TCI in this setup was within reasonable limits. This ensured the best possible numerical setup to characterize the ignition behavior and flame structure of OME_{3-5}, even though the differences to simulations with the multi-zone approach were very limited.

3.1.4 Dedicated Analysis Tools

The techniques used to extract the spray characteristics from the CFD results discussed in this section are used throughout all publications of this thesis [57–60]. The basis of the post-processing is the modeling standards and recommendations published by the Engine Combustion Network (ECN) and can be reviewed in [46].

Determining the Liquid and Vapor Penetration Length

Throughout the research for the present thesis, the *Projected Liquid Volume* (PLV) approach was employed to calculate the penetration of the liquid droplets. It is the designated method encouraged by the ECN and specified in [46]. Alternative methods, e.g., determining the distance where 99% of the liquid mass in the computational domain is located upstream, have no physical correlation to the experimental techniques (Mie, DBI in Chapter 3.2). Pickett et al. [93] recommended the usage of a path integral analysis of the liquid volume fraction (LVF) for CFD simulations (Equation 16) while at the same time stressing the advantages of light-extinction diagnostics (DBI) over Mie-scatter lighting and summarizing the problems associated with the latter.

$$\overbrace{\tau_{opt}\frac{\pi d_d^3/6}{C_{ext}}}^{Experimental} = \overbrace{\int_{-y_\infty}^{y_\infty} LVF\ dy}^{Modeling} = \int_{-y_\infty}^{y_\infty} \frac{volume\ liquid}{unit\ volume}\ dy \tag{16}$$

This equation illustrates the link between the DBI measurements and the CFD simulations to determine the liquid penetration via the PLV method. Within the experimental setup, the optical thickness is referred to as τ_{opt}, and the extinction coefficient is denoted by C_{ext}. A detailed description of the values and the procedure can be found in [94]. A threshold of $\int_{-y_\infty}^{y_\infty} LVF\ dy = 0.2{\cdot}10^{-3}\frac{mm^3 liquid}{mm^2}$ was used throughout this thesis to determine the liquid penetration length.

The vapor penetration was defined as the maximum distance from the nozzle outlet where the mixture fraction (Equation 17) is at least 0.1% ($Z \geq 0.001$). The calculation of this passive scalar is related to element mass fractions Z_i of the i^{th} element, with superscripts f and ox denoting the specific element mass fraction for the pure fuel and oxidizer. In [95], the nitrogen element mass fraction was used to calculate the mixture fraction, which is also utilized throughout this thesis.

$$Z = \frac{Z_i - Z_i^{ox}}{Z_i^f - Z_i^{ox}} \tag{17}$$

High-Temperature Ignition

The ignition of the high-temperature flame of the reactive diesel-like spray was defined by the ignition delay time (ID) and the flame lift-off length (LOL). The ignition delay was calculated

based on when the temperature profile experiences the maximum gradient.

$$ID = t(max[dT/dt]) \tag{18}$$

The rise of the simulated *OH* species mass fraction determines the flame lift-off length. The first axial location, where it reaches 14% of its maximum value of the entire combustion process, is defined as the location of the flame establishment.

$$LOL = min[x(w_{OH} \geq 0.14 \cdot w_{OH,max})] \tag{19}$$

Mixing Analysis for Oxygenated Fuels

Instantaneous mixing of oxygenated fuels was shown in [96] to be incorrectly defined by the traditional formulation of the equivalence ratio ϕ (Equation 1). The existence of chemically bound oxygen in fuels was found to cause the equivalence ratio not to accurately quantify the proximity of a reactant mixture to its stoichiometric condition [96]. To properly analyze the mixing state of the OME_{3-5} fuel, the quantity proposed by Mueller [96] was used, namely the *oxygen equivalence ratio* ϕ_Ω. Equation 20 describes its dependence on the regular equivalence ratio, which is valid if the oxidizer contains no C- and H-atoms. This adapted definition accurately represents the distance of local mixtures to their respective stoichiometric conditions for oxygenated fuels.

The correct interpretation of the oxygen bound in the chemical structure of the fuel is accomplished by introducing the oxygen ratio of the fuel Ω_f, formulated in Equation 21. It is a property of the fuel itself. It represents the number of oxygen atoms per molecule of fuel divided by the number of oxygen atoms needed for the stoichiometric reaction of all C- and H- atoms of the fuel. In Equation 21, the subscript i denotes the index over all fuel species, and a_i describes the number of moles of the i^{th} fuel species. The OME_{3-5} fuel, detailed in its component composition in Table 3.1, has an oxygen fuel ratio of $\Omega_{f,OME_{3-5}} = 0.2566$.

$$\phi_\Omega = \frac{\phi}{1 + \Omega_f \cdot (\phi - 1)} \tag{20}$$

$$\Omega_f = \frac{\sum_i a_i n_{O,i}}{\sum_i a_i (2n_{C,i} + \frac{1}{2} n_{H,i})} \tag{21}$$

3.2 Experimental Validation

The numerical results were extensively validated for the different applications in constant pressure or constant volume combustion chambers and an engine cylinder. These measurements were conducted at various project partner institutions and collected and processed to generate a validation database for the numerical models.

The free-jet analyses were carried out at the Institute of Fluid System Technology (FST) at the University of Erlangen-Nuremberg as well as at the Combustion Research Facility (CRF) at Sandia National Laboratories (SNL). The engine experiments were conducted at the Institute for Combustion and Gas Dynamics - Reactive Fluids (IVG) at the University of Duisburg-Essen (UDE).

At the FST, the spray experiments were realized with an optically accessible high-temperature and high-pressure injection chamber with constant pressure. The liquid phase was diagnosed via Mie-scattering. The fuel vapor was analyzed using a typical schlieren setup. The high-temperature ignition was characterized by employing OH^*-chemiluminescence signal detection. For a detailed description of the experimental setup, the reader is referred to the corresponding publications that are part of this thesis [57, 58].

The constant-volume pre-burn spray chamber at Sandia delivered the additional free-jet measurements for the present research, albeit applying different techniques. The liquid penetration was determined with diffuse back-illuminated imaging (DBI). The fuel vapor and mixing were tracked with time-resolved Rayleigh scattering. The latter enables the quantification of the mixture fraction of the fuel spray, which constitutes a valuable measure to validate the CFD spray model. During the research, the different experimental techniques employed by FST and Sandia to measure the high-pressure injection fuel spray, Mie, DBI, schlieren, and Rayleigh, yielded consistent and comparable data. This fact confirmed the quality of the setup of both test benches and the techniques they employed. In addition, a characterization of the low- and high-temperature ignition was conducted at Sandia. High-speed planar laser-induced fluorescence (PLIF) imaging tracked the development of CH_2O, indicating the low-temperature ignition. To capture the high-temperature ignition, Sandia also used the OH^*-chemiluminescence technique. Further information about the setup at Sandia can be found in [57, 59].

Experiments investigating n-dodecane and OME_{3-5} in an optically accessible single-cylinder Diesel engine were conducted at UDE. The Bowditch-type [97] engine consisted of a fused silica piston window and was operated in skip-fire mode. Quantifying the liquid and vapor penetration length was done by taking advantage of the retro-reflection of LED light at the cylinder head (fire-deck retro-reflection). The chemiluminescence of the flame was recorded with two different high-speed cameras simultaneously in the UV (OH^*) and visible (CH^*) channels. Detailed information about the test bench is presented in [60].

4 Summary of Publications

1. Wiesmann, F., Strauß, L., Rieß, S., Manin, J., Wan, K., and Lauer, T. **Numerical and Experimental Investigations on the Ignition Behavior of OME.** *Energies*, 15(18):6855, 2022, doi:10.3390/en15186855.

   - Corresponding Author:
     Frederik Wiesmann

   - Contribution:
     Implementation of spray combustion model for OME and n-dodecane; execution of free-jet CFD simulations for inert and reactive conditions; validation of numerical models with experimental data; scientific documentation of results.

   - Summary:
     This research investigated the free-jet spray characteristics of the OME_{3-5}, or simply OME, fuel compared to diesel-like n-dodecane for inert and reactive conditions. Numerical simulations were carried out for various operating conditions, including a range of ambient temperatures from 800 K to 1000 K, an ambient oxygen content of 0 %, 15 %, and 21 %, and single and multiple injection patterns. The analysis in an atmosphere devoid of oxygen showed that OME liquid penetrates further into the spray chamber than n-dodecane. When changing the ambient temperature, the location and timing of high-temperature ignition for OME followed a different trend than for n-dodecane. Generally speaking, OME tended to ignite earlier with a longer flame lift-off length. However, when lowering the ambient temperature to 800 K, the OME took longer to ignite than n-dodecane, with an observed temperature threshold for an identical ignition delay between 800 K and 900 K. Similarly, the simulated OME flame lift-off length suddenly dropped below the level of n-dodecane in a 1000 K atmosphere. The experiments showed an almost identical distance for the flame establishment at this temperature. This behavior signaled a diverging temperature dependency for OME, as the characteristic linear behavior between ignition delay and lift-off length for n-paraffinic fuels like n-dodecane could not be observed.

The high-temperature flame, observed by the onset of simulated *OH* species or detection of *OH** signals, was proven to differ significantly for OME and n-dodecane. For OME, the highest intensity occurred in the center of the spray, whereas n-dodecane showed high reaction activity at the distinct boundary of the ambient air and the fuel spray. Only there n-dodecane mixed into a combustible mixture. On the other hand, OME ignited at locations where it is impossible for non-oxygenated fuels to do so due to the chemically bound oxygen in OME.

Another major aspect of the research was the mixing regime of the combustion process for the two fuels. OME was proven to burn in an extremely lean mixture without a single computational cell experiencing an oxygen equivalence ratio above two. Hence, the region of increased soot production was never entered for OME simulations, in contrast to calculations with n-dodecane.

A transient analysis of short pilot injections demonstrated that the combustion process distinguishes more rapidly for OME due to the lower overall chemical energy content (lower LHV) introduced by OME when injecting for the same duration.

2. Wiesmann, F., Bauer, E., Kaiser, S. A., and Lauer, T. **Ignition and Combustion Characteristics of OME_{3-5} and N-Dodecane: A Comparison Based on CFD Engine Simulations and Optical Experiments.** *SAE Technical Paper 2023-01-0305*, 2023, doi:10.4271/2023-01-0305.

   - Corresponding Author:
     Frederik Wiesmann

   - Contribution:
     Transfer of free-jet spray combustion model to engine cycle simulations; establishment of CFD model that incorporates blow-by; validation of numerical models with experimental data; scientific documentation of results.

   - Summary:
     Using the free-jet spray combustion model of the previous work as a baseline, a CFD model of a single-cylinder engine representing an optically accessible vessel for experimental validation was developed. At first, the gas exchange process was simulated with a moving mesh describing the intake manifold and ports, cylinder and exhaust ports of the engine. The turbulent flow field was then mapped to a dedicated sector mode of engine cylinder. As a standard ECN Spray B 3-hole injector was used, only a third of the cylinder was considered. This sector model was equipped with a specific boundary to incorporate blow-by, observed on the test bench. Piston leakages caused it, which is typical for optically accessible engines operated in skip-fire mode.
     The previously determined characteristics of OME, regarding liquid length, ignition delay,

and lift-off length, compared to n-dodecane, were also confirmed to be present in an engine cycle operation. With constant injection duration, the pressure curve proved to be consistently lower, and the burnout phase was shorter for OME due to the lower heating value.

Experiments and simulations showed a distinct re-ignition of OME after short pilot injections, with ignition and re-ignition occurring in a narrow window of (oxygen) equivalence ratios. For n-dodecane, the ongoing high-temperature combustion made it impossible to detect a second ignition.

3. Wiesmann, F., Han, D., Qiu, Z., Strauß, L., Rieß, S., Wensing, M., and Lauer, T. **Numerical Study on Novel OME_{1-6} Combustion Mechanism and Spray Combustion at Changed Ambient Environments.** *Frontiers in Energy*, 2024, doi:10.1007/s11708-024-0926-8.

   - Corresponding Author:
     Frederik Wiesmann

   - Contribution:
     Integration of new OME reaction mechanism into spray combustion model; execution of CFD calculations; validation of numerical models with experimental data; scientific documentation of results.

   - Summary:
     Prior studies of the spray combustion characteristics of OME showed that different reaction mechanisms could not accurately predict ignition delay and lift-off length. In general, the ignition delay was underestimated by the CFD simulation. More detailed reaction mechanisms, which predicted an ignition delay closer to the measured values, tended to overestimate the flame lift-off length drastically. This behavior resulted in an incorrect representation of the flame morphology. Furthermore, the location of maximum high-reaction intensity for OME was measured to be in the center of the spray. The trend of that observation, compared to n-dodecane, could be captured by the CFD simulations. However, a significant difference between experiments and simulations remained, especially close to lift-off length. Therefore, the reaction mechanism used previously for the OME combustion [53] was modified via a sensitivity analysis that marked the *OH* radical of the mechanism. The ten most significant reactions were identified, and their reaction rate constants were modified.
     The newly developed OME reaction mechanism was applied to the free-jet CFD spray combustion model. An in-depth analysis was conducted comparing the new mechanism to its original counterpart. The results showed a considerable improvement in the quality of the predicted ignition delays for varying ambient conditions. Crucially, this improvement of the simulated ignition timing did not deteriorate results for the simulated lift-off length,

which were still in excellent agreement with the *OH**-chemiluminescence measurements. Elevated levels of simulated CH_2O species concentration on the spray center axis for the new mechanism did not translate into a significant improvement regarding the distribution of high-temperature *OH* species. The differences to the original mechanism by Niu et al. were relatively small.

4. Wiesmann, F., Nguyen, T. M., Manin, J., Pickett, L. M., Wan, K., Tagliante, F., and Lauer, T. **LES and RANS Spray Combustion Analysis of OME_{3-5} and n-Dodecane.** *Energies*, 17(10):2265, 2024, doi:10.3390/en17102265.

   - Corresponding Author:
     Frederik Wiesmann

   - Contribution:
     Execution of RANS calculations; collection and preparation of LES calculations; analysis of differences caused by usage of LES and RANS; validation of numerical models with experimental data; scientific documentation of results.

   - Summary:
     The influence of turbulence modeling on the quality of the high-temperature flame results and the description of the cool-flame evolution for OME_{3-5} are presented. A special focus was set on the impact of a highly elevated ambient temperature on the flame structure. In general, the LES was able to predict the levels of *OH** intensity, recorded via *OH**-chemiluminescence signal detection, in the jet center with a higher degree of accuracy, though still not accurate enough to pinpoint the turbulence modeling approach as the dominant cause for deviations between simulations and experiments. However, when raising the ambient temperature within the pre-burn chamber at SNL from 900 K to 1200 K, the measured flame shape altered significantly, falling more in line with the simulations, especially with the RANS calculations. The flame still showed peak intensities at the spray center, in contrast to n-dodecane. But, instead of generating only one lobe of peak signal intensity close to the flame lift-off length, the spray tip also indicated high reaction activity. Time-averaged flame contours for the quasi-steady combustion delivered promising agreement with RANS simulations, proving the quality of the numerical setup. This observation led to the conclusion that the shortcomings of the OME_{3-5} simulations, RANS and LES, at lower ambient temperatures could arise from inaccuracies of the kinetic reaction mechanism to account for the chemically bound oxygen in fuel-rich spray regions, like the jet center. This aspect could occur in conjunction with the fact that the more stable ground *OH* species in the simulations was compared to the shorter-lived *OH** excited species detected by the measurements.
     The rise of CH_2O concentration sweeping from lean to rich fuel mixtures, shown in a

previous study for n-dodecane, was confirmed for OME_{3-5} as well. However, significant differences were observed, with OME_{3-5} passing through this first ignition stage at lower temperatures and significantly smaller equivalence ratio values. The subsequent combustion analysis proved that polycyclic aromatic hydrocarbon (PAH) formation for n-dodecane occurs precisely where fuel-rich spray enters the high-temperature region of the combustion process. For OME_{3-5}, no fuel-rich spray comes close to the high-temperature combustion region, and no PAH signal was detected. At 900 K, a distinct axial separation of areas with fuel-rich spray, cool- and high-temperature flame was simulated. This observation could not be made for simulations with 1200 K ambient temperature, where small amounts of fuel-rich spray reach the high-temperature region. Still, even for OME_{3-5}, the PLIF experiments could not detect any PAH signal.

5 Scientific Contribution

This thesis presents scientific contributions in the research area of the autoignition and spray combustion of oxygenated fuels. The spray characteristics of an OME_{3-5} fuel mixture with properties comparable to standard diesel were investigated. A focus was set on the flame morphology and the differences to diesel-like fuels like n-dodecane.

A comprehensive CFD model was developed first to characterize the free jet and later the engine cycle properties of the OME fuel. The correct modeling of the physics governing spray breakup, air entrainment, and evaporation was imperative for the methodology of this thesis. Using the same spray and combustion model for different applications, this approach delivered novel insights into OME spray combustion. The guidelines and modeling standards of the Engine Combustion Network (ECN) were followed to help advance this global network of researchers on their path to establish a comprehensive and comparable database of fuel injection experiments and simulation efforts.

Consequently, the mixing regime of the combustion process of the OME fuel was shown to occur in an extreme fuel-lean range of equivalence ratios for the free jet and within the single-cylinder engine. Hereby, the chemically bound oxygen in OME needed to be considered to correctly display the proximity or distance of the local mixture to stoichiometric conditions. During the entire in-cylinder combustion process, OME_{3-5} almost completely avoided the conditions of increased soot yield ($\phi > 2$ at 1200 K < T < 2000 K according to [70, 98]).

Ignition delay and flame lift-off length were proven to react to ambient temperature changes differently for OME_{3-5} and n-dodecane. The linear relationship between ignition delay and flame lift-off length as experienced by n-paraffinic fuels like n-dodecane was shown to be different for OME_{3-5}. The drop in ignition delay time and flame lift-off length in the temperature range of $800\ K \leq T \leq 1000\ K$ is significantly sharper.

The lower LHV for OME_{3-5} resulted in significantly lower peak pressure in the single-cylinder engine compared to n-dodecane when the injection duration is kept constant. The transient behavior of OME_{3-5} caused by short pilot injections was demonstrated to alter significantly from n-dodecane, with distinct re-ignitions after the start of the main injection. This behavior

is essential to take into account for future applications, as injection control is a critical element in controlling the combustion cycle in an ICE. Additionally, it was shown that after short pilot injections, OME_{3-5} tends to concentrate its remaining reaction activity in the spray tip near the cylinder wall, in contrast to n-dodecane, which showed elevated reaction activity after the end of injection and close to the nozzle.

CFD simulations in the course of this research delivered reasonable and satisfactory results overall. However, the tendency of OME_{3-5} to ignite and burn in the center of the fuel spray was underestimated throughout the research. This led to an extensive investigation of the low- and high-temperature flame characteristics of OME_{3-5}. A novel reaction mechanism, adapted from the literature to enhance the prediction quality, especially of the ignition delay, was implemented into the CFD model. Significantly improved ignition delay predictions compared to experimental data were reported, albeit without impactfully improving the simulated high-temperature reaction activity in the fuel spray center.

An in-depth comparison of RANS and LES calculations modeling the same experimental spray chamber setup delivered valuable insights into what may cause the problems when modeling the combustion of OME_{3-5} in the spray center. It was shown that OME intensifies a generic problem, also present for n-dodecane, albeit less pronounced, of underestimating the reaction activity in the fuel-rich region of the spray center. Hence, this observation highlights possible deficiencies in current OME reaction mechanisms to adequately model the impact of the chemically bound oxygen on the high-temperature ignition in the fuel-rich spray center. Leveraging the capability of the experimental pre-burn chamber, the ambient temperature regime of 1200 K changed the spatial flame distribution substantially, with two peak intensities for the OME_{3-5} high-temperature reaction activity, which is simulated by both LES and RANS with better agreement compared to the 900 K case. The RANS simulations proved to be very accurate in predicting the overall flame shape, especially at 1200 K.

Finally, the LES calculations demonstrated the limitations of RANS by capturing small-scale fluctuations, which were impossible for the RANS setup to resolve. These oscillations, proven for n-dodecane in a previous study [43], occur in a very narrow mixing range for OME_{3-5}. However, the low-temperature *cool-flame wave* of rising CH_2O concentrations propagating from lean to rich mixing states before ignition was proven to exist for OME_{3-5} as well, albeit at lower equivalence ratios and temperatures.

6 Outlook

The investigation of the OME_{3-5} spray combustion within this thesis represents a significant step forward in characterizing the potential and adaptations needed for applying this e-fuel within an ICE. Nonetheless, the numerical calculations in the course of this research highlighted several aspects that still have room for improvement:

- As of now, the kinetic reaction mechanisms used for detailed CFD simulations resolving the hot-flame distribution do not appropriately model the conversion and reaction of chemically bound oxygen within oxygenated fuels in fuel-rich regions like the center of sprays.
- Future analysis should focus on consistency when validating high-temperature reactions of CFD simulations with experimental data. In the case of *OH**-chemiluminescence measurements as validation database, the numerical setup, hence the used reaction mechanism, should incorporate an equivalent species to the excited *OH** radical detected by the experiments. Otherwise, the combination of simulated *OH* species and ground state *OH*-PLIF measurements should be considered.
- RANS calculations were demonstrated to be quite capable and effective in modeling the overall flame shape and identifying global characteristics like ignition delay and flame lift-off. But the investigation also hinted at its limitations in capturing small-scale structures. Therefore, future research may need to use LES to improve the prediction quality of CFD models simulating oxygenated fuels.
- Next to the e-fuel OME_{3-5} considered in this thesis, other oxygenated fuels should be of interest for future research. Fuels like n-octanol also promise to reduce particulate matter emissions, albeit with different intrinsic properties.

Bibliography

[1] IEA. The Role of E-fuels in Decarbonising Transport. License: CC BY 4.0, IEA, Paris, 2023.

[2] IEA. The Future of Trucks: Implications for energy and the environment. Technical report, OECD, Paris, 2017.

[3] Schmidt, P., Weindorf, W., Zittel, W., Raksha, T., Zerhusen, J., Siegemund, S., Trommler, M., Kolb, O., and Zinnecker, V. The potential of electricity-based fuels for a low-emission transport sector in the EU. E-Fuels Study, German Energy Agency GmbH (dena), Ludwig-Bölkow-Systemtechnik (LBST), Berlin, 2017.

[4] Liu, J., Wang, H., Li, Y., Zheng, Z., Xue, Z., Shang, H., and Yao, M. Effects of diesel/PODE (polyoxymethylene dimethyl ethers) blends on combustion and emission characteristics in a heavy duty diesel engine. *Fuel*, 177:206–216, 2016, doi:10.1016/j.fuel.2016.03.019.

[5] Omari, A., Heuser, B., and Pischinger, S. Potential of oxymethylenether-diesel blends for ultra-low emission engines. *Fuel*, 209:232–237, 2017, doi:10.1016/j.fuel.2017.07.107.

[6] Gelner, A. D., Rothe, D., Kykal, C., Irwin, M., Sommer, A., Pastoetter, C., Härtl, M., Jaensch, M., and Wachtmeister, G. Particle emissions of a heavy-duty engine fueled with polyoxymethylene dimethyl ethers (OME). *Environ. Sci.: Atmos.*, 2(2):291–304, 2022, doi:10.1039/D1EA00084E. Publisher: RSC.

[7] Virt, M. and Arnold, U. Effects of Oxymethylene Ether in a Commercial Diesel Engine. *Cognitive Sustainability*, 1(3), August 2022, doi:10.55343/cogsust.20.

[8] Pélerin, D., Gaukel, K., Härtl, M., Jacob, E., and Wachtmeister, G. Potentials to simplify the engine system using the alternative diesel fuels oxymethylene ether OME1 and OME3-6 on a heavy-duty engine. *Fuel*, 259:116231, 2020, doi:10.1016/j.fuel.2019.116231.

[9] Joos, F. *Technische Verbrennung: Verbrennungstechnik, Verbrennungsmodellierung, Emissionen ; mit 65 Tabellen*. Springer, Berlin, 2006. OCLC: 636909068.

[10] Oinuma, R., Takuma, S., Koyano, T., and Takiguchi, M. Effects of Post Injection on Piston Lubrication in a Common Rail Small Bore Diesel Engine. *SAE Technical Paper 2005-01-2166*, 2005, doi:10.4271/2005-01-2166. ISSN: 0148-7191, 2688-3627.

[11] Song, B.-H. and Choi, Y.-H. Investigation of variations of lubricating oil diluted by post-injected fuel for the regeneration of CDPF and its effects on engine wear. *Journal of Mechanical Science and Technology*, 22(12):2526–2533, 2008, doi:10.1007/s12206-008-0903-x.

[12] Bozic, G., Kook, S., Ekoto, I. W., Petersen, B. R., and Miles, P. C. Optical Investigation Into Wall Wetting From Late-Cycle Post-Injections Used for Diesel Particulate Filter Regeneration. *Journal of Engineering for Gas Turbines and Power*, 133(092803), 2011, doi:10.1115/1.4002917.

[13] Kashdan, J. T., Mendez, S., and Bruneaux, G. On the origin of Unburned Hydrocarbon Emissions in a Wall Guided, Low NOx Diesel Combustion System. *SAE Transactions*, 116:234–257, 2007. Publisher: SAE International.

[14] Martin, G. C., Mueller, C. J., Milam, D. M., Radovanovic, M. S., and Gehrke, C. R. Early Direct-Injection, Low-Temperature Combustion of Diesel Fuel in an Optical Engine Utilizing a 15-Hole, Dual-Row, Narrow-Included-Angle Nozzle. *SAE International Journal of Engines*, 1(1):1057–1082, 2009. Publisher: SAE International.

[15] Erman, A. G., Hellier, P., and Ladommatos, N. The impact of ignition delay and further fuel properties on combustion and emissions in a compression ignition engine. *Fuel*, 262:116155, 2020, doi:10.1016/j.fuel.2019.116155.

[16] Merker, G. P. and Teichmann, R., editors. *Grundlagen Verbrennungsmotoren: Funktionsweise und alternative Antriebssysteme Verbrennung, Messtechnik und Simulation*. Springer Fachmedien, Wiesbaden, 9 edition, 2019.

[17] Dec, J. E. A Conceptual Model of DI Diesel Combustion Based on Laser-Sheet Imaging*. *SAE Technical Paper 970873*, 1997, doi:10.4271/970873.

[18] Flynn, P. F., Durrett, R. P., Hunter, G. L., Zur Loye, A. O., Akinyemi, O. C., Dec, J. E., and Westbrook, C. K. Diesel Combustion: An Integrated View Combining Laser Diagnostics, Chemical Kinetics, And Empirical Validation. *SAE Technical Paper 1999-01-0509*, pages 1999–01–0509, 1999, doi:10.4271/1999-01-0509.

[19] Chomiak, J. and Karlsson, A. Flame liftoff in diesel sprays. *Symposium (International) on Combustion*, 26(2):2557–2564, 1996, doi:10.1016/S0082-0784(96)80088-9.

[20] Siebers, D. and Higgins, B. Flame Lift-Off on Direct-Injection Diesel Sprays Under Quiescent Conditions. *SAE Transactions*, 110:400–421, 2001. Publisher: SAE International.

[21] Pickett, L. M. and Siebers, D. L. Fuel Effects on Soot Processes of Fuel Jets at DI Diesel Conditions. page 2003, 2003, doi:10.4271/2003-01-3080.

[22] Ito, T., Kitamura, T., Ueda, M., Matsumoto, T., Senda, J., and Fujimoto, H. Effects of Flame Lift-Off and Flame Temperature on Soot Formation in Oxygenated Fuel Sprays. *SAE Technical Paper 2003-01-0073*, 2003, doi:10.4271/2003-01-0073.

[23] Mueller, C. J., Pitz, W. J., Pickett, L. M., Martin, G. C., Siebers, D. L., and Westbrook, C. K. Effects of Oxygenates on Soot Processes in DI Diesel Engines: Experiments and Numerical Simulations. *SAE Transactions*, 112:964–982, 2003. Publisher: SAE International.

[24] Pickett, L. M., Siebers, D. L., and Idicheria, C. A. Relationship Between Ignition Processes and the Lift-Off Length of Diesel Fuel Jets. *SAE Transactions*, 114:1714–1731, 2005. Publisher: SAE International.

[25] Som, S. and Aggarwal, S. K. Effects of primary breakup modeling on spray and combustion characteristics of compression ignition engines. *Combustion and Flame*, 157(6):1179–1193, 2010, doi:10.1016/j.combustflame.2010.02.018.

[26] Riess, S., Klima, T., Wensing, M., and Braeuer, A. Influence of Bio-Diesel and Ethanol on the Diesel Engine Process Chain Investigated by Optical Measurement Techniques. In *ILASS - Europe*, Brighton, UK, 2016.

[27] Riess, S., Weiss, L., Peter, A., Rezaei, J., and Wensing, M. Air entrainment and mixture distribution in Diesel sprays investigated by optical measurement techniques. *International Journal of Engine Research*, 19(1):120–133, 2018, doi:10.1177/1468087417742527. Publisher: SAGE Publications.

[28] Burger, J., Siegert, M., Ströfer, E., and Hasse, H. Poly(oxymethylene) dimethyl ethers as components of tailored diesel fuel: Properties, synthesis and purification concepts. *Fuel*, 89(11):3315–3319, 2010, doi:10.1016/j.fuel.2010.05.014. Number: 11.

[29] Härtl, M., Pélerin, D., Gaukel, K., Dworschak, P., and Wachtmeister, G. OME als Reinstoff: Emissionsreduktion bei Dieselmotoren durch sauerstoffhaltige synthetische Kraftstoffe. In Maus, W., editor, *Zukünftige Kraftstoffe: Energiewende des Transports als ein weltweites Klimaziel*, ATZ/MTZ-Fachbuch, pages 799–813. Springer, Berlin, Heidelberg, 2019.

[30] Pellegrini, L., Marchionna, M., Patrini, R., Beatrice, C., Del Giacomo, N., and Guido, C. Combustion Behaviour and Emission Performance of Neat and Blended Polyoxymethylene

Dimethyl Ethers in a Light-Duty Diesel Engine. *SAE Technical Paper 2012-01-1053*, 2012, doi:10.4271/2012-01-1053.

[31] Liu, J., Wang, L., Wang, P., Sun, P., Liu, H., Meng, Z., Zhang, L., and Ma, H. An overview of polyoxymethylene dimethyl ethers as alternative fuel for compression ignition engines. *Fuel*, 318:123582, 2022, doi:10.1016/j.fuel.2022.123582.

[32] Lautenschütz, L., Oestreich, D., Seidenspinner, P., Arnold, U., Dinjus, E., and Sauer, J. Physico-chemical properties and fuel characteristics of oxymethylene dialkyl ethers. *Fuel*, 173:129–137, 2016, doi:10.1016/j.fuel.2016.01.060.

[33] H. H. Fechter, M., Haspel, P., Hasse, C., and Braeuer, A. S. Vapor pressures and latent heats of vaporization of Poly(oxymethylene) Dimethyl Ethers (OME3 and OME4) up to the vicinity of the critical temperature. *Fuel*, 303:121274, 2021, doi:10.1016/j.fuel.2021.121274.

[34] Kim, T. and Ghandhi, J. B. Characterization Of Evaporating Diesel Sprays Using Exciplex Laser-Induced Fluorescence Measurements. *Atomization and Sprays*, 13(5&6), 2003, doi:10.1615/AtomizSpr.v13.i56.60. Publisher: Begel House Inc.

[35] Desantes, J. M., Lopez, J. J., Garcia, J. M., and Pastor, J. M. Evaporative Diesel Spray Modeling. *Atomization and Sprays*, 17(3), 2007, doi:10.1615/AtomizSpr.v17.i3.10. Publisher: Begel House Inc.

[36] Fisher, B. T. and Mueller, C. J. Liquid penetration length of heptamethylnonane and trimethylpentane under unsteady in-cylinder conditions. *Fuel*, 89(10):2673–2696, 2010, doi:10.1016/j.fuel.2010.04.024.

[37] Pischinger, F., Reuter, U., and Scheid, E. Self-Ignition of Diesel Sprays and Its Dependence on Fuel Properties and Injection Parameters. *Journal of Engineering for Gas Turbines and Power*, 110(3):399–404, 1988, doi:10.1115/1.3240135.

[38] Canaan, R. E., Dec, J. E., Green, R. M., and Daly, D. T. The Influence of Fuel Volatility on the Liquid-Phase Fuel Penetration in a Heavy-Duty D.I. Diesel Engine. *SAE Transactions*, 107:583–602, 1998. Publisher: SAE International.

[39] Siebers, D. L. Liquid-Phase Fuel Penetration in Diesel Sprays. *SAE Transactions*, 107:1205–1227, 1998. Publisher: SAE International.

[40] Kook, S. and Pickett, L. M. Liquid length and vapor penetration of conventional, Fischer–Tropsch, coal-derived, and surrogate fuel sprays at high-temperature and high-pressure ambient conditions. *Fuel*, 93:539–548, 2012, doi:10.1016/j.fuel.2011.10.004.

[41] Pastor, J. V., García-Oliver, J. M., Micó, C., García-Carrero, A. A., and Gómez, A. Experimental Study of the Effect of Hydrotreated Vegetable Oil and Oxymethylene Ethers on Main Spray and Combustion Characteristics under Engine Combustion Network Spray A Conditions. *Applied Sciences*, 10(16):5460, 2020, doi:10.3390/app10165460. Number: 16.

[42] Strauß, L., Rieß, S., and Wensing, M. Mixture formation of OME3-5 and 1-Octanol in comparison with diesel-like Dodecane under ECN Spray A conditions. *Frontiers in Mechanical Engineering*, 9:1083658, 2023, doi:10.3389/fmech.2023.1083658.

[43] Tagliante, F., Nguyen, T. M., Dhanji, M. P., Sim, H. S., Pickett, L. M., Manin, J., Kukkadapu, G., Whitesides, R., and Wan, K. The role of cool-flame fluctuations in high-pressure spray flames, studied using high-speed optical diagnostics and Large-Eddy Simulations. *Proceedings of the Combustion Institute*, 39(4):4871–4879, 2023, doi:10.1016/j.proci.2022.07.242.

[44] Anand, K. and Reitz, R. Exploring the benefits of multiple injections in low temperature combustion using a diesel surrogate model. *Fuel*, 165:341–350, 2016, doi:10.1016/j.fuel.2015.10.087.

[45] Pickett, L. M., Manin, J., Payri, R., Bardi, M., and Gimeno, J. Transient Rate of Injection Effects on Spray Development. *SAE Technical Paper 2013-24-0001*, 2013, doi:10.4271/2013-24-0001.

[46] ECN. Engine Combustion Network. https://ecn.sandia.gov/.

[47] Frühhaber, J., Peter, A., Schuh, S., Lauer, T., Wensing, M., Winter, F., Priesching, P., and Pachler, K. Modeling the Pilot Injection and the Ignition Process of a Dual Fuel Injector with Experimental Data from a Combustion Chamber Using Detailed Reaction Kinetics. *SAE Technical Paper 2018–01–1724*, 2018, doi:10.4271/2018-01-1724.

[48] Westbrook, C. K., Pitz, W. J., Herbinet, O., Curran, H. J., and Silke, E. J. A comprehensive detailed chemical kinetic reaction mechanism for combustion of *n*-alkane hydrocarbons from *n*-octane to *n*-hexadecane. *Combustion and Flame*, 156(1):181–199, 2009, doi:10.1016/j.combustflame.2008.07.014.

[49] Sun, W., Wang, G., Li, S., Zhang, R., Yang, B., Yang, J., Li, Y., Westbrook, C. K., and Law, C. K. Speciation and the laminar burning velocities of poly(oxymethylene) dimethyl ether 3 (POMDME3) flames: An experimental and modeling study. *Proceedings of the Combustion Institute*, 36(1):1269–1278, 2017, doi:10.1016/j.proci.2016.05.058.

[50] He, T., Wang, Z., You, X., Liu, H., Wang, Y., Li, X., and He, X. A chemical kinetic mechanism for the low- and intermediate-temperature combustion of Polyoxymethylene Dimethyl Ether 3 (PODE3). *Fuel*, 212:223–235, 2018, doi:10.1016/j.fuel.2017.09.080.

[51] Cai, L., Jacobs, S., Langer, R., vom Lehn, F., Heufer, K. A., and Pitsch, H. Auto-ignition of oxymethylene ethers (OMEn, n = 2–4) as promising synthetic e-fuels from renewable electricity: shock tube experiments and automatic mechanism generation. *Fuel*, 264:116711, 2020, doi:10.1016/j.fuel.2019.116711.

[52] Jacobs, S., Döntgen, M., Alquaity, A. B. S., Kopp, W. A., Kröger, L. C., Burke, U., Pitsch, H., Leonhard, K., Curran, H. J., and Heufer, K. A. Detailed kinetic modeling of dimethoxymethane. Part II: Experimental and theoretical study of the kinetics and reaction mechanism. *Combustion and Flame*, 205:522–533, 2019, doi:10.1016/j.combustflame.2018.12.026.

[53] Niu, B., Jia, M., Chang, Y., Duan, H., Dong, X., and Wang, P. Construction of reduced oxidation mechanisms of polyoxymethylene dimethyl ethers (PODE1–6) with consistent structure using decoupling methodology and reaction rate rule. *Combustion and Flame*, 232:111534, 2021, doi:10.1016/j.combustflame.2021.111534.

[54] Chang, Y., Jia, M., Li, Y., Liu, Y., Xie, M., Wang, H., and Reitz, R. D. Development of a skeletal mechanism for diesel surrogate fuel by using a decoupling methodology. *Combustion and Flame*, 162(10):3785–3802, 2015, doi:10.1016/j.combustflame.2015.07.016.

[55] Gillespie, F. R. *An experimental and modelling study of the combustion of oxygenated hydrocarbons*. PhD Thesis, National University of Ireland, Galway, 2014.

[56] ASG. ASG Analytik-Service. https://asg-analytik.de/.

[57] Wiesmann, F., Strauß, L., Rieß, S., Manin, J., Wan, K., and Lauer, T. Numerical and Experimental Investigations on the Ignition Behavior of OME. *Energies*, 15(18):6855, 2022, doi:10.3390/en15186855.

[58] Wiesmann, F., Han, D., Qiu, Z., Strauß, L., Rieß, S., Wensing, M., and Lauer, T. Numerical study of novel OME1-6 combustion mechanism and spray combustion at changed ambient environments. *Frontiers in Energy*, 2024, doi:10.1007/s11708-024-0926-8.

[59] Wiesmann, F., Nguyen, T. M., Manin, J., Pickett, L. M., Wan, K., Tagliante, F., and Lauer, T. LES and RANS Spray Combustion Analysis of OME3-5 and n-Dodecane. *Energies*, 17(10):2265, 2024, doi:10.3390/en17102265.

[60] Wiesmann, F., Bauer, E., Kaiser, S. A., and Lauer, T. Ignition and Combustion Characteristics of $OME_{3\text{-}5}$ and N-Dodecane: A Comparison Based on CFD Engine Simulations and Optical Experiments. *SAE Technical Paper 2023-01-0305*, 2023, doi:10.4271/2023-01-0305.

[61] Sim, H. S., Maes, N., Weiss, L., Pickett, L. M., and Skeen, S. A. Detailed measurements of transient two-stage ignition and combustion processes in high-pressure spray flames using simultaneous high-speed formaldehyde PLIF and schlieren imaging. *Proceedings of the Combustion Institute*, 38(4):5713–5721, 2021, doi:10.1016/j.proci.2020.09.026.

[62] CMT. Spray B Rate of Injection. https://www.cmt.upv.es.

[63] Nguyen, T. M., Dahms, R. N., Pickett, L. M., and Tagliante, F. The Corrected Distortion model for Lagrangian spray simulation of transcritical fuel injection. *International Journal of Multiphase Flow*, 148:103927, 2022, doi:10.1016/j.ijmultiphaseflow.2021.103927.

[64] Hanjalić, K., Popovac, M., and Hadžiabdić, M. A robust near-wall elliptic-relaxation eddy-viscosity turbulence model for CFD. *International Journal of Heat and Fluid Flow*, 25(6):1047–1051, 2004, doi:10.1016/j.ijheatfluidflow.2004.07.005.

[65] Reitz, R. D. and Bracco, F. V. Mechanisms of Breakup of Round Liquid Jets. In *The Encyclopedia of Fluid Mechanics, ed Cheremisinoff NP*, volume 3, pages 233–249. Gulf Publishing, Houston, TX, 1986.

[66] Leick, P. *Quantitative Untersuchungen zum Einfluss von Düsengeometrie und Gasdichte auf den Primärzerfall von Dieselsprays*. PhD Thesis, Technische Universität, 2008.

[67] Reitz, R. D. Modeling atomization processes in high-pressure vaporizing sprays. *Atomisation Spray Technology*, 3:309–337, 1987.

[68] Jiang, X., Siamas, G., Jagus, K., and Karayiannis, T. Physical modelling and advanced simulations of gas–liquid two-phase jet flows in atomization and sprays. *Progress in Energy and Combustion Science*, 36(2):131–167, 2010, doi:10.1016/j.pecs.2009.09.002.

[69] Taylor, G. The instability of liquid surfaces when accelerated in a direction perpendicular to their planes. I. *Proceedings of the Royal Society of London. Series A. Mathematical and Physical Sciences*, 201(1065):192–196, 1950, doi:10.1098/rspa.1950.0052. Number: 1065.

[70] Stiesch, G. *Modeling engine spray and combustion processes*. 2003. OCLC: 861705857.

[71] Reitz, R. D. and Diwakar, R. Structure of High-Pressure Fuel Sprays. *SAE Transactions*, 96:492–509, 1987. Publisher: SAE International.

[72] Reitz, R. D. and Beale, J. C. Modeling Spray Atomization with the Kelvin-Helmholtz/Rayleigh-Taylor Hybrid Model. *Atomization and Sprays*, 9(6):623–650, 1999, doi:10.1615/AtomizSpr.v9.i6.40.

[73] O'Rourke, P. J. and Amsden, A. A. The Tab Method for Numerical Calculation of Spray Droplet Breakup. page 872089, 1987, doi:10.4271/872089.

[74] Patterson, M. A. and Reitz, R. D. Modeling the Effects of Fuel Spray Characteristics on Diesel Engine Combustion and Emission. *SAE Transactions*, 107:27–43, 1998. Publisher: SAE International.

[75] Payri, R., Salvador, F. J., Gimeno, J., and Bracho, G. A new methodology for correcting the signal cumulative phenomenon on injection rate measurements. *Experimental Techniques*, 32(1):46–49, 2008, doi:10.1111/j.1747-1567.2007.00188.x.

[76] CMT. Virtual Injection Rate Generator. https://www.cmt.upv.es.

[77] Naber, J. and Siebers, D. L. Effects of Gas Density and Vaporization on Penetration and Dispersion of Diesel Sprays. page 960034, 1996, doi:10.4271/960034.

[78] O'Rourke, P. J. and Bracco, F. Modelling of Drop Interactions in Thick Sprays and a Comparison with Experiments. *I. Mech. E., C*, 404(80):101–116, 1980. Number: 80.

[79] Gosman, A. D. and loannides, E. Aspects of Computer Simulation of Liquid-Fueled Combustors. *Journal of Energy*, 7(6):482–490, 1983, doi:10.2514/3.62687. Number: 6.

[80] Brenn, G., Deviprasath, L. J., and Durst, F. Computations and experiments on the evaporation of multi-component droplets. In *Proceedings / ICLASS 2003*, Sorrento, Italy, 2003.

[81] Abramzon, B. and Sirignano, W. Droplet vaporization model for spray combustion calculations. *International Journal of Heat and Mass Transfer*, 32(9):1605–1618, 1989, doi:10.1016/0017-9310(89)90043-4. Number: 9.

[82] Schiller, L. and Naumann, A. Z. A Drag Coefficient Correlation. *Zeit. Ver. Deutsch. Ing.*, 77:318–320, 1933.

[83] Novella, R., García, A., Pastor, J., and Domenech, V. The role of detailed chemical kinetics on CFD diesel spray ignition and combustion modelling. *Mathematical and Computer Modelling*, 54(7-8):1706–1719, 2011, doi:10.1016/j.mcm.2010.12.048. Number: 7-8.

[84] Yao, T., Pei, Y., Zhong, B.-J., Som, S., Lu, T., and Luo, K. H. A compact skeletal mechanism for n-dodecane with optimized semi-global low-temperature chemistry for diesel engine simulations. *Fuel*, 191:339–349, 2017, doi:10.1016/j.fuel.2016.11.083.

[85] You, X., Egolfopoulos, F. N., and Wang, H. Detailed and simplified kinetic models of *n*-dodecane oxidation: The role of fuel cracking in aliphatic hydrocarbon combustion. *Proceedings of the Combustion Institute*, 32(1):403–410, 2009, doi:10.1016/j.proci.2008.06.041.

[86] Sarathy, S. M., Westbrook, C. K., Mehl, M., Pitz, W. J., Togbe, C., Dagaut, P., Wang, H., Oehlschlaeger, M. A., Niemann, U., Seshadri, K., Veloo, P. S., Ji, C., Egolfopoulos, F. N., and Lu, T. Comprehensive chemical kinetic modeling of the oxidation of 2-methylalkanes from C7 to C20. *Combustion and Flame*, 158(12):2338–2357, 2011, doi:10.1016/j.combustflame.2011.05.007.

[87] Wang, M., Kukkadapu, G., Zhang, K., Wagnon, S. W., Mehl, M., Pitz, W. J., Westbrook, C. K., and Sung, C.-J. Autoignition of CRC diesel surrogates at low temperature combustion conditions: Rapid compression machine experiments and modeling. *Combustion and Flame*, 219:178–197, 2020, doi:10.1016/j.combustflame.2020.05.017.

[88] Gerlinger, P. *Numerische Verbrennungssimulation*. Springer Berlin Heidelberg, Berlin, Heidelberg, 2005.

[89] AVL List GmbH. FIRE Spray Manual 2020 R1. Manual.

[90] Kundu, P., Ameen, M. M., and Som, S. Importance of turbulence-chemistry interactions at low temperature engine conditions. *Combustion and Flame*, 183:283–298, 2017, doi:10.1016/j.combustflame.2017.05.025.

[91] Liang, L., Stevens, J. G., and Farrell, J. T. A Dynamic Multi-Zone Partitioning Scheme for Solving Detailed Chemical Kinetics in Reactive Flow Computations. *Combustion Science and Technology*, 181(11):1345–1371, November 2009, doi:10.1080/00102200903190836. Publisher: Taylor & Francis _eprint: https://doi.org/10.1080/00102200903190836.

[92] AVL List GmbH. FIRE General Gas Phase Reactions Module v2018. Manual.

[93] Pickett, L. M., Genzale, C. L., and Manin, J. Uncertainty quantification for liquid penetration of evaporating sprays at diesel-like conditions. *Atomization and Sprays*, 25(5), 2015, doi:10.1615/AtomizSpr.2015010618. Publisher: Begel House Inc.

[94] Maes, N., Skeen, S. A., Bardi, M., Fitzgerald, R. P., Malbec, L.-M., Bruneaux, G., Pickett, L. M., Yasutomi, K., and Martin, G. Spray penetration, combustion, and soot formation characteristics of the ECN Spray C and Spray D injectors in multiple combustion facilities. *Applied Thermal Engineering*, 172:115136, 2020, doi:10.1016/j.applthermaleng.2020.115136.

[95] Tagliante, F., Sim, H. S., Pickett, L. M., Nguyen, T., and Skeen, S. Combined Experimental/Numerical Study of the Soot Formation Process in a Gasoline Direct-Injection Spray in the Presence of Laser-Induced Plasma Ignition. *SAE Technical Paper 2020-01-0291*, 2020, doi:10.4271/2020-01-0291.

[96] Mueller, C. J. The Quantification of Mixture Stoichiometry When Fuel Molecules Contain Oxidizer Elements or Oxidizer Molecules Contain Fuel Elements. *SAE Technical Paper 2005-01-3705*, 2005, doi:10.4271/2005-01-3705.

[97] Bowditch, F. W. A New Tool for Combustion Research A Quartz Piston Engine. page 610002, 1961, doi:10.4271/610002.

[98] Pischinger, F. and Schulte, H. Grundlagen und Entwicklungslinien der diesel-motorischen Brennverfahren. volume 714, pages 61–93. VDI-Verlag, Düsseldorf, 1988.

Part II

Publications

1

Wiesmann, F.; Strauß, L.; Rieß, S.; Manin, J.; Wan, K.
and Lauer, T.

Numerical and Experimental Investigations on the Ignition Behavior of OME

Energies, 15:6855
2022

doi: 10.3390/en15186855

energies

MDPI

Article

Numerical and Experimental Investigations on the Ignition Behavior of OME

Frederik Wiesmann [1,*], Lukas Strauß [2], Sebastian Rieß [2], Julien Manin [3], Kevin Wan [3] and Thomas Lauer [1]

[1] Institute of Powertrains and Automotive Technology, TU Wien, 1060 Vienna, Austria
[2] Institute of Fluid System Technology, FAU Erlangen-Nuremberg, 91058 Erlangen, Germany
[3] Sandia National Laboratories, 7011 East Ave, Livermore, CA 94551, USA
* Correspondence: frederik.wiesmann@ifa.tuwien.ac.at; Tel.: +43-1-58801-31560

Abstract: On the path towards climate-neutral future mobility, the usage of synthetic fuels derived from renewable power sources, so-called e-fuels, will be necessary. Oxygenated e-fuels, which contain oxygen in their chemical structure, not only have the potential to realize a climate-neutral powertrain, but also to burn more cleanly in terms of soot formation. Polyoxymethylene dimethyl ethers (PODE or OMEs) are a frequently discussed representative of such combustibles. However, to operate compression ignition engines with these fuels achieving maximum efficiency and minimum emissions, the physical-chemical behavior of OMEs needs to be understood and quantified. Especially the detailed characterization of physical and chemical properties of the spray is of utmost importance for the optimization of the injection and the mixture formation process. The presented work aimed to develop a comprehensive CFD model to specify the differences between OMEs and dodecane, which served as a reference diesel-like fuel, with regards to spray atomization, mixing and auto-ignition for single- and multi-injection patterns. The simulation results were validated against experimental data from a high-temperature and high-pressure combustion vessel. The sprays' liquid and vapor phase penetration were measured with Mie-scattering and schlieren-imaging as well as diffuse back illumination and Rayleigh-scattering for both fuels. To characterize the ignition process and the flame propagation, measurements of the OH* chemiluminescence of the flame were carried out. Significant differences in the ignition behavior between OMEs and dodecane could be identified in both experiments and CFD simulations. Liquid penetration as well as flame lift-off length are shown to be consistently longer for OMEs. Zones of high reaction activity differ substantially for the two fuels: Along the spray center axis for OMEs and at the shear boundary layers of fuel and ambient air for dodecane. Additionally, the transient behavior of high temperature reactions for OME is predicted to be much faster.

Keywords: CFD; OME; e-Fuels; Multi-Injection; Oxygenated Fuels; Spray Modeling

Citation: Wiesmann, F.; Strauß, L.; Rieß, S.; Manin, J.; Wan, K.; Laue, T. Numerical and Experimental Investigations on the Ignition Behavior of OME. *Energies* **2022**, *15*, 6855. https://doi.org/10.3390/en15186855

Academic Editor: Constantine D. Rakopoulos

Received: 16 August 2022
Accepted: 13 September 2022
Published: 19 September 2022

1. Introduction

In order to achieve climate-neutrality, research into the applicability and behavior of CO_2-neutral synthetic fuels is essential. Therefore, a steadily growing interest in academic research in this topic can be observed [1]. Oxygenated fuels in particular are of special interest as they provide beneficial combustion properties that can help solve the soot-NO*x* trade-off [2]. Polyoxymethylene dimethyl ethers (PODEs), also known as oxymethylene ethers (OMEs), are a quite promising class of such synthetic and oxygenated fuels. Extensive research for various engine types has been done to confirm the potential of OMEs regarding the reduction of soot emissions [3–5] and increased engine efficiency [6]. The lack of *C-C* bonds within the chemical structure of OMEs— $CH_3O(\text{-}CH_2O)_n\text{-}CH_3$—together with the high oxygen content (42.1–49.5 wt% for OME1-6 with $1 \leq n \leq 6$) is responsible for the nearly sootless combustion.

Most academic research so far focused on OME_1 as OMEs with more than one formaldehyde (CH_2O) group have been difficult to synthesize [7–10]. However, in general

terms, OME_{3-6} were determined to be of best suitability for diesel engine applications, considering their boiling point, lubricity and viscosity are close to diesel itself [9,11,12]. Therefore, recently the focus shifted towards higher OMEs. Previous findings for OME_1 regarding very low soot and particle emissions were also confirmed for OME_{3-6} [2,4,13,14].

Special emphasis in this work is placed on the effects caused by multiple injection strategies. Choi and Reitz [15] investigated the impacts of oxygenated fuel blends and multiple injections on DI diesel engines. The study concluded that oxygenated fuel blends reduced soot emissions at high engine loads without increasing NO*x* emissions. Furthermore, it was shown that a split injection pattern had an additional favorable effect on soot formation at high engine loads and was particularly effective at reducing particulate emissions at low engine loads.

Therefore, concluding from the findings in [3–6,15], the combination of oxygenated fuels and multiple injection strategies has the potential to significantly reduce particulate matter emissions over a wide range of engine operating conditions.

The used injection pattern in this study consists of a short pilot (or pre) and a longer main injection. Short pilot injections result in a ballistic injector operation regime, which strongly influences the spray propagation, mixture formation and ignition behavior. Previous studies emphasized the challenges to properly model highly transient ballistic working regimes of an injector [16] and to correctly specify the small quantities of fuel injected [17]. The authors in [18] found that multiple injection strategies using pilot injections result in an in-cylinder charge that is more fuel lean, which yields a more complete combustion. The resulting effect of a reduced fuel fraction reaching the cylinder wall and crevice regions leads to lower UHC and CO emissions in comparison with single injection strategies.

In order to fully leverage the potential of OMEs in combination with multi-injection events it is essential to study their physical-chemical behavior in depth. The primary aim of this study is to advance the understanding of OMEs in terms of spray atomization, mixture formation and auto-ignition for single and multiple injection strategies and highlight the differences to diesel-like fuels. For this purpose, a comprehensive 3D CFD model using the commercial software AVL FIRE® was developed.

Detailed reaction mechanisms are used for an OME_{3-6} fuel and dodecane, which serves as a diesel surrogate fuel, to identify the differences in the combustion regimes before and after a stable flame lift-off is established. The spray and combustion models are validated with experimental data from a constant pressure combustion vessel.

The presentation of the present work is organized as follows. First the experimental and numerical setup is introduced in Section 2. Then the numerical results are validated against the experimental data in Section 3. Thereafter, the results are discussed in Section 4 and a summary with possible future research directions is given in Section 5.

2. Setup

2.1. Used Fuels

The fuels used in this study are dodecane, serving as diesel surrogate, and a mix of OMEs, hereinafter referred to as *OME*, with its composition shown in Table 1. The different fuel properties of dodecane and OME are described in Table 2. Dodecane is a single component *n*-paraffinic fuel and the standard diesel surrogate of the engine combustion network (ECN) [19]. In contrast to dodecane, the used OME mix is a multi-component oxymethylene ether blended with components of different chain lengths. The OME batch was analyzed by Analytik Service Gesellschaft (ASG) [20].

Choosing these fundamentally different fuels serves as a further challenge for the validity of the CFD model that is developed in this study.

Energies **2022**, *15*, 6855

Table 1. OME mix composition.

Molecule	Content [wt %]
OME_1	0.01
OME_2	< 0.01
OME_3	57.90
OME_4	28.87
OME_5	10.07
OME_6	1.91

Table 2. Fuel properties for dodecane and OME.

Property	Unit	Dodecane	OME
Density	kg/m^3 (T = 15 °C)	751.20	1057.10
Viscosity	mm^2/s (T = 40 °C)	1.44	1.08
Cetane number	-	74	68.6
Lubricity	µm	563	320
Flash point	°C	83	65
Lower heating value	MJ/kg	44.20	19.26
Initial boiling point	°C	214.00	144.40
Final boiling point	°C	218	242.4
Total contaminations	mg/kg	-	< 1
Carbon content	% [m/m]	84	43
Hydrogen content	% [m/m]	16	8.53
Oxygen content	% [m/m]	0	46.4
$(A/F)_{st}$ at 21% of O_2	-	14.92:1	5.89:1
$(A/F)_{st}$ at 15% of O_2	-	20.72:1	8.18:1

2.2. Experimental Setup

The experiments for the spray investigation are carried out with optically accessible high-temperature and high-pressure constant volume injection chambers.

The test bench at Institute of Fluid System Technology (FST) is continuously scavenged with gas mixtures, which can be freely adjusted from pure nitrogen to pure air, making it possible to perform both reactive and inert investigations and a simulation of EGR as well. The gas temperature inside the vessel can be set from room temperature to 1000 K and is controlled automatically. The pressure can be regulated from 0,1 MPa up to 10 MPa simultaneously. Both parameters are held constant during the experiments. A research fuel system, which can be used with different rails and injectors, provides the required fuel pressure up to 400 MPa. To obtain data about the fuel spray and its mixture, optical measurement techniques are used. The cubic chamber has a window on each side (except for the one where the injector is mounted) so that one can apply high-speed imaging techniques.

The optics are placed in such a way, that the fuel spray is shown in side view. The gaseous penetration is measured with a typical schlieren setup under inert conditions (Figure 1, left): Light from a monochromatic LED at 528 nm is parallelized by a lens with a diameter of 152 mm and a focal length of 1216 mm and guided into the chamber via the optical access. Density gradients due to the spray result in a change of the refractive index, causing the previously parallel beams to be bent in different directions. The light beams are collected through a second lens with the same optical properties as the first one and are recorded with a Photron SA-Z, which is equipped with a Tamron SP 70-200 mm F/2.8, at a framerate of 40,000 fps. In order to measure the liquid phase, the fuel spray is illuminated with white LED chips from three of the five windows. The Mie scattered light is then detected with the high-speed camera setup via the schlieren optics mentioned above.

To characterize the ignition, the OH*-chemiluminescence is detected. For this, the OH*-signal is filtered out of the flame signal by a 307 nm ± 25 nm bandpass filter and

focused with a Sill Optics 105 mm F/4.5 objective lens on the high-speed intensifier IRO X of LaVision (Figure 1, right). Afterwards, the amplified signal is recorded with a Photron SA-Z at a framerate of 40,000 fps. For each operation point, 32 injections are performed, filmed and evaluated with a self-developed MATLAB-based program. In addition, mass flow rate measurements are performed utilizing a Moehwald HDA-500.

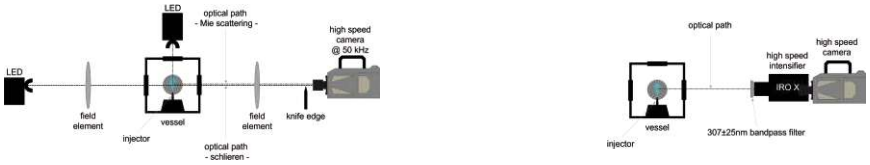

Figure 1. Experimental setup schematic: (**left**) Mie-scattering and schlieren setup. (**right**) OH*-chemiluminescence setup.

The experiments at Sandia National Laboratories (Sandia) were carried out using an optically accessible constant-volume spray chamber. The chamber is approximately a 108 mm cube. The injector is mounted on one face of the cube, and the remaining 5 faces allow optical access. The thermodynamic operating conditions are achieved by spark igniting a tailored pre-burn mixture of acetylene, hydrogen, oxygen, and nitrogen. Further details of the chamber can be found in previous works [21].

Time-resolved vapor penetration and mixing was imaged using Rayleigh scattering from a pulsed burst-mode 532-nm Nd:YAG laser operating at 70 kHz. The laser was shaped into a sheet approximately 0.2 mm thick and passed orthogonally through the injector axis. The scattered light was passed through a 532 nm bandpass filter and collected with a high-speed Phantom v2512 camera equipped with a 85 mm f/1.8 lens and 500D close-up lens. Details on the high-speed Rayleigh scattering technique and calculation of mixture fraction are available [22].

Liquid length was visualized simultaneously using diffuse back illuminated (DBI) imaging using a 385 nm LED operating at the laser frequency and 300 ns pulses with a Fresnel lens and engineered diffuser. The diffuse light was passed through a dichroic beam splitter and collected using a second Phantom v2512 camera with a 50 m f/1.2 lens, 500D close-up lens. Details of the DBI technique and the procedure for evaluating liquid length can be found in Section 2.4.4.

Injectors

This study utilizes two different injectors for validation of the simulation model: The Continental 3 Hole injector (Conti3L) and the SprayA3 injector. Table 3 lists the characteristics of the two injectors.

The SprayA3 injector used in this study is a piezo-actuated injector with a highly convergent single-hole orifice nozzle.

The Conti3L injector is also piezo-driven but has three holes and is based on a common rail high-pressure diesel injector unit PCRs2. Its orifices are oriented at 45°elevation from the injector axis and with a constant angle of 120° between orifices.

Table 3. Injector properties.

	Conti3L	SprayA3
Orifice exit diameter [µm]	115	97
Contraction coefficient [-]	0.98	0.98
Number of holes [-]	3	1
Elevation angle [°]	45	0

Energies **2022**, *15*, 6855

2.3. Operating Points

The operating points of the experiments and simulations in this study are shown in Table 4. The letter *M* indicates an operating point with multiple injections, the letter *i* signals inert (nitrogen) atmosphere and *r* specifies reactive conditions. It can be seen that two major sweeps are studied in the present work. First the temperature varies from 800 K (*T2*) to 900 K (*A*) and 1000 K (*T3*) is. Also the volume content of oxygen in the chamber atmosphere is altered from inert conditions to 15 % and 21 %. The density was kept constant at 22.8 kg/m^3 in order to focus on the influence of temperature and oxygen content on the spray propagation and combustion. The changing ambient conditions have a significant influence on liquid penetration, vapor entrainment, ignition delay and flame lift-off.

Table 4. Operating points.

Name	T_{CC} [K]	p_{CC} [bar]	ρ_{CC} [kg/m^3]	T_{inj} [K]	p_{inj} [bar]	t_{inj} [ms]	O_2-Content [vol. %]
T2i	800	55	22.8	363	1500	1.5	0
T2r	800	54	22.8	363	1500	1.5	15
T2iM	800	55	22.8	363	1500	0.3/0.5/1.2	0
T2rM	800	54	22.8	363	1500	0.3/0.5/1.2	15
Ai	900	62	22.8	363	1500	1.5	0
Ar	900	61	22.8	363	1500	1.5	15
AiM	900	62	22.8	363	1500	0.3/0.5/1.2	0
ArM	900	61	22.8	363	1500	0.3/0.5/1.2	15
O2	900	60	22.8	363	1500	1.5	21
T3i	1000	69	22.8	363	1500	1.5	0
T3r	1000	68	22.8	363	1500	1.5	15

2.4. Numerical Setup

The modeling of the reactive spray is carried out as RANS simulations using a discrete droplet approach to track the liquid parcels in the computational domain in a Lagrangian manner (Section 2.4.2). The gaseous phase is modeled on an Eulerian grid.

2.4.1. Eulerian Mesh And Models

The present work utilizes a simplified spray-box mesh of 120 mm in length and 60 mm in width including several refinements reaching a maximum resolution of 125 µm. The dimensions of the mesh are chosen to provide a spray propagation unperturbed by boundaries. The local refinements (Table 5), integrated in the spray center axis, aim for an adequate spatial resolution of the spray plume.

Table 5. Mesh refinements.

Refinement	L [mm]	R1 [mm]	R2 [mm]	Cell Size [mm]
0 (Base Mesh)	120	30	30	1.000
1	80	5	10	0.500
2	50	3	5	0.250
3	25	2	3	0.125

Figure 2 shows a cut though the center plane of the mesh as visualization of the refinement levels. The small cell size in the vicinity of the nozzle is essential to correctly model the momentum exchange between liquid and vapor phase. The boundaries of the mesh are modeled as walls with fixed temperature, except the boundary opposite the nozzle, which is set as a non-reflecting outlet. The investigated operating points in Section 2.3 result in high injection velocities, which, in conjunction with the small cell sizes close to the nozzle, require a high temporal resolution in order to comply with the condition

of Courant numbers smaller than unity. Therefore, the time step size during injection is set to 0.5 µs and to 1.0 µs once the injection process is finished and the vapor phase is observed.

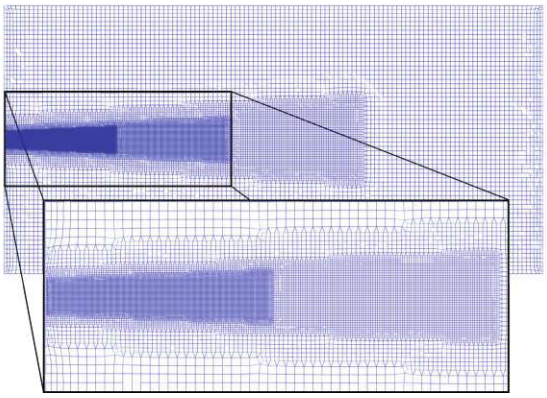

Figure 2. Cut through computational mesh visualizing refinement levels.

The turbulent flow field is modeled using a RANS approach with the k-ζ-f turbulence model [23]. This model contains all necessary near-wall modifications, which makes it an appropriate choice even for transferring the simulation results of the present work to an engine application. A compound wall treatment proposed by [24] is selected to model the near wall regions of the computational domain. The pressure-velocity coupling is done via the SIMPLE/PISO algorithm where the first pressure correction is conducted with the SIMPLE logic and an additional pressure correction is made using the standard PISO correction. Table 6 summarizes the numerical setup for the gaseous phase within the computational domain.

Table 6. Summary of Eulerian numerical setup.

Meshing	
Type	Cylindrical spray-box
Cell refinement	1 mm–0.125 mm
Dimensions	Length = 120 mm; Diameter = 60 mm
Boundaries	Fixed temperature walls; non-reflecting outlet
Gaseous phase models	
Temporal discretization	0.5 µs (during injection); 1.0 µs (after injection)
Turbulence modeling	RANS approach; k-ζ-f model
Wall treatment	Compound (hybrid)
Pressure-correction	SIMPLE (1st) / PISO (2nd)

2.4.2. Lagrangian Spray Modeling

The liquid phase is modeled by introducing a statistically significant number of discrete parcels at every time step, which are tracked through the numerical domain. These parcels consist of a certain number of identical, non-interacting droplets. The main force acting on the parcels and determining their trajectories is the drag force F_D described by Equation (1) [25]

$$\rho_l V_d \vec{F}_{D,d} = \frac{1}{2}\rho_g C_d A_d * |\vec{u} - \vec{v}_d| * (\vec{u} - \vec{v}_d) \quad (1)$$

with $\vec{u}$ as the velocity vector of the gaseous phase, $\vec{v}_d$ as droplet velocity, C_d droplet drag coefficient and V_d and A_d describing the droplet volume and frontal area respectively. The subscript l denotes the liquid and g the gaseous properties. The methodical approach for introducing the liquid parcels in the present spray modeling is the *Blob* method [26].

Energies **2022**, *15*, 6855

Hereby, large liquid parcels (blobs) are continuously initialized with diameters comparable to the nozzle orifice approximating the intact liquid core in the vicinity of the nozzle exit. The main assumption underlying this procedure is that the atomization of the introduced liquid and the split-up of liquid blobs are indistinguishable processes within the dense liquid core region [27].

The breakup of the liquid blobs is modeled with the *KHRT* liquid breakup model. It combines the Kelvin-Helmholtz (KH) instabilities [26], and the Rayleigh-Taylor (RT) breakup model, which is based on the findings of Taylor [28].

The KH instabilities describe growing oscillations on the droplet surface caused by high relative velocities. There are two key parameters defining this breakup model for diesel-like sprays. The first one is the calculated stable radius of the broken up droplet ($r_{d,KH}$ in Equation (2)), which is proportional to the wavelength of the fasted growing oscillation (Λ_{KH}). The second one is the necessary breakup time (τ_{KH} in Equation (4)), determined by the wavelength and growth rate (Ω_{KH}) of the fasted growing oscillation breaking up the parent droplet ($r_{p,KH}$).

$$r_{d,KH} = C_1 \Lambda_{KH} \tag{2}$$

$$\frac{dr_{p,KH}}{dt} = -\frac{r_{p,KH} - r_{d,KH}}{\tau_{KH}} \tag{3}$$

$$\tau_{KH} = 3.726\, C_2 \frac{r_{p,KH}}{\Lambda_{KH}\Omega_{KH}} \tag{4}$$

The parameter C_1 is set to 0.61 following the original findings of Reitz [26]. The model parameter C_2 however is the main fitting parameter for the KH breakup. The reported values vary significantly from 1.73 [29] to 30 [30], which is a clear indication of the influence of the inner nozzle flow on the primary breakup that is attempted to be modeled by this parameter.

The RT instabilities are caused when a liquid-gas interface is accelerated in a direction opposite to the density gradient. This means that drag forces causing the droplet to decelerate result in growing RT instabilities at the trailing edge.

Both breakup models are driven by the aerodynamics drag force given by Equation (1). They are implemented in a competing manner, meaning the mechanism predicting the shorter breakup time for a given droplet is applied. In proximity to the injector nozzle the droplet velocities and accelerations are highest, which results in the RT breakup governing the near nozzle regions. The KH breakup becomes more dominant further downstream [25]. The only constraint needed for the KHRT implementation is a definition of a certain length downstream of the nozzle where the liquid droplets only undergo KH breakup in the form of Equation (5) [31]. This way the CFD code can circumvent the fact that the RT model would predict an extremely rapid breakup in close vicinity to the nozzle exit.

$$L_{KH,breakup} = C_3 \sqrt{\frac{\rho_l}{\rho_g}}\, d_{Nozzle} \tag{5}$$

Table 7 shows the breakup models parameters used for all CFD simulations within this study. A minor adaption of the C_2 parameter was necessary when switching from the Conti3L to the SprayA3 injector to get a better representation of the measured liquid length. However, all other sub-models of the Lagrangian and the Eulerian phase remain the same.

Table 7. KHRT breakup model parameters.

Parameter	Value	Description
C_1	0.61	Parameter for stable child droplet radius
C_2	8.5 (Conti3L) 10 (SprayA3)	Parameter for child droplet breakup time
C_3	10	Parameter to only undergo KH breakup near the nozzle

The interaction between turbulent flow field and Lagrangian droplet trajectories is described using turbulent dispersion models. This study utilizes the approach proposed by O'Rourke and Bracco [32], which adds fluctuating velocity components to the spray velocity based on Gaussian distributions using the gaseous turbulent kinetic energy at the particle location.

The evaporation of the liquid droplets is modeled via the multi-component modeling approach outlined by Brenn et al. [33]. The model is based on the work of Abramzon-Sirignano [34] using classical film theory where resistance to heat and mass transfer is modeled by fictional gas films of constant thicknesses. The defining difference to the single-component case is that mass transfer of every component is calculated separately, whereas heat transfer is still treated as a global mechanism.

The model computing the drag force imposed from the gaseous phase onto the liquid droplets used in the present work is the Schiller-Naumann drag law [35]. Table 8 summarizes the Lagrangian numerical setup for the liquid phase.

Table 8. Summary of Lagrangian numerical setup.

Liquid Spray Submodels	
Injection type	Blob
Breakup	KHRT
Turbulent dispersion	O'Rourke
Evaporation	Brenn et al. (Multi-Component)
Drag Law	Schiller-Naumann

2.4.3. Modeling Mass Rates Of Injection

The rates of injection boundary condition used in CFD modeling was identified as a source of possible errors for the Spray A injector [36]. Especially the initial ramp-up transient until up to 200 µs proved to be very challenging in order to generate consistent ensemble-averaged mass flow rates of injection using standard long-tube type instruments (HDA) described in Section 2.2. Overestimated rate fluctuations due to mechanical vibrations as well as an underestimation of the initial ramp-up gradient were reported.

As a consequence, the rate of injection for the highly transient ramp-up and ramp-down phases needed to be modeled, leading to a virtual rate of injection. Figure 3 shows the virtual injection rate utilized for ECN standard conditions (*Ar* and *Ai* in Table 4).

It can be seen that the initial ramp-up and the ramp-down of the injection rate is assumed to be faster than measured with the HDA flowmeter. However, the overall fuel mass injected into the chamber is maintained. The influence of the modeled ramp-up and ramp-down phases on the spray propagation and mixing in case of a single injection event is minor, albeit non-negligible.

For the multi-injection operating points the pilot injection is dominated by the transient phases of ramping-up and down. Therefore, HDA experiments cannot provide reliable data for the mass flow rate profiles for pilot injections. The ramp-up and ramp-down transients would be too slow to correctly simulate the observed penetration of the liquid and vapor phase. The short pilot injection forces the injector to operate in a ballistic working regime, where the correlation between coil energizing time and injected fuel amount becomes highly non-linear. This led the authors in [16] to develop a model based on the conservation of momentum along the spray axis to calculate the maximum initial velocity of the spray.

Utilizing this approach in combination with maintaining the measured overall injected fuel mass led to mass flow rates that could be used as valid inputs for the CFD simulations.

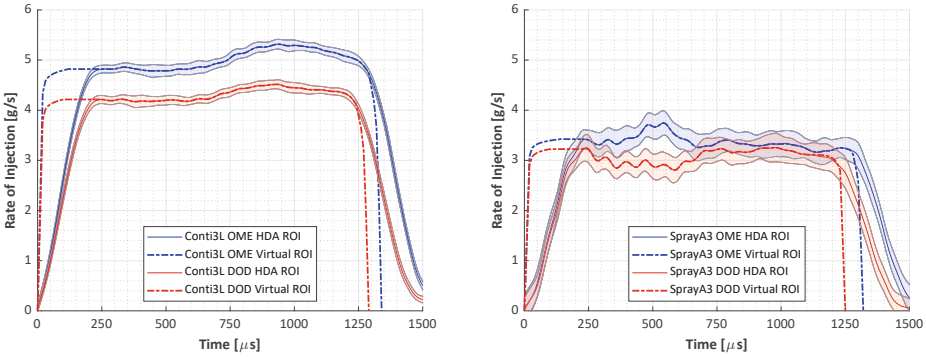

Figure 3. Virtual rate of injection used as CFD boundary condition (p_{inj}=1500 bar, p_{CC}=60 bar and t_{inj}=1.5 ms): (**left**) Conti3L. (**right**) SprayA3.

2.4.4. Liquid Penetration Length Calculation

This study utilizes the *Projected Liquid Volume* (PLV) for calculating the penetration of the liquid droplets into the simulation domain [19]. Previous methods, e.g., determining the distance where 99% of the liquid mass in the computational domain is located upstream, have no actual physical connection to the measurement techniques in use (Mie, DBI in Section 2.2). In [37] Pickett et al. summarized the problems associated with Mie-scatter lighting and proposed the usage of light-extinction diagnostics (DBI) in combination with a path integral analysis of the liquid volume fraction (LVF) for CFD simulations (Equation (6)).

$$\overbrace{\tau_{opt}\frac{\pi d_d^3/6}{C_{ext}}}^{Experimental} = \overbrace{\int_{-y_\infty}^{y_\infty} LVF\, dy}^{Modeling} = \int_{-y_\infty}^{y_\infty} \frac{volume\ liquid}{unit\ volume}\, dy \tag{6}$$

In this equation, τ_{opt} is the optical thickness and C_{ext} describes the extinction coefficient. A detailed description of the values and the procedure can be found in [38]. This study uses a threshold of $\int_{-y_\infty}^{y_\infty} LVF\, dy = 0.2 \cdot 10^{-3} \frac{mm^3 liquid}{mm^2}$ to determine the liquid penetration.

2.4.5. Combustion Modeling

The combustion modeling is realized using detailed reaction mechanisms. Especially the accurate prediction of auto-ignition and flame lift-off locations necessitate the incorporation of the complex oxidation chemistry for the different fuels researched in this study. The implementation in the CFD code treats every computational cell as a well-mixed homogeneous reactor at every time step.

The turbulence chemistry interaction (TCI) is modeled via a presumed (Gaussian) probability density function (pPDF) acting primarily on the local instantaneous temperature, which acts as the random variable satisfying the Gaussian distribution. This way the pPDF implementation affects any non-linear function of the temperature ($\overline{f(T)}$, Equation (7)) [39].

$$\overline{f(T)} = \int_{-\infty}^{+\infty} f\left(\overline{T} + \sqrt{\overline{T'T'}} \cdot x\right) \cdot \frac{1}{\sqrt{2\pi}} exp\left(-\frac{x^2}{2}\right) dx \tag{7}$$

A main indicator of the mixing field in the spray is the mixture fraction. It is defined as a passive scalar, meaning that its value changes due to mixing, but not due to reactions. Its definition in Equation (8) is related to element mass fractions Z_i of the i^{th} element, with

superscripts f and ox denoting the specific element mass fraction for the pure fuel and oxidizer. In [40] the nitrogen element mass fraction was used to calculate the mixture fraction, which is also the method utilized in this study.

$$Z = \frac{Z_i - Z_i^{ox}}{Z_i^f - Z_i^{ox}} \tag{8}$$

When identifying the instantaneous mixing state of oxygenated fuels, it was shown in [41] that the traditional definition of the equivalence ratio ϕ (Equation (9)) is not accurate enough when dealing with oxygenated fuels. Therefore, a new quantity was introduced, namely the *oxygen equivalence ratio* ϕ_Ω. It provides a more precise measure to quantify the instantaneous mixture stoichiometry for oxygenated fuels, as it correctly accounts for the oxygen bound in the chemical structure of the fuel. It can be defined depending on the oxygen ratio of the fuel Ω_f, which is a property of the fuel and resembles the number of oxygen atoms per mole of fuel divided by the number of oxygen atoms needed to convert all C- and H-atoms in a mole of fuel to stoichiometric products. For the used OME mix in this study the oxygen fuel ratio can be given as $\Omega_{f,OME}$=0.2567. The relationship between oxygen equivalence ratio and the conventional equivalence ration is stated in Equation (10) (assuming no C- and H-atoms are present in the oxidizer).

$$\phi = \frac{m_f / m_{ox}}{(m_f / m_{ox})_{st}} \tag{9}$$

$$\phi_\Omega = \frac{\phi}{1 + \Omega_f \cdot (\phi - 1)} \tag{10}$$

The reaction kinetics for the oxidization of dodecane are described in this study by the mechanism proposed by Yao et al. [42]. It generally shows good agreement with experimental data incorporating 54 species and 269 reactions. Additional calculations were performed using a longer mechanism derived by the CRECK modeling group [43] and presented in [44]. It consists of 130 species and 2323 reactions and will be labeled further as the *POLIMI* mechanism.

As the present work uses an OME mix consisting of molecules with a number of oxymethylene groups ranging from one to six (OME_1 to OME_6), the reaction mechanisms need to incorporate as many different OME molecules as possible. Therefore, the recently published reaction mechanism by Niu et al. [45] is utilized to calculate the oxidation of the OME. It consists of 92 species and 389 reactions. In order to classify the obtained results, auxiliary simulations were conducted using the mechanism by Cai et al. [46]. However, though being the reference mechanism of the ECN for the oxidization of OME_3, it has to be taken into account that this reaction scheme only comprises OME_2 to OME_4, meaning that the components OME_5 and OME_6 are neglected. Nevertheless, it is a quite extensive mechanism considering 322 species contributing to the combustion of OME.

3. Results

In the following section the numerical results are compared to the experimental measurements. The general idea of the spray modeling in this work follows the logic of stepwise validation for single and multi-injection simulations. The first step is the validation of the CFD model in evaporating inert chamber conditions (*Ai* in Section 2.3). Special focus is hereby placed on liquid and vapor penetration, spray dispersion as well as mixing. The validated spray model is then transfered into a reacting chamber atmosphere utilizing the reactions mechanism for the respective fuel described in Section 2.4.5. The combustion results are validated in terms of ignition delay, flame lift-off and propagation. Additionally the ignition zones and mixture stoichiometry are identified by transferring the simulation domain into mixture fraction (Equation (8)) and oxygen equivalence ratio (Equation (10)) space illustrating the mixing field of the hot reactive regions.

Energies **2022**, *15*, 6855

The obtained results aim to highlight and emphasize the differences found between dodecane and OME.

3.1. Spray Results

The computation of the liquid length of the spray follows the description in Section 2.4.4. For the Mie-scatter data the simulated liquid length is compared with the furthest position where a Mie signal is detectable for at least 50% of the 32 injection repetitions. The measured liquid length using diffuse back illumination (DBI) corresponds to a defined optical thickness and droplet extinction cross section following the ECN guidelines [19] already mentioned in Sections 2.2 and 2.4.4.

The vapor penetration into the combustion chamber is identified for inert conditions by tracking the vapor front of the spray with the distance from the nozzle to the furthest computational cell containing a fuel vapor mass fraction of at least 0.001 kg/kg. For inert conditions this definition corresponds to a mixture fraction of $Z = 0.001$ for the tracked vapor front. This simulated penetration is validated by schlieren measurements. With this method the furthest position downstream of the nozzle at which a schlieren signal is detectable for at least 50% of the injection repetitions determines the vapor penetration. The Rayleigh technique uses the quantification of the mixture fraction to determine the spray penetration at the furthest downstream location with the threshold of $Z \geq 0.001$.

The same fuel vapor threshold as for determining the spray vapor penetration is used to determine the center point and near cone angle of the simulated spray. For calculating the near cone angle the outer spray boundary within the section in between the center of spray and half its distance from the nozzle orifice is averaged at every given time step.

3.1.1. Single-Injection

Before addressing the influence of the multiple injection pattern, the CFD model has to be validated for the single injection case. The top two plots of Figure 4 depict the liquid and vapor penetration for dodecane and OME for the operating point *Ai* (900 K, 22.8 kg/m^3 and 0% O_2). Additionally the spray contour is plotted at 500 µs and 1000 µs after SOI. The left half of the spray cut illustrates the probability to detect a schlieren signal in false coloring and its right counterpart shows the simulated fuel mass fraction bound by the threshold of 0.001 kg/kg. At the bottom of Figure 4 the vapor dispersion in terms of vapor near cone angle and axial spray center is shown. These plots actually quantify the contour outlines of the spray cuts.

In general a good agreement for both fuels can be observed. It is noticeable that the vapor penetration for dodecane and OME do not differ significantly, which is expected taking into account the same chamber conditions and pressure drop from injection (1500 bar) to chamber (62 bar) pressure. According to Kook and Picket [47] the momentum flux is not correlated to the fuel density in case of a fixed pressure drop and nozzle area resulting in a unaffected vapor penetration. This statement also remains valid when considering the vapor dispersion. For both fuels the near cone angle and the axial position of the spray center do not differ significantly.

However, fuel density does have an impact on the liquid length, as shown in [47], because a more dense fuel decreases the entrained hot ambient mass per fuel mass and hence increases the liquid length. In case of OME and dodecane, the higher density of the OME mix is listed in Table 2 where it is also shown that the final boiling point is significantly higher for OME. Another parameter affecting the liquid length is the surface tension. According to [48] the surface tension for OMEs is higher compared to n-alkanes like dodecane. This would mean, in general, that the droplet breakup process shows a stronger resistance towards the aerodynamic forces driving the atomization. Furthermore, the vapor pressure of the studied OME mix is significantly higher than that of dodecane [49], indicating a higher volatility of OME. All of the differences in fuel properties described above result in a greater liquid length for OME, as seen in Figure 4.

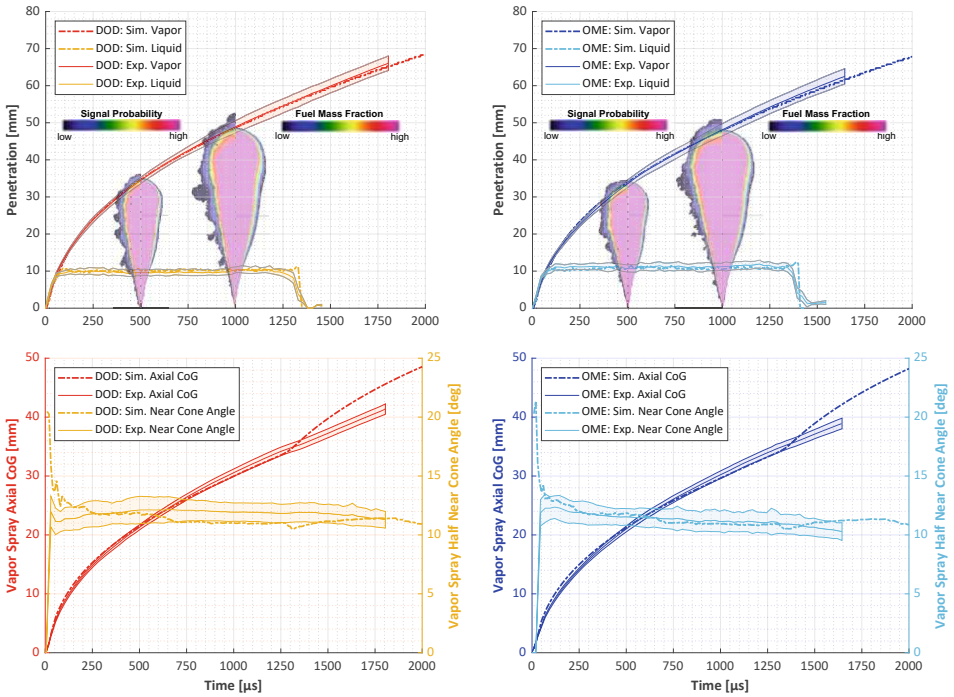

Figure 4. Conti3L: Spray penetration (**top**, projected liquid volume and vapor) and vapor dispersion (**bottom**, half near cone spreading angle and axial center of gravity) for inert chamber conditions (*Ai*: T_{CC}=900 K, ρ_{CC}=22.8 kg/m^3 and 0% O_2): (**left**) Dodecane. (**right**) OME.

A simple analysis of the critical Weber number ($We = \frac{\rho_d v_d^2 D_d}{\sigma_d}$) can lead to a first approximation of the ratio of liquid penetration of the droplets for dodecane and OME. Assuming a constant critical Weber number for both fuels, the ratio of the critical droplet diameter after initial breakup of the injected blobs ($D_{d,crit}$) can be calculated with Equation (11). The fuel properties are evaluated at the liquid injection temperature of 363.15 K and the droplet velocities in Equation (11) are equal to the average steady state injection velocities. The result or the critical diameter ratio indicates that the liquid phase of OME will penetrate further into the chamber than dodecane, as the droplets after initial breakup tend to be larger.

$$\frac{D_{d,crit,OME}}{D_{d,crit,DOD}} = \frac{\sigma_{d,OME} \cdot \rho_{d,DOD} \cdot v_{d,DOD}^2}{\sigma_{d,DOD} \cdot \rho_{d,OME} \cdot v_{d,OME}^2} \approx 1.29 \tag{11}$$

Evaluating the measured steady state liquid length for dodecane and OME for 900 K and 800 K chamber temperature, as shown in the left plot of Figure 5, actually yields a ratio between $1.15 \leq LL_{OME}/LL_{DOD} \leq 1.21$. Figure 5 also shows that the trends of higher liquid length for a lower temperature is clearly captured by the model. The estimation of Equation (11) is also reflected in the right plot within Figure 5, which depicts a droplet diameter distribution for both fuels through a plane at 5 mm axial distance to the nozzle and 1 ms after start of injection for a chamber temperature of 900 K. The greater Sauter-mean diameter ($D_{32,OME}/D_{32,DOD} \approx 1.34$) as well as the shift towards higher probability for larger droplets for OME is visible.

As the difference in liquid length is the main distinction between OME and dodecane for inert operating conditions, the plot in the center of Figure 5 depicts the relative difference between fuels for experiment and simulation. The longer liquid penetration for OME is represented by the CFD simulation, however it can be noticed that the effect is slightly underestimated compared to the experimental data. A summary of the liquid lengths for simulations and experiments is shown in Table 9.

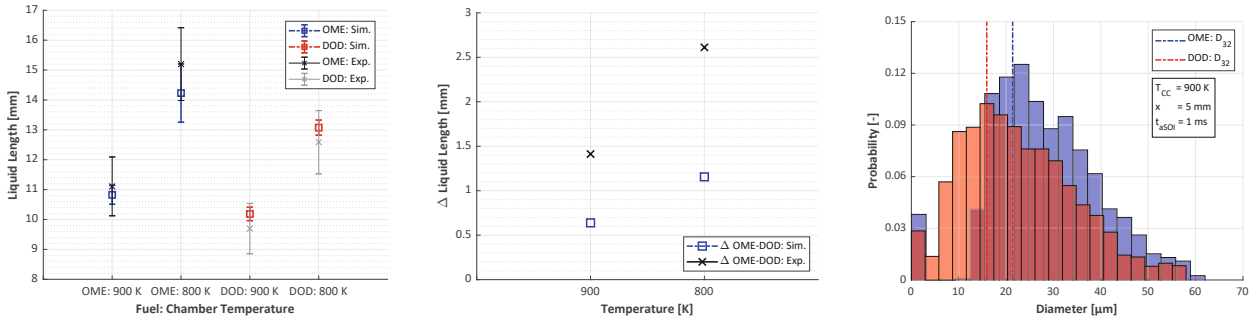

Figure 5. Conti3L: (**left**) Steady state liquid length (plv penetration). (**center**) Difference in liquid length between fuels. (**right**) Droplet diameter distribution.

Table 9. Conti3L: Inert liquid length results for OME and dodecane.

Fuel	T_{CC} [K]	Liquid Length Simulation [mm]	Liquid Length Experiment [mm]	Relative Simulation Error [%]
OME	800	14.08	15.20	−7.38
	900	10.78	11.11	−2.94
Dodecane	800	13.07	12.59	3.86
	900	10.19	9.70	5.06

As a means to expand the validity of the CFD model, simulations were also carried out representing the SprayA3 injector. The only difference in the simulation model for the SprayA3 simulations is an adaptation of the C_2 breakup time parameter from 8.5 to 10, see Table 7. Figure 6 illustrates the differences in liquid and vapor penetration for OME (right) and dodecane (left) determined with different measurement techniques compared to the simulation. The agreement between techniques and between experiment and simulation is obvious. Nevertheless, small differences can be observed in the liquid length for OME. The DBI measurements evaluate the liquid length to be slightly higher, roughly 1 mm, than the Mie-scattering would suggest.

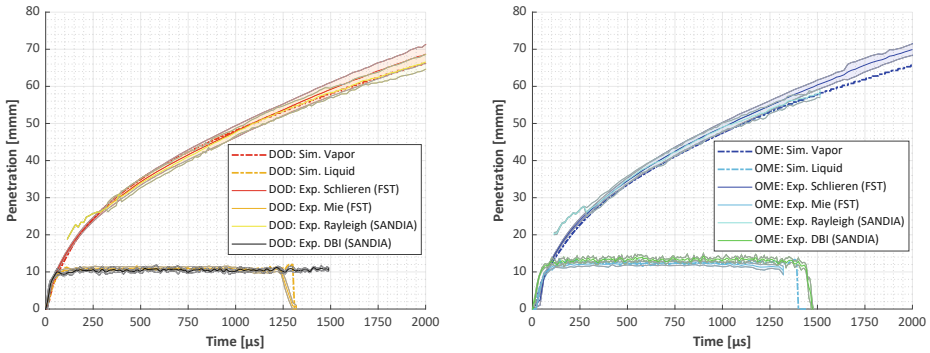

Figure 6. SprayA3 (*Ai*): Spray penetration comparison across experimental facilities: PLV penetration vs Mie (FST) and DBI (Sandia). Vapor penetration vs schlieren (FST) and Rayleigh (Sandia) diagnostics. (**left**) Dodecane. (**right**) OME.

The next step to validate the spray model, before analyzing the simulated combustion, is to quantify the possible errors in the predicted mixing fields. For this purpose the measured Rayleigh data was transferred to represent a two-dimensional and time-resolved mixing field quantifying the mixture fraction, Equation (8), for OME and dodecane. Figure 7 compares the mixture fraction in the spray center plane for simulation and experiment at

1000 µs after SOI. As the Rayleigh measurements have to avoid the Mie-scattering caused by the liquid phase, the initial part of the spray cannot be captured experimentally. At the top the contour plots of the mixing field show that simulation and experiment are in very good agreement. The bottom two plots of Figure 7 represent the radial mixture fraction profiles at several axial positions. Interestingly, OME tends to mix with a higher mixture fraction initially, but evolving into very similar profiles compared to dodecane further downstream. In case of OME the simulated mixture fraction profiles tend to be slightly overestimated for x = 30 mm and x = 40 mm.

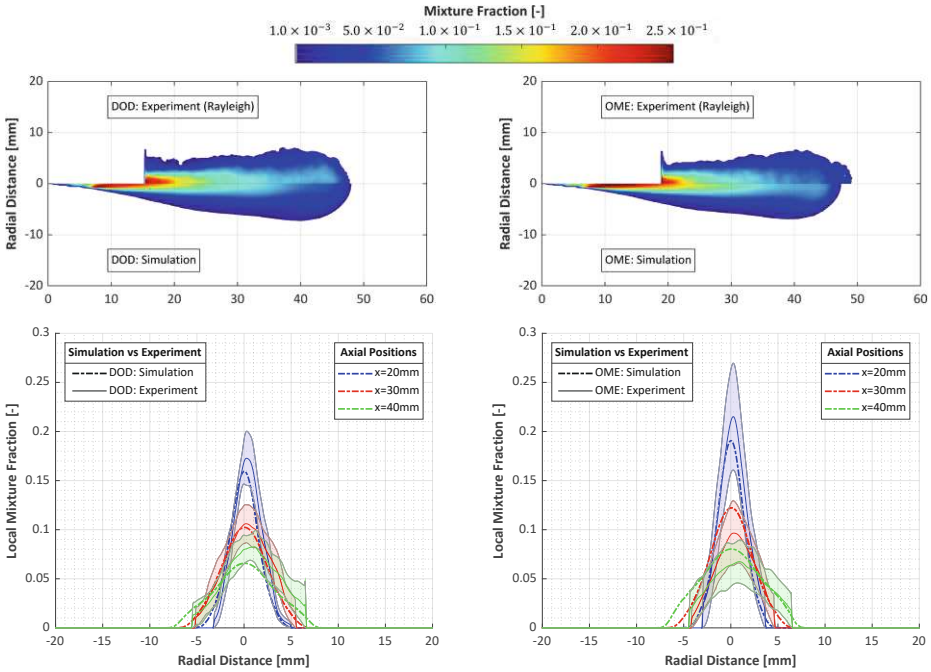

Figure 7. SprayA3 (*Ai*) @ $t_{aSOI} = 1000\mu s$: Mixture fraction in central spray axis plane: Contour (**top**) and radial profiles (**bottom**): (**left**) Dodecane. (**right**) OME.

The centerline mixture fraction is plotted on the left in Figure 8. The dodecane data shows an almost perfect match between simulation and experiment in between 20 < x < 40 mm. For OME the overestimation of the mixture fraction is also visible on the center line, hinting at possible errors in simulating the entrainment of ambient nitrogen into the fuel vapor spray. However, the error remains within the standard deviation of the experiment.

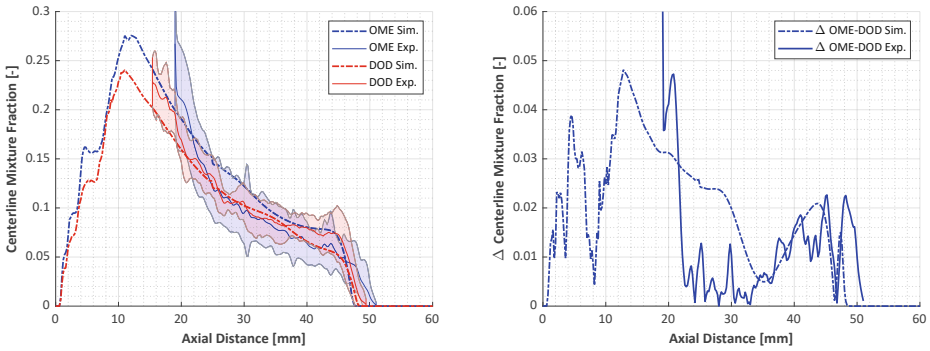

Figure 8. SprayA3 (*Ai*) @ $t_{aSOI} = 1000\mu s$: (**left**) Mixture fraction in centerline of spray axis. (**right**) Difference of centerline mixture fraction between fuels.

The fuel specific differences in the centerline mixing field are characterized within the right plot of Figure 8. The simulations show a greater change in mixture fraction than is apparent in the experiments. The differences in the mixing field for OME and dodecane are distinct at the position of the liquid penetration length. The further downstream the spray penetrates, the smaller the deviations between the fuels get.

The mixing field analysis shows that the model is capable to predict the mixing of fuel with the ambient atmosphere in a very reasonable quality and allows to transfer this model to a reactive atmosphere studying the auto-ignition and flame morphology for dodecane and OME in Section 3.2.

3.1.2. Multi-Injection

The starting point of the multi-injection analysis is once again the liquid and vapor penetration for 900 K and 800 K chamber temperature shown in Figure 9 for the Conti3L injector. Both fuels show good agreement between the schlieren and Mie measured data and the CFD model predicted spray tip penetration for the liquid and gaseous phase. As for the single-injection case, the vapor penetration, especially for the main injection, remains largely independent of the used fuel and operating point.

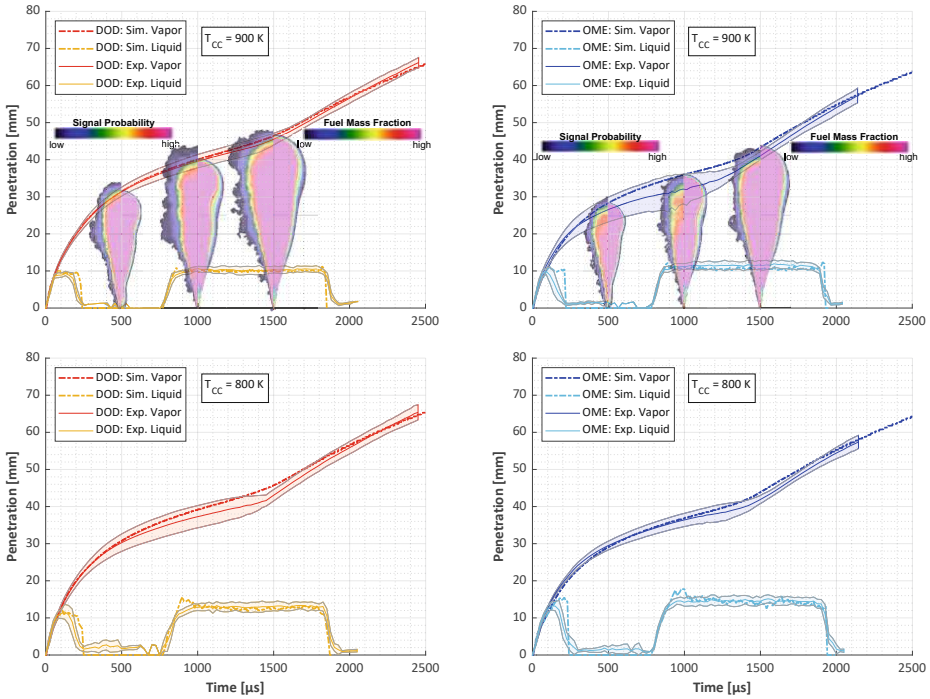

Figure 9. Conti3L: Multi-injection (t_{inj}=300/500/1200 µs) spray penetration (projected liquid volume and vapor) for inert conditions: (**top**) *AiM*: T_{CC}=900 K. (**bottom**) *T2iM*: T_{CC}=800 K. (**left**) Dodecane. (**right**) OME.

The injector dwell phase, in between pilot and main injection, is characterized by significant deviation for OME at 900 K compared to dodecane in terms of schlieren measured spray tip penetration uncertainty. This can also be noticed in the spray contour cuts of Figure 9, where again the probability of schlieren signal detection is plotted against the simulated fuel vapor mass fraction at 500, 1000 and 1500 µs. For dodecane the congruence between experiment and simulation is evident. For OME the larger experimental uncertainty is clearly visible as well as the tendency of the simulation to accumulate to much fuel vapor at the nozzle tip after the pilot injection. The schlieren diagnostics in general proved to be more challenging using OME as fuel as the signal is much weaker, which makes the detection of only small amounts of injected fuel, as is the case for short pilot injections,

especially hard. Nevertheless, it should be noted that the simulated vapor penetration stays within the experimental standard deviation at nearly all times for both fuels and operating points.

The main difference in modeling and experimental data is again observed in the liquid penetration for pilot and main injection. The trend toward higher liquid length at lower chamber temperature is realized in the model, however slightly underestimated for the main injection at 800 K for both fuels. The main point to extract from Figure 9 is that the liquid breakup following the highly transient pilot injection is modeled in very good agreement across fuels and chamber temperatures.

The significant schlieren data uncertainty can also be noticed when analyzing the the vapor near cone angle and axial spray center in Figure 10. When comparing the multi-injection with the single injection, it becomes apparent that the challenge of adequately modeling the spray propagation and dispersion for a multi-injection pattern is hardest during the injector dwell phase after the end of the pilot injection. One can see that the axial position of the spray center is overestimated after the pilot injection ramps down. The start of the main injection at around t_{aSOI} = 800 µs seems to be more precise for OME, keeping in mind the larger error in the experimental dataset during this phase. During the dwell and main-injection phase OME tends to form a slightly narrower spray with a smaller vapor near cone angle.

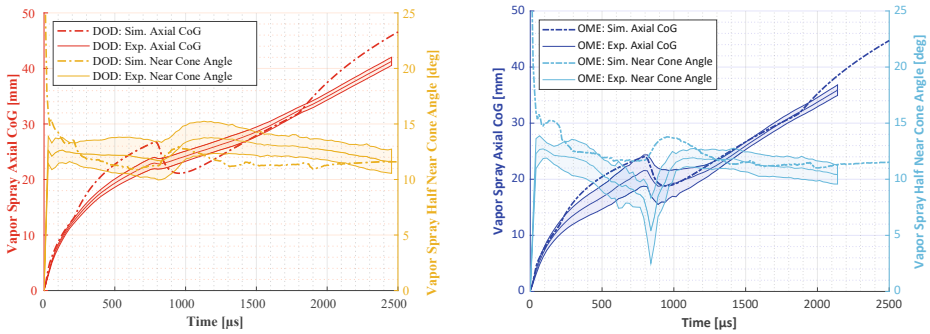

Figure 10. Conti3L (*AiM*): Multi-injection vapor spray dispersion (half near cone spreading angle and axial center of gravity): (**left**) Dodecane. (**right**) OME.

3.2. Combustion Results

The combustion modeling is validated against OH*-chemiluminescence experimental data specifying ignition delay times as well as flame morphology. This study follows the ECN standard to define the ignition delay time for the CFD calculation as the moment of the largest temperature gradient due to the onset of reactions. The experimental ignition delay time is based on the first detection of a OH* signal in at least half of the conducted measurements. Following the definition in [50], the evaluated signal probability determines the ignition delay time.

Furthermore, the lift-off length is determined to be the first axial location where the OH-mass fraction reaches 14 percent of its maximum in the computational domain. The flame penetration into the combustion chamber is identified by tracking the reactive front of the spray with a mixture fraction, Equation (8), of $Z = 0.001$ [19].

When not specifically listed, the used reaction mechanisms to simulate the combustion are the standard mechanisms described in Section 2.4.5 (Dodecane: Yao, OME: Niu).

3.2.1. Single-Injection

The first analysis of the combustion concerns the time-resolved lift-off length and flame penetration shown in Figure 11 for 900 K and 15% oxygen content. It is clearly visible that the simulated OME combustion under-predicts the ignition delay but yields very reasonable results in terms of established flame lift-off and penetration. For dodecane the

Energies **2022**, *15*, 6855

lift-off length is significantly overestimated, but ignition delay and flame penetration are in good agreement with the experimental data provided by the FST.

Figure 11 shows that the experimental data suggests a higher lift-off length for OME compared to dodecane which is not apparent for the CFD simulation. Therefore, the relationship between lift-off length and ignition delay is studied more closely in Figure 12. The left plot depicts the standard 900 K chamber condition where multiple reaction mechanisms where used for OME and dodecane to simulate the same operating point. The calculated ignition delay times are plotted against the corresponding lift-off length for each simulation. The trends for the two fuels clearly highlight a flame lift-off further downstream in case the ignition delay gets longer. With this analysis it can also be shown that the CFD model consistently predicts a longer lift-off for OME than for dodecane, which can also be noticed for the experiments.

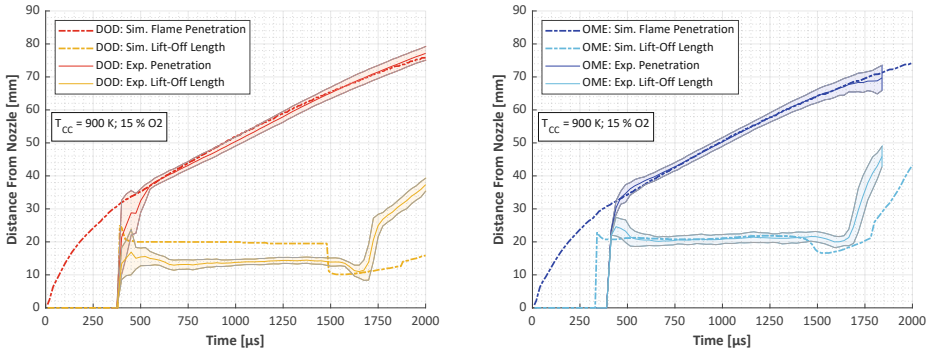

Figure 11. Conti3L: Spray lift-off length and penetration for reactive conditions: *Ar*: T_{CC}=900 K and 15% O_2. (**left**) Dodecane. (**right**) OME.

For a more detailed analysis of the validity of the combustion modeling the trends regarding the effects of oxygen content and chamber temperature on lift-off length and ignition delay are also illustrated in Figure 12. The trends for varying oxygen content in the center show a steeper rise in flame lift-off length for OME with decreasing oxygen content and hence longer ignition delay. The changes on lift-off length between OME and dodecane are comparable, whereas dodecane shows a stronger dependency on the oxygen content regarding the ignition delay time. This can be stated for simulation and experiments although the slopes do not completely agree.

An increasing chamber temperature results in a shorter lift-off length and earlier ignition as seen on the right plot in Figure 12. It is noticeable that the gradient of the OME trends for experiments and simulations along lower chamber temperatures is higher than for dodecane between 800 K and 900 K. For 1000 K OME deviates from the linear behavior for simulation and experiment in contrast to dodecane, which shows a strictly linear dependence on temperature. OME is igniting earlier than dodecane for the 1000 K case and has a very similar ignition delay at 900 K chamber temperature. For 800 K the experimentally detected ignition delay is significantly longer for OME. This observation is not perfectly matched by the simulation. However, the trend is visible as the simulated ignition delay times for 800 K are nearly identical, whereas OME consitently ignites earlier than dodecane at higher temperatures. Once again the lift-off length is consistently overpredicted by the CFD model, except for the 1000 K and OME fuel. However, the different behavior for OME can be deducted and the simulated trends plotted for varying chamber temperature are nearly parallel to the experimental ones. The summary of the ignition delay and lift-off length results for simulations and experiments for all analyzed operating points can be found in Table 10.

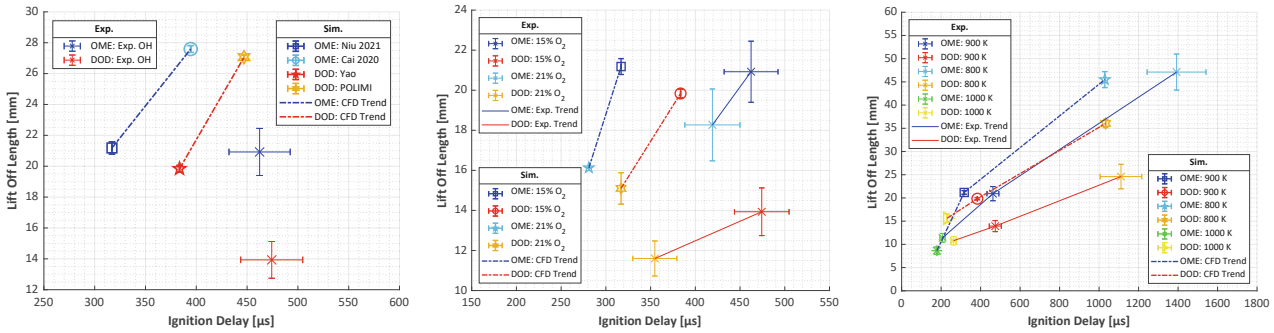

Figure 12. Conti3L: Lift-off length vs ignition delay for standard reaction mechanisms (OME: Niu [45], DOD: Yao [42]). (**left**) Multiple reaction mechanisms per fuel: *Ar*: T_{CC}=900 K, 15% O_2. (**center**) O_2 content trends: T_{CC}=900 K, 15% O_2 (*Ar*) and 21% O_2 (*O2r*). (**right**) Temperature dependency: 15% O_2, 800 K (*T2r*), 900 K (*Ar*) and 1000 K (*T3r*).

Table 10. Conti3L: Ignition delay and lift-off length results for OME (mechanism: Niu [45]) and dodecane (mechanism: Yao [42]).

Fuel	T_{CC} [K]	Oxygen content [%]	Ignition delay Sim. [µs]	Ignition delay Exp. [µs]	Lift-off length Sim. [mm]	Lift-off length Exp. [mm]
OME	800	15	1029	1392	45.50	47.12
	900	15	317	462	21.18	20.92
	900	21	281	419	16.13	18.27
	1000	15	179	207	8.64	11.41
Dodecane	800	15	1033	1111	36.04	24.61
	900	15	384	474	19.84	13.93
	900	21	317	355	15.10	11.60
	1000	15	231	263	15.64	10.80

The visual signal extracted from OH*-chemiluminescence experiments gives additional insight into the different ignition behavior between OME and dodecane. It is shown in Figure 13 as an average of 32 injection events and is compared to the respective simulated OH mass fraction contour in the spray center plane for 900 K and a varying oxygen content of 15% O_2 (left side) and 21% O_2 (right side). In order to compare the two operating points and fuels systematically the respective experimentally determined ignition delay was chosen ($t_{SOC,Exp}$) as reference point before increasing the time up until 0.55 ms after ignition. Additionally, auxiliary lines are inserted within the simulated pictures of the flames at 25 and 50 mm axial distance from the nozzle. From beginning to end of the combustion it can be seen that dodecane is forming a kidney-shaped or "V" contour with distinctive high-intensity regions at the shear boundary of the spray and the ambient air. The center axis of the spray does not show any OH-signal, neither in the experiment nor in the simulation.

In contrast the OME results show significant reaction activity in the spray center axis. The flame shape does not bend towards the shear boundary layer of fuel spray and ambient air, but rather straight high-intensity regions emerge, which bend towards the spray tip as the combustion proceeds. This trend is very well captured by the CFD simulation, although the very high-intensity regions in the near nozzle region could not be fully replicated by the model for 15% oxygen. The different flame shapes and ignition zones for OME are driven by the oxygen bound in the chemical formula of the fuel, delivering oxygen and therefore an ignitable mixture in regions where it is impossible for dodecane to ignite. This behavior could be the decisive factor for OME to lift-off further downstream compared to dodecane. The regions of stoichiometric mixture and higher reaction intensity are closer to the center axis of the spray, as shown in Figure 13, where the spray velocity is greater than

in the shear layer regions where dodecane is showing high reactive zones. This could push the flame lift-off for OME further downstream.

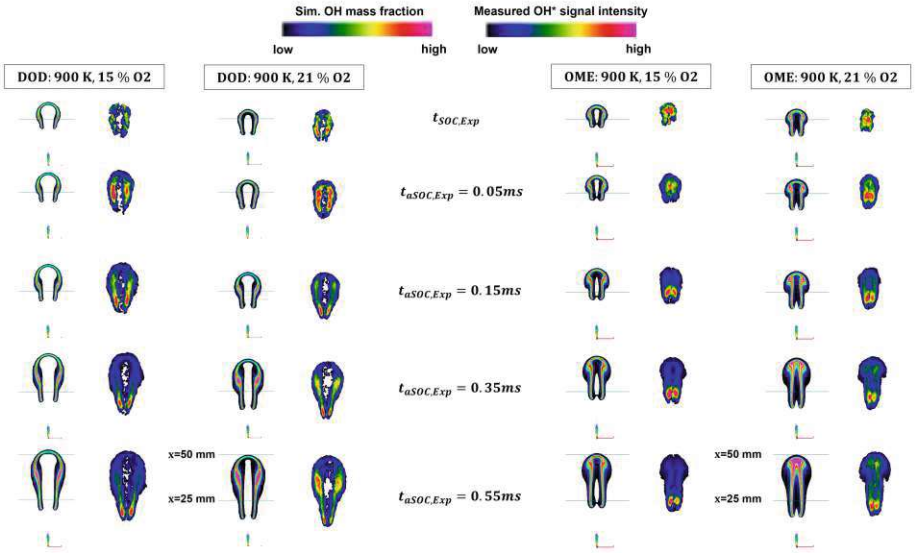

Figure 13. Conti3L (*Ar*): OH flame shape in center plane: Simulation vs experiment. (**left**) Dodecane. (**right**) OME.

3.2.2. Multi-Injection

The characterization of the combustion of the multi-injection follows the same logic as for the single injection. At first, the time-resolved lift-off length and penetration of the reactive spray front is compared to the OH*-measurements in Figure 14. Already major differences are noticeable for the two fuels. Dodecane already ignites after the short pilot injection during the injector dwell phase, which can also be reproduced by the simulation. The lift-off length prediction is quite realistic, although less fluctuating with time than the experiments and slightly overestimated for approximately the first half of the main injection. The flame penetration is slightly overestimated especially during the injector dwell phase before the main injection starts. The simulation for OME predicts an auto-ignition shortly after the pilot injection ends, which cannot be validated by the experiments. The lift-off length is somewhat overestimated except at the very end of the main injection. The flame penetration is once again modeled with very high accuracy.

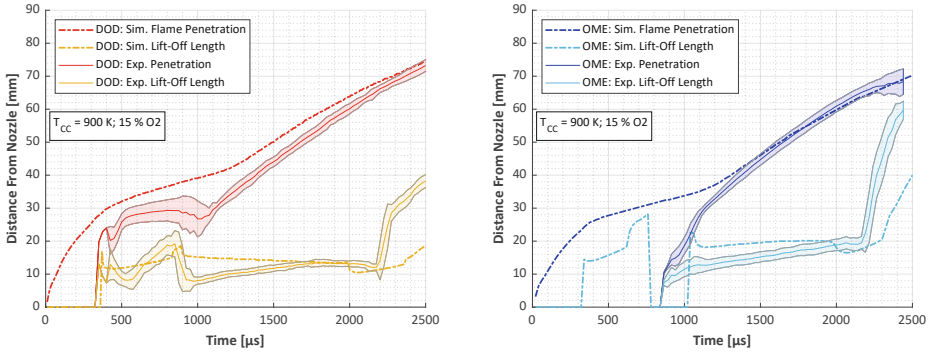

Figure 14. Conti3L: Multi-injection spray lift-off length and penetration for reactive conditions. *ArM*: T_{CC}=900 K, 15% O_2 and t_{inj}=300/500/1200 µs. (**left**) Dodecane. (**right**) OME.

A more detailed view into the temporal evolution of the multi-injection combustion is given in Figure 15. The left plot shows the profiles of the maximum temperature in the

simulation domain and the respective ignition delay at their maximum gradients. The most obvious difference is the stark decline in maximum temperature for OME during the injector dwell phase, which results in a second ignition, which is quite accurate in comparison with the experimentally observed ignition delay. The auto-ignition after the pilot injection at around 300 µs aSOI (pilot) cannot be validated. This is either due to a too reactive reaction mechanism, or the experimental setup was not able to detect a signal because the injected mass for the pilot injection was too small to produce a strong enough signal. The maximum temperature profile for dodecane only yields one ignition delay timing after the pilot injection, which is congruent with the experiments. Once again the ignition delay is slightly underestimated but within acceptable limits. The decline in maximum temperature as for OME cannot be observed. Only slight dip is visible at around 1100 µs aSOI (pilot) which is quickly compensated after the main injection delivers new fuel to the combustion process.

The plot in the center of Figure 15 describes the time dependent mean mass fractions for formaldehyde (CH_2O) and hydroxyl (OH) within the simulation domain.The plot on the right expresses their respective mean reaction rate. Both plots visualize that in case of OME the mean formaldehyde content remains greater during the injector dwell phase after being almost identical during the pilot injection. The main injection accounts for a large difference for mass fraction and reaction rate of CH_2O between OME and dodecane. Both peak at levels almost three times greater for OME. Interestingly, the production of OH during the injector dwell phase is larger for dodecane. Especially the significantly negative reaction rate of CH_2O at ca. 350 µs aSOI (pilot) signals that more OH is formed shortly thereafter. This can be seen in the reaction rates diagram but also in the higher plateau of OH mass fraction for dodecane during the injector dwell period. During the main injection OME forms OH faster than dodecane but the further reaction of OH into other reaction products is slower, meaning that dodecane and OME start to equalize their respective OH amount. After the main injection is finished, however, the same process as already described for the pilot injection materializes. The maximum temperature for OME declines sharply in conjunction with an abrupt reduction of reaction rates of first CH_2O and consequently later also of OH. The reaction rate of CH_2O for dodecane also decreases, albeit relatively less. However, the OH reaction rate remains constant after the end of the main injection and the mass fraction continues to increase, meaning that the high-temperature reaction processes still occur for dodecane, whereas the low-temperature reactions stop for both fuels.

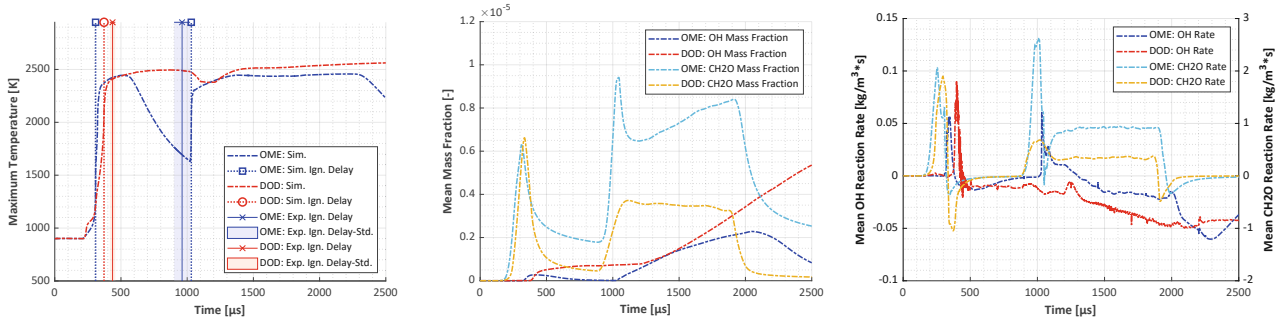

Figure 15. Conti3L (*ArM*): Time−resolved multi-injection profiles. (**left**) Maximum temperature. (**center**) Hydroxyl (OH) and Formaldehyde (CH_2O) mass fractions. (**right**) Hydroxyl (OH) and Formaldehyde (CH_2O) reaction rates.

The last analysis concerns the OH contour for the multi-injection once again compared to OH*-chemiluminescence measurements in Figure 16. The measurements are, as for the single injection case, averaged out of 32 injection events and plotted against the simulated OH mass fraction shown as a cut in the spray center plane. The differences in the high-temperature combustion reactions as already described for the previous figure, can clearly

Energies **2022**, *15*, 6855

be validated by the simulated and experimentally derived contours. The plots are separated in pre- or pilot injection and main injection combustion and again auxiliary lines are shown for the simulated flame shapes at 25 and 50 mm axial distance from the nozzle. The experiments show a signal for dodecane for the entire time once the mixture ignited at approximately 437 µs aSOI (pilot). The initial simulated flame shape is too differentiated at the shear boundary layer of spray and ambient air. Experiment and simulation converge as the combustion proceeds, although the relative OH amount at the simulated spray tip is overestimated before the main injection dominates the combustion. During the main injection the "V" shape of the flame contour becomes once again visible and is quite similar to the single injection case.

The comparison between experiments and simulation for OME can only be conducted for the main injection, as no OH*-signal was detected for the pilot injection. However, quite similar to the single injection case, the different flame contour is apparent and a higher signal intensity and simulated mass fraction in the center axis of the spray can be observed.

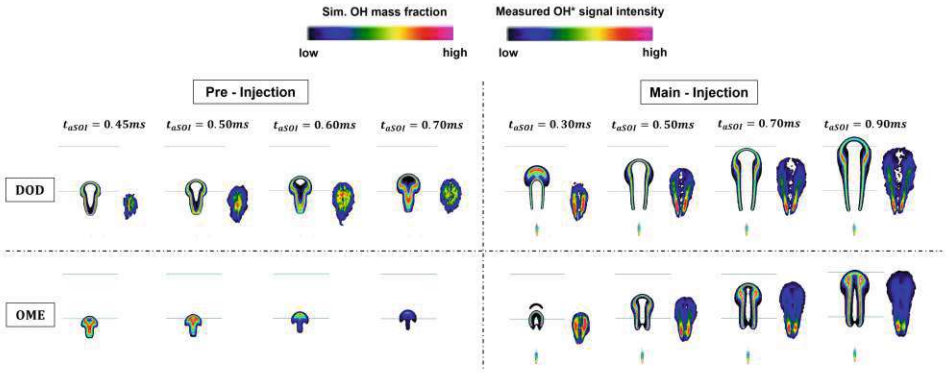

Figure 16. Conti3L (*ArM*): OH flame shape for multi-injection: Simulation vs experiment. (**top**) Dodecane. (**bottom**) OME.

4. Discussion

The presented experimental and numerical results show that the regions of the ignition and high reaction activity differ significantly for the investigated fuels. To further analyze these differences, the entire simulation domain was transformed in order to represent different mixing regimes present during combustion of OME and dodecane. Figure 17 displays scatter plots of the temperature of each simulation cell in dependency of mixture fraction (top) or oxygen equivalence ratio (bottom, see Equation (10)), which is utilized as a passive scalar. For each plot the stoichiometric condition is indicated as a vertical dash-dotted line. Each cell is scaled in size by the mass of OH it contains and colored by the mass fraction of OH present in it. The scatter plots were evaluated at 1000 µs aSOI. The difference in the mixing space for the two fuels is evident.

The ignition zones for OME are located at higher mixture fraction values and are simulated to be cooler than for dodecane. A higher stoichiometric mixture fraction also implies a cooler adiabatic mixing temperature for cool fuel injected into hot ambient air.

The most obvious difference for the two fuels is shown in the plots using the oxygen equivalence ratio. For dodecane the simulated range is quite large and extending to $0 < \phi_{\Omega,DOD} \leq 5$. However for OME, the oxygen equivalence ratio barely even exceeds two. According to [25,51] increased soot yield only materializes for equivalence ratios $\phi_\Omega \geq 2$. Leaner mixtures than that primarily convert the hydrocarbons molecules to carbon monoxide (CO) instead of soot. In addition, soot formation is occurring within a temperature range between 1200 K $\leq T \leq$ 2000 K, which is due to the need of radical precursors, such as C_3H_3, that do not exist at lower temperatures. On the other hand, these precursors are pyrolized and oxidized at higher temperatures [52]. These soot yield limits are highlighted in the bottom two plots of Figure 17. It is quite obvious that the

dodecane combustion does indeed generate mixing and temperature regimes which result in the formation of soot. For OME however, not a single cell is placed within the soot yield limits. This observation, combined with the lack of carbon to carbon (*C-C*) bonds within the chemical structure of OME, is a strong indication that the formation of soot is effectively prohibited for the OME mix used in this study. A separate analysis of the influence of mixing field and suppression of soot precursors, like C_2H_2 and C_3H_3, because of missing *C-C* bonds, on the overall formation of soot requires further research into this topic.

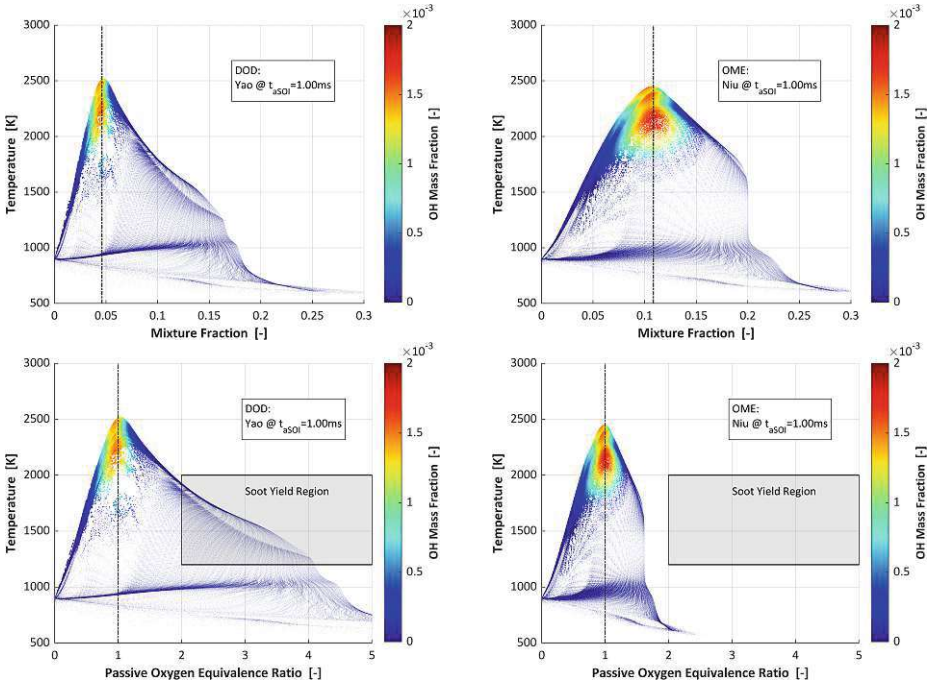

Figure 17. Conti3L (*Ar*): Simulation temperature in mixture fraction space (**top**) and passive scalar oxygen equivalence ratio space (**bottom**). (**left**) Dodecane. (**right**) OME.

5. Conclusions

In this study numerical investigations were carried out to study the differences between an OME mixture and dodecane in terms of spray propagation, mixing behavior and combustion. Furthermore, the influence of a multi-injection pattern was analyzed. The developed CFD model is capable of adequately predicting the measured liquid and vapor penetration as well as mixing field across fuels, chamber temperatures and injection patterns. The trends for flame lift-off and ignition delay for varying oxygen content and temperature are adequately modeled. However, the lift-off length was consistently overestimated for each simulation that came close to correctly predicting the ignition delay. The good agreement of inert results with experimental data implies that the deviations between measurements and simulation observed for the combustion process are mainly driven by the reaction kinetics, at least downstream of the liquid length. For the multi-injection the differences in the transient evolution of temperature and key species were determined.

The main conclusions describing the differences between OME and dodecane are as follows:

- The liquid phase penetrates further in the chamber for OME.
- OME mixes with an elevated mixture fraction in the vicinity of the liquid penetration length with a harmonization of the mixing field between OME and dodecane further downstream of the nozzle.
- Dodecane shows a stronger influence on ignition delay time with varying ambient oxygen content compared to OME.

- The ignition delay times at varying ambient temperatures demonstrate that OME ignites earlier than dodecane for 1000 K and has a similar ignition delay for 900 K. At 800 K the ignition delay of OME is found to be longer, which indicates that the turning point temperature where dodecane yields a faster ignition is in between the range of 800 K and 900 K.
- OME has a flame lift-off further downstream of the nozzle compared to dodecane, with the possible explanation for this being the observation that OME ignites closer to the center axis of the spray, where velocities are highest, which could push the establishment of a stable flame further downstream. However, at higher chamber temperatures at or above 1000 K the difference in lift-off length seems to be minimized or even at an inflection point.
- The mixing regimes of the ignition zones are very different for the two fuels. The absent of soot for the OME combustion, as referenced in [3–5], was underpinned by the investigation that the combustible mixture for OME is much leaner and that not a single simulation cell is entering neither temperature range nor the oxygen equivalence ratio limit of at least two for increased soot formation.
- For multi-injection patterns with a short pilot injection the high-temperature reactions, signaled by the OH reaction rates, differ substantially for OME and dodecane. The high-temperature combustion is progressing longer in time after injection events ended for dodecane.

The main challenges regarding the modeling of OME for single and multi-injection are:

- Correct modeling of fuel entrainment after short pilot injections;
- Adequate reaction kinetics encompassing all of the studied OME components;
- Reasonable prediction of lift-off length incorporating correct ignition delay.

Overall, the findings in this study outline the following practical impacts:

- Engine applications must incorporate the longer liquid and lift-off length for OME to prevent possible piston damage.
- The diesel characteristic soot-NOx trade-off can be avoided when using OME as fuel, due to the absent of soot.

However, further research is necessary to determine the extent of the effect of the leaner mixture in contrast to the effect caused by missing *C*-*C* bonds within the chemical structure of OME regarding the formation of soot. Future investigations will therefore focus on the formation of soot precursors, e.g., C_2H_2 and C_3H_3, as well as turbulence modeling by comparing the developed RANS model with LES calculations of the same setup.

The developed model will also be transferred to a CFD model of an optically accessible single cylinder research engine to further investigate the differences of OME and dodecane.

Author Contributions: Conceptualization, F.W.; methodology, F.W. and T.L.; software, F.W.; validation, F.W., L.S., K.W and S.R.; formal analysis, F.W.; investigation, F.W., L.S and K.W; data curation, F.W., L.S. and K.W.; writing—original draft preparation, F.W., L.S and K.W; writing—review and editing, T.L., S.R. and J.M; visualization, F.W.; supervision, T.L, S.R. and J.M; project administration, T.L.; funding acquisition, T.L. All authors have read and agreed to the published version of the manuscript.

Funding: This paper is the scientific result of a research project undertaken by the *Research Association for Combustion Engines eV* (FVV). Parts of this work were funded by the *Federal Ministry for Economic Affairs and Energy* (BMWi) through the *German Federation of Industrial Research Associations eV* (AiF). The work at the TU Wien was funded by the *Ministry for Transport, Innovation and Technology* (BMVIT) through the *Austrian Research Promotion Agency* (FFG), grant number 874418. The research was carried out in the framework of the *collective research networking program* (CORNET) project "eSpray".

Data Availability Statement: Confidentiality agreements do not allow the publication of the data presented in this study.

Acknowledgments: The authors acknowledge TU Wien Bibliothek for financial support through its Open Access Funding Program. The experiments performed at Sandia Nat. Labs were supported by the U.S. Department of Energy (DOE) Office of Vehicle Technologies. Sandia is a multi-mission laboratory managed and operated by National Technology and Engineering Solutions of Sandia, LLC., a wholly owned subsidiary of Honeywell International, Inc., for the U.S. Department of Energy's National Nuclear Security Administration under contract DE-NA000352. The authors would like to thank Jens Frühaber for the discussions and inputs. The computational results presented have been achieved using the Vienna Scientific Cluster (VSC) via the funded project No. 71485

.

Conflicts of Interest: The authors declare no conflict of interest.

Abbreviations

The following abbreviations are used in this manuscript:

A_d	Droplet frontal area
Ai	ECN Spray A standard inert chamber conditions (900 K, 22.8 kg/m^3, 0% O_2)
Ar	ECN Spray A standard reacting chamber conditions (900 K, 22.8 kg/m^3, 15% O_2)
C_1,C_2,C_3	KHRT breakup model parameters
C_d	Droplet drag coefficient
C_D	Discharge coefficient
C_v	Velocity coefficient
d	Diameter
ECN	Engine Combustion Network
F_D	Drag force
FST	Institute of Fluid System Technology
g	Gaseous
l	Liquid
KHRT	Kelvin-Helmholtz-Rayleigh-Taylor breakup model
L	Length
LVF	Liquid Volume Fraction
$\dot{m}$	Mass flow
$\dot{M}$	Momentum flux
MDPI	Multidisciplinary Digital Publishing Institute
O2	ECN Spray A high oxygen chamber conditions (900 K, 22.8 kg/m^3, 21% O_2)
p	Pressure
r	Radius
RANS	Reynolds averages Navier-Stokes equations
SOC	Start of combustion
SOI	Start of injection
t	Time
T2i	ECN Spray A low temperature inert chamber conditions (800 K, 22.8 kg/m^3, 0% O_2)
T2r	ECN Spray A low temperature inert chamber conditions (800 K, 22.8 kg/m^3, 15% O_2)
T3i	ECN Spray A low temperature inert chamber conditions (1000 K, 22.8 kg/m^3, 0% O_2)
T3r	ECN Spray A low temperature inert chamber conditions (1000 K, 22.8 kg/m^3, 15% O_2)
u,v	Velocity
We	Weber number
x	Distance
Z	Mixture fraction
Z_i	Element mass fraction
Λ	Wavelength
ρ	Density
τ	breakup time, optical thickness
ϕ	Equivalence ratio
ϕ_Ω	Oxygen equivalence ratio
Ω	Wave growth rate, Oxygen ratio

References

1. Deutz, S.; Bongartz, D.; Heuser, B.; Kätelhön, A.; Langenhorst, L.S.; Omari, A.; Walters, M.; Klankermayer, J.; Leitner, W.; Mitsos, A.; et al. Cleaner production of cleaner fuels: Wind-to-wheel—Environmental assessment of CO2-based oxymethylene ether as a drop-in fuel. *Energy Environ. Sci.* **2018**, *11*, 331–343. https://doi.org/10.1039/C7EE01657C.
2. Damyanov, A.; Hofmann, P.; Geringer, B.; Schwaiger, N.; Pichler, T.; Siebenhofer, M. Biogenous ethers: Production and operation in a diesel engine. *Automot. Engine Technol.* **2018**, *3*, 69–82. https://doi.org/10.1007/s41104-018-0028-x.
3. Liu, J.; Wang, H.; Li, Y.; Zheng, Z.; Xue, Z.; Shang, H.; Yao, M. Effects of diesel/PODE (polyoxymethylene dimethyl ethers) blends on combustion and emission characteristics in a heavy duty diesel engine. *Fuel* **2016**, *177*, 206–216. https://doi.org/10.1016/j.fuel.2016.03.019.
4. Härtl, M.; Gaukel, K.; Pélerin, D.; Wachtmeister, G. Oxymethylene Ether as Potentially CO_2-neutral Fuel for Clean Diesel Engines Part 1: Engine Testing. *MTZ Worldw* **2017**, *78*, 52–59. https://doi.org/10.1007/s38313-016-0163-6.
5. Omari, A.; Heuser, B.; Pischinger, S. Potential of oxymethylenether-diesel blends for ultra-low emission engines. *Fuel* **2017**, *209*, 232–237. https://doi.org/10.1016/j.fuel.2017.07.107.
6. Liu, H.; Ma, X.; Li, B.; Chen, L.; Wang, Z.; Wang, J. Combustion and emission characteristics of a direct injection diesel engine fueled with biodiesel and PODE/biodiesel fuel blends. *Fuel* **2017**, *209*, 62–68. https://doi.org/10.1016/j.fuel.2017.07.066.
7. Lumpp, B.; Rothe, D.; Pastoetter, C.; Laemmermann, R.; Jacob, E. Oxymethylenether als Dieselkraftstoffzusaetze der Zukunft. *Mot. Z.* **2011**, *72*, 198–202.
8. Härtl, M.; Seidenspinner, P.; Wachtmeister, G.; Jacob, E. Synthetischer Dieselkraftstoff OME1 — Lösungsansatz für den Zielkonflikt NOx-/Partikel-Emission. *MTZ Motortech. Z.* **2014**, *75*, 68–73. https://doi.org/10.1007/s35146-014-0392-7.
9. Härtl, M.; Seidenspinner, P.; Jacob, E.; Wachtmeister, G. Oxygenate screening on a heavy-duty diesel engine and emission characteristics of highly oxygenated oxymethylene ether fuel OME1. *Fuel* **2015**, *153*, 328–335. https://doi.org/10.1016/j.fuel.2015.03.012.
10. Feiling, A.; Münz, M.; Beidl, C. Potential of the Synthetic Fuel OME1b for the Soot-free Diesel Engine. *ATZextra Worldw.* **2016**, *21*, 16–21. https://doi.org/10.1007/s40111-015-0516-1.
11. Pellegrini, L.; Marchionna, M.; Patrini, R.; Beatrice, C.; Del Giacomo, N.; Guido, C. *Combustion Behaviour and Emission Performance of Neat and Blended Polyoxymethylene Dimethyl Ethers in a Light-Duty Diesel Engine*; SAE International: Warrendale, PA, USA, 2012; pp. 2012–01–1053. https://doi.org/10.4271/2012-01-1053.
12. Gaukel, K.; Pélerin, D.; Härtl, M.; Wachtmeister, G.; Burger, J.; Maus, W.; Jacob, E. *Der Kraftstoff OME2: Ein Beispiel für den Weg zu emissionsneutralen Fahrzeugen mit Verbrennungsmotor /The Fuel OME2: An Example to Pave the Way to Emission-Neutral Vehicles with Internal Combustion Engine*; VDI Verlag: Düsseldorf, Germany, 2016; pp. II–223. https://doi.org/10.51202/9783186799128-II-193.
13. Richter, G.; Zellbeck, H. OME als Kraftstoffersatz im Pkw-Dieselmotor. *MTZ Motortech. Z.* **2017**, *78*, 66–73. https://doi.org/10.1007/s35146-017-0131-y.
14. Maus, W., Ed. *Zukünftige Kraftstoffe: Energiewende des Transports als ein weltweites Klimaziel*; Springer: Berlin/Heidelberg, Germany, 2019. https://doi.org/10.1007/978-3-662-58006-6.
15. Choi, C.Y.; Reitz, R.D. An experimental study on the effects of oxygenated fuel blends and multiple injection strategies on DI diesel engine emissions. *Fuel* **1999**, *78*, 1303–1317.
16. Frühhaber, J.; Peter, A.; Schuh, S.; Lauer, T.; Wensing, M.; Winter, F.; Priesching, P.; Pachler, K. *Modeling the Pilot Injection and the Ignition Process of a Dual Fuel Injector with Experimental Data from a Combustion Chamber Using Detailed Reaction Kinetics*; SAE International: Warrendale, PA, USA, 2018; pp. 2018–01–1724. https://doi.org/10.4271/2018-01-1724.
17. Lee, C.H.; Reitz, R.D. CFD simulations of diesel spray tip penetration with multiple injections and with engine compression ratios up to 100:1. *Fuel* **2013**, *111*, 289–297. https://doi.org/10.1016/j.fuel.2013.04.058.
18. Anand, K.; Reitz, R. Exploring the benefits of multiple injections in low temperature combustion using a diesel surrogate model. *Fuel* **2016**, *165*, 341–350. https://doi.org/10.1016/j.fuel.2015.10.087.
19. ECN. Engine Combustion Network. Available online: https://ecn.sandia.gov/ (accessed on 29 March 2022).
20. ASG. ASG Analytik-Service. Available online: https://asg-analytik.de/ (accessed on 1 February 2022).
21. Skeen, S.A.; Yasutomi, K. Measuring the soot onset temperature in high-pressure n-dodecane spray pyrolysis. *Combust. Flame* **2018**, *188*, 483–487.
22. Manin, J.; Pickett, L.M.; Skeen, S.A.; Frank, J.H. Image processing methods for Rayleigh scattering measurements of diesel spray mixing at high repetition rate. *Appl. Phys. B* **2021**, *127*, 79.
23. Hanjalić, K.; Popovac, M.; Hadžiabdić, M. A robust near-wall elliptic-relaxation eddy-viscosity turbulence model for CFD. *Int. J. Heat Fluid Flow* **2004**, *25*, 1047–1051. https://doi.org/10.1016/j.ijheatfluidflow.2004.07.005.
24. Popovac, M.; Hanjalic, K. Compound wall treatment for RANS computation of complex turbulent flows. *Flow Turbul. Combust.* **2007**, *78*, 177–202.
25. Stiesch, G. *Modeling Engine Spray and Combustion Processes*; Springer: Berlin/Heidelberg, Germany, 2003; OCLC: 861705857.
26. Reitz, R.D. Modeling atomization processes in high-pressure vaporizing sprays. *At. Spray Technol.* **1987**, *3*, 309–337.
27. Jiang, X.; Siamas, G.; Jagus, K.; Karayiannis, T. Physical modelling and advanced simulations of gas–liquid two-phase jet flows in atomization and sprays. *Prog. Energy Combust. Sci.* **2010**, *36*, 131–167. https://doi.org/10.1016/j.pecs.2009.09.002.
28. Taylor, G. The instability of liquid surfaces when accelerated in a direction perpendicular to their planes. I. *Proc. R. Soc. Lond. A* **1950**, *201*, 192–196. https://doi.org/10.1098/rspa.1950.0052.

29. O'Rourke, P.J.; Amsden, A.A. *The Tab Method for Numerical Calculation of Spray Droplet Breakup*; SAE International: Warrendale, PA, USA, 1987; p. 872089. https://doi.org/10.4271/872089.
30. Patterson, M.A.; Reitz, R.D. Modeling the Effects of Fuel Spray Characteristics on Diesel Engine Combustion and Emission. *SAE Trans.* **1998**, *107*, 27–43.
31. AVL List GmbH. FIRE Spray Manual 2020 R1. Manual. AVL List GmbH, Graz, Austria
32. O'Rourke, P.J.; Bracco, F. Modelling of Drop Interactions in Thick Sprays and a Comparison with Experiments. *I. Mech. E. C* **1980**, *404*, 101–116.
33. Brenn, G.; Deviprasath, L.J.; Durst, F. Computations and experiments on the evaporation of multi-component droplets. In Proceedings of the Proceedings/ICLASS 2003, Sorrento, Italy, 13–17 July 2003.
34. Abramzon, B.; Sirignano, W. Droplet vaporization model for spray combustion calculations. *Int. J. Heat Mass Transf.* **1989**, *32*, 1605–1618. https://doi.org/10.1016/0017-9310(89)90043-4.
35. Schiller, L.; Naumann, A.Z. A Drag Coefficient Correlation. *Zeit. Ver. Deutsch. Ing.* **1933**, *77*, 318–320.
36. Pickett, L.M.; Manin, J.; Payri, R.; Bardi, M.; Gimeno, J. *Transient Rate of Injection Effects on Spray Development*; SAE International: Warrendale, PA, USA, 2013; pp. 2013–24–0001. https://doi.org/10.4271/2013-24-0001.
37. Pickett, L.M.; Genzale, C.L.; Manin, J. UNCERTAINTY QUANTIFICATION FOR LIQUID PENETRATION OF EVAPORATING SPRAYS AT DIESEL-LIKE CONDITIONS. *At. Sprays* **2015**, *25*, 425–452. https://doi.org/10.1615/AtomizSpr.2015010618.
38. Maes, N.; Skeen, S.A.; Bardi, M.; Fitzgerald, R.P.; Malbec, L.M.; Bruneaux, G.; Pickett, L.M.; Yasutomi, K.; Martin, G. Spray penetration, combustion, and soot formation characteristics of the ECN Spray C and Spray D injectors in multiple combustion facilities. *Appl. Therm. Eng.* **2020**, *172*, 115136.
39. AVL List GmbH. FIRE General Gas Phase Reactions Module v2018. Manual. AVL List GmbH, Graz, Austria
40. Tagliante, F.; Sim, H.S.; Pickett, L.M.; Nguyen, T.; Skeen, S. *Combined Experimental/Numerical Study of the Soot Formation Process in a Gasoline Direct-Injection Spray in the Presence of Laser-Induced Plasma Ignition*; SAE International: Warrendale, PA, USA, 2020; pp. 2020–01–0291. https://doi.org/10.4271/2020-01-0291.
41. Mueller, C.J. *The Quantification of Mixture Stoichiometry When Fuel Molecules Contain Oxidizer Elements or Oxidizer Molecules Contain Fuel Elements*; SAE International: Warrendale, PA, USA, 2005; pp. 2005–01–3705. https://doi.org/10.4271/2005-01-3705.
42. Yao, T.; Pei, Y.; Zhong, B.J.; Som, S.; Lu, T.; Luo, K.H. A compact skeletal mechanism for n-dodecane with optimized semi-global low-temperature chemistry for diesel engine simulations. *Fuel* **2017**, *191*, 339–349. https://doi.org/10.1016/j.fuel.2016.11.083.
43. CRECK Modeling Group Website. Available online: http://creckmodeling.chem.polimi.it/menu-kinetics/menu-kinetics-reduced-mechanisms/menu-kinetics-reduced-n-dodecane (accessed on 17 November 2021).
44. Ranzi, E.; Frassoldati, A.; Stagni, A.; Pelucchi, M.; Cuoci, A.; Faravelli, T. Reduced Kinetic Schemes of Complex Reaction Systems: Fossil and Biomass-Derived Transportation Fuels: Reduced Kinetic Schemes of Complex Reaction Systems. *Int. J. Chem. Kinet.* **2014**, *46*, 512–542. https://doi.org/10.1002/kin.20867.
45. Niu, B.; Jia, M.; Chang, Y.; Duan, H.; Dong, X.; Wang, P. Construction of reduced oxidation mechanisms of polyoxymethylene dimethyl ethers (PODE1–6) with consistent structure using decoupling methodology and reaction rate rule. *Combust. Flame* **2021**, *232*, 111534. https://doi.org/10.1016/j.combustflame.2021.111534.
46. Cai, L.; Jacobs, S.; Langer, R.; vom Lehn, F.; Heufer, K.A.; Pitsch, H. Auto-ignition of oxymethylene ethers (OMEn, n = 2–4) as promising synthetic e-fuels from renewable electricity: Shock tube experiments and automatic mechanism generation. *Fuel* **2020**, *264*, 116711. https://doi.org/10.1016/j.fuel.2019.116711.
47. Kook, S.; Pickett, L.M. Liquid length and vapor penetration of conventional, Fischer—Tropsch, coal-derived, and surrogate fuel sprays at high-temperature and high-pressure ambient conditions. *Fuel* **2012**, *93*, 539–548. https://doi.org/10.1016/j.fuel.2011.10.004.
48. Lautenschütz, L.; Oestreich, D.; Seidenspinner, P.; Arnold, U.; Dinjus, E.; Sauer, J. Physico-chemical properties and fuel characteristics of oxymethylene dialkyl ethers. *Fuel* **2016**, *173*, 129–137. https://doi.org/10.1016/j.fuel.2016.01.060.
49. H. H. Fechter, M.; Haspel, P.; Hasse, C.; Braeuer, A.S. Vapor pressures and latent heats of vaporization of Poly(oxymethylene) Dimethyl Ethers (OME3 and OME4) up to the vicinity of the critical temperature. *Fuel* **2021**, *303*, 121274. https://doi.org/10.1016/j.fuel.2021.121274.
50. Riess, S.; Vogel, T.; Wensing, M. Influence of Exhaust Gas Recirculation on Ignition and Combustion of Diesel Fuel under Engine Conditions Investigated by Chemical Luminescence. In Proceedings of the 13th Triennial Conference on Liquid Atomization and Spray Systems (ICLASS 2015), Tainan, Taiwan, 23–27 August 2015.
51. Pischinger, F.; Schulte, H. *Grundlagen und Entwicklungslinien der diesel-motorischen Brennverfahren*; VDI-Verlag: Düsseldorf, Germany, 1988; Volume 714, pp. 61–93.
52. Warnatz, J.; Maas, U.; Dibble, R.W. *Combustion: Physical and Chemical Fundamentals, Modeling and Simulation, Experiments, Pollutant Formation*, 4th ed.; Springer: Berlin, Germany; New York, NY, USA, 2006; OCLC: Ocm75427408.

2

Wiesmann, F.; Bauer, E.; Kaiser, S. A. and Lauer, T.

Ignition and Combustion Characteristics of OME_{3-5} and N-Dodecane: A Comparison Based on CFD Engine Simulations and Optical Experiments

SAE Technical Paper, 2023-01-0305
2023

doi: 10.4271/2023-01-0305

3

Wiesmann, F.; Han, D.; Qiu Z.; Strauß, L.; Rieß, S.;Wensing, M. and Lauer, T.

Numerical Study of Novel OME_{1-6} Combustion Mechanism and Spray Combustion at Changed Ambient Environments

Frontiers in Energy

2024

doi: 10.1007/s11708-024-0926-8

Front. Energy
https://doi.org/10.1007/s11708-024-0926-8

RESEARCH ARTICLE

Frederik WIESMANN, Dong HAN, Zeyan QIU, Lukas STRAUβ, Sebastian RIEβ, Michael WENSING, Thomas LAUER

Numerical study of novel OME_{1-6} combustion mechanism and spray combustion at changed ambient environments

Abstract For a climate-neutral future mobility, the so-called e-fuels can play an essential part. Especially, oxygenated e-fuels containing oxygen in their chemical formula have the additional potential to burn with significantly lower soot levels. In particular, polyoxymethylene dimethyl ethers or oxymethylene ethers (PODEs or OMEs) do not contain carbon-carbon bonds, prohibiting the production of soot precursors like acetylene (C_2H_2). These properties make OMEs a highly interesting candidate for future climate-neutral compression-ignition engines. However, to fully leverage their potential, the auto-ignition process, flame propagation, and mixing regimes of the combustion need to be understood. To achieve this, efficient oxidation mechanisms suitable for computational fluid dynamics (CFD) calculations must be developed and validated. The present work aims to highlight the improvements made by developing an adapted oxidation mechanism for OME_{1-6} and introducing it into a validated spray combustion CFD model for OMEs. The simulations were conducted for single- and multi-injection patterns, changing ambient temperatures, and oxygen contents. The results were validated against high-pressure and high-temperature constant-pressure chamber experiments. OH*-chemiluminescence measurements accomplished the characterization of the auto-ignition process. Both experiments and simulations were conducted for two different injectors. Significant improvements concerning the prediction of the ignition delay time were accomplished while also retaining an excellent agreement for the flame lift-off length. The spatial zones of high-temperature reaction activity were also affected by the adaption of the reaction kinetics. They showed a greater tendency to form OH* radicals within the center of the spray in accordance with the experiments.

Keywords oxygenated fuels, reaction kinetics, oxidation mechanisms, computational fluid dynamics (CFD), oxymethylene ethers (OME), e-fuels, multi-injection, spray-combustion

Received Oct. 10, 2023; accepted Nov. 30, 2023; online Jan. 10, 2024

Frederik WIESMANN (✉), Thomas LAUER
Institute of Powertrains and Automotive Technology, TU Wien, 1060 Vienna, Austria
E-mail: frederik.wiesmann@ifa.tuwien.ac.at

Dong HAN, Zeyan QIU
Key Laboratory for Power Machinery and Engineering of Ministry of Education, Shanghai Jiao Tong University, Shanghai 200240, China

Lukas STRAUβ, Sebastian RIEβ, Michael WENSING
Professorship for Fluid Systems Technology, Friedrich-Alexander-Universität Erlangen-Nürnberg, 91058 Erlangen, Germany

1 Introduction

The detailed investigation of possible future climate-neutral fuels is a prerequisite for any industrial application. Different pathways to produce renewable synthetic fuels are examined by Huang et al. [1], highlighting their advantages in high energy density, easy storage and transportation, and long-term storage compared to physical and electrochemical energy storage technology. Oxygenated synthetic fuels without C−C bonds combine the two essential aspects of CO_2 neutrality and soot-free combustion, thus enabling the solution of the soot-NO_x trade-off for diesel engines [2]. In recent years, polyoxymethylene dimethyl ethers (PODEs), alternatively called oxymethylene ethers (OMEs), were investigated intensively, confirming their potential as a transportation fuel for the reduction of soot emissions [3–6].

As the properties of OMEs like viscosity, lubricity, and boiling point depend on the quantity of oxymethylene ether groups (CH_2−O) within its chemical structure ($CH_3O(-CH_2-O)_n-CH_3$), it is found that OME_{3-5} represents suitable surrogates for diesel fuel. It can be used purely or blended with diesel. Virt and Arnold [7] demonstrated lower particle emissions and shorter ignition delay times (IDTs) for diesel blends with up to 45 vol.% of OME_{3-5} in a four-cylinder diesel engine. The

latter effect originates from the higher cetane number of $OME_{3–5}$ compared to diesel.

Pélerin et al. [8] compared a neat $OME_{3–6}$ fuel to paraffinic diesel fuel in a heavy-duty engine, identifying drastically reduced soot and particulate emissions, while retaining the same level of NO_x emissions. The tolerance against exhaust gas recirculation (EGR) was found to be very high, pointing to the potential to further reduce the NO_x emissions without the restrictions of a trade-off with soot or particle concentrations. The particle size distribution emitted by an $OME_{3–6}$ fuel in a heavy-duty engine was analyzed by Gelner et al. [9], showing ultra-low levels of particle emissions independent of the usage of diesel particle filters or urea dosing. The measured particle number emissions were found to be smaller than for diesel. A detailed analysis of the influence of OME chain length on NO_x emissions was given by Dworschak et al. [10] on a single-cylinder diesel engine. A higher chain length was found to be beneficial in terms of NO_x emissions with only little drawbacks on thermal efficiency. The added benefit of reduced NO_x emissions was reported to outweigh the small reduction in engine efficiency for higher OME chain lengths.

The mixture formation of the same $OME_{3–5}$ fuel mix, injector, and injection timing used in this study was analyzed and compared to *n*-dodecane and 1-octanol by Strauß et al. [11]. It was concluded that the mass distributions within the sprays of single injections were independent of the used fuel. Subsequent leaner or richer air−fuel equivalence distributions resulted from different air requirements of the fuels for stoichiometric conditions. For the multi-injection, the $OME_{3–5}$ mix proved challenging as its relatively high density and low viscosity prolonged the opening time of the nozzle. Short pilot injections with a targeted injection time of 300 µs were too short for the injector to open completely.

Future industrial applications of OME_n necessitate an extensive knowledge of the ignition and combustion characteristics of this fuel. Wiesmann et al. [12] reported significant differences in simulated and experimentally determined ignition delay, flame morphology, and mixture formation between an $OME_{3–5}$ fuel mix and *n*-dodecane in a constant pressure injection chamber. Numerical and experimental research conducted on an optically accessible single-cylinder engine showed similar results with shorter ignition delays and strong intensity levels of high-temperature reactions in the spray axis for $OME_{3–5}$ when compared to *n*-dodecane [13].

The accurate prediction of IDTs, lift-off lengths, and other flame characteristics with the help of computational fluid dynamics (CFD) requires the utilization of optimized and validated oxidization mechanisms. Especially in Wiesmann et al. [12], it was concluded that the used reaction mechanism for the $OME_{3–5}$ combustion, developed by Niu et al. [14], consistently underestimated the ignition delay and the intensity of high-temperature reactions in the spray axis with changing ambient temperatures and oxygen contents. Lift-off length and flame propagation showed good agreement with the measurements, leading to the assessment that modifying the reaction mechanism can improve CFD results and, therefore, has a considerable potential.

This study aims to introduce an enhanced reaction mechanism for the oxidization of OME fuels with components ranging from OME_1 to OME_6. The new mechanism is validated with 0D-simulations against jet-stirred reactor (JSR) experiments conducted for this paper, as well as IDTs in shock tubes taken from the literature. The new mechanism is then applied to CFD calculations modeling a high-pressure, high-temperature, constant-pressure combustion chamber at changing ambient temperatures and oxygen contents with AVL FIRE®. The validation of the CFD simulations is achieved by OH*-chemiluminescence experiments. The reaction mechanisms used in the CFD simulations in this study do not consist of an excited OH* species but of unexcited hydroxyl (OH) as a species. Therefore, OH* is referenced for the experiments as the detected species, whereas the simulations track the OH mass fraction. The influence of multi-injection patterns with highly transient short pilot injections on the flame structure is analyzed. A particular focus is set on IDTs and the flame morphology in the spray axis.

2 Setup

2.1 Properties of OME fuel

The OME mix used in the present work is identical with the OME fuel used in Refs. [11–13], and is, hereinafter, referred to as OME. Its composition is shown in Table 1 [15], and its properties are described in Table 2 [15,16], derived from the OME batch analysis conducted by Analytik Service Gesellschaft (ASG) [15] and Pastor et al. [16].

The notation $(A/F)_{st}$ describes the air-to-fuel ratio at stoichiometric conditions. The remaining traces checked in the batch report of the fuel composition studied, other than OME groups, are sulfur (< 5 mg/kg), ash content (< 0.001 wt.%), and water (146 mg/kg).

Table 1 OME fuel composition

Molecule	Content/wt.%
OME_1	0.01
OME_2	<0.01
OME_3	57.90
OME_4	28.87
OME_5	10.07
OME_6	1.91

Table 2 Fuel properties of OME mixture

Property	Unit	Value
Density	kg/m^3 (t = 15 °C)	1057.10
Viscosity	mm^2/s (t = 40 °C)	1.08
Cetane number	–	68.6
Lubricity	μm	320
Flash point	°C	65
Lower heating value	MJ/kg	19.26
Initial boiling point	°C	144.40
Final boiling point	°C	242.40
Total contaminations	mg/kg	<1
Carbon content	wt.%	43
Hydrogen content	wt.%	8.53
Oxygen content	wt.%	46.4
(A/F)st at 21% of O_2	–	5.89:1
(A/F)st at 15% of O_2	–	8.18:1

Using an OME mix with components ranging from OME_1 to OME_6 ensures that the CFD validation process represents all relevant reaction pathways (Section 2.2) altered for the new oxidation mechanism.

2.2 Development of the new OME oxidation mechanism

Niu et al. [14] constructed an OME_{1-6} reduced mechanism with a consistent reaction structure (including 92 species and 389 reactions). First, the OME_{1-2} sub-mechanism was established using the decoupling methodology and sensitivity analysis (SA). The reaction classes of OME_{3-6} sub-mechanism was derived from the OME_2 sub-mechanism, and the rate parameters were determined through the enhanced linear lumping method and analogy based on reaction rate rules. To validate the mechanism, comprehensive comparisons were conducted with experimental data from previous studies, such as IDTs in shock tubes, mole fraction profiles of key intermediates and products in JSR, burning velocity and flame species concentrations in premixed laminar flames, as well as in-cylinder pressures, heat release rates, and emissions in homogeneous charge compression ignition (HCCI) combustion. The results showed that the experimental data were predicted well by the current model.

The modification of the mechanism by Niu et al. [14], hereinafter referred to as the Niu mechanism, and the validation of the newly developed mechanism, hereinafter referred to as the Shanghai Jiao Tong University (SJTU) mechanism, is detailed in the following sections. At first, the experimental procedure using JSR is outlined. Next, the modifications to the Niu mechanism are described. Both mechanisms are then compared to the JSR experiments conducted for this study and with IDT data in the literature.

2.2.1 Experimental procedure of JSR

The OME mixture oxidation experiment is conducted on the JSR experimental platform. The oxidant is oxygen (99.99% purity), and the carrier gas is nitrogen (99.99% purity). The JSR used in this study has an internal volume of 75 cm^3 and an inner nozzle diameter of 0.3 mm. The reactor is placed in a heating furnace with a temperature control program, which can be heated to 1000 °C at most. A K-type thermocouple (OMEGA, TJ36-CAXL) monitors the real-time internal temperature of the reactor. The species detection and analysis system are a gas chromatograph (GC, Agilent 7890B). Gas chromatography is the most widely used detection and analysis technology in JSR experiments, which can quickly separate and identify various components in the mixed gas. In this study, the GC is outfitted with a thermal conductivity detector (TCD), allowing for the detection of permanent gases such as CO, CO_2, H_2, and O_2. The estimated uncertainty of measurements, considering reactant flow rates, temperature, calibration gases, and analytical equipment repeatability is approximately 10%.

The oxidation of OME blends is investigated at atmosphere pressure, temperature range of 500 to 900 K, and equivalence ratios of 0.5, 1.0, and 2.0. The temperature interval of each test point is 25 K. Two tests are conducted at each temperature point, and the reported value is determined as the average of the measured species concentrations. The initial fuel mole fraction and the residence time are fixed at 0.005 and 2 s, respectively.

During the experiments, the temperature of the fuel evaporation chamber is kept constant at 250 °C, which can vaporize OME fuel. All pipeline is kept at 100 °C to avoid an excessive temperature gradient and condensation. GC is used for the qualitative and quantitative detection of five substances, including O_2, CO, CO_2, H_2, and CH_4.

2.2.2 Mechanism modification and validation

First, the SA was performed to identify the important reactions. In the SA calculations of the IDT, the sensitivity coefficient is defined as

$$S = \frac{\tau(2.0k_i) - \tau(0.5k_i)}{1.5\tau(k_i)}, \quad (1)$$

where S is the sensitivity coefficient, τ is the IDT, and k_i is the pre-exponential factor of the ith reaction.

In the SA calculations of mole fraction profiles, the OH radical was selected as the marked species because of its significant role in fuel combustion. The top ten reactions with higher absolute sensitivity coefficient were identified. Then, the rate constants of the important reactions were modified manually to obtain a better agreement with both JSR and IDT measurements.

Table 3 shows the modification details of the mechanism. The pre-exponential factor of the reactions numbered 313 and 314 were modified, mainly to reduce the difference between the model simulation and the JSR measurements in the mole fraction of essential intermediate products at about 600 K. The modification of reactions numbered 295, 311, 336, 361, and 386 is to decrease the predicted IDT.

Figure 1 shows the mole fractions of species measured in the oxidation experiments and provided by a kinetic simulation at the three equivalent ratios (0.5, 1.0, 2.0). The simulation is carried out in the closed zero-dimensional homogeneous reactor module using the Chemkin Pro software [17]. The OME mechanisms used in the simulation include the SJTU and Niu mechanisms to compare the prediction performances of these two mechanisms.

As shown in Fig. 1, the Niu and SJTU mechanisms can well capture the trend of mole fraction change at intermediate-to-high temperatures. However, it underestimates the O_2 mole fraction and overestimates the CO and CO_2 mole fraction at low temperatures. In contrast, the predictions from the SJTU mechanism align more closely with the mole fraction profiles across the three equivalence ratios and most temperature conditions. The SJTU mechanism predicts a lower oxygen consumption in the 500–600 K range, but a higher one in the 750–900 K range. For CO_2, the SJTU mechanism reduces the predicted value and the deviation from the experimentally observed values at 500–600 K. For CO, CO_2, and H_2, the SJTU mechanism improves the prediction quality at the temperatures of 750–900 K.

To ascertain the applicability and reliability of the newly developed mechanism, the IDTs of OME_3 reported in the literature are employed to verify the mechanism. Cai et al. [18] studied the spontaneous ignition behavior of OME_{2-4} in a shock tube and measured the IDTs of an OME_{2-4}/air mixture in a series of initial conditions (10 and 20 bar pressure, 663–1137 K temperature range, equivalent ratio of 0.5, 1.0, and 2.0). Regarding the IDTs data of Cai et al. [18], the simulation in similar test conditions is carried out using the Niu mechanism and SJTU mechanism. The IDTs measured in the shock tube are generally short (0.01–2 ms), and the thermal change of fuel and oxidant mixture before ignition is small. An ideal constant volume combustion can approximate the whole combustion process. Therefore, the constant volume assumption is used to simulate the IDT of the shock tube. The instant when the OH concentration reaches the peak value during the ignition process is defined as the ignition time.

Figure 2 shows the measured IDT data at three equivalent ratios (0.5, 1.0, 2.0) and 10 and 20 bar pressure, comparing the simulation results of the two mechanisms. The results indicate that the SJTU mechanism improves the accuracy of predicting the IDT of OME_3/air. At the pressure of 20 bar, the results simulated from SJTU mechanism are closer to the experimental data in the 750–1000 K range at the equivalence ratio of 0.5 and 1.0. With an ambient pressure of 10 bar, the SJTU mechanism mainly reduces the IDTs calculated in the temperature range of 750–900 K and minimizes the deviation from the experimental values.

2.3 Operating points

The operating points for the spray combustion measurements and CFD simulations in the present work are presented in Table 4. The ambient density (ρ_{CC}) is kept constant at 22.8 kg/m^3. The primary focus is on the influence of temperature, oxygen content, and multi-injection pattern on the auto-ignition process. The temperature (T_{CC}) increases from 800 (OP1) to 900 K (OP2) and 1000 K (OP3). Additionally, the ambient volume content of oxygen in the combustion chamber is modified from 15% (OP2) to 21% (OP5). The multi-injection pattern is realized in the operating point (OP4).

2.4 Experimental setup

The experiments for investigating the fuel sprays are conducted using a high-temperature and high-pressure constant-volume injection chamber that is optically accessible. The test bench at the Professorship for Fluid Systems Technology (FST) is continuously scavenged with gas. The mixture can be adjusted from pure nitrogen to pure air, allowing reactive and inert investigations and

Table 3 Mechanism modification

No.	Reaction	Modification
295	$OME_3 + HO_2 = OME3RX1 + H_2O_2$	$A_{295} \rightarrow 3A_{295}$
313	$CH_3OCH_2OCH_2OCHO + OH = HOCHO + CO + CH_3OCH_2 + H_2O$	$A_{313} \rightarrow 4A_{313}$
314	$CH_3OCH_2OCH_2OCHO + OH = 2CH_2O + CH_3O + CO + H_2O$	$A_{314} \rightarrow 6A_{314}$
311	OME3X1OOHX3OO = OME3XKET1X3 + OH	$A_{311} \rightarrow 0.5A_{311}$
336	OME4X1OOHX3OO = OME4XKET1X3 + OH	$A_{336} \rightarrow 0.1A_{336}$
361	OME5X1OOHX3OO = OME5XKET1X3 + OH	$A_{361} \rightarrow 0.1A_{361}$
386	OME6X1OOHX3OO = OME6XKET1X3 + OH	$A_{386} \rightarrow 0.1A_{386}$

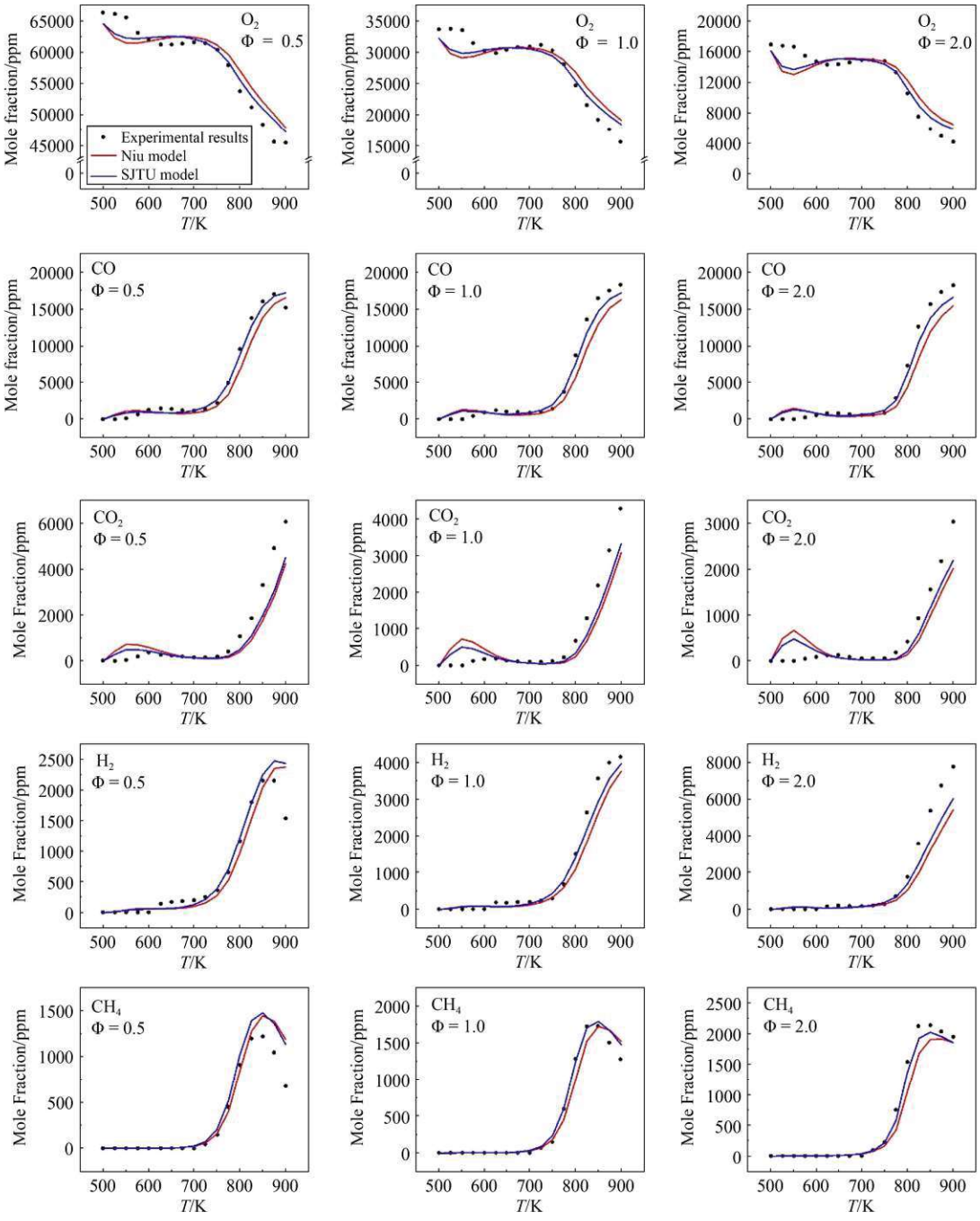

Fig. 1 Measured and 0D-simulated O_2, CO, CO_2, H_2, CH_4 mole fraction profiles in OME oxidation (symbols: measurements; red lines: simulation results with the Niu mechanism; blue lines: simulation results with the SJTU mechanism).

the simulation of EGR. The gas temperature inside the chamber can be set from room temperature to 1000 K and is automatically controlled. The pressure can be regulated from 0.1 up to 10 MPa simultaneously. Both parameters are kept constant during the experiments. A research fuel system, compatible with different rails and injectors, provides the required fuel pressure up to 400 MPa.

Optical measurement techniques are used to obtain data about the fuel spray, its mixture, the ignition, and the combustion. The cubic chamber has windows on all sides (except where the injector is mounted) to allow high-speed imaging techniques. The optics are positioned to capture a side view of the fuel spray. The OH*-chemiluminescence is used to determine the

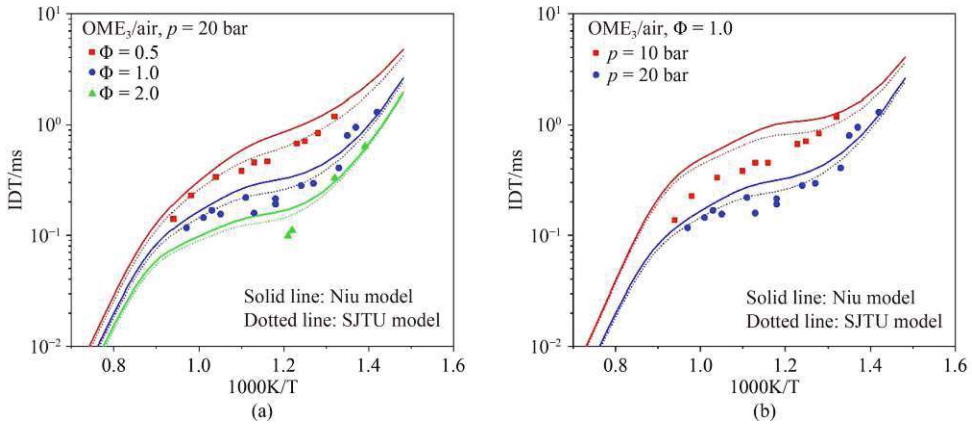

Fig. 2 Experimental and 0D-simulation IDT results of OME_3/air mixture in a shock tube (point: experimental measurement of Cai et al. [18]; solid line: simulation results with the Niu mechanism; dotted line: simulation results with the SJTU mechanism).
(a) Effects of equivalence ratio; (b) effects of pressure.

Table 4 Operating points

Label	Ambient temperature: T_{CC}/K	Ambient pressure: p_{CC}/bar	Ambient Density: ρ_{CC}/(kg·m^{-3})	Inj. temperature: T_{inj}/K	Inj. pressure: p_{inj}/bar	Inj. Duration: t_{inj}/ms	O_2-content/vol.%
OP1	800	54	22.8	363	1500	1.5	15
OP2	900	61	22.8	363	1500	1.5	15
OP3	1000	68	22.8	363	1500	1.5	15
OP4	900	61	22.8	363	1500	0.3/0.5/1.2	15
OP5	900	60	22.8	363	1500	1.5	21

ignition delay. To filter the OH* signal from the flame signal, a 307 ± 25 nm bandpass filter is used. The remaining radiation is focused on the high speed IRO X amplifier of LaVision using a 105 mm F/4.5 lens from Sill Optics. The amplified signal is then captured using a Photron SA-Z high speed camera at a framerate of 40000 fps (Fig. 3).

For each operating condition, 32 injections are performed, recorded, and analyzed using a purpose-built MATLAB-based program. The injected masses and mass flow rates are determined using the commercially available HDA 500 from Moehwald. This device consists of a pressurized volume filled with fuel, into which the injector injects fuel. The change in mass can be calculated by measuring the resulting pressure increase and the speed of sound within the volume. Integrating over the entire injection event leads to the total injected mass. For each operating point, 150 injections are recorded, and the results are subsequently averaged.

2.5 Injectors

This study shows experimental and numerical results for two different injectors, the Continental 3-hole injector (Conti3L) and the single-hole SprayA3 injector (see Table 5). Both injectors are described in more detail by Wiesmann et al. [12].

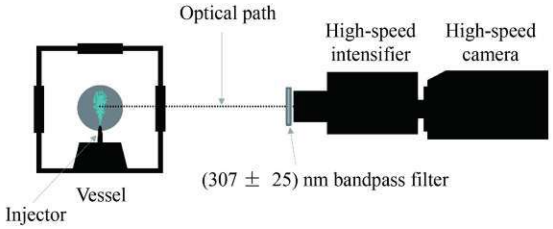

Fig. 3 Schematic of experimental OH*-chemiluminescence setup.

Table 5 Injector properties

Property	Conti3L	SprayA3
Orifice exit diameter/μm	115	97
Contraction coefficient (C_A)	0.98	0.98
Number of holes	3	1
Elevation angle/(°)	45	0

2.6 Numerical setup

The simulations of the present work are Reynolds averaged Navier–Stokes (RANS) equations calculations. The liquid droplets are modeled with a Lagrangian discrete droplet method (DDM) to track the liquid parcels throughout the numerical domain. In contrast, the

gaseous phase is modeled with a static Eulerian grid. The numerical setup used in this study was validated extensively by Wiesmann et al. [12].

2.6.1 Mesh

A simple spray-box mesh is utilized to determine the performance of the novel OME_{1-6} reaction mechanism. The dimensions of the mesh are 120 mm in length and 60 mm in width. Three refinements up to a minimum cell size of 125 µm are implemented and described in Table 6 [12] and shown in Fig. 4. The notations R1 and R2 signify the radii at beginning and end of the respective refinement. The fine resolution of the mesh ensures converged calculations for both phases, liquid and gaseous, especially in the vicinity of the nozzle hole. The refinements chosen ensure that, for both injectors, the liquid phase evaporates within the area of the highest resolution for all operating points. Minimizing the cell size even further does not show any improvement regarding the quality of the results, while only pushing the necessary simulation time to unjustifiable limits. The boundary opposite to the nozzle is set as a non-reflecting outlet. All other mesh boundaries are set up as walls with fixed temperatures.

2.6.2 Submodels

This chosen turbulence model within the RANS framework for this study is the k-ζ-f turbulence model [19]. The near wall regions are modeled with a compound wall treatment described by Popovac & Hanjalic [20]. The pressure correction is done with the SIMPLE algorithm with an additional correction using the standard pressure-implicit with splitting of operators (PISO) formulation.

The chosen fuel injection pressure of 1500 bar results in high injection velocities. During injection, the temporal resolution is set to 0.5 µs to ensure the satisfaction of the Courant criterion with the given fine mesh. After the injection ended, the time step is increased to 1.0 µs.

The introduction of the liquid parcels is realized with the Blob method [21], initializing liquid blobs continuously with the same size as the effective nozzle hole diameter. The primary and secondary droplet breakup is simulated with the Kelvin-Helmholtz-Rayleigh-Taylor (KHRT) breakup model [21,22]. The OME mix used in the present work comprises multiple components (see Table 1). This requires an evaporation model of the liquid parcels capable of accounting for a multi-component fuel. Therefore, the model described by Brenn et al. [23] is used, an enhancement of the model by Abramzon & Sirigano [24], treating the mass transfer from liquid droplet to gaseous phase separately for every component. Table 7 summarizes the numerical models[12,13].

Determining the transient liquid injection rates used for the spray modeling within this study follows the same methodology described in by Wiesmann et al. [12]. In particular, the ramp-up and ramp-down phases while opening and closing the injector cannot be deducted straightforwardly from standard experiments with long-tube type instruments (HDAs) described in Section 2.4. In Pickett et al. [27], it was shown for the Spray A injector that mechanical vibrations lead to an overestimation of rate fluctuations and that the initial ramp-up is underestimated.

Consequently, the present work models the rates of injection with virtual rates of injection, which differ from the experimentally determined ones. Figure 5 depicts both the virtual injection rates for single and multi-injection of the injectors. For the Conti3L injector, the HDA experiments already provide an average for the three nozzle holes. The steady-state phase between ramp-up and ramp-down transients is modeled by replicating the mean value per nozzle hole of the HDA experiments. The SprayA3 injector is characterized by unsteady behavior even between the ramp-up and ramp-down transients. Therefore, the standardized method published by the Polytechnical University of Valencia [28] was used to generate the injection rates for SprayA3 injector. The generated rates for the CFD calculations clearly show a faster ramp-up and ramp-down than the profiles

Table 6 Mesh refinement

Refinement	*L*/mm	R1/mm	R2/mm	Cell size/mm
0 (base mesh)	120	30	30	1.000
1	80	5	10	0.500
2	50	3	5	0.250
3	25	2	3	0.125

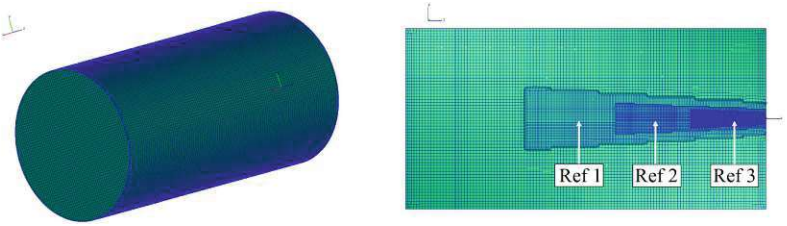

Fig. 4 Spray-box mesh with cut-through center plane visualizing refinement levels.

Table 7 Summary of numerical submodels

	Injection type	Blob [21]
Liquid spray models	Breakup	KHRT [21,22]
	Turbulent dispersion	O'Rourke & Bracco [25]
	Evaporation	Brenn et al. (multi-component) [23]
	Drag Law	Schiller-Naumann [26]
Gaseous phase models	Temporal discretization	0.5 μs (during injection); 1.0 μs (after injection)
	Turbulence modeling	RANS approach; k-ζ-f model [19]
	Wall treatment	Compound (hybrid) [20]
	Pressure-correction	SIMPLE (1st) / PISO (2nd)

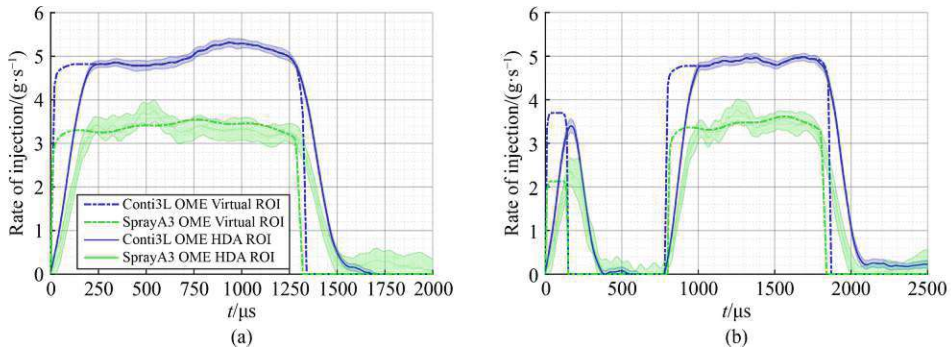

Fig. 5 Rates of injection (ROI) for numerical input (p_{inj} = 1500 bar, p_{CC} = 60 bar). (a) Single injection; (b) multi-injection.

measured by the HDA flowmeter.

The most challenging aspect is the adequate modeling of the highly transient pilot injection for the multi-injection operating point (OP4, Table 4). The pilot injections do not comprise any steady-state phase but are entirely dominated by the ballistic operating conditions the injector is forced into. In Peter et al. [29], it was shown that the fuel properties, i.e., relatively high density and low viscosity, of an OME_3 and OME_4 mix directly influence the needle motion and, consequently, the mass flow rate development. This observation was also confirmed by Strauß et al. [11] with the same $OME_{3–5}$ mixture, SprayA3 injector, and injector timing as in the present work. For the short pilot injection, the opening process of the needle was found to take significantly longer for $OME_{3–5}$ compared to *n*-dodecane and 1-octanol. Furthermore, the $OME_{3–5}$ mixture led to the injector not even opening completely.

The maximum velocity of the spray during the pilot injection can be calculated by the method presented by Frühhaber et al. [30] using the conservation of momentum along the spray axis. This method allows for the generation of accurate injection rates.

2.6.3 Combustion modeling

The modeling of the OME fuel oxidization is conducted by applying the detailed reaction mechanisms for every time step. The gas phase reactions in AVL FIRE® treat every computational cell as a well-mixed homogeneous reactor. To increase the accuracy of the simulations, turbulence chemistry interaction (TCI) is considered. Its implementation via a Gaussian presumed probability density function (pPDF) applied to the local temperature is described in detail in AVL List Gmbh [31] and has been already utilized by Wiesmann et al. [12]. However, the impact of the TCI for the CFD simulations of the present work is very small. It does not affect the lift-off length and has only a minor influence on the IDT. The different reactions kinetics used in this study result in changes for the lift-off length and ignition delay which are at least an order of magnitude greater. The high resolution of the computational mesh is assumed to minimize the influence of the TCI.

The mixing state of fuels is usually defined by the equivalence ratio (ϕ) (Eq. (2)). However, it was found by Mueller [32] that the existence of chemically bound oxygen in fuels leads to an overestimation of the distance from stoichiometric ratios. This results in mixtures appearing to be significantly farther away from stoichiometry than they are in reality. Hence, a new formulation was described by Mueller [32] to eradicate this error. The so-called oxygen equivalence ratio (ϕ_Ω) is defined in Eq. (3) for the case that neither C- nor

H-atoms is present in the oxidizer. The term Ω_f describes the oxygen ratio of the fuel. It is a property of the fuel itself, representing "the number of O-atoms per mole of fuel divided by the number of O-atoms required to convert all C- and H-atoms of the fuel in a mole of fuel to saturated stoichiometric products [32]". It is specified in Eq. (4). The subscript i in Eq. (4) denotes the index over all fuel species, and a_i describes the number of moles of the ith fuel species. For this study, the OME fuel mix has an oxygen fuel ratio of $\Omega_{f,OME} = 0.2566$.

$$\phi = \frac{m_f/m_{ox}}{(m_f/m_{ox})_{st}}, \tag{2}$$

$$\phi_\Omega = \frac{\phi}{1+\Omega_f\cdot(\phi-1)}, \tag{3}$$

$$\Omega_f = \frac{\sum_i a_i n_{O,i}}{\sum_i a_i\left(2n_{C,i}+\frac{1}{2}n_{H,i}\right)}, \tag{4}$$

The super- or subscripts f and ox indicate the respective element mass fraction within the fuel and oxidizer. In addition to the newly developed reaction mechanism for simulating the oxidization of OME, described in Section 2.2 and the original mechanism published by Niu et al. [14], calculations were performed with the mechanism by Cai et al. [18]. This reaction scheme only incorporates oxymethylene groups extending from two to four (OME_2 to OME_4), whereby the components OME_5 and OME_6 of the OME mix used are dismissed. It considers 322 species for the oxidation of OME.

3 Results

In this section, the results of the novel OME reaction mechanism are shown in comparison with the original one developed by Niu et al. [14]. At first, the global quantities ignition delay and flame lift-off length are analyzed in Section 3.1. Furthermore, the flame morphology, especially the spatial and temporal distribution of the low- and high-temperature reactions characterized by formaldehyde (CH_2O) and OH, are presented in Section 3.2. The differences in the mixing regimes due to applying the novel reaction mechanism are shown in Section 3.3. For each analysis, single and multi-injection patterns are considered.

3.1 Ignition delay and lift-off length

For identifying the IDT, this study utilizes the standard definition of Engine Combustion Network (ECN) [33], specifying the start of combustion for CFD calculations as the moment of the greatest temperature gradient. The lift-off length is based on a threshold of the OH mass fraction of 14 percent. The nearest axial downstream distance where this threshold is exceeded, determines the lift-off length. The penetration of the flame front is calculated by evaluating the maximum distance from the nozzle where the mixture fraction satisfies the condition of $Z \geq 0.001$.Equation (5) describes the calculation of the mixture fraction with Z_i specifying element mass fractions of the ith element.

$$Z = \frac{Z_i - Z_i^{ox}}{Z_i^f - Z_i^{ox}}. \tag{5}$$

Both ignition delay and flame lift-off length are validated against OH*-chemiluminescence experimental data. The measured IDT is determined as the first detection of an OH*-signal in at least half of the conducted experimental repetitions. According to Riess et al. [34], the evaluated signal probability determines the IDT.

3.1.1 Single injection

For the first validation of the spray combustion model utilizing the novel SJTU reaction mechanism, the IDT is plotted against the lift-off length in Fig. 6 for the standard ECN operating of 900 K chamber temperature at an oxygen content of 15% (OP2 in Table 4). Next to the novel SJTU mechanism, the original Niu mechanism and the reaction mechanism developed by Cai et al. [18] were employed to simulate the OME spray combustion. The shown standard deviations of the measurements were derived from 32 injection repetitions for each operating point. The standard deviations for the simulated lift-off length were determined by averaging the calculated lift-off after a stable flame was established and before the end of injection. Figure 13 visualizes the same period for OP2 (see Table 4) for averaging the CH_2O and OH distribution discussed in Section 3.2.1.

The SJTU mechanism increases the IDT for both injectors while retaining the same lift-off length as the Niu mechanism. The more detailed Cai mechanism, consisting of 322 species, also yields an increased IDT, albeit while overestimating the lift-off length. The significant overestimation of the lift-off length by the CFD calculations using the mechanism of Cai et al. [18] leads to a flame morphology that cannot capture the shape of the flame seen in the experiments. Therefore, it was concluded that the Niu mechanism has a greater potential for modification than the Cai mechanism.

Hereinafter, the SJTU mechanism will be compared directly to the original Niu mechanism. The general trend of overestimating the lift-off length when predicting the ignition delay more accurately was analyzed in the case of n-dodecane and OME serving as fuels by Wiesmann et al. [12]. Therefore, the fact that the new SJTU mechanism achieves a better prediction of the ignition delay and a good agreement with the measured lift-off

length is already a significant improvement.

The same conclusion can be drawn from analyzing other operating points that vary in chamber temperature (Fig. 7) and oxygen content (Fig. 8). For all investigated cases, the SJTU mechanism predicts the IDT with a very good accuracy. The lift-off length is only slightly affected compared to the Niu mechanism, maintaining a good agreement with the measurements.

The elongation of the ignition delay for the SJTU mechanism is more pronounced at lower temperatures. For an alternating oxygen content, the ignition delay is shifted toward greater values for the SJTU mechanism with the same relative difference between the two mechanisms. It is also illustrated in Fig. 8 that the measured deviation in the ignition delay for the two injectors at 900 K chamber temperature could not be reproduced by the CFD model.

3.1.2 Multi-injection

The highly transient injection profile for the multi-injection pattern (see Fig. 5), with its short pilot injection, causes ignition of the OME spray during the dwell period of the injector. The top two plots in Fig. 9 indicate the time-resolved development of the maximum temperature within the entire simulation domain, with the vertical

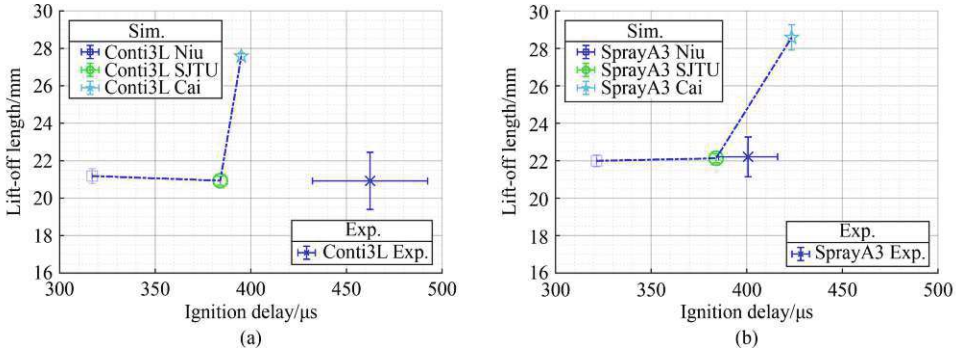

Fig. 6 Lift-off length versus ignition delay for different reaction mechanisms for OP2 (900 K and 15% O_2). (a) Conti3L injector; (b) SprayA3 injector.

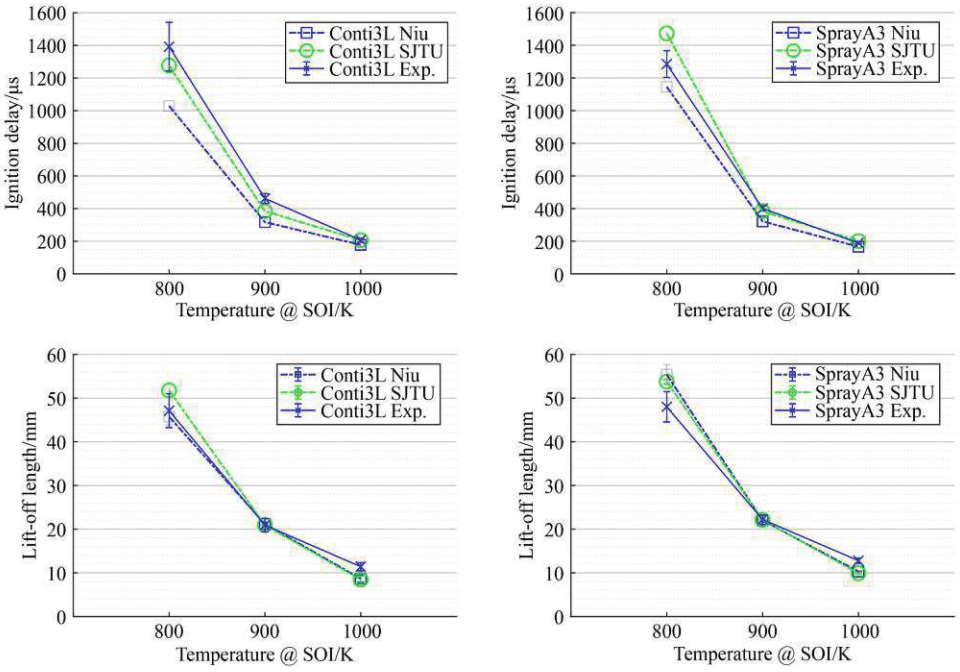

Fig. 7 Comparison of Niu and SJTU reaction mechanism for temperature sweep at 15% O_2. (left) Conti3L injector; (right) SprayA3 injector; (top) ignition delay; (bottom) lift-off length.

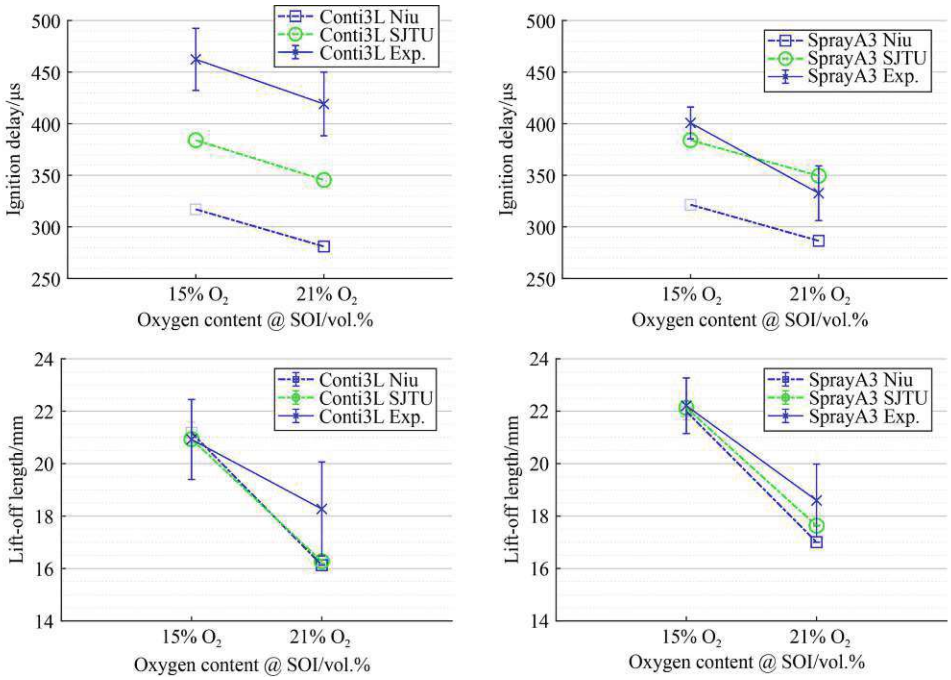

Fig. 8 Comparison of Niu and SJTU reaction mechanism for oxygen content sweep at 900 K.
(left) Conti3L injector; (right) SprayA3 injector; (top) ignition delay; (bottom) lift-off length.

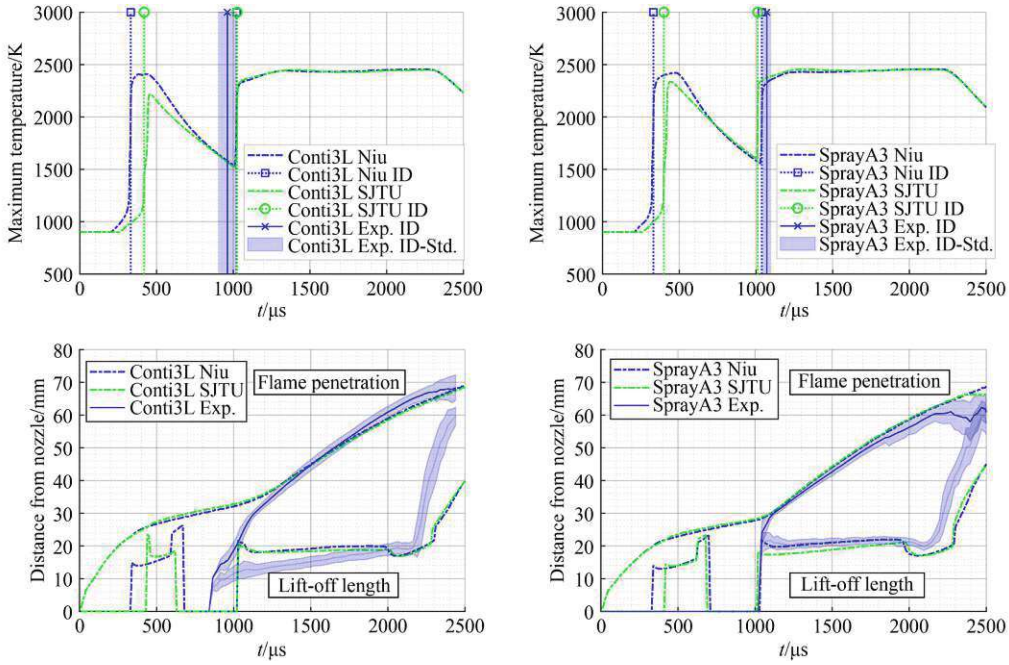

Fig. 9 Transient profiles for multi-injection.
(left) Conti3L injector; (right) SprayA3 injector; (top) maximum simulation temperature with ignition delay (ID); (bottom) lift-off length and flame (mixture fraction) penetration.

lines signaling the ignition. The CFD simulation predicts an ignition for both mechanisms shortly after the pilot injection ended. A distinctive re-ignition of the spray is noticeable after a rapid decline in simulated maximum temperature and the subsequent start of the main injection. However, the experiments could not validate this behavior as no ignition was detected before the main injection. This behavior was already reported by Wiesmann et al. [12], using the same CFD and experimental setup, speculating that either a too-reactive OME mechanism (Niu) or a too-weak OH*-signal resulting from the small amount of OME introduced into the spray chamber during the pilot injection is causing this discrepancy between simulation and experiment. The occurrence of the same ignition pattern calculated with the less-reactive SJTU mechanism, causing a longer ignition delay, indicates that the weak OH*-signal is the reason for this observation. The difference in the ignition delay predicted for the two reaction mechanisms for the main injection changes only a little for the SprayA3 and not at all for the Conti3L injector.

Following the observation from the single injection, the flame penetration and lift-off length remain virtually unaffected by the updated reaction mechanism, depicted in the bottom two plots in Fig. 9. The flame penetration was calculated with the condition of the mixture fraction (Eq. (5)) reaching the threshold of $Z \geqslant 0.001$.

3.2 Flame morphology

For the analysis of the shape and structure of the OME spray combustion flame, the low-temperature and high-temperature reactions are studied. The former is characterized by the formation and subsequent decomposition of CH_2O. The latter is dominated by the emergence of OH, which can be validated against the experimental data yielding qualitative results about the location and distribution of OH* via chemiluminescence.

All simulated distributions are presented for the symmetry plane of the spray. For an adequate comparison to the simulated results, the OH*-chemiluminescence measurements were deconvoluted to obtain the OH* signal distribution in the symmetry plane of the spray for each time step, following the methodology described by Peter [35]. Hereby, the integral flame signal is converted into a three-dimensional object using tomographic reconstruction. Intensity values from the flame can then be transferred to the symmetry plane of the flame assuming rotational symmetry.

The analysis considers the operating points with single (OP2) and multi-injection patterns (OP4) at a chamber temperature of 900 K and an oxygen content of 15 vol.%. The detailed transient evolutions of the CH_2O and OH distributions are shown for both injection strategies, differentiating the low- from the high-temperature reaction zones. The measurements and simulations are also averaged over time for the single injection to deliver a more precise and compact comparison between the two reaction mechanisms. The averaging period is set to start after a stable lift-off length is established, at 500 µs after the start of injection (SOI), and to end before the subsiding injection rate starts to influence the flame at 1350 µs.

3.2.1 Single injection

The first aspect of the analysis of the flame morphology is the comparison of the reaction rates and mass fractions for CH_2O and OH for the two reaction mechanisms under investigation. The values are averaged over all cells, yielding the profiles shown in Fig. 10.

At first glance, it is discernible that the SJTU mechanism produces higher levels of CH_2O throughout the combustion process. The reaction rate of CH_2O consists of a higher initial burst and is elevated during the steady-state phase of the OME spray injection (500 µs < t_{aSOI} < 1350 µs). This results in a significantly higher predicted mean mass fraction in the simulation domain. The SJTU mechanism shows a more minor initial burst of the OH reaction rate. Shortly after high-temperature ignition, though, the mean mass fraction and the OH reaction rate no longer differ between the two reaction mechanisms. The start of significant production for both species, CH_2O and OH, is shifted toward later during the combustion process. On a closer look into Fig. 10, it is also recognizable that the delay between the onset of CH_2O and OH production is slightly longer for the SJTU mechanism, further adding to the increased ignition delay described in Section 3.1.1

The difference in CH_2O production leads to the transient analysis of the CH_2O distribution maps for both mechanisms. Figure 11 illustrates the temporal evolution of the molar concentration of the simulations with the Niu and the SJTU mechanisms in a slice through the center of the SprayA3 injector. The time interval was shortened in proximity to the ignition delays for both mechanisms (ID_{Niu} = 321.5 µs and ID_{SJTU} = 384.0µs). Stoichiometric mixing conditions ($\phi_\Omega = 1$) are plotted into the contours as black solid iso-lines. To distinguish between the low-temperature cool-flame contour, characterized by CH_2O, and the areas of the high-temperature flame, characterized by OH, the high-temperature front of 1400 K is tracked by magenta solid iso-lines. According to Tagliante et al. [36], the consumption of CH_2O occurs approximately at this temperature.

The initial production of CH_2O occurs along the lines of stoichiometry for both mechanisms, only shifted to a later time after injection for the SJTU mechanism. Elevated levels of CH_2O concentration form on the

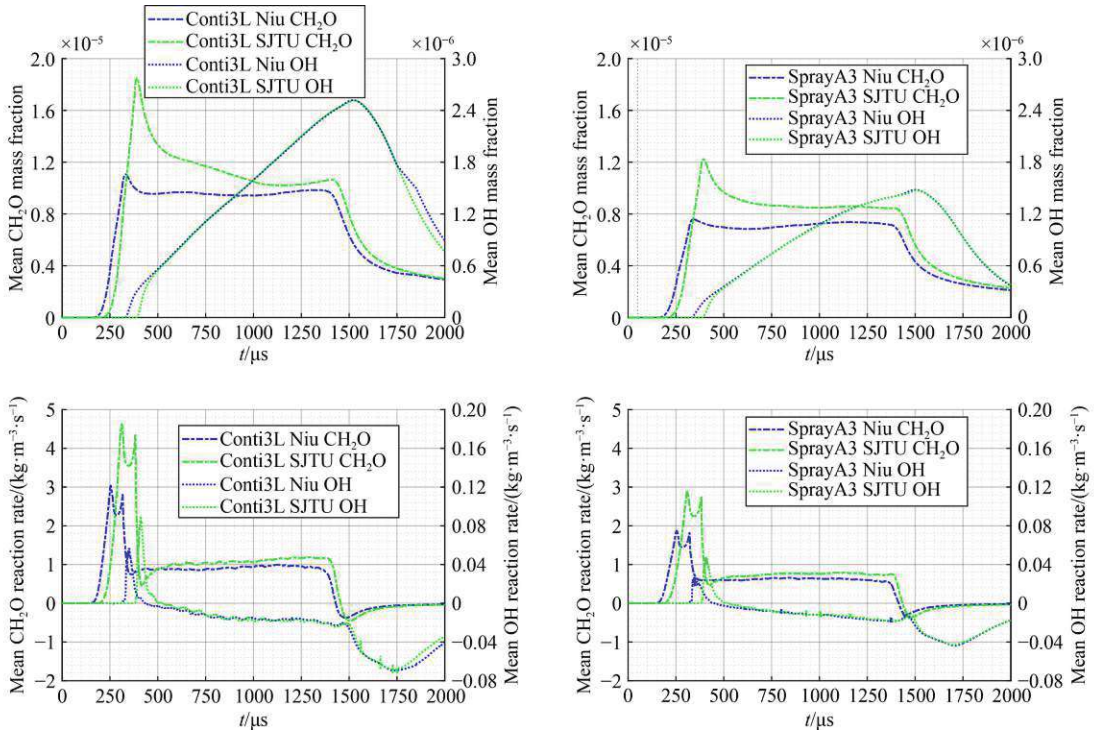

Fig. 10 Transient profiles for CH_2O and OH for single injection.
(left) Conti3L injector; (right) SprayA3 injector; (top) mean mass fractions; (bottom) mean reaction rates.

centerline of the spray approximately 20 to 30 μs before ignition. It is noticeable that the SJTU mechanism accumulates more CH_2O before igniting at the cool-flame front. In addition, high levels of CH_2O concentration reach further upstream along the centerline of the spray. These observations reflect the higher plateau of CH_2O mean mass fractions seen in Fig. 10. After ignition, the high-temperature reactions consume the CH_2O within the area enclosed by the magenta lines, showing the temperature front of 1400 K.

After inspecting the cool-flame evolution, Fig. 12 depicts the temporal development of the high-temperature flame, characterized by OH*-intensity for the experiments and the molar concentration of the OH species for the simulations. To ensure a better comparison, simulations and experiments are normalized with their respective maximum value for the displayed time step. Both mechanisms capture the general shape and spatial dimensions of the high-temperature flame. The SJTU mechanism shows a slightly higher activity in the centerline of the spray. However, it is still insufficient compared to the high intensity measured at the center of the OME spray. Both mechanisms overestimate the reaction activity in the shear layer of spray and ambient air. Especially within the initial stages of combustion, the SJTU mechanism seems to be able to capture the experimentally observed high-temperature flame better than the Niu mechanism, probably due to the improved and prolonged ignition delay and the greater accumulation of CH_2O in the center of the spray prior to ignition. The slight improvements in the SJTU mechanism diminish as the injection process continues, leading to a similar high-temperature flame distribution at one millisecond after SOI. The experimentally observed high intensity of OH* near the nozzle at the root of the spray is not reproduced by either reaction mechanism. One possible explanation for this behavior is that the experiments measure the excited OH* signal, which is very volatile and quickly consumed by the high-temperature reactions. This is compared to the presumably more stable OH mass fraction of the simulations, as neither the Niu nor the SJTU mechanism comprises an excited OH species for a more adequate comparison to the experiments.

To better compare the differences between the two mechanisms, the spatial distributions of the cool-flame (CH_2O) and high-temperature (OH) contours were averaged once a stable flame lift-off could be detected. Figure 13 depicts the flame penetration and lift-off length for OP2, indicating the averaging period. For both injectors, the flame stabilizes around 500.0 μs after SOI, entering the quasi-steady period in terms of flame lift-off.

The reactive front, tracked by the mixture fraction threshold of $Z \geqslant 0.001$, propagated approximately 34 mm

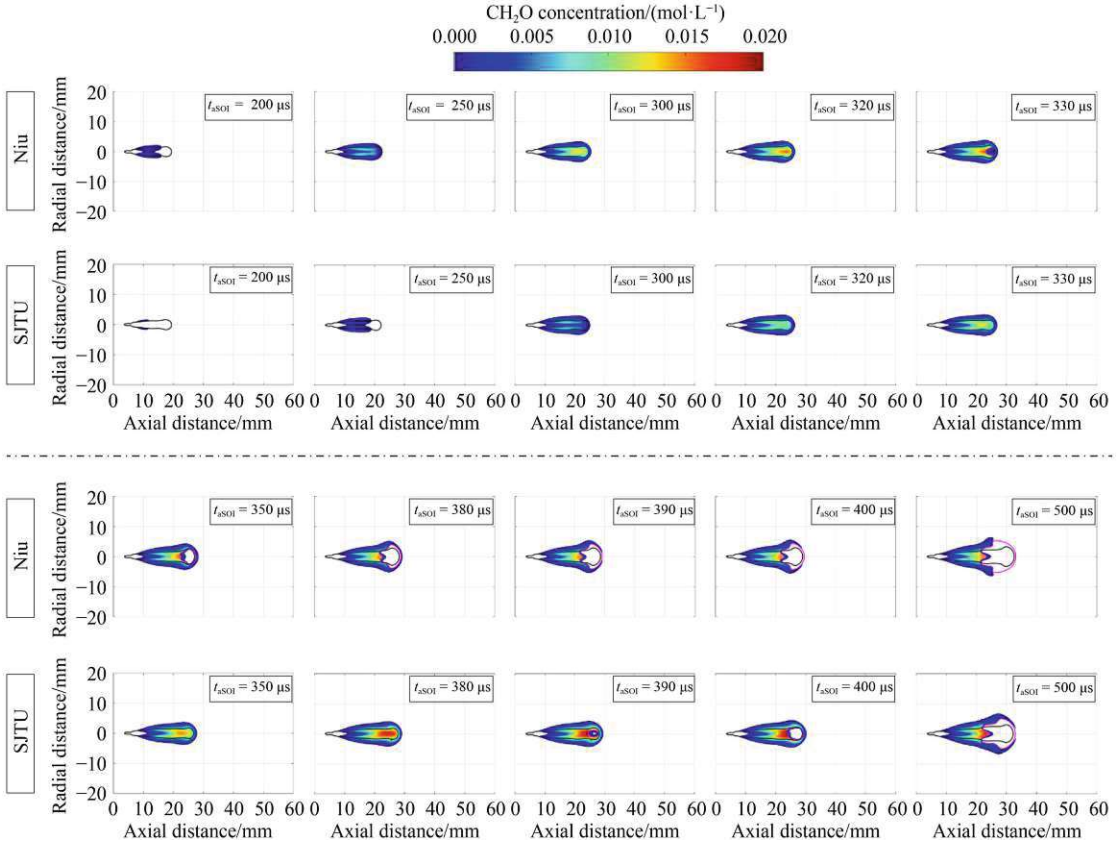

Fig. 11 SprayA3-OP2 (900 K and 15% O_2): CH_2O molar concentration contours in the center plane for single injection (black lines depict stoichiometric mixing, and magenta lines show the temperature front of 1400 K).

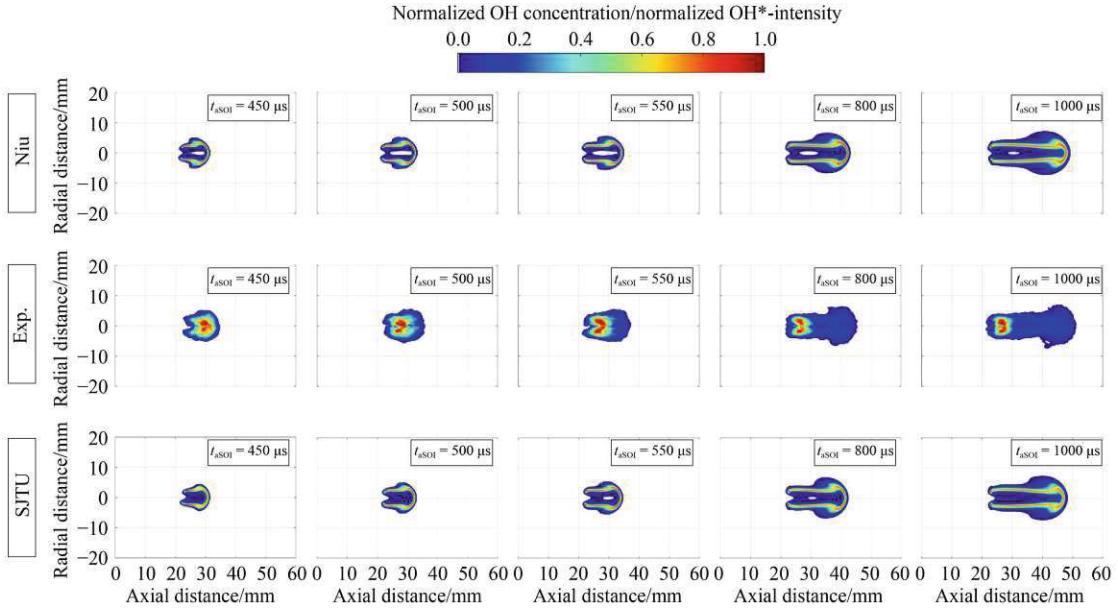

Fig. 12 SprayA3-OP2 (900 K and 15% O_2): normalized OH*-intensity (experiment) and OH molar concentration (simulation) contours in the center plane for single injection.

for simulations and experiments for both injectors. Figure 11 clearly shows that the CH_2O is consumed 30 mm downstream of the nozzle, which means the averaging process captured the entire CH_2O field present in the simulation. However, the averaging process affects the OH/OH* averaged results for simulations and experiments downstream of 34 mm as the flame front is still propagating. As simulations and experiments are averaged by the same method, comparisons are nevertheless considered valid.

As the experiments showed that most of the high-temperature flame activity occurred in the center of the spray, the centerline profiles of the CH_2O and OH were of interest for a detailed comparison of the two mechanisms. The top two plots of Fig. 14 display the differences between the SJTU and Niu mechanisms in accumulating CH_2O in the center axis of the spray, with the SJTU mechanism amassing significantly more CH_2O

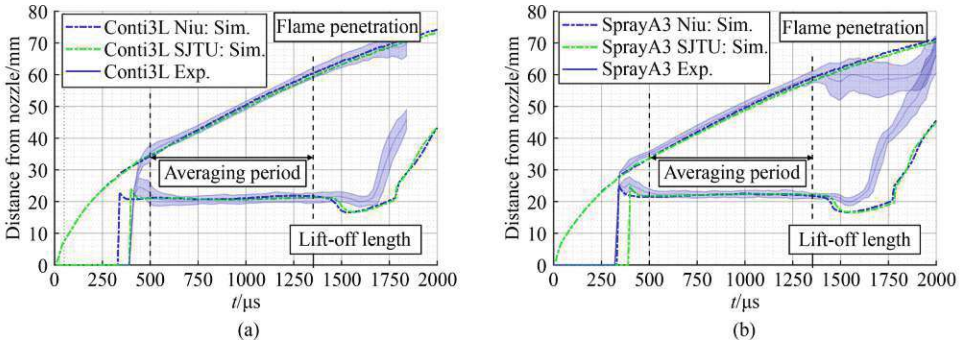

Fig. 13 Transient profiles for lift-off length and mixture fraction penetration and time-averaging period indication for OP2 (900 K and 15% O_2) single injection.

(a) Conti3L injector; (b) SprayA3 injector.

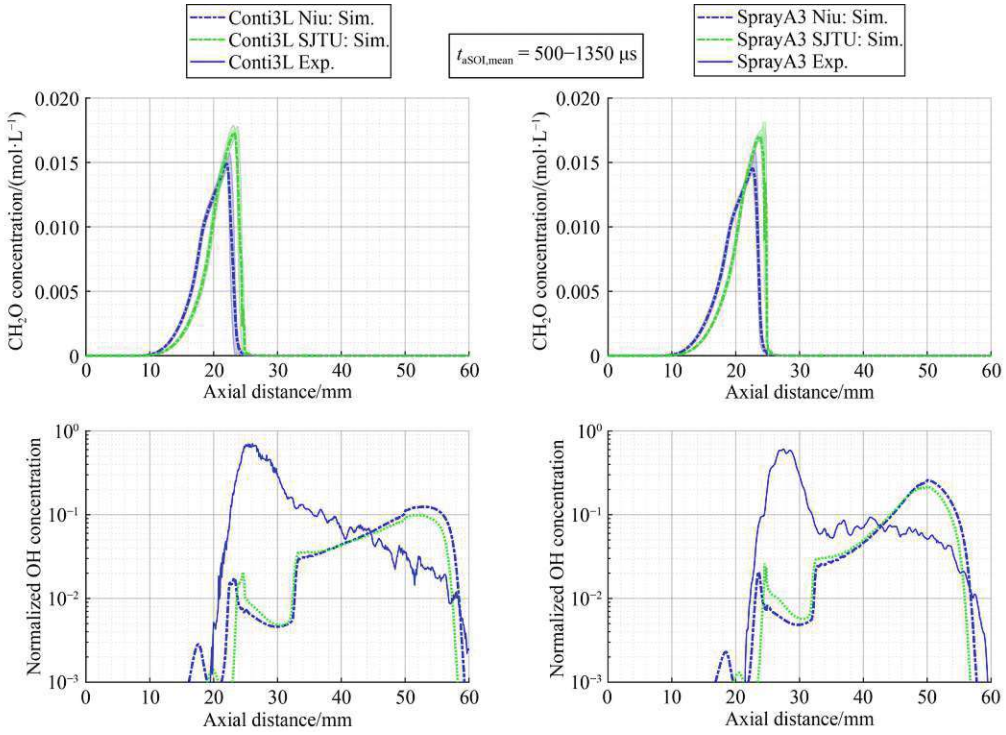

Fig. 14 Time-averaged centerline profiles for OP2 (900 K and 15% O_2) single injection.

(left) Conti3L injector; (right) SprayA3 injector; (top) CH_2O molar concentration; (bottom) normalized OH concentration (simulation) and OH*-intensity (experiment) with logarithmic ordinate.

in the center slightly downstream of the calculated lift-off length. The OH/OH* profiles at the center axis of the spray are shown in the bottom two plots of Fig. 14 with a logarithmically plotted ordinate. The concentration of OH*-intensity at the center axis of the spray, measured by the experiments, cannot be reproduced by either mechanism. The higher CH_2O accumulation for the SJTU mechanism in the center translates to only slightly greater OH concentration downstream of the flame lift-off. At the tip of the averaged profile, the Niu mechanism exceeds the SJTU one in OH concentration, which also signals an improvement for the novel mechanism compared to the experiments.

To improve the visualization of the OH distribution of the simulations in comparison with the OH*-intensity of the experiments, radial profiles at axial positions a few millimeters downstream of the steady-state lift-off length are shown in Fig. 15, again with a logarithmic ordinate. The deviation between experiments and simulations in the center axis is visible for all positions. Still, there is also a slight increase in the levels of OH concentration for the SJTU mechanism. As no axial positions beyond 30 mm were evaluated, the averaging process did not affect the results shown in Fig. 15.

Compared to the differences seen for the CH_2O centerline profile and maps, the differences in OH formation between the two mechanisms are significantly smaller. This indicates that the transition from low-temperature (CH_2O) to high-temperature (OH) flame remains the key area for further improvements regarding the reaction kinetics modeling for OME spray combustion.

3.2.2 Multi-injection

The approach in analyzing the two mechanisms in the case of the multi-injection event follows the same logic as for the single injection, however, focusing on the transient development of the flame during the short pilot injection. At first, the global mass fractions and reaction rates of CH_2O and OH, characterizing the cool-flame and high-temperature reactions, respectively, are compared in Fig. 16. The pilot injection is characterized by a higher plateau of CH_2O formation for the SJTU mechanism. For the main injection, this is only the case for the Conti3L injector simulations, delivering a more complex picture than the single injection in Fig. 10. The formation of OH after the ignition of the pilot injection is barely noticeable for the SJTU mechanism, suggesting that a reaction mechanism with an even longer ignition delay might eventually lead to the pilot injection not igniting at all. Another observation from Fig. 16 is that the delay between the beginning of the CH_2O and the OH production is increased for the SJTU mechanism.

The transient development of the distribution of molar concentration of CH_2O is plotted in Fig. 17 for a slice through the center plane of the SprayA3 injector. The top half of each plot represents the calculation with the Niu mechanism, and the bottom half shows the SJTU mechanism simulation. As for the single injection case, stoichiometric mixing conditions are visualized as black solid lines. The area where high-temperature reactions consume the CH_2O is indicated in each plot with magenta solid lines tracking the temperature front of 1400 K.

The earlier ignition of the Niu mechanism is shown, as well as the ignition in the center of the spray at fuel-rich conditions within the boundary set by the black lines of stoichiometric mixing. The flame expands outwards simultaneously when the stoichiometric area starts to shrink until it vanishes entirely due to the small amount of OME injected. This outward expansion process is initiated for the SJTU mechanism when almost the entire mixture is lean. This suggests that the pilot ignition for

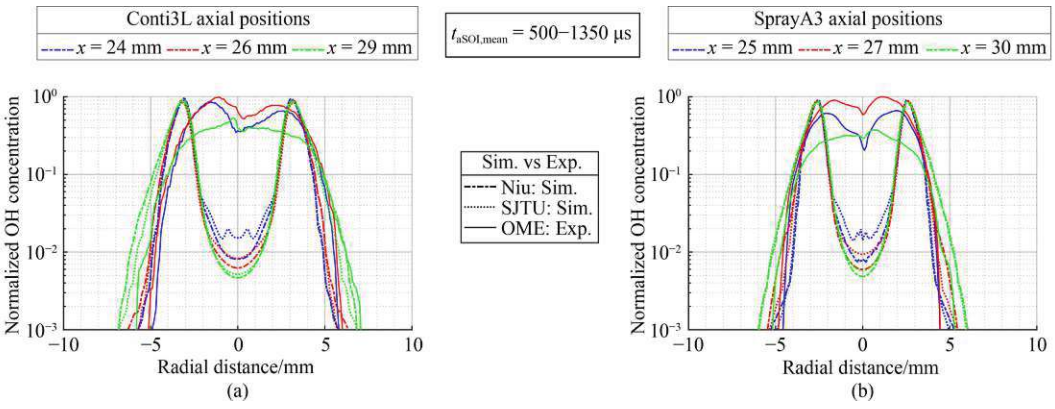

Fig. 15 Time-averaged OH radial profiles for single injection after stable lift-off length is established for OP2 (900 K and 15% O_2) single injection.

(a) Conti3L injector; (b) SprayA3 injector.

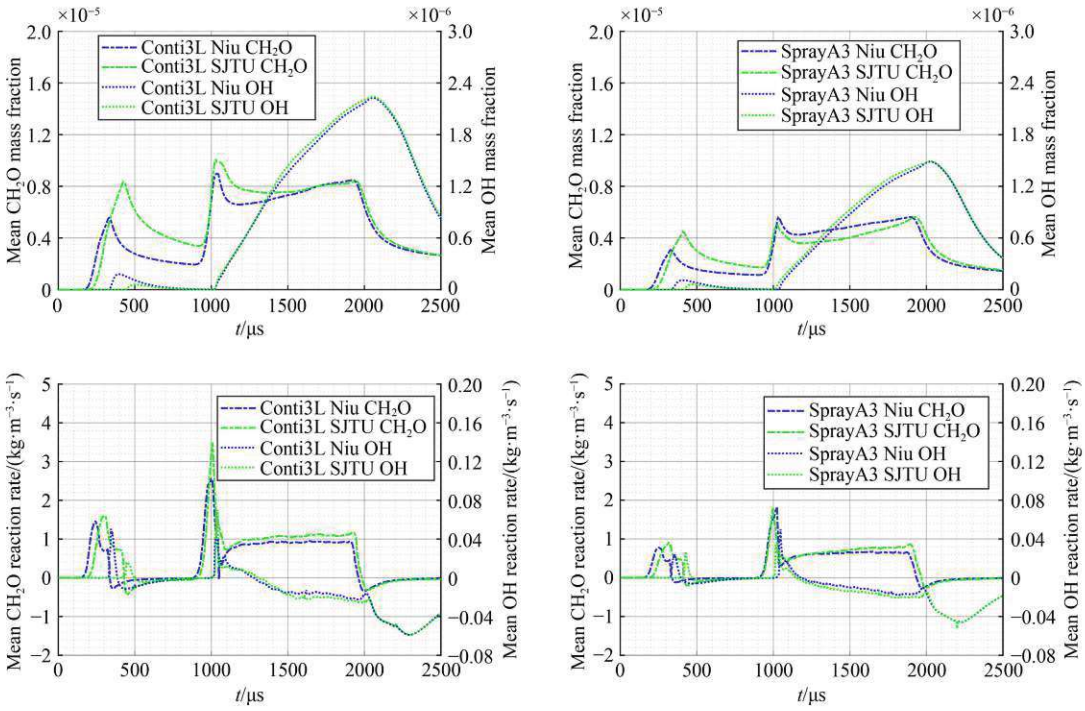

Fig. 16 Transient profiles for CH_2O and OH for multi-injection.
(left) Conti3L injector; (right) SprayA3 injector; (top) mean mass fractions; (bottom) mean reaction rates.

the SJTU mechanism occurs in very lean conditions. The delay of ignition and increased accumulation of CH_2O throughout the pilot injection is visible for the SJTU mechanism.

At the end of the pilot injection, the high-temperature flame detaches from the cool flame. It is eventually merged with the reignited spray of the main injection, which develops a high-temperature flame at the spray tip, reaching further upstream along the line of stoichiometric mixing.

The flame reaches farther back upstream for the SJTU mechanism, resulting in a slightly shorter lift-off length already visualized in Fig. 9. The ignition within the mixing field created by the pilot injection differs from the single injection in that there is no significant and consistent difference in ignition delay (of the main injection) and that the accumulation of CH_2O at this elevated temperature does not vary substantially between the two reaction mechanisms.

In Fig. 18, the planar contours of the concentration of the OH species and OH*-intensity for the measured data are plotted for the pilot and main injection. The ignition of the pilot injection is concentrated in the spray center for both mechanisms, albeit more evenly distributed in the case of the SJTU mechanism. The experiments could not detect an OH*-signal for the pilot injection. Only the main injection generated a string-enough signal so that the OH*-intensity could be processed into qualitative plots showing the intensity distribution of the high-temperature flame. As for the cool flame characterized by CH_2O, the high-temperature reaction activity does not differ significantly between the two mechanisms. Both mechanisms underestimate the reaction activity within the center axis of the spray. The elevated temperatures and the mixing field resulting from the ignition of the pilot injection impede the improvements otherwise noticeable for the new SJTU mechanism.

3.3 Mixing regimes

In Wiesmann et al. [12], spray combustion simulations with the Niu mechanism and the same OME mix did not produce any mixing states, which could be considered as potentially forming soot. The limits for an increased soot yield are defined by equivalence ratio and temperature. According to Refs. [37,38], the equivalence ratio, or in the case of oxygenated fuels like OME, the oxygen equivalence ratio (ϕ_Ω, see Eq. (3)), needs to exceed two ($\phi_\Omega \geqslant 2$). The temperature range of 1200 K $\leqslant T \leqslant$ 2000 K to form soot is set by the need for radical precursors such as acetylene (C_2H_2) or C_3H_3 [39]. Below that, these precursors do not exist, and above 2000 K, they are pyrolyzed and oxidized. Figure 19 illustrates scatter plots, with each dot representing one simulation cell with the

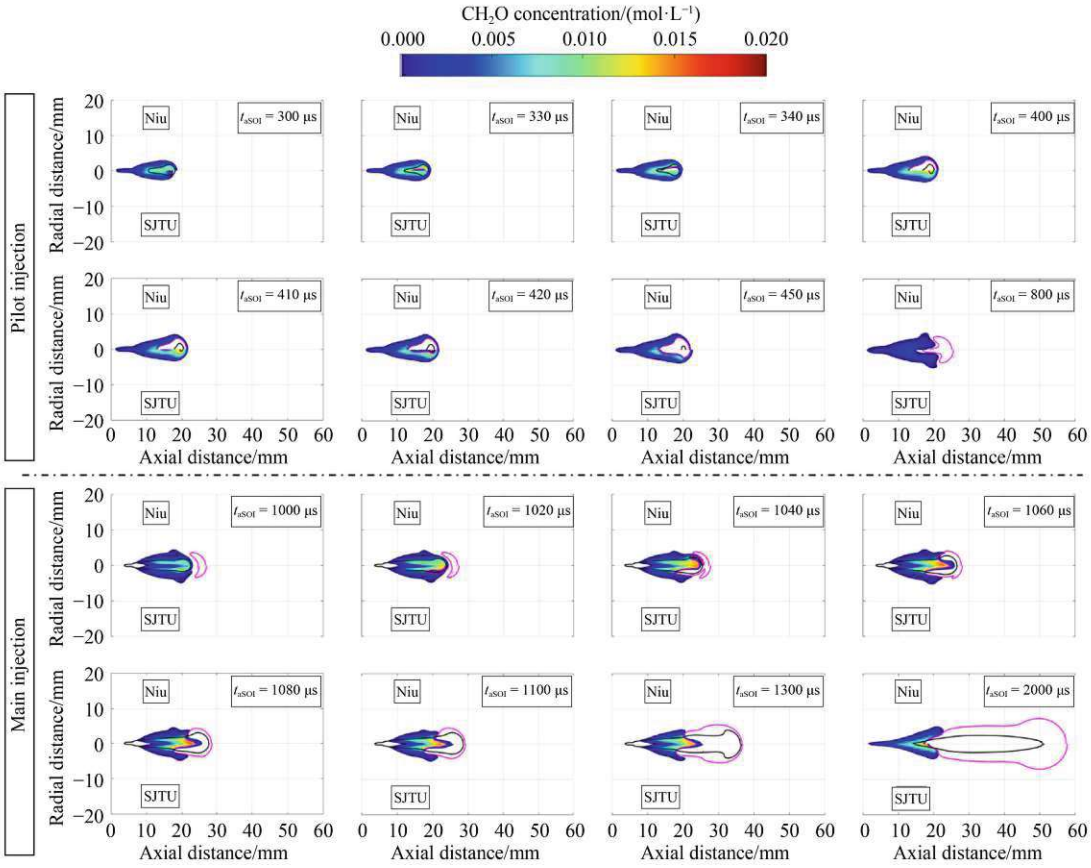

Fig. 17 SprayA3-OP4 (900 K and 15% O_2): CH_2O molar concentration contours in the center plane for multi-injection (black lines depict stoichiometric mixing, and magenta lines show the temperature front of 1400 K).
(top) the Niu mechanism; (bottom) the SJTU mechanism.

increased soot yield region indicated within the plots as gray boxes. The top two plots have all simulation cells scaled with their respective OH mass and colored with their OH mass fraction. In the bottom plots of Fig. 19, each cell is scaled with its CH_2O mass and colored with its respective CH_2O mass fraction.

This visualization enables one to differentiate the low- and high-temperature combustion within the given time step of t_{aSOI} = 1000 μs. Both mechanisms do not come close to mixing regimes that potentially form soot. The combustion for this snapshot in time for the SJTU mechanism seems slightly leaner. The OH high-temperature stage of the combustion process does not differ substantially between the two reaction mechanisms. It is centered around temperatures above 1500 K, and most of the OH production occurs in an area close to stoichiometric conditions. However, the cool-flame CH_2O occurrence differs from the SJTU mechanism to the Niu mechanism. The temperature range of CH_2O production is similar for both mechanisms, but for the SJTU one, CH_2O is present in leaner conditions, with the highest observed CH_2O mass fractions reaching back to oxygen equivalence ratios smaller than unity ($\phi_\Omega < 1$).

A simple way to capture the entire transient combustion process and not only a snapshot in time is to focus on the simulation cell with the maximum temperature. Figure 20 displays the maximum temperature of the simulation plotted against its corresponding oxygen equivalence ratio. For the single injection, top plots in Fig. 20, leaner combustion can be identified. For the multi-injection, bottom plots in Fig. 20, the profiles are split into pilot and main injection. A significant difference between the two oxidization mechanisms can be recognized for the pilot injection, as the SJTU mechanism ignites in very lean conditions with equivalence ratios smaller than unity ($\phi_\Omega < 1$). This observation coincides with Fig. 16, showing little OH production for the pilot injection ignition when using the SJTU mechanism. Both mechanisms experience a rapid cool-down after the pilot injection and follow a similar trend once the main injection starts. However, even

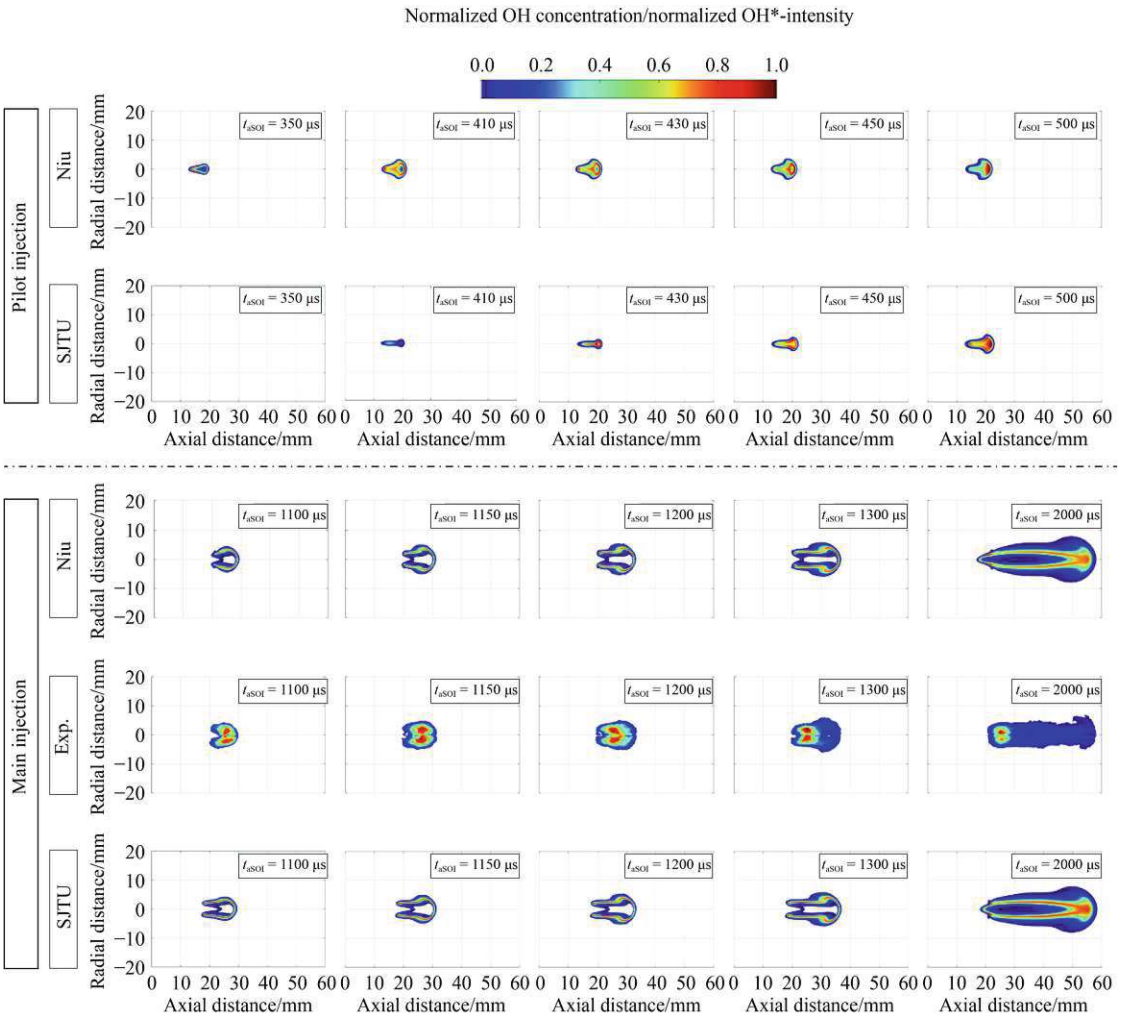

Fig. 18 SprayA3-OP4 (900 K and 15% O_2): Normalized OH*-intensity (experiment) and OH molar concentration (simulation) contours in the center plane for multi-injection and SprayA3 injector.

(top) the Niu mechanism; (bottom) the SJTU mechanism.

during the main injection, a slightly leaner combustion for the SJTU mechanism is revealed.

4 Conclusions

The presented study analyzed the impact of a novel reaction mechanism suitable for CFD simulations describing the oxidization of PODE or OME with a chain length of n = 1–6 (OME_{1-6}). At first, the new oxidization mechanism (SJTU mechanism), based on the work of Niu et al. [14] (Niu mechanism), was utilized in a 0D homogeneous reactor model. The mole fractions simulated were compared to JSR experiments. The new reaction mechanism was shown to predict the measured data for CO, CO_2, O_2, and H_2 with a higher accuracy over a range of equivalence ratios and temperatures compared to the original mechanism. Furthermore, the IDTs reported by Cai et al. [18] for OME_3 in air were utilized to validate the 0D-simulated ignition delays by the SJTU and Niu mechanisms. The results yielded that the SJTU mechanism consistently performed better in predicting the ignition delay.

The CFD simulations were validated against OH*-chemiluminescence experimental data within an optically accessible constant-volume injection chamber. The main conclusions describing the improvements achieved with the new SJTU mechanism for OME are:

1) The quality of the IDTs predicted by the SJTU mechanism is significantly improved for a temperature range of at least 800–1000 K and oxygen content levels of 15% and 21%. The lift-off length and flame front

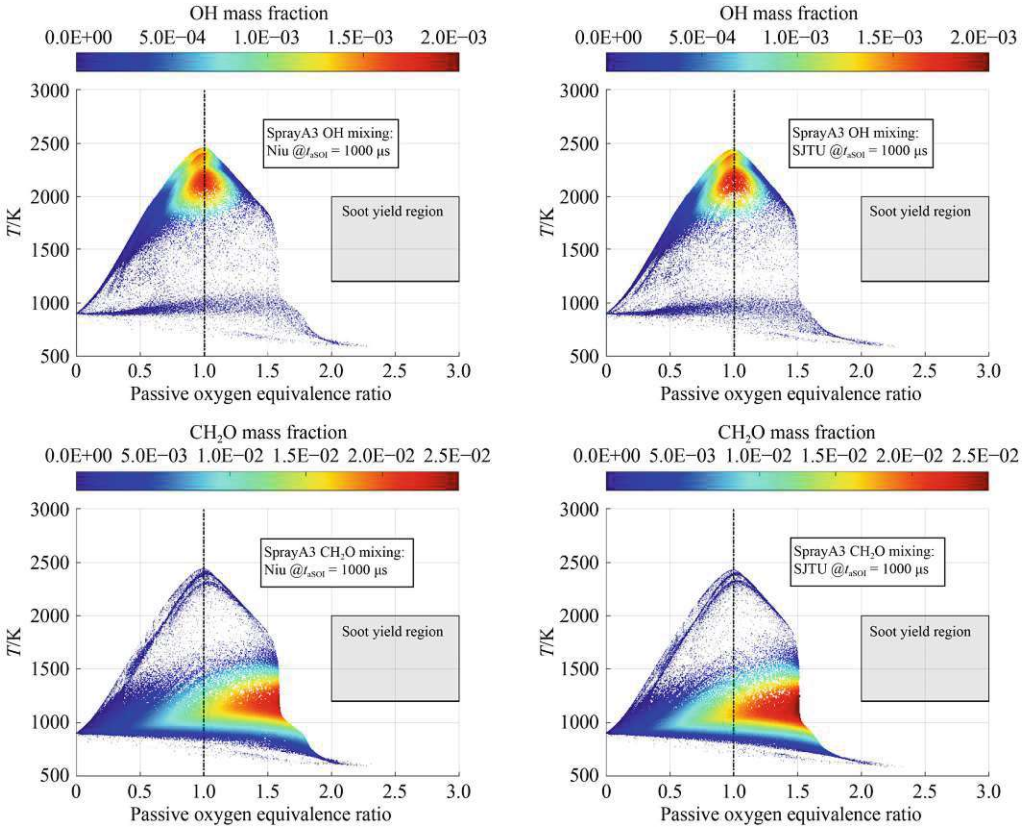

Fig. 19 SprayA3 and OP2 (900 K and 15% O_2) (*T* vs. passive scalar oxygen equivalence ratio for single injection at 1000 µs after SOI). (left) Niu reaction mechanism; (right) SJTU reaction mechanism; (top) colored with OH cell mass fraction and scaled with OH cell mass; (bottom) colored with CH_2O cell mass fraction and scaled with CH_2O cell mass.

penetration are not influenced by the SJTU mechanism, retaining the already excellent agreement with the measurements achieved with the Niu reaction mechanism.

2) The low-temperature CH_2O production is elevated and more concentrated toward the spray center axis. Higher levels of CH_2O concentration are present closer to the nozzle. The high-temperature (OH/OH*) reaction activity is slightly increased in the spray axis, likely due to the increased CH_2O formation along the spray centerline, constituting a positive trend compared to the measurements. The fuel mechanisms used in this study cannot fully reproduce the experimentally observed high concentration of OH*-radicals near the spray axis.

3) Mixing regimes in the case of the single injection pattern are only slightly affected by the new mechanism toward an even leaner mixing state. In the case of multi-injection patterns, the delayed ignition of the new mechanism influences the high-temperature mixing field. The ignition following the short pilot injection occurs at an ultra-lean condition, not even reaching stoichiometry. Once the main injection reignites the mixture, the SJTU and Niu mechanisms only show minor differences in terms of mixing, cool-flame, and high-temperature flame distribution.

The tendency of the RANS OME simulation conducted to overestimate the high-temperature reaction activity within the shear layer of spray and ambient air remains a major challenge for research efforts into this topic. The main focus of future investigations will, therefore, be on the role of turbulence modeling in flame morphology by comparing RANS and Large Eddy Simulation (LES) simulations in terms of their impact on ignition locations and high-temperature reaction zones.

Another aspect for future research is the strong OH*-signal intensity observed experimentally at the root of the spray near the nozzle for OME. This behavior cannot be reproduced by the simulations. The differences between the volatile excited OH*-signal and the presumably more stable OH mass fraction within the CFD simulations suggest a possible improvement for reaction mechanisms by incorporating a species that reflects the volatility of excited OH* more adequately.

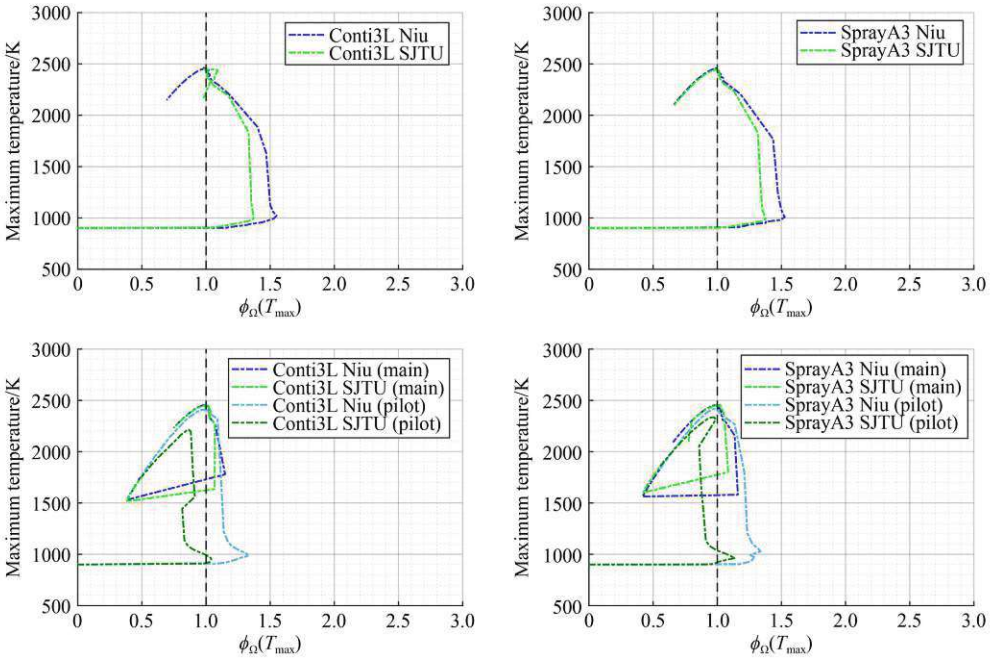

Fig. 20 Maximum temperature versus its corresponding oxygen equivalence ratio at 900 K and 15% O_2. (left) Conti3L injector; (right) SprayA3 injector; (top) single injection; (bottom) multi-injection.

Notations

Abbreviations

C_2H_2	Acetylene molecule
CFD	Computational fluid dynamics
CH_2O	Formaldehyde molecule
$CH_3O(-CH_2O)_n-CH_3$	Polyoxymethylene dimethyl ether molecule
ECN	Engine Combustion Network
FST	Institute of Fluid System Technology
ID/IDT	Ignition delay timeJSR
KHRT	Kelvin–Helmholtz–Rayleigh–Taylor
LES	Large Eddy Simulation
OH	Hydroxyl radical
OME	Oxymethylene ethers
PODE	Polyoxymethylene dimethyl ethers
OP1	ECN Spray A low temperature conditions (800 K, 22.8 kg/m^3, 15% O_2)
OP2	ECN Spray A conditions (900 K, 22.8 kg/m^3, 15% O_2)
OP3	ECN Spray A high temperature conditions (1000 K, 22.8 kg/m^3, 15% O_2)
OP4	ECN Spray A conditions with multi-injection (900 K, 22.8 kg/m^3, 15% O_2
OP5	ECN Spray A high oxygen content conditions (900 K, 22.8 kg/m^3, 21% O_2)
RANS	Reynolds averaged Navier–Stokes equations
SJTU	Shanghai Jiao Tong University
SOC	Start of combustion
SOI	Start of injection

Variables

C_A	Injector nozzle hole area contraction coefficient
d	Diameter
k	Pre-exponential factor of reaction
L	Length
$\dot{m}$	Mass flow
p	Pressure
r/R	Radius
S	Sensitivity coefficient
t	Time
T	Temperature
x	Distance
Z	Mixture fraction
Zi	Element mass fraction
ρ	Density
τ	Ignition delay time
ϕ	Equivalence ratio
ϕ_Ω	Oxygen equivalence ratio
Ω	Oxygen ratio

Acknowledgements This work was the scientific result of a research project undertaken by the Research Association for Combustion Engines

eV (FVV). The work at the SJTU was funded by the National Key R&D Program of China (Grant No. 2022YFE0209000) and the National Natural Science Foundation of China (Grant No. 52022058). Parts of this work were funded by the Federal Ministry for Economic Affairs and Energy (BMWi) through the German Federation of Industrial Research Associations eV (AiF). The work at the TU Wien was funded by the Ministry for Transport, Innovation and Technology (BMVIT) through the Austrian Research Promotion Agency (FFG, Grant No. 874418). The research was conducted in the framework of the collective research networking program (CORNET) project "eSpray." The computational results presented were achieved using the Vienna Scientific Cluster (VSC) via the funded project No. 71485.

Competing interests The authors declare that they have no conflict of interest.

References

1. Huang Z, Zhu L, Li A, et al. Renewable synthetic fuel: Turning carbon dioxide back into fuel. Frontiers in Energy, 2022, 16(2): 145–149
2. Damyanov A, Hofmann P, Geringer B, et al. Biogenous ethers: Production and operation in a diesel engine. Automotive and Engine Technology, 2018, 3: 69–82
3. Liu J, Wang H, Li Y, et al. Effects of diesel/PODE (polyoxymethylene dimethyl ethers) blends on combustion and emission characteristics in a heavy duty diesel engine. Fuel, 2016, 177: 206–216
4. Härtl M, Gaukel K, Pélerin D, et al. Oxymethylene ether as potentially CO_2-neutral fuel for clean diesel engines part 1: Engine testing. MTZ worldwide 2017, 78: 52–59
5. Omari A, Heuser B, Pischinger S. Potential of oxymethylenether-diesel blends for ultra-low emission engines. Fuel, 2017, 209: 232–237
6. Qiu Z, Zhong A, Huang Z, et al. An experimental and modeling study on polyoxymethylene dimethyl ether 3 (PODE3) oxidation in a jet stirred reactor. Fundamental Research, 2022, 2(5): 738–747
7. Virt M, Arnold U. Effects of oxymethylene ether in a commercial diesel engine. Cognitive Sustainability, 2022, 1(3)
8. Pélerin D, Gaukel K, Härtl M, et al. Potentials to simplify the engine system using the alternative diesel fuels oxymethylene ether OME_1 and $OME_{3–6}$ on a heavy-duty engine. Fuel, 2020, 259: 116231
9. Gelner A D, Rothe D, Kykal C, et al. Particle emissions of a heavy-duty engine fueled with polyoxymethylene dimethyl ethers (OME). Environmental Science: Atmospheres, 2022, 2(2): 291–304
10. Dworschak P, Berger V, Härtl M, et al. Neat Oxymethylene Ethers: Combustion Performance and Emissions of OME_2, OME_3, OME_4 and OME_5 in a Single-Cylinder Diesel Engine. SAE Technical Report 2020-01-0805, 2020
11. Strauß L, Rieß S, Wensing M. Mixture formation of $OME_{3–5}$ and 1-octanol in comparison with diesel-like dodecane under ECN Spray A conditions. Frontiers in Mechanical Engineering, 2023, 9: 1083658
12. Wiesmann F, Strauß L, Rieß S, et al. Numerical and experimental investigations on the ignition behavior of OME. Energies, 2022, 15(18): 6855
13. Wiesmann F, Bauer E, Kaiser S A, et al. Ignition and Combustion Characteristics of $OME_{3–5}$ and N-Dodecane: A Comparison Based on CFD Engine Simulations and Optical Experiments. SAE Technical Report 2023-01-0305, 2023
14. Niu B, Jia M, Chang Y, et al. Construction of reduced oxidation mechanisms of polyoxymethylene dimethyl ethers ($PODE_{1–6}$) with consistent structure using decoupling methodology and reaction rate rule. Combustion and Flame, 2021, 232: 111534
15. ASG. ASG analytik-service. 2022-8-2, available at website of ASG Analytik
16. Pastor J V, García-Oliver J M, Micó C, et al. Experimental study of the effect of hydrotreated vegetable oil and oxymethylene ethers on main spray and combustion characteristics under engine combustion network Spray A conditions. Applied Sciences, 2020, 10(16): 5460
17. ,Chemkin-Pro 15131. San Diego: Reaction Design, 2013
18. Cai L, Jacobs S, Langer R, et al. Auto-ignition of oxymethylene ethers (OME_n, n = 2–4) as promising synthetic e-fuels from renewable electricity: Shock tube experiments and automatic mechanism generation. Fuel, 2020, 264: 116711
19. Hanjalić K, Popovac M, Hadžiabdić M. A robust near-wall elliptic-relaxation eddy-viscosity turbulence model for CFD. International Journal of Heat and Fluid Flow, 2004, 25(6): 1047–1051
20. Popovac M, Hanjalic K. Compound wall treatment for RANS computation of complex turbulent flows. In: Proceedings of the 3rd MIT Conference on Computational Fluid and Solid Mechanics. Boston: Elsevier, 2005
21. Reitz R D. Modeling atomization processes in high-pressure vaporizing sprays. Atomisation Spray Technology, 1987, 3: 309–337
22. Taylor G. The instability of liquid surfaces when accelerated in a direction perpendicular to their planes. I. Proceedings of the Royal Society of London. Series A, Mathematical and Physical Sciences, 1950, 201(1065): 192–196
23. Brenn G, Deviprasath L J, Durst F. Computations and experiments on the evaporation of multi-component droplets. In: Proceedings of the 9th International Conferences on Atomization and Spray Systems. Sorrento, 2003
24. Abramzon B, Sirignano W. Droplet vaporization model for spray combustion calculations. International Journal of Heat and Mass Transfer, 1989, 32(9): 1605–1618
25. O'Rourke P J, Bracco F. Modelling of drop interactions in thick

sprays and a comparison with experiments. Proceedings of the Institution of Mechanical Engineers, Part C: Journal of Mechanical Engineering Science, 1980, 404(80): 101–116
26. Schiller L, Naumann A Z. A drag coefficient correlation. Zeitschrift des Vereins Deutscher Ingenieure, 1933, 77: 318–320
27. Pickett L M, Manin J, Payri R, et al. Transient Rate of Injection Effects on Spray Development. SAE Technical Report 2013-24-0001, 2013
28. CMT. Virtual injection tate generator. 2022–04-07, available at website of Universitat Politècnica de València
29. Peter A, Siewert B, Riess S, et al. Mixture formation analysis of polyoxymethylenether injection. Atomization and Sprays, 2020, 30(11): 843–859
30. Frühhaber J, Peter A, Schuh S, et al. Modeling the Pilot Injection and the Ignition Process of a Dual Fuel Injector with Experimental Data from a Combustion Chamber Using Detailed Reaction Kinetics. SAE Technical Report 2018-01-1724, 2018
31. AVL List GmbH. User Manual for FIRE General Gas Phase Reactions Module Version 2018, 2018
32. Mueller C J. The Quantification of Mixture Stoichiometry When Fuel Molecules Contain Oxidizer Elements or Oxidizer Molecules Contain Fuel Elements. SAE Technical Report 2005-01-3705, 2005
33. ECN. Engine combustion network. 2022-4-7, available at website of Sandia National Laboratories
34. Riess S, Vogel T, Wensing M. Influence of exhaust gas recirculation on ignition and combustion of diesel fuel under engine conditions investigated by chemical luminescence. In: Proceedings of the 13th Triennial Conference on Liquid Atomization and Spray Systems. Tainan, China, 2015
35. Peter A. Charakterisierung der Gemischbildung und Zündung in Diesel- und Dual-Fuel-Brennverfahren. In: Berichte zur Thermodynamik und Verfahrenstechnik. Düren: Shaker Verlag, 2022
36. Tagliante F, Nguyen T M, Dhanji M P, et al. The role of cool-flame fluctuations in high-pressure spray flames, studied using high-speed optical diagnostics and large-eddy simulations. Proceedings of the Combustion Institute, 2023, 39(4): 4871–4879
37. Stiesch G. Modeling Engine Spray and Combustion Processes. Berlin: Springer Heideberg, 2003
38. Pischinger F, Schulte H. Grundlagen und entwicklungslinien der diesel-motorischen brennverfahren. düsseldorf. VDI-Verlag, 1988, 714: 61–93
39. Warnatz J, Maas U, Dibble R W. Combustion: Physical and Chemical Fundamentals, Modeling and Simulation, Experiments, Pollutant Formation. 4th ed. New York: Springer, 2006

4

Wiesmann, F.; Nguyen, T. M.; Manin, J.; Pickett, L. M.; Wan, K.; Tagliante, F. and Lauer, T.

LES and RANS Spray Combustion Analysis of OME_{3-5} and n-Dodecane

Energies, 17:2265

2024

doi: 10.3390/en17102265

energies

MDPI

Article

LES and RANS Spray Combustion Analysis of OME_{3-5} and n-Dodecane

Frederik Wiesmann [1,*], Tuan M. Nguyen [2], Julien Manin [2], Lyle M. Pickett [2], Kevin Wan [2], Fabien Tagliante [2] and Thomas Lauer [1]

[1] Institute of Powertrains and Automotive Technology, TU Wien, 1060 Vienna, Austria; thomas.lauer@ifa.tuwien.ac.at
[2] Sandia National Laboratories, 7011 East Ave, Livermore, CA 94551, USA; nguyen147@llnl.gov (T.M.N.); jmanin@sandia.gov (J.M.); lmpicke@sandia.gov (L.M.P.); kwan@sandia.gov (K.W.); tagliante.fabien@gmail.com (F.T.)
* Correspondence: frederik.wiesmann@ifa.tuwien.ac.at; Tel.: +43-1-588-013-1560

Abstract: Clean-burning oxygenated and synthetic fuels derived from renewable power, so-called e-fuels, are a promising pathway to decarbonize compression–ignition engines. Polyoxymethylene dimethyl ethers (PODEs or OMEs) are one candidate of such fuels with good prospects. Their lack of carbon-to-carbon bonds and high concentration of chemically bound oxygen effectively negate the emergence of polycyclic aromatic hydrocarbons (PAHs) and even their precursors like acetylene (C_2H_2), enabling soot-free combustion without the soot-NO_x trade-off common for diesel engines. The differences in the spray combustion process for OMEs and diesel-like reference fuels like n-dodecane and their potential implications on engine applications include discrepancies in the observed ignition delay, the stabilized flame lift-off location, and significant deviations in high-temperature flame morphology. For CFD simulations, the accurate modeling and prediction of these differences between OMEs and n-dodecane proved challenging. This study investigates the spray combustion process of an OME_{3-5} mixture and n-dodecane with advanced optical diagnostics, Reynolds-Averaged Navier–Stokes (RANS), and Large-Eddy Simulations (LESs) within a constant-volume vessel. Cool-flame and high-temperature combustion were measured simultaneously via high-speed (50 kHz) imaging with formaldehyde (CH_2O) planar laser-induced fluorescence (PLIF) representing the former and line-of-sight OH^* chemiluminescence the latter. Both RANS and LES simulations accurately describe the cool-flame development process with the formation of CH_2O. However, CH_2O consumption and the onset of high-temperature reactions, signaled by the rise of OH^* levels, show significant deviations between RANS, LES, and experiments as well as between n-dodecane and OME. A focus is set on the quality of the simulated results compared to the experimentally observed spatial distribution of OH^*, especially in OME fuel-rich regions. The influence of the turbulence modeling is investigated for the two distinct ambient temperatures of 900 K and 1200 K within the Engine Combustion Network Spray A setup. The capabilities and limitations of the RANS simulations are demonstrated with the initial cool-flame propagation and periodic oscillations of CH_2O formation/consumption during the quasi-steady combustion period captured by the LES.

Keywords: CFD; OME; PODE; polyoxymethylene ether; e-fuels; oxygenated fuels; ECN; RANS; LES; spray combustion

Citation: Wiesmann, F.; Nguyen, T.M.; Manin, J.; Pickett, L.M.; Wan, K.; Tagliante, F.; Lauer, T. LES and RANS Spray Combustion Analysis of OME_{3-5} and n-Dodecane. *Energies* **2024**, *17*, 2265. https://doi.org/10.3390/en17102265

Academic Editor: Constantine D. Rakopoulos

Received: 5 April 2024
Revised: 24 April 2024
Accepted: 26 April 2024
Published: 8 May 2024

1. Introduction

Oxygenated synthetic fuels promise to be a viable pathway to significantly reduce the CO_2 footprint of hard-to-decarbonize applications. Concerning the potential of OMEs within engine applications, several studies identified mixtures of OME_{3-5} to be the most suitable alternative for diesel fuel because of the similar viscosity, lubricity, and boiling point, as well as lower volatility and higher cetane number compared to OME_1 [1–3].

Hereby, the chemical structure of OMEs ($CH_3O(\text{-}CH_2\text{-}O)_n\text{-}CH_3$) is characterized by the number of oxymethylene ether groups (CH_2-O) within. According to [4], a greater number of oxymethylene ether groups is beneficial for NO_x emissions and only slightly reduces the thermal efficiency observed in a single-cylinder diesel engine. While Virt and Arnold [5] showed reduced particulate emissions and faster ignition, i.e., shorter ignition delays, for blends of diesel with up to 45 vol.% of OME_{3-5}, Pélerin et al. [6] used a pure OME_{3-6} fuel comparing it to diesel in a heavy-duty engine. It was found that the OME_{3-6} fuel had drastically reduced soot and particulate emissions without increasing emission levels of NO_x, hence effectively mitigating the soot-NO_x trade-off typical for diesel engines. These observations were confirmed for engines fueled with both diesel–OMEs blends [7–10] and neat OMEs [3,11–13].

Besides engine operation aspects, the mixing and combustion characteristics of OMEs are crucial to extracting the fuel's full potential and possibly guiding adaptations to future engine design needed for the widespread usage of OME fuels. Several studies, especially within the framework of the Engine Combustion Network (ECN) [14], worked with the same OME_{3-5} fuel composition used in this study. The macroscopic characteristics of the OME_{3-5} fuel mix compared to OME_1, n-dodecane, and hydrotreated vegetable oil (HVO) were reported in [15] showing a longer liquid length and shorter ignition delay for OME_{3-5} compared to n-dodecane, despite its lower cetane number. The mixing process of OME_{3-5} was analyzed in comparison to n-dodecane and 1-octanol [16]. All fuels proved to have very similar mass distributions, and the differences in equivalence ratio distributions were solely a consequence of the different air requirements for stoichiometric mixing of the oxygenated fuels. Non-reacting as well as ignition characteristics of the OME_{3-5} fuel were studied in [17] within a constant-pressure vessel experimentally and numerically, employing Reynolds-Averaged Navier–Stokes (RANS) calculations. Significant differences to n-dodecane were reported concerning the distribution of high-temperature reaction zones characterized by OH^* chemiluminescence. The RANS calculations, tracking the OH species rather than the excited OH^* radical, were able to depict the trends of higher OH accumulation in the spray symmetry plane for OME. The entire combustion process was shown not to exceed equivalence ratios greater than two for OME, which is, of course, in stark contrast to the combustion of n-paraffinic fuel like n-dodecane. These observations were confirmed for a single-cylinder optically accessible diesel engine in [18] using the same RANS setup and injection strategy and also recently by García-Oliver et al. [19] utilizing a different simulation setup and injection strategy but the same OME fuel. However, the simulations could not reproduce the strong OH^* chemiluminescence signal in the spray center axis and the peak intensity near the flame lift-off length in either the constant-pressure vessel or the single-cylinder engine.

Pastor et al. [20] investigated the combustion characteristics of the OME_{3-5} fuel mixture for the standard operating condition of the ECN [14] using formaldehyde PLIF, signaling the rise of low-temperature reactions, and OH^* chemiluminescence, indicating the onset of the high-temperature flame. The results demonstrated a clear separation of the cool flame and high-temperature reaction zone for one ECN standard injector (Spray A), but also a propagation of CH_2O downstream of the flame lift-off length for a different injector with more than twice the size of the actual nozzle diameter (Spray D). The richer spray in the case of Spray D was assumed to impede the CH_2O consumption at the spray axis.

A recent study by Kaario et al. [21] demonstrated the two-stage ignition characteristics for another oxygenated fuel, namely methanol, using Large-Eddy Simulations (LESs). The simulations showed that the methanol ignition is characterized by a higher heat release rate during the low-temperature chemistry or first-stage ignition and not during the high-temperature reactions, which is opposite to the behavior of classical two-stage ignition phenomena, e.g., for n-dodecane. The first-stage ignition was also shown to occur in a narrow range of temperatures and equivalence ratios for methanol, with its heat release rate two orders of magnitude smaller than that of n-dodecane. It was also demonstrated that n-dodecane has a temporally much more distinct two-stage ignition compared to methanol.

The differences in the transient two-stage ignition for OME fuels and n-dodecane are not yet determined conclusively. The present work aims to leverage numerical models to gain additional insights into the transition of the cool-flame propagation to the high-temperature ignition of an OME_{3-5} fuel mixture. Additionally, previous studies mainly focused on the standard ECN Spray A operating point with an ambient temperature of 900 K at the start of injection. Therefore, the impact of highly elevated ambient temperature on the auto-ignition process and the flame morphology of OME_{3-5} is investigated in the current study. For this, the ability of the constant volume pre-burn chamber at Sandia National Laboratories was utilized to achieve an ambient temperature of 1200 K at the start of fuel injection. The impact of the elevated temperature on the distribution of simulated *OH* and measured *OH** chemiluminescence, especially, were of interest. Another focus of this work is to conduct an in-depth comparative analysis concerning the quality and limitations of the simulated results for RANS and LES calculations to identify possible areas of improvement for both turbulence modeling approaches based on experimental measurement.

First, the impact of highly elevated ambient temperature is described. Secondly, the findings on the cool-flame propagation and transition to high-temperature reactions are presented.

2. Setup

Experiments and simulations were conducted using a common-rail single axial hole piezo injector named Spray A3 with a measured diameter of 94 µm. The injector has a convergent nozzle with a K-factor of 3.2. More details of the injector are referenced in [22].

2.1. Fuels

The multi-component oxymethylene ether fuel mix in the study, from now on simply *OME*, is detailed in its composition of different components by an analysis conducted by Analytik Service Gesellschaft (ASG) [23] shown in Table 1.

The most important physical and chemical properties of n-dodecane, hereinafter simply *DOD*, and OME are given in Table 2 with values taken from the batch report of ASG and from [15]. Additionally, the heat of evaporation derived from the internal AVL FIRE® database at a temperature of 90 °C is shown in Table 2 for both fuels.

Table 1. OME fuel mix.

Molecule	Content [wt%]
OME_1	0.01
OME_2	<0.01
OME_3	57.90
OME_4	28.87
OME_5	10.07
OME_6	1.91

Table 2. Fuel properties for n-dodecane and OME.

Property	Unit	n-Dodecane	OME
Density	kg/m^3 (T = 15 °C)	751.20	1057.10
Viscosity	mm^2/s (T = 40 °C)	1.44	1.08
Cetane number	-	74	68.6
Lubricity	µm	563	320
Flash point	°C	83	65

Table 2. *Cont.*

Property	Unit	n-Dodecane	OME
Lower heating value	MJ/kg	44.20	19.26
Initial boiling point	°C	214.00	144.40
Final boiling point	°C	218	242.4
Total contaminations	mg/kg	-	<1
Carbon content	% [m/m]	84	43
Hydrogen content	% [m/m]	16	8.53
Oxygen content	% [m/m]	0	46.4
$(A/F)_{st}$ at 21% of O_2	-	14.92:1	5.89:1
$(A/F)_{st}$ at 15% of O_2	-	20.72:1	8.18:1
Heat of Vaporization (T = 90 °C)	kJ/mol	62.80 *	52.23 *

* Taken from internal AVL FIRE database.

2.2. Operating Points

The operating points realizing the medium (OP1) and high ambient temperature (OP2) conditions used for the experiments and simulations in this study are shown in Table 3.

Table 3. Operating points.

Name	T_{CC} [K]	p_{CC} [bar]	ρ_{CC} [kg/m^3]	T_{inj} [K]	p_{inj} [bar]	t_{inj} [ms]	O_2-Content [vol.%]
OP1	900	61	22.8	363	1500	1.5	15
OP2	1200	78	22.8	363	1500	1.5	15

2.3. Experimental Setup

Experiments were performed inside an optically accessible constant volume pre-burn chamber at Sandia. The operating conditions can be found in Table 3. Ambient conditions were controlled using a pre-burn technique. Details on the vessel and its operation can be found in previous works and on the ECN website. High-speed planar laser-induced fluorescence (PLIF) imaging of CH_2O was performed using a burst-mode Quasi-Modo Nd:YAG laser operating at 355 nm and 50 kHz. A Semrock multiline CH_2O filter was used for spectral filtering, as well as a 450 nm shortpass filter to attenuate soot incandescence at longer wavelengths. Further details on the PLIF technique can be found in [22] regarding corrections for background luminosity and laser spatial and temporal variations. High-speed OH* chemiluminescence was performed simultaneously with a 308 nm OH* filter and 358 nm shortpass filter. Further details on the OH* technique can be found in [24]. Phantom v2512 high-speed cameras were used for imaging of both diagnostics. The ignition delay was also measured by using a piezoelectric pressure transducer. It was positioned in a lower corner of the vessel, opposite the injector. The pressure measurements were adjusted for the the time delay caused by the speed of sound and the distance from ignition site to pressure transducer according to [25]. Further details can be found on the ECN website [14].

2.4. Numerical Setup

The RANS calculations were carried out with AVL FIRE® R2020.1. LES calculations were performed using CONVERGE 3.0 CFD code.

However, both codes have employed a similar modeling framework using the Lagrangian–Eulerian approach. In this framework, liquid fuels are modeled as stochastic particles in a Lagrangian manner. On the other hand, the gaseous flow field is solved in the traditional Eulerian formulation. The momentum and heat/mass exchange processes between the liquid and gaseous phases are modeled and not resolved. Spray breakup was modeled in all cases by the KH-RT methods [26]. The spray plume cone angle for the simulations was set to 14°, following the results on Spray A near-field measurements in [27].

Energies **2024**, *17*, 2265

The liquid injection was realized with the *Blob* method that initializes the liquid parcels with a size corresponding to the actual nozzle exit diameter of the injector. The same methodology to generate the injection rates is employed for all calculations. The publicly available tool from the Polytechnical University of Valencia [28] guarantees a standardized method for numerical studies to create consistent injection rate profiles for the ECN Spray A3 injector. Figure 1 depicts the rates of injections for DOD and OME for an injection pressure of p_{inj} = 1500 bar and for an injection duration of t_{inj} = 1500 µs as stated in Table 3 for the studied operating points.

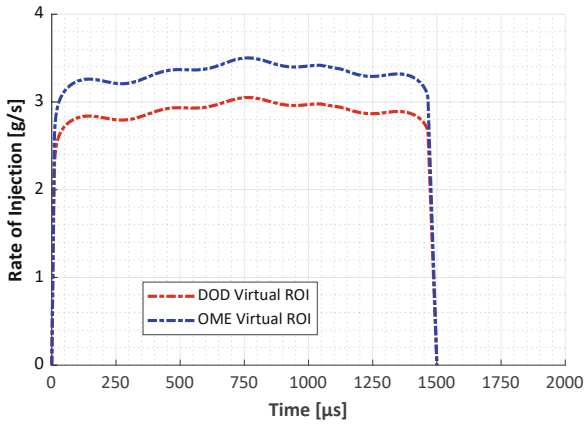

Figure 1. Rates of injection for n-dodecane and OME for Spray A3 injector according to [28].

In all cases, the combustion was modeled using chemical kinetic solvers with the well-stirred reactor assumption for each computational cell using the multi-zone technique. This approach clusters cells with similar thermodynamic conditions (temperature and equivalence ratio). The chemical reactions are solved for the mean of these clusters and the results are mapped back to the respective cells. The clustering and mapping-back procedures are applied according to [29].

A major goal of the current research is to ensure sufficient resolution of the mixture within the turbulent flow field when coupled to a direct chemistry integration approach that avoids mechanism-reduction compromises that alter or de-emphasize cool-flame (CH_2O) prediction. RANS calculations with enabled turbulence chemistry interaction (TCI) were set as benchmark tests and did not show any meaningful differences in global ignition characteristics (ignition delay, flame lift-off length) or flame morphology when compared to simulations using the multi-zone speed-up option. This indicates a well-resolved flow field due to the high grid resolution. Hence, this approach was used for the detailed analysis comparing RANS to LES, as for the latter the multi-zone approach was adopted for keeping the computational time within reasonable limits.

For n-dodecane, a 251-species and 1484-reactions chemical mechanism, developed by the Lawrence Livermore National Laboratory (LLNL) and described in the supplementary material in [24], was used. The OME simulations were carried out with the Niu mechanism [30] consisting of 92 species and 389 reactions. For validation of the used mechanisms regarding ignition delay and laminar flame speeds using 0-D simulations, the reader is referred to the respective reference.

The approach in this current work is to compare our best effort simulations using each institution's respective tool. As shown in this work, these LES and RANS methods have been extensively validated in previous works. Combined with the efforts to match chemical kinetic mechanisms and combustion models, the focus of this work is not only to compare RANS and LES results, but to identify the area of improvements for approaches by performing in-depth analysis grounded by the experimental measurements. The following subsections describe the differences in the modeling setup for the LES and RANS simulations.

2.4.1. LES Setup

The Lagrangian spray and LES turbulence models used in this work have been extensively validated for non-reacting [31] and reacting flow [24]. The parameters for different models are summarized in Table 4.

Both fixed-cell embedding and adaptive mesh refinement (AMR), with the smallest cell size of 62.5 µm, were used to sufficiently resolve both spray and flame dynamics. The fixed-cell embedding region has the shape of 20 mm long cone, centered around the injector axis. Such a fine mesh region is required to adequately resolve both the spray dynamics upstream and the subsequent low-temperature flame downstream of the liquid length. In an attempt to resolve as much as possible the high-temperature flame region, AMR is activated on velocity and temperature gradients, which is most active in the edge flame region downstream of the lift-off length. At steady state, 50 million cells were used in some calculations.

In the fixed embedding region, especially around the flame core where the low-temperature chemistry is the most relevant, less than 20 % of the total kinetic energy has to be modeled. However, more than 20 % of the total kinetic energy has to be modeled in the high-temperature flame region, despite the aggressive AMR strategy. So the overall LES can be considered well resolved, where less than 20 % of the total kinetic energy has to be modeled [32]. The main purpose of the meshing strategy in these LES calculations is to alleviate some weakness associated with the well-stirred reactor model employed in this work. To the authors' best knowledge, these LESs are the finest ones compared to other LESs of Spray A [33–35]. The above discussion provides confidence for the low- and high-temperature flame analysis presented in this work.

2.4.2. RANS Setup

The RANS simulations of this study were conducted on a fixed mesh with a base cell size of 1 mm. Three refinement steps in the near-nozzle area resulted in a minimum cell edge length of 125 µm. Figure 2 visualizes the spray-box mesh with its refinement areas and a cell count of 966,000.

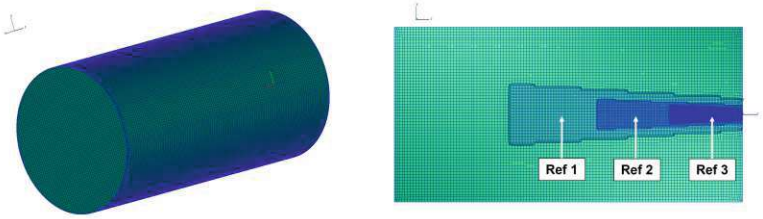

Figure 2. Mesh with refinements in symmetry plane for RANS calculations. The terms Ref 1 to Ref 3 visualize the mesh refinements with Ref 1, Ref 2 and Ref 3 denominating cells with an edge length of 500 µm, 250 µm and 125 µm respectively.

The mesh and the models for the liquid and gaseous phase for the RANS calculations were validated extensively in [17,18]. The validation included a grid independence study, which was conducted for non-reacting as well as reacting conditions. Using a temporal resolution of dt = 0.5 µs, the utilized cell sizes for the RANS computations represent a higher spatial resolution than recommended by the modeling standards of the ECN, which propose a minimum cell size of 250 µm [14]. This way the setup ensures that the liquid droplets evaporate within the highest resolution region of 125 µm and that the subsequent ignition occurs within cells with a maximum edge length of 250 µm. The chosen RANS turbulence model is the k-ζ-f model proposed in [36], which is the further development of the k-$\overline{v^2}$-f model derived by Durbin [37]. This k-$\overline{v^2}$-f model enhances the classic isotropic k-ϵ model [38] by introducing an additional transported variable, the wall-normal velocity scale ($\overline{v^2}$), which is sensitive to the wall-blocking effect and imposes the correct (anisotropic)

kinematic boundary condition on the normal component of the turbulent intensity in near-wall regions of turbulent shear flows via an elliptic relaxation function (f). Hanjalić et al. proposed in [36] to solve not for the velocity scale but rather alternatively for the velocity scale ratio ($\zeta = \overline{v^2}/k$), thus delivering a numerically more robust and efficient model.

The constants for the KH-RT [26] spray breakup model within the RANS setup were set to $B_0 = 0.61$ and $B_1 = 10$. Liquid spray evaporation is modeled with the method of Brenn et al. [39], which accounts for the multiple oxymethylene ether components of the OME fuel.

Table 4. Summary of simulation setup.

Liquid Spray Models	**RANS**	**LES**
Injection type	Blob [40]	
Breakup (KH-RT [26])	$B_0 = 0.61$, $B_1 = 10$	$B_0 = 0.6$, $B_1 = 7$
Turbulent dispersion	O'Rourke [41,42]	
Evaporation	Brenn et al. [39]	Frossling [42] including corrected distortion [31]
Drag Law	Schiller-Naumann [43]	Liu et al. [44] with corrected distortion [31]
Gaseous phase models	**RANS**	**LES**
Maximum cell count	966,000	≈60 million
Minimum grid size	125 µm	62.5 µm
Turbulence modeling	k-ζ-f model [36]	One-equation Dynamic Structure LES model [45]

3. Results and Discussion

LES and RANS calculations adhere to the ECN modeling standards [14] to determine ignition delay and flame lift-off length. Ignition is calculated by identifying the time of the maximum gradient in temperature. The flame lift-off is set to be the axial location closest to the nozzle at which the *OH* mass fraction reaches 14% of its maximum in the computational domain. In the experiments, ignition and flame lift-off length are measured based on *OH** chemiluminescence following a similar procedure to that described in [24]. To summarize, lift-off length is measured using the time-averaged quasi-steady chemiluminescence intensity field to obtain two lobes of high intensity at the top and bottom of the jet near the lift-off length. The ECN defines the lift-off length as the average axial distance between the injector and the first axial locations of the two lobes with an intensity greater than 50%, compared to the leveling-off value. The onset of ignition is measured as the first frame, where 10 pixels reach this same 50% threshold. Additionally, the pressure-based ignition delay was detected by the start of the rapid pressure rise caused by high-temperature ignition.

Figure 3 compares the results for LES, RANS, and experiments for high-temperature ignition delay (ID) and flame lift-off length (LOL) for both operating points. It can be seen that the simulations reproduce the experimental data well in general. However, the LES seems to overestimate the lift-off for n-dodecane in the case of 1200 K ambient temperature and slightly underestimate the lift-off length for OME for 900 K ambient temperature. Remarkably, LES and RANS predict an identical ignition delay for n-dodecane in the case of 900 K ambient temperature, namely 340 µs, which is valuable for being able to compare the transition from the cool-flame to high-temperature combustion for both turbulence modeling approaches.

At first, the influence of the ambient temperature on the high-temperature flame morphology for both fuels will be discussed in Section 3.1. A detailed analysis of the spatial distribution of the measured and simulated hot-flame shapes for 900 K and 1200 K is presented.

Finally, the transient development of the cool flame with a focus on the different combustion stages for n-dodecane and OME is described in Section 3.2.

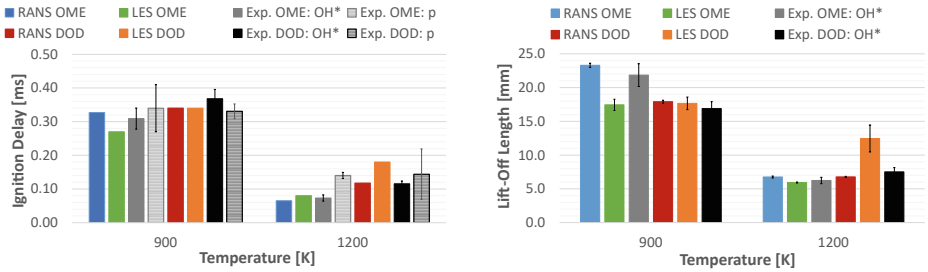

(**a**) Ignition delay. (**b**) Lift-off length.

Figure 3. Simulated versus experimental ignition delay and lift-off length. *OH** describes experimental data based on *OH** chemiluminescence and *p* denotes pressure-based determination of the ignition delay.

3.1. Influence of Ambient Temperature on Hot-Flame Morphology

To interpret the transient evolution of the low- and high-temperature flame in a compact manner, spatiotemporal plots in the form $I_{xt} = \int_{y_{min}}^{y_{max}} c_{CH_2O}(x, y, t)dy$ are shown in Figure 4, with c_{CH_2O} referencing either the measured PLIF intensity or the simulated CH_2O molar concentration, x the axial location, and y the cross-stream radial coordinate. Additionally, *OH** intensity and *OH* molar concentration are plotted into the contour, with the respective intensity and concentration present at the flame lift-off length. The *OH* species was chosen as a simulation reference to the *OH** chemiluminescence experiments because the used OME reaction mechanism does not contain an excited *OH** species. The *OH** chemiluminescence experiments are line-of-sight *OH**. For LES and RANS, the *OH* species mass fractions were first integrated in the normal direction to the visualized plane and then projected onto it. This ensures an accurate comparison.

The most significant difference between the fuels is the complete absence of polycyclic aromatic hydrocarbons (PAHs) for OME, which form for n-dodecane separated in space and time from the detected formaldehyde for $t_{aSOI} \geq 520$ µs and $x > 30$ mm in the case of a 900 K ambient temperature (Figure 4a). Hereby, the normalization of the measured intensity was rendered with the maximum value PLIF intensity before the onset of PAH formation. According to Sim et al. [22], several key PAH molecules are excited by the used 355 nm of the PLIF diagnostic. The main difference between turbulence modeling approaches is that the RANS calculations show a steady distribution of CH_2O in time. The LES is characterized by the cyclic rise and fall of CH_2O concentration as the injection progresses. It is also visible that these oscillations of the LES lead to the formation of CH_2O far upstream compared to the RANS calculations for both fuels. The contours of the cool and hot flame in axial space and time are well represented by both simulations, with the LES showing a slightly better match, at least for the 900 K ambient temperature.

For all realizations, CH_2O is formed after the first ignition stage and then accumulates to its maximum concentration before being consumed by the high-temperature flame. At 900 K ambient temperature, Figure 4a, CH_2O forms well upstream of the lift-off length and shows a significantly high concentration of CH_2O at the location of flame stabilization. This confirms for OME the previous findings for n-dodecane in [24] that CH_2O promotes ignition and helps stabilize the high-temperature flame at the 900 K operating point.

In the case of 1200 K, Figure 4b, the spatial sequence of CH_2O formation and consumption is more challenging to interpret. Experimentally, two factors are affecting the results. For n-dodecane, the formation of PAHs occurs from approximately $t_{aSOI} \geq 160$ µs onwards, which is very soon after the initial formation of CH_2O. Only a small temporal window separates the region of increased PAH yield with the measurement of actual CH_2O intensity. This separation is even absent when considering the axial distance. Starting at $x \geq 13$ mm downstream of the nozzle, PAHs form for n-dodecane. Secondly, the PLIF measurements can only detect signals downstream of the liquid length. The thresholds for the PLIF experiments were set up to a fixed number of 35 counts for all experiments

except for the case of 1200 K ambient temperature (OP2) and using OME as fuel. In that case, only five frame counts were set as thresholds. As the liquid phase of OME penetrates further into the combustion chamber than n-dodecane, as shown in [17], part of the CH_2O formation when using OME as fuel at the 1200 K operating point cannot be captured experimentally. For both fuels, the flame stabilization in Figure 4b occurs upstream of the maximum concentration of CH_2O, which differs from the 900 K case. The periodic oscillations of CH_2O formation and consumption are also present for the LES in the case of 1200 K ambient temperature.

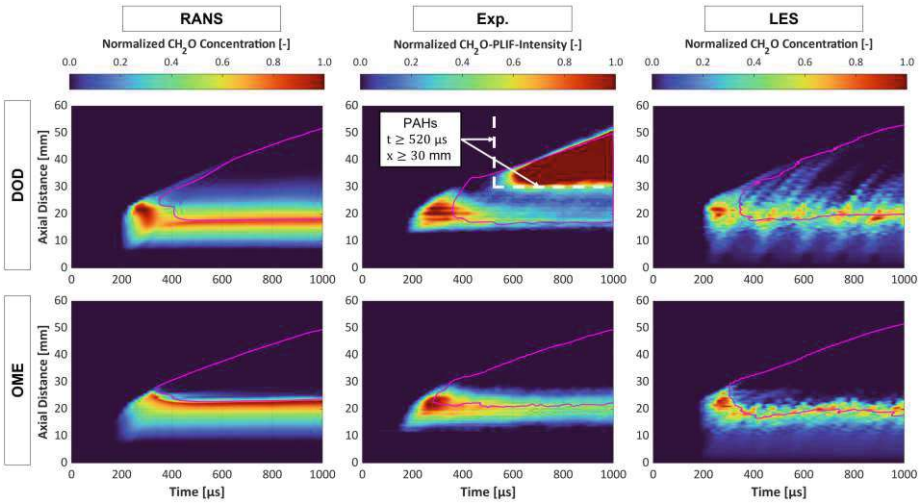

(**a**) OP1: 900 K

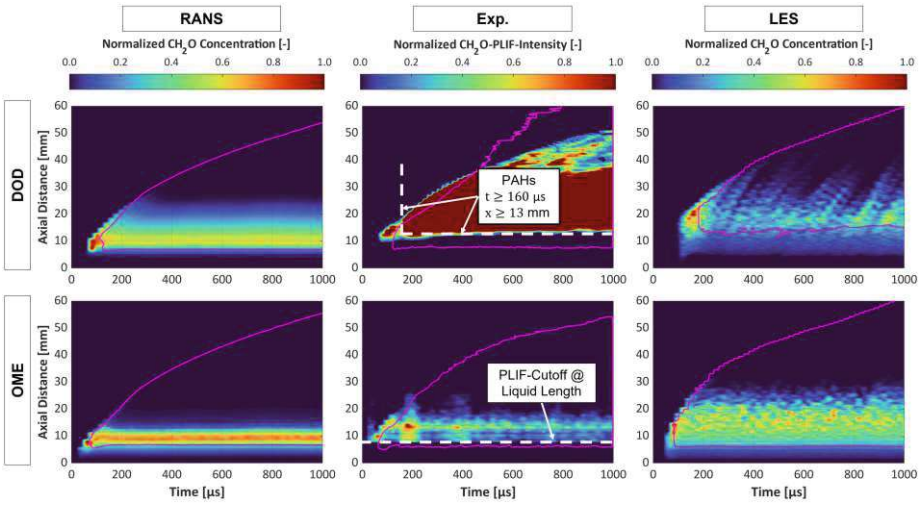

(**b**) OP2: 1200 K

Figure 4. Ensemble-averaged I_{xt} plot of CH_2O PLIF intensity (experiment) and molar concentration (simulations) in a slice cutting through the injector center. The magenta iso-lines indicate the line-of-sight OH^* and simulated projected OH molar concentration at the flame lift-off length.

After analyzing the global combustion behavior for both fuels and operating points, the spatial distribution of the high-temperature flame morphology will be discussed in detail. The results in Figures 5 and 6 are line-of-sight with the LES and RANS results showing projected OH species mass fractions.

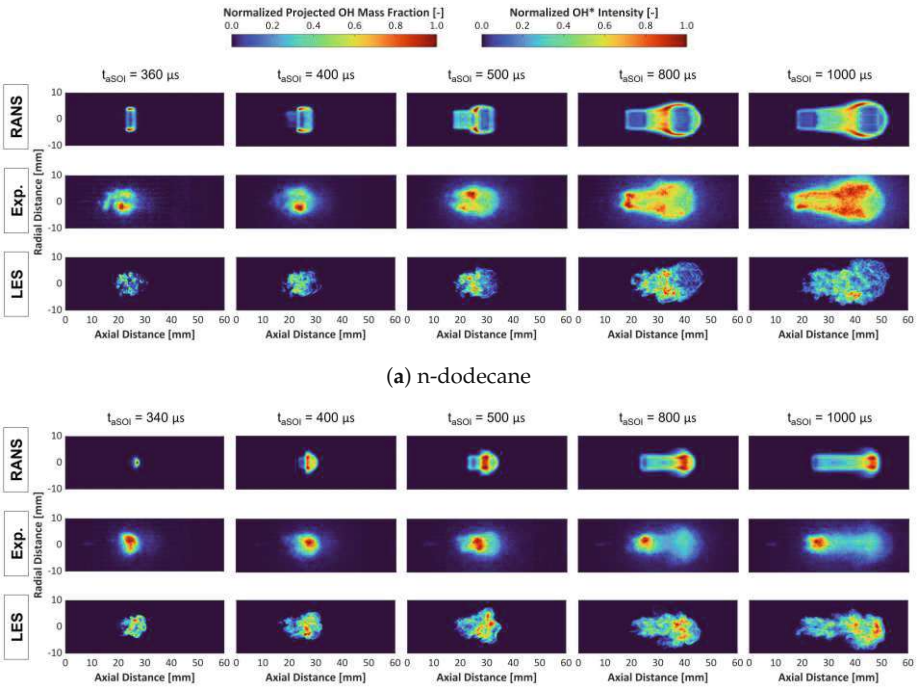

(**a**) n-dodecane

(**b**) OME

Figure 5. Time evolution of projected *OH* species mass fraction distribution for simulations and line-of-sight *OH** chemiluminescence intensity for experiments at 900 K ambient temperature (OP1).

The comparison between the two fuels for OP1 (900 K) in Figure 5 demonstrates significant differences in the spatial distribution of the high-temperature reaction zone, already observed in [17,18]. For n-dodecane (Figure 5a), the highest intensity is measured and simulated in the shear layer of spray and ambient air, which are also the locations of the first ignition kernels. As the flame propagates downstream, the high-intensity region stretches with it along the length of the spray. For OME (Figure 5b), the kernel of the ignition is at the tip of the spray in the center of the symmetry plane. The fuel-rich center of the spray remains the high-intensity region for the entire high-temperature combustion. Both simulations differ from the experiments in that the simulated peak of the *OH* species concentration travels with the flame downstream of the lift-off length. The experimentally observed peak of the excited *OH** radical maintains its position near the flame lift-off length. The overall contour is well represented by both simulations, with the LES being able to reproduce the high intensity in the spray center better than the RANS calculations.

The observation for the 1200 K operating point (OP2) in Figure 6 differs substantially from the 900 K case for OME. Now, the measured peak intensity location travels downstream in line with the simulation results instead of maintaining a high intensity near the lift-off length. Whereas the n-dodecane flame shape is similar to the 900 K case in forming high concentrations of *OH*/OH* in the shear boundary layer between spray and ambient air, the analysis for OME shows that only its tendency to form high *OH*/OH* concentrations in the spray center axis is also visible in the 1200 K case. The difference in the axial position of the peak intensity for OME when increasing the ambient temperature might be due to the decreased mixing time before high-temperature ignition. At 1200 K, the shortened ignition delay might cause fewer oxygen radicals to be present close to the flame lift-off length, which would generate a lower relative *OH** concentration.

The simulations' overall development and flame contour agree well with the experiments. The RANS calculations especially accurately replicate the radial and axial locations of the high intensity in the *OH** chemiluminescence experiments.

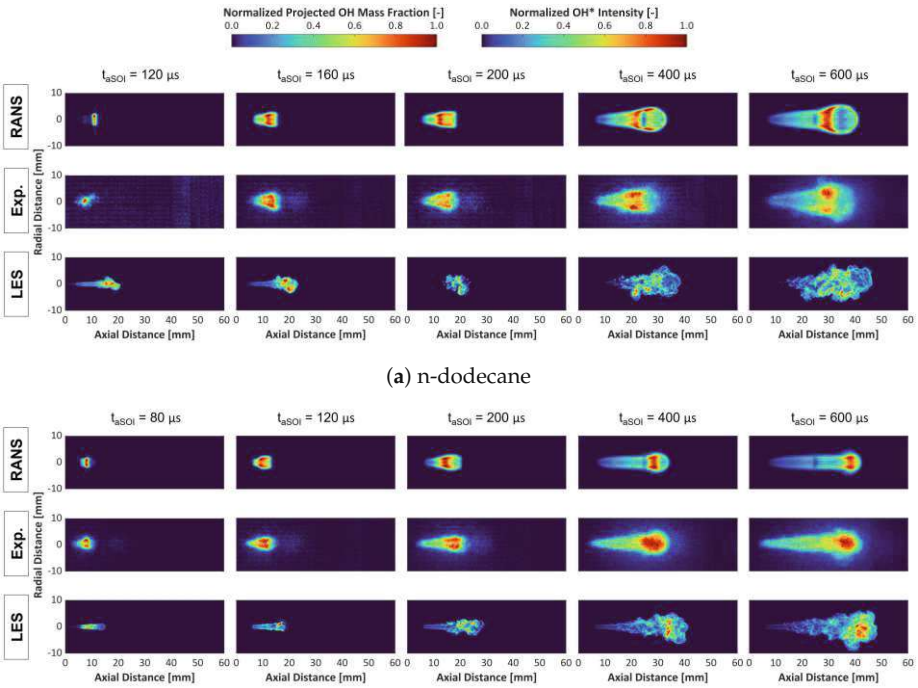

(**a**) n-dodecane

(**b**) OME

Figure 6. Time evolution of projected *OH* species mass fraction distribution for simulations and line-of-sight *OH** chemiluminescence intensity for experiments at 1200 K ambient temperature (OP2).

The experiments and simulations were averaged in time using the identical time window once a stable lift-off length was established for a more meaningful comparison of the low- and high-temperature species distribution. To analyze the high-temperature zones, the experimentally recorded *OH** line-of-sight data were deconvoluted using an inverse Radon transform to represent their distribution in the symmetry plane for the quasi-steady period. Table 5 shows the different averaging windows by fuel and operating point. In Figure 4, the quasi-steady period for the flame lift-off starting at approximately $t_{aSOI} > 500$ µs for each case indicates the timing for averaging the results for both fuels after establishing a stable flame lift-off.

As all contour plots were normalized by their respective maximum value for a better comparison between RANS and LES, the maximum simulated values for the concentrations of CH_2O and OH in the injector symmetry plane are listed in Table 6.

The influence of the ambient temperature on the time-averaged results for both fuels will be discussed in the following.

Figure 7 delivers a comprehensive comparison between simulations and experiments, n-dodecane and OME, as well as low- and high-temperature combustion for OP1 at 900 K ambient temperature. The contour plots show mean and normalized values, which were temporally averaged according to Table 5. At the top, Figure 7a displays the mean contour of the low-temperature steady-state combustion characterized by the distribution of formaldehyde in the spray symmetry plane. As indicated in the figure, the PLIF intensity for n-dodecane was only evaluated until an axial position of 30 mm downstream of the nozzle. Increased formation of PAHs was only detected for distances further downstream than that for 900 K ambient temperature, as seen in Figure 4a.

Table 5. Averaging periods for different experimental techniques and fuels.

Experiment	Temperature [K]	DOD Averaging Window [ms]	OME Averaging Window [ms]
*OH** Chemiluminescence	900	0.8–1.6	0.6–1.5
	1200	0.8–1.5	0.6–1.6
CH_2O PLIF	900	0.8–1.6	0.6–1.5
	1200	0.8–1.5	0.6–1.6

Table 6. Maximum simulated concentrations in symmetry plane.

Simulation	Temperature [K]	Max. CH_2O Concentration [mol/L]	Max. OH Concentration [mol/L]
RANS-DOD	900	1.37×10^{-2}	2.05×10^{-3}
RANS-OME		1.72×10^{-2}	1.65×10^{-3}
LES-DOD		2.18×10^{-2}	8.29×10^{-4}
LES-OME		2.56×10^{-2}	9.90×10^{-4}
RANS-DOD	1200	2.53×10^{-2}	2.62×10^{-3}
RANS-OME		3.29×10^{-2}	2.51×10^{-3}
LES-DOD		2.09×10^{-2}	1.36×10^{-3}
LES-OME		3.04×10^{-2}	2.34×10^{-3}

The peak in PLIF intensity and simulated CH_2O concentration can be located at approximately 20 mm in the center of the spray for both fuels. OME tends to concentrate its CH_2O formation a few millimeters further downstream. For the simulations, the zone of high-temperature combustion is shown with magenta iso-lines indicating a temperature of 1600 K, which, according to Idicheria and Pickett [46], serves as the best reference for marking the threshold of the destruction of CH_2O and the regime of high-temperature (OH*) reactions. This observation is confirmed when analyzing Figure 7a, and later on in Figure 13 within Section 3.2, as for both fuels no significant amount of CH_2O enters the high-temperature zone. Additionally, fuel-rich regions in Figure 7 satisfying the criterion of $\phi = 2$ are shown with white iso-lines. Hereby, the equivalence ratio (ϕ) is defined as a passive scalar independent of the reaction state. For oxygenated fuels, such as OME, this definition has to be adapted by the chemically bound oxygen within the fuel structure following the conclusions of Mueller [47]. The existence of chemically bound oxygen causes the traditional definition of the equivalence ratio (ϕ) to incorrectly calculate the distance of a reactant mixture from its stoichiometric condition. Hence, the appropriate passive scalar mixing parameter for oxygenated fuels is the *oxygen equivalence ratio* (ϕ_Ω).

The differences between the two fuels are apparent when comparing the simulations. n-Dodecane fuel-rich zones penetrate the high-temperature regions for RANS and LES. For OME, the peak CH_2O concentration forms a distinct frontier separating the fuel-rich zone from the high-temperature flame. The clear spatial separation of the cool flame (CH_2O formation) and high-temperature (OH) reactions for OME at 900 K ambient temperature was also observed by simultaneous PLIF planar measurements of CH_2O and OH in [20] for an older generation of the Spray A injector.

When observing the high-temperature combustion, Figure 7b, the center region into which the n-dodecane-rich mixture ($\phi = 2$) penetrates is characterized by low OH* intensity for the experiment and even lower OH concentration for the simulations. The lean OME spray, with its separated cool and hot flame, shows a very different flame morphology in the spray center plane. In the experiments especially, the OH* intensity peaks only a few millimeters downstream of the lift-off length and remains elevated at the spray axis. Neither simulation can fully reproduce the stark contrast to n-dodecane in the high-temperature flame morphology. Notably, the simulations do not show the high-intensity blob shortly after the flame lift-off. The LES seems to be more capable in that regard, as it yields a higher OH concentration along the spray axis compared to RANS calculations.

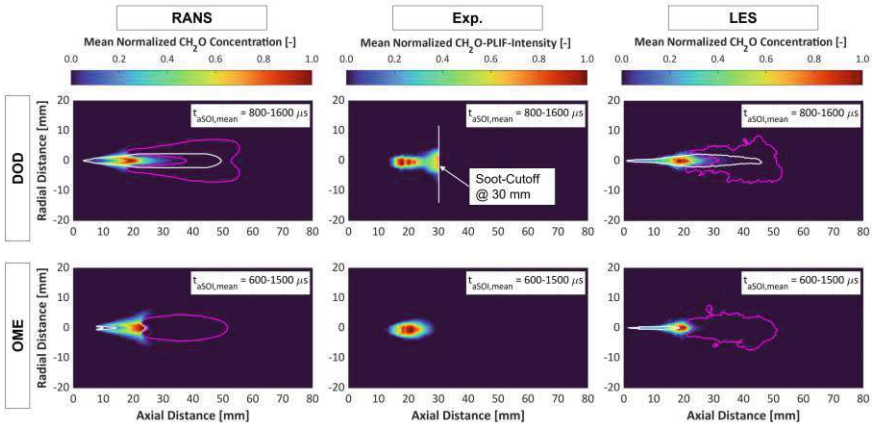

(**a**) Mean formaldehyde (CH_2O) distribution.

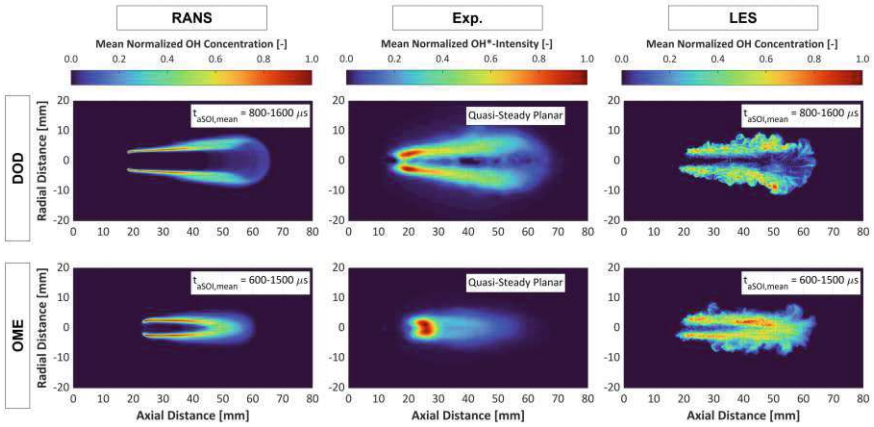

(**b**) Mean hydroxyl (OH^*/OH) distribution.

Figure 7. Time-averaged planar distribution of simulated OH (**bottom**) and CH_2O (**top**) concentration and experimental intensity for ambient conditions of 900 K and 15% oxygen content (OP1) in the spray symmetry plane.

It must be pointed out that differences are expected when comparing simulated *OH* concentration to measured *OH** chemiluminescence intensity. Maes et al. [48] investigated the flame structure differences of excited *OH** chemiluminescence and ground state *OH* PLIF. The flame structure differed depending on the measurement technique, with *OH** found further upstream than *OH* and the latter extending to a greater radial distance from the spray centerline. It was concluded that *OH* is more stable and in partial equilibrium with the water vapor produced during combustion. *OH**, on the other hand, is instead a reaction zone product for which spontaneous emission rates determine the lifetime.

These observations explain the discrepancies between experiment and simulations, seen in Figure 7b, to some extent, but not sufficiently. The differences between simulations and experiments concerning the high-temperature flame shape seem significantly greater for OME than for n-dodecane. Even the computationally expensive LES calculations cannot fully capture the flame morphology of OME reliably for the presented ambient conditions of 900 K.

The interpretation of the differences between simulations and experiments and between n-dodecane and OME slightly changes when studying the time-averaged contour maps with 1200 K ambient temperature in Figure 8. As seen with the transient *OH*/OH* plots for OME in Figure 6b, the time-averaged experimental results at 1200 K in Figure 8b show an entirely different *OH** distribution compared to its 900 K counterpart. The peak

intensity is close to the flame lift-off length and the spray tip. The spray center axis displays an elevated OH^* concentration. Still, high levels are also seen a few millimeters away from the centerline in what appears to be the boundary shear layer of OME fuel spray and ambient air. Interestingly, n-dodecane also shows some differences at 1200 K in its high-temperature flame shape. The peak of its mean distribution is now further upstream along the shear boundary of spray and air and not near the lift-off length as seen in Figure 7b at 900 K ambient temperature. The 1200 K simulations match the experiments more accurately than in the 900 K case, especially for OME.

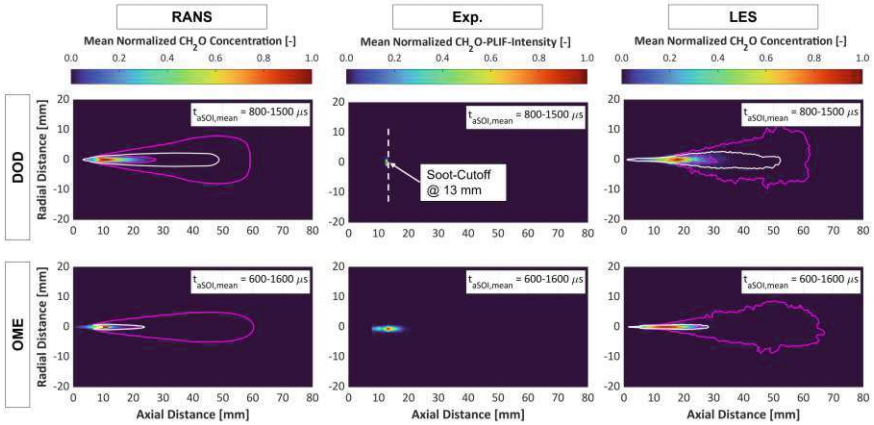

(**a**) Mean formaldehyde (CH_2O) distribution.

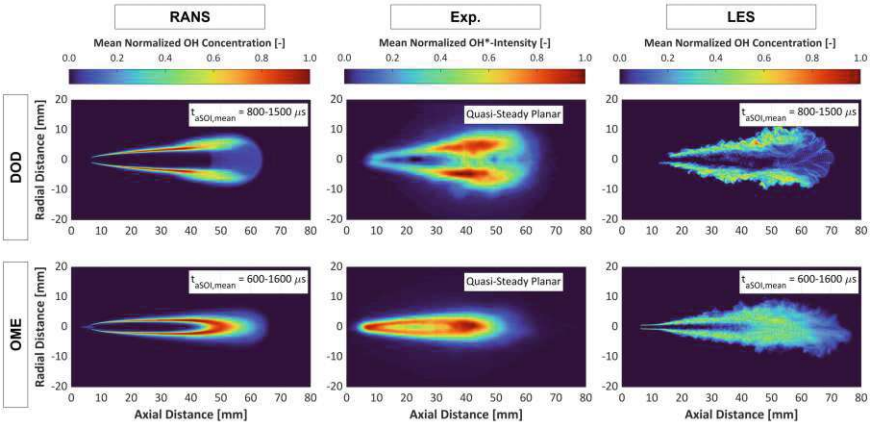

(**b**) Mean hydroxyl (OH^*/OH) distribution.

Figure 8. Time-averaged distribution of simulated OH (**bottom**) and CH_2O (**top**) concentration and experimental intensity for ambient conditions of 1200 K and 15 % oxygen content (OP2).

The results for the mean cool-flame shape are displayed in Figure 8a. As is indicated in the I_{xt} plots of Figure 4b, the PLIF measurements for n-dodecane are impaired by the presence of PAHs, which are entirely absent for OME. The soot cutoff axial position shown in Figure 8a virtually denies an adequate assessment of the time-averaged cool-flame distribution for n-dodecane. When comparing RANS and LES at 1200 K for n-dodecane, it is noticeable that the LES predicts an CH_2O distribution that penetrates further into the combustion chamber compared to RANS, which also pushes the high-temperature zone (magenta iso-line) further downstream. The same observation is made for OME. Here, because of the absence of PAH concentration, it is discernable that the RANS calculation delivers results closer to predicting the measurements.

The clear axial separation of the cool and hot OME spray flame is not present at 1200 K. Fuel-rich spray ($\phi = 2$, white iso-lines) penetrates along the centerline and forms CH_2O

with the high-temperature zone already present in short radial distance to it. However, the fuel-rich spray enters the area of $T \geq 1600$ K only very marginally, especially compared to n-dodecane.

For a more detailed analysis of the spatial high-temperature flame distribution, radial profiles are drawn at axial positions, starting a few millimeters downstream of the lift-off length, into the time-averaged contours. Figure 9 shows the normalized *OH* and *OH** profiles for simulations and experiments at 900 K ambient temperature, respectively. The differences between n-dodecane and OME become visible once again, with OME not displaying any drop in its *OH** intensity at the center of the spray.

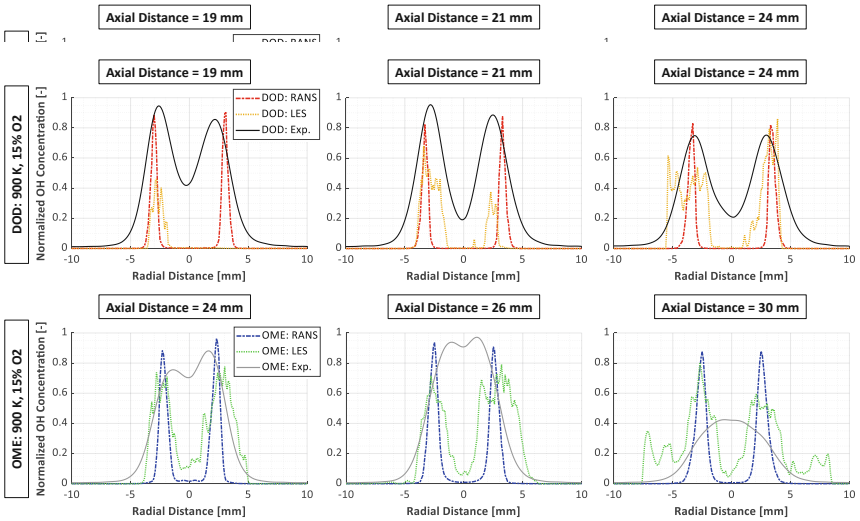

(**b**) OME

Figure 9. OH radial profiles for time-averaged contours at different axial positions at 900 K ambient temperature (OP1).

The simulations are able to predict the peak intensity location for n-dodecane with good agreement to the experiments, with the LES showing a radially wider distribution of high *OH* concentration peaks stretching further away from the shear layer of fuel and ambient air. For n-dodecane, a reduction in the *OH** intensity in the center is measured, which falls to approximately 20% of its peak intensity 24 mm downstream of the nozzle and several millimeters downstream of the lift-off length. The fact that the *OH** profile does not entirely subside to zero in the center for the experiments with n-dodecane cannot be reproduced by either simulation.

This behavior is even more pronounced for OME, where the respective experimentally observed peak intensity is right in the center axis of the spray. The RANS simulations again show sharp concentration peaks roughly one millimeter closer to the center axis than the respective RANS n-dodecane calculation. The LES shows slightly more evenly distributed profiles, which have an elevated *OH* concentration in the center, albeit not enough to align with the experiments.

When considering the 1200 K operating point in Figure 10, it can be seen that for n-dodecane, the *OH** intensity does not drop at all the further downstream the radial profiles are extracted (Figure 10a). It instead increases, which is reflected by the LES calculation. The peak intensity can be found at $x = 40$ mm, with both simulations predicting the radial position of the peak intensity correctly. The RANS calculation cannot replicate the increase in *OH* concentration and only shows a widening of the radial profiles. Both simulations cannot reproduce the level of *OH** intensity in the spray center, similar to the 900 K ambient conditions.

The radial profiles for OME at 1200 K, Figure 10b, show a distinct difference from their 900 K counterparts. A few millimeters downstream of the lift-off length, the typical peak *OH** intensity in the spray center axis is measured. However, further downstream at $x = 20$ mm, a drop in intensity in the spray center is visible, producing a similar radial profile shape compared to n-dodecane, with higher relative values for *OH** intensity. At the flame tip, the intensity peaks again at the center, which the simulations can partly capture, showing elevated *OH* concentrations on the spray center axis at $x = 45$ mm downstream of the nozzle.

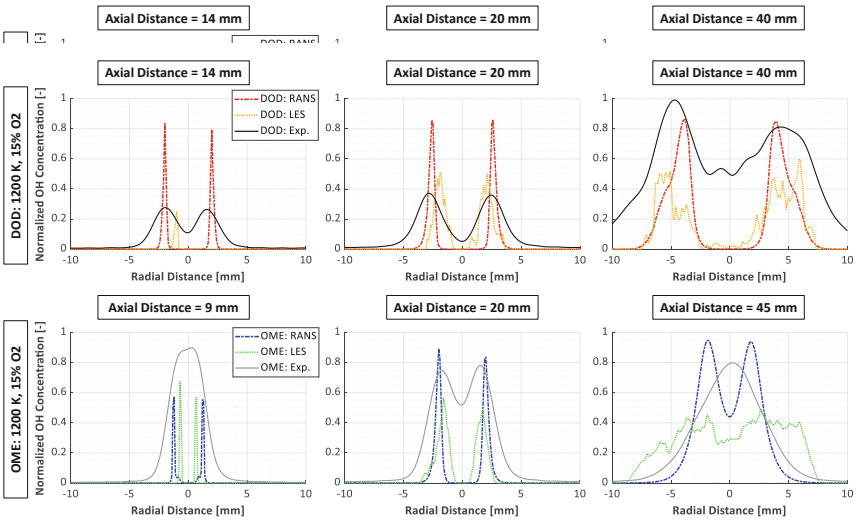

(**b**) OME

Figure 10. OH radial profiles for time-averaged contours at different axial positions at 1200 K ambient temperature (OP2).

The following analysis aims at depicting the spatial transition of cool (CH_2O) to hot flame *OH*/OH* for the two studied ambient temperatures and fuels with Figure 11, where the transition from cool- to high-temperature flame along the spray centerline is depicted for the time-averaged results of the measurements and simulations.

At 900 K, OME decreases its *OH** intensity level faster than n-dodecane the greater the distance downstream of the lift-off length. This sharp drop in high-temperature reaction activity can also be noticed in Figure 11b. In contrast to n-dodecane, Figure 11a, the maximum *OH** intensity for OME drops from approximately 90% to below 25% within only 5 mm along the centerline.

Another important aspect is the location of the first rise of *OH** intensity compared to the location of maximum CH_2O formation. For n-dodecane at 900 K, the measured peak *OH** intensity in Figure 11a falls precisely within the space of elevated and peak CH_2O PLIF intensity. The simulations capture the formation and conversion of CH_2O in the center of the spray very well. However, the transition to *OH* is less accurate due to the already shown lack of simulated *OH* species concentration in the spray center.

In the case of OME fuel, a clear shift of the maximum *OH** intensity further downstream relative to the maximum CH_2O PLIF intensity is visible in Figure 11b. The peak of *OH** intensity now occurs at an axial location of approximately 26 mm where all CH_2O is already destroyed, leading to a clear separation of the cool flame and the zone of high-temperature combustion. The RANS calculations slightly overestimate the axial distance of maximum CH_2O formation, which the LES predicted with higher accuracy. The underestimation of the *OH* reaction activity in the spray center is also responsible for the late rise in *OH* concentration in both simulations.

Energies **2024**, *17*, 2265 17 of 26

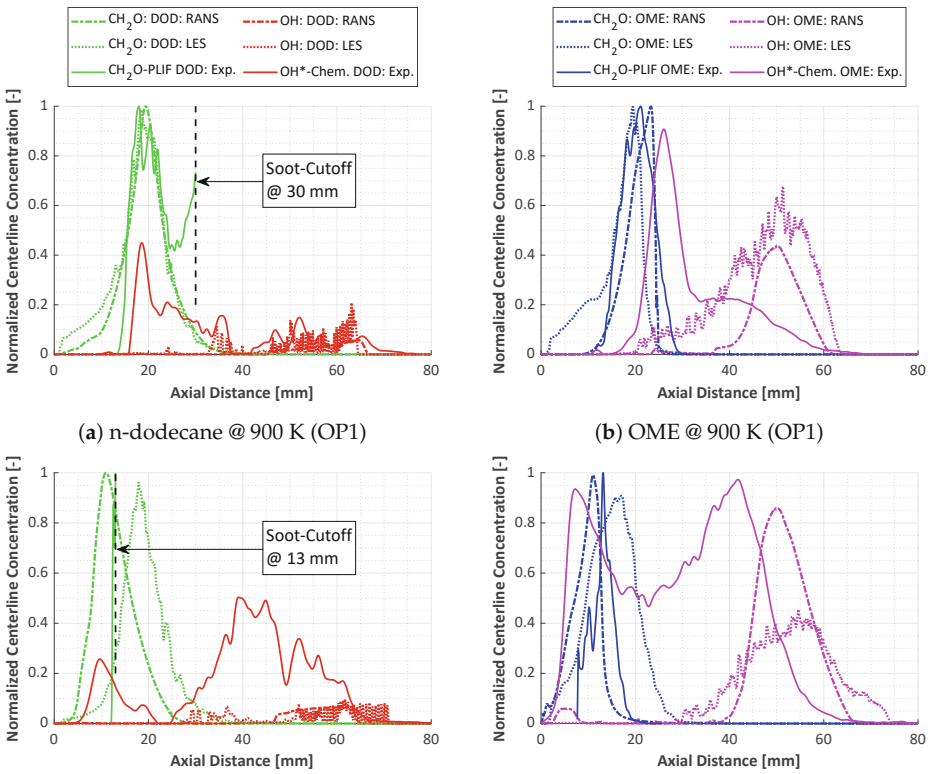

(**a**) n-dodecane @ 900 K (OP1)

(**b**) OME @ 900 K (OP1)

(**c**) n-dodecane @ 1200 K (OP2)

(**d**) OME @ 1200 K (OP2)

Figure 11. CH_2O and OH profiles at the center axis of spray for time-averaged contours.

By increasing the combustion chamber temperature to 1200 K, the OH^* chemiluminescence experiments show two peaks in intensity for both fuels, one close to the lift-off length and one further downstream. For n-dodecane, Figure 11c, the first peak of OH^* intensity at approximately $x = 9$ mm occurs even before any CH_2O PLIF signal is detected. The same observation is valid for OME in Figure 11d, with the maximum of OH^* intensity appearing before the maximum of CH_2O, and the second one at the end of the flame at approximately $x = 42$ mm. However, it must be noted that the PLIF measurements cannot detect any signal where liquid fuel is present. Hence, the axial location of CH_2O maximum PLIF intensity cannot be determined with certainty for both fuels in 1200 K hot ambient temperature. For OME, though, the centerline profile strongly suggests that the maximum of CH_2O intensity does not form upstream of the PLIF starting threshold of $x = 8$ mm. For n-dodecane, between soot cutoff and PLIF threshold, the first rise and onset of CH_2O are very challenging to discern, with only a few millimeters of actual CH_2O signal detectable.

The LES at 1200 K pushes its CH_2O maximum further downstream compared to RANS, and there seems to be a smooth transition from consumed CH_2O to forming of OH, especially for OME. The RANS calculation for OME in Figure 11d shows a slight increase in OH concentration at the exact location of the first axially measured OH^* intensity peak. It also predicts a comparable, and higher in comparison to the 900 K case, level of OH concentration only slightly downstream of the second OH^* intensity peak. The LES cannot replicate the changed hot-flame morphology for this case and shows a similar profile compared to 900 K ambient temperature.

In general, RANS and LES struggle to reproduce the high level of high-temperature reactions in the spray center close to the lift-off length of the flame for both fuels and ambient temperatures, especially for OME.

3.2. Cool-Flame Evolution

Tagliante et al. identified in [24] several distinct stages for the combustion of n-dodecane using the same injector at 900 K ambient temperature to characterize the transition from cool flame to high-temperature combustion. Figure 12 displays the different ignition stages using the spatially averaged but transient profiles of planar formaldehyde (CH_2O) and line-of-sight *OH*/OH* for n-dodecane (Figure 12a) and OME (Figure 12b) at 900 K ambient temperature. Because of the rapidness of the combustion process, the PLIF signal axial thresholds and early formation of PAHs in case of 1200 K, see Figure 4b, the cool-flame transient development and subsequent combustion stages will be discussed in detail for the 900 K case only.

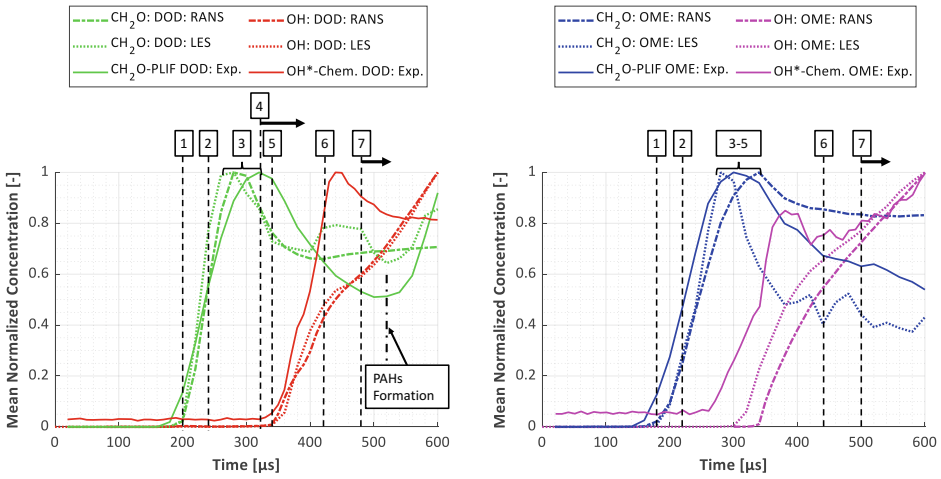

(**a**) n-dodecane (**b**) OME

Figure 12. Time- resolved and spatially averaged evolution of planar CH_2O and line-of-sight *OH/OH** profiles with indicated combustion stages at 900 K ambient temperature (OP1).

In general, seven stages can be distinguished in Figure 12: (1) first stage of ignition, (2) cool flame (low-temperature) propagation, (3) maximum CH_2O, (4) CH_2O consumption, (5) second stage ignition, (6) turbulent high-temperature flame propagation, and (7) quasi-steady combustion. Depending on the fuel characteristics and ambient conditions, these stages occur at different time intervals, which may overlap. For n-dodecane in Figure 12a, it is indicated that stages are quite distinct from each other when considering that the ignition delay, signaling the combustion stage (5), of the simulations is $ID_{DOD,RANS,LES} = 340$ µs and that of the experiments ranges from $ID_{DOD,EXP} = 331 - 368$ µs.

For OME in Figure 12b, the analysis is more complex, as the measured ignition delay time ranges from $ID_{OME,EXP} = 309 - 340$ µs. The LESs predict an ID of $ID_{OME,LES} = 270$ µs, whereas the RANS calculations pinpoint the largest temperature gradient at $ID_{OME,RANS} = 327$ µs. It is therefore challenging to differentiate between the stages (3), (4), and (5) for OME in simulations and experiments, as the second stage ignition, i.e., ignition delay, occurs almost simultaneously with the maximum yield of CH_2O and its subsequent consumption. OME tends to pass through the initial stages of combustion earlier than n-dodecane, with both simulations somewhat overpredicting the delay of the first ignition stage for both fuels. The LES shows a steeper accumulation curve of CH_2O compared to RANS, which is more pronounced for OME. The consumption of CH_2O (stage 4) in the case of n-dodecane is quite similar for LES and RANS and only shifted compared to the measurements. For OME, this combustion stage deviates significantly for LES and RANS, leading to a difference in ignition delay prediction of more than 50 µs. The consumption of the CH_2O concentration after its maximum was reached is more rapid for the LES and seems too fast compared to the experiment.

The quasi-steady combustion for n-dodecane is characterized by increased measured PLIF intensity after $t_{aSOI} > 520$ µs. This uptake is due to the formation of PAHs.

The spatial distribution of the temporal development of the cool flame and the onset of the high-temperature reactions, referring to the combustion stages shown in Figure 12, are depicted in Figure 13 for the 900 K ambient temperature (OP1). The planar contour plots show the PLIF intensity for the experiment and molar concentration for the simulations. The intensity and concentration were normalized to accurately compare each time step. For the simulations, the fuel-rich ($\phi = 2$) and high-temperature reaction ($T = 1600$ K) zones are again outlined in white and magenta iso-lines, respectively.

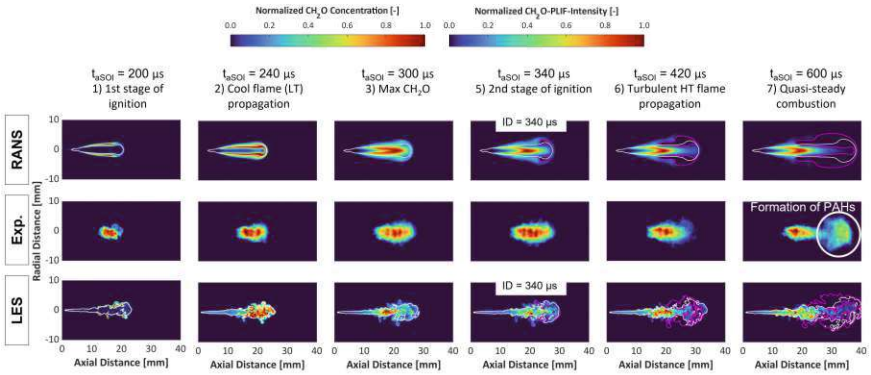

(**a**) n-dodecane

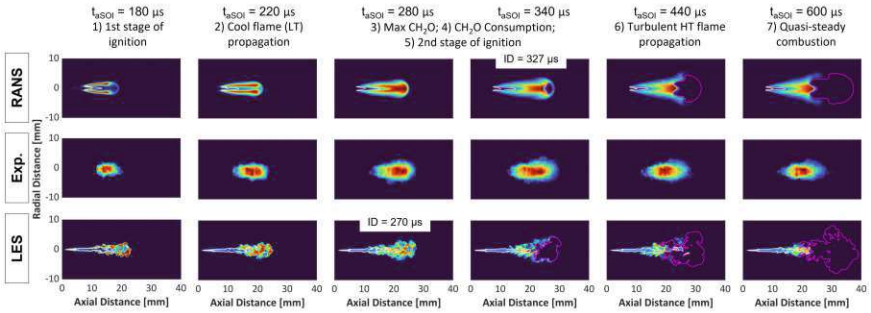

(**b**) OME

Figure 13. Time evolution of CH_2O concentration distribution for simulations and PLIF intensity for experiments in the symmetry plane at 900 K ambient temperature (OP1). The high-temperature zones with $T > 1600$ K are indicated with magenta iso-lines. Fuel-rich regions ($\phi = 2$) are shown with white iso-lines.

In Figure 13a, n-dodecane is simulated by the RANS and LES methods to penetrate with a fuel-rich spray into the high-temperature zone. The first low-temperature ignition kernels (first stage) can be seen at the shear layer of the fuel spray with ambient air, which differs from the experiments, where the initial CH_2O formation appears in the spray center. The simulations correctly predict the location of maximum CH_2O (third stage) in the spray center. The first spots of high-temperature ignition (fifth stage) for n-dodecane are simulated at the spray tip but again in the shear layer between fuel spray and ambient air. At $t_{aSOI} = 600$ µs, during the quasi-steady combustion, it is noticeable that the PLIF experiments start to show elevated concentrations of PAHs at the spray tip precisely at the locations where the RANS and LES methods predict the fuel-rich mixture to enter the high-temperature region. In contrast, Figure 13b visualizes the absence of any fuel-rich spray entering the simulated spray region with $T > 1600$ K for OME. The simulations predict a clear spatial separation of the cool flame (CH_2O formation) and high-temperature

(*OH*) reactions for every time step, as was already observed for the time-averaged plots in Figure 7a.

The first ignition stage appears more accurate for OME simulations, with CH_2O forming closer to the spray center axis. The LES represents both fuels' cool-flame propagation (second stage) well. Both simulations can capture the position of maximum CH_2O. In contrast to n-dodecane, high-temperature ignition locations for OME are spotted at the spray tip instead of at the shear layer between the spray and ambient air.

In general, the locations of CH_2O formation are well captured by LES and RANS calculations, with the experimental intensity and simulated concentration for both fuels peaking at approximately 20 mm downstream of the nozzle.

The last aspect of the present study concerns the initial cool-flame propagation of accumulated CH_2O mass within the mixing space, as well as its periodic formation and destruction during the quasi-steady combustion. Figures 14 and 15 show the simulated CH_2O and *OH* mass binned by equivalence ratios (ϕ) from 0 to 10 for n-dodecane and OME, respectively, for both turbulence models, with a bin size of 0.05. The symbols show the average mass of CH_2O (left y-axis) and *OH* (right y-axis) in each bin, color-coded by temperature. The shaded areas represent the standard deviations, with CH_2O in blue and *OH* in red. The top plots focus on the cool-flame formation and consumption before high-temperature ignition for each fuel and simulation model. The bottom plots show CH_2O and *OH* during quasi-steady combustion.

Tagliante et al. [24] demonstrated an initial *cool-flame wave*, identified by CH_2O and defined in [49], for n-dodecane and LES, as well as its periodic formation/consumption during the quasi-steady phase. This study also calculated this process and it is shown in Figure 14b. The comparison between LES and RANS for n-dodecane and 900 K is particularly interesting as both simulations predict the exact same high-temperature ignition delay of 340 µs; see Figure 3a. The RANS calculations with n-dodecane in Figure 14a also visualize a cool-flame wave, albeit at leaner mixtures and slightly lower temperatures. At 240 µs CH_2O peaks at $\phi = 4.3$ and *OH* at $\phi = 5$ for the LES. For this time step, the RANS model, on the other hand, simulates a peak CH_2O concentration for $\phi = 2.6$. Corresponding to the trend for the LES, the maximum *OH* accumulated mass is found for a slightly richer mixture at $\phi = 2.8$. 40 µs later in the injection process, the LES predicts that the cool flame propagated to leaner mixtures peaking at $\phi = 7$ and starts being consumed at $\phi = 2$. At this point in time, the RANS model simulates the CH_2O mass to peak already at $\phi = 4$. The high-temperature consumption forming *OH* shows two maxima at $\phi = 4.4$ and $\phi = 2.8$, with the leaner value being the mixing region of increased *OH* production, ultimately peaking at stoichiometry. The entire process of the initial cool-flame propagation is limited in temperature for the LES by $T \leq 1400$ K and for RANS by $T \leq 1200$ K.

Within the LES framework, the quasi-steady combustion period for n-dodecane is characterized by the cyclic formation and consumption of CH_2O, as shown at the bottom in Figure 14b. According to [24], this process is most likely caused by gas pressure oscillations generated by the low-temperature combustion. The oscillation frequency qualitatively matched the resonance frequency of the combustion chamber (5.7 kHz) because the length of LES mesh matched the length of the pre-burn chamber. The LES can capture these fluctuations affecting the CH_2O distribution at the jet center, potentially because of its well-resolved turbulent mixing field, which is fine enough to resolve at least 80% of the turbulent kinetic energy. The RANS calculations, however, are not able to resolve these small-scale fluctuations. The turbulent mixing field is too smooth to reproduce the oscillations. No cyclic behavior in the formation and consumption of CH_2O during quasi-steady combustion, at the bottom in Figure 14a, could be observed for the RANS computations.

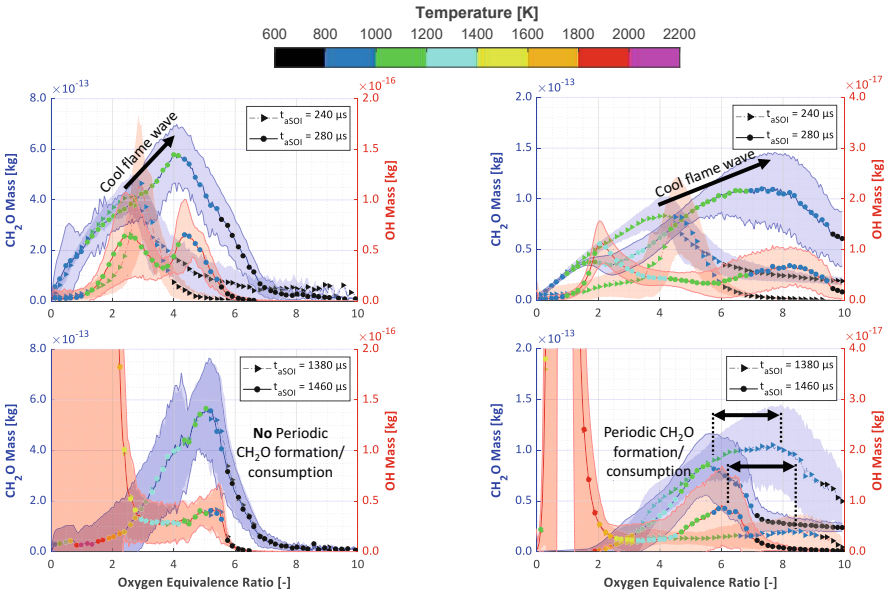

(**a**) RANS: n-dodecane (**b**) LES: n-dodecane

Figure 14. *CH_2O* and *OH* mass binned by equivalence ratio from 0 to 10 for n-dodecane fuel at 900 K ambient temperature (OP1) with a bin size of 0.05. The symbols show the average mass of *CH_2O* (left *y*-axis) and *OH* (right *y*-axis) in each bin sample, colored with its average temperature.

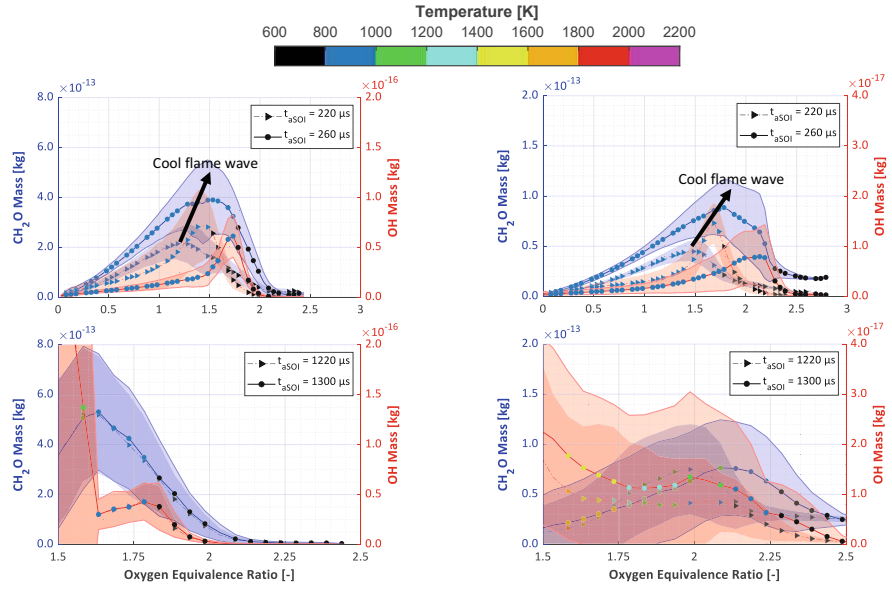

(**a**) RANS: OME (**b**) LES: OME

Figure 15. *CH_2O* and *OH* mass binned by equivalence ratio from 0 to 10 for OME fuel at 900 K ambient temperature (OP1) with a bin size of 0.05. The symbols show the average mass of *CH_2O* (left *y*-axis) and *OH* (right *y*-axis) in each bin sample, colored with its average temperature.

For OME, both LES (Figure 15b) and also RANS (Figure 15a) depict the cool-flame propagation from lean to rich mixtures after the first stage of ignition. In this case, however, the propagation ends at mixtures with $\phi < 3$ and for RANS even $\phi < 2.5$. LES and RANS show a similar initial process, only shifting to smaller equivalence ratio values by 0.3–0.5. Interestingly, the average temperature for each bin does not exceed 1000 K for both

simulations during the cool-flame propagation and is, therefore, significantly cooler than its counterpart for n-dodecane.

Concerning the quasi-steady combustion, it is quite challenging to discern cyclic behavior for OME, even when analyzing LES calculations. The bottom plot in Figure 15b hints at a possible periodic behavior. However, the small range of equivalence ratios in which the entire combustion process occurs complicates the identification of cycles. The RANS calculations, again, show a complete absence of periodic behavior, as the averaging process of the simulations makes it impossible to capture the small-scale oscillations caused by the low-temperature flame forming and consuming CH_2O and transmitted by acoustic pressure waves in the combustion chamber.

4. Summary and Conclusions

This study focused on the influence of high ambient temperature on the cool- and hot-flame morphology, represented by CH_2O and OH^*/OH, for the synthetic e-fuel OME_{3-5} compared to the diesel-like reference fuel n-dodecane. Besides the standard and well-documented ECN Spray A operating point of 900 K, the spray combustion of the two fuels in an ambient temperature of 1200 K was analyzed with PLIF CH_2O and OH^* chemiluminescence experiments, as well as RANS and LES calculations. In addition, the initial cool-flame wave and the periodic formation and consumption during the quasi-steady combustion regime were compared for the two fuels and turbulence modeling methods. The following conclusions were drawn:

- OME forms no visible PAHs or soot signature within the CH_2O PLIF experiments at neither 900 K nor 1200 K. This contrasts with n-dodecane, which shows PAH formation at both temperatures. In the case of 1200 K and n-dodecane, the early onset of PAHs generation after high-temperature ignition and its proximity to the injector nozzle makes it very challenging to differentiate between actual CH_2O signal detection and PAH interference.
- At 900 K, OME shows a distinct separation between the fuel-rich ($\phi = 2$) spray, the cool-flame distribution signaled by CH_2O, and the high-temperature region ($T \geq 1600$ K) of the spray. No fuel-rich spray enters the high-temperature zone, either for LES or RANS. At 1200 K, this clear axial separation does not exist. However, little fuel-rich spray enters the simulated zone with $T \geq 1600$ K. For n-dodecane, the fuel-rich spray is simulated to penetrate the hot-flame region, and PAH formation is experimentally detected at identical locations.
- The spatial cool-flame (CH_2O) distribution and its temporal evolution are predicted by both turbulence modeling techniques with good agreement to the experiments.
- The high-temperature flame distribution shows significant differences between fuels and ambient temperatures. At 900 K, the simulations fail to predict the high OH^* intensity close to the lift-off length, especially for OME, where the signal intensity at the spray tip is only a fraction of its maximum close to the root of the flame. This picture changes significantly for 1200 K, where the peak intensity for OME travels along the spray tip and two distinct OH^* maxima of intensity are detected, which is simulated by both LES and RANS with better agreement compared to the 900 K case. This difference in the axial location of the peak intensity for OME for an increased ambient temperature might be caused by the decreased mixing time before high-temperature ignition, with possibly fewer oxygen radicals present close to the flame lift-off length, generating a lower relative OH^* concentration.
- The LES calculations are better suited to reproduce the higher OH^* intensity for OME in the spray centerline and its radial distribution close to the lift-off length. However, especially for the lower ambient temperature of 900 K, the discrepancies between experimental OH^* and simulated OH species contours are significant. The deviations are less severe but still present for n-dodecane. This indicates a generic problem, which only intensifies for OME.

  An explanation might be that the studied reaction mechanism for OME developed by

Niu et al. [30] does not contain an equivalent excited *OH** species, which is assumed to be less stable with its lifetime limited by spontaneous emission rates and also appears to be present further upstream than the ground state *OH* species [48].
Another possibility, which refers to the differences seen for OME and n-dodecane, is that the current OME mechanism incorrectly models the impact of the chemically bound oxygen, or its release via fuel decomposition, on the high-temperature reactivity in the fuel-rich center of the spray.

- The overall high-temperature flame morphology at 1200 K is well captured by the RANS computations.
- The cool-flame wave of CH_2O formation within different mixing states for n-dodecane, previously shown in [24], was demonstrated for OME too. Both LES and RANS predict an increase in CH_2O mass after the first stage of ignition, which materializes initially at small equivalence ratio values and then propagates to reach its peak at fuel-rich mixtures. The LES predicts this process within a wider range of equivalence ratios. The most significant differences regarding this analysis are shown between the two fuels, with OME barely exceeding values for equivalence ratios of $\phi > 2.5$ and n-dodecane, especially for LES, showing accumulations of CH_2O with $\phi > 10$. Also, the initial cool-flame wave occurs at lower temperatures for OME ($T \leq 1000$ K) compared to n-dodecane ($T \leq 1400$ K).
- The periodic formation and consumption of formaldehyde described in [24] could not be reproduced with RANS calculations. In the case of LES with OME as fuel, oscillations for the formation and subsequent destruction of CH_2O in the mixing space are visible but occur within a very narrow range of equivalence ratios.

Future work in the area of this study should focus on the development of numerical reaction mechanisms for OME, which contain excited *OH** as well as ground state *OH* species, to be able to reference experiments that use either *OH** chemiluminescence or *OH* PLIF.

In addition, the influence of chemically bound oxygen in oxygenated fuels on high-temperature reactions needs further investigation. Currently, fuel-rich regions, like the center of a spray jet, are the primary source of modeling errors when dealing with oxygenated fuels like OME. Identifying the origin of the error, be it incorrect fuel decomposition or inadequate reaction rates of specific reactions, will be the main challenge to improving CFD modeling quality for OME fuel.

Author Contributions: Conceptualization, F.W.; methodology, F.W., T.M.N., F.T., L.M.P., J.M. and T.L.; software, F.W. and T.M.N.; validation, F.W., T.M.N. and J.M.; formal analysis, F.W.; investigation, F.W., T.M.N., F.T., K.W. and J.M.; data curation, F.W., T.M.N. and K.W.; writing—original draft preparation, F.W. and T.M.N.; writing—review and editing, T.L. and K.W.; visualization, F.W.; supervision, T.L., J.M. and L.M.P.; project administration, T.L.; funding acquisition, T.L. All authors have read and agreed to the published version of the manuscript.

Funding: The work at the TU Wien was funded by the *Federal Ministry of Climate Action, Environment, Energy, Mobility, Innovation and Technology* (BMK) through the *Austrian Research Promotion Agency* (FFG), grant number 874418. The research was carried out in the framework of the *collective research networking program* (CORNET) project "eSpray". The experiments performed at Sandia Nat. Labs were supported by the U.S. Department of Energy (DOE) Office of Vehicle Technologies. Sandia is a multi-mission laboratory managed and operated by National Technology and Engineering Solutions of Sandia, LLC., a wholly owned subsidiary of Honeywell International, Inc., for the U.S. Department of Energy's National Nuclear Security Administration under contract DE-NA000352.

Data Availability Statement: The raw data supporting the conclusions of this article will be made available by the authors on request.

Acknowledgments: The authors would like to thank TU Wien Bibliothek for financial support through its Open Access Funding Program. The authors gratefully acknowledge Convergent Science Inc. for their licensing and technical supports. The authors would like to thank Steven Luna for his support this research. The computational results presented in this study have been achieved using

the Vienna Scientific Cluster (VSC) via the funded project No. 71485 and the computational resources sponsored by the Department of Energy's Office of Energy Efficiency and Renewable Energy and located at the National Renewable Energy Laboratory.

Conflicts of Interest: The authors declare that they have no known competing financial interests or personal relationships that could have appeared to influence the work reported in this paper.

Abbreviations

The following abbreviations are used in this manuscript:

AMR	Adaptive Mesh Refinement
ASG	Analytik Service Gesellschaft
B_0,B_1	KH-RT breakup Model Parameters
ECN	Engine Combustion Network
f	Elliptic Relaxation Function in $k-\zeta-f$ Turbulence Model
ID	Ignition Delay
k	Turbulent Kinetic Energy
KH-RT	Kelvin–Helmholtz–Rayleigh–Taylor Breakup Model
LES	Large-Eddy Simulations
LLNL	Lawrence Livermore National Laboratory
LOL	Lift-Off Length
OME/PODE	Polyoxymethylene Dimethyl Ethers
OP1	ECN Spray A standard reacting chamber conditions (900 K, 22.8 kg/m^3, 15% O_2)
OP2	ECN Spray A high-temperature reacting chamber conditions (1200 K, 22.8 kg/m^3, 15% O_2)
p	Pressure
PAH	Polycyclic Aromatic Hydrocarbons
PLIF	Planar Laser-Induced Fluorescence
RANS	Reynolds Averaged Navier–Stokes Equations
SOC	Start of Combustion
SOI	Start of Injection
t	Time
$\overline{v^2}$	Velocity Scale (wall-normal)
x	Distance
ϵ	Turbulent Dissipation Rate
ζ	Velocity Scales Ratio
ρ	Density
ϕ	Equivalence Ratio
ϕ_Ω	Oxygen Equivalence Ratio
Ω	Oxygen Ratio

References

1. Burger, J.; Siegert, M.; Ströfer, E.; Hasse, H. Poly(oxymethylene) dimethyl ethers as components of tailored diesel fuel: Properties, synthesis and purification concepts. *Fuel* **2010**, *89*, 3315–3319. [CrossRef]
2. Pellegrini, L.; Marchionna, M.; Patrini, R.; Beatrice, C.; Del Giacomo, N.; Guido, C. *Combustion Behaviour and Emission Performance of Neat and Blended Polyoxymethylene Dimethyl Ethers in a Light-Duty Diesel Engine*; SAE Technical Paper 2012-01-1053; SAE: Warrendale, PA, USA, 2012. [CrossRef]
3. Härtl, M.; Gaukel, K.; Pélerin, D.; Wachtmeister, G. Oxymethylene Ether as Potentially CO2-neutral Fuel for Clean Diesel Engines Part 1: Engine Testing. *MTZ Worldw.* **2017**, *78*, 52–59. [CrossRef]
4. Dworschak, P.; Berger, V.; Härtl, M.; Wachtmeister, G. *Neat Oxymethylene Ethers: Combustion Performance and Emissions of OME_2, OME_3, OME_4 and OME_5 in a Single-Cylinder Diesel Engine*; SAE Technical Paper 2020-01-0805; SAE: Warrendale, PA, USA, 2020. [CrossRef]
5. Virt, M.; Arnold, U. Effects of Oxymethylene Ether in a Commercial Diesel Engine. *Cogn. Sustain.* **2022**, *1*. [CrossRef]
6. Pélerin, D.; Gaukel, K.; Härtl, M.; Jacob, E.; Wachtmeister, G. Potentials to simplify the engine system using the alternative diesel fuels oxymethylene ether OME1 and OME3-6 on a heavy-duty engine. *Fuel* **2020**, *259*, 116231. [CrossRef]
7. Omari, A.; Heuser, B.; Pischinger, S. Potential of oxymethylenether-diesel blends for ultra-low emission engines. *Fuel* **2017**, *209*, 232–237. [CrossRef]
8. Liu, J.; Wang, H.; Li, Y.; Zheng, Z.; Xue, Z.; Shang, H.; Yao, M. Effects of diesel/PODE (polyoxymethylene dimethyl ethers) blends on combustion and emission characteristics in a heavy duty diesel engine. *Fuel* **2016**, *177*, 206–216. [CrossRef]

9. Ma, Y.; Cui, L.; Ma, X.; Wang, J. Optical study on spray combustion characteristics of PODE/diesel blends in different ambient conditions. *Fuel* **2020**, *272*, 117691. [CrossRef]
10. Pastor, J.V.; García, A.; Micó, C.; Lewiski, F. Simultaneous high-speed spectroscopy and 2-color pyrometry analysis in an optical compression ignition engine fueled with OMEX-diesel blends. *Combust. Flame* **2021**, *230*, 111437. [CrossRef]
11. Damyanov, A.; Hofmann, P.; Geringer, B.; Schwaiger, N.; Pichler, T.; Siebenhofer, M. Biogenous ethers: Production and operation in a diesel engine. *Automot. Engine Technol.* **2018**, *3*, 69–82. [CrossRef]
12. Qiu, Z.; Zhong, A.; Huang, Z.; Han, D. An experimental and modeling study on polyoxymethylene dimethyl ether 3 (PODE3) oxidation in a jet stirred reactor. *Fundam. Res.* **2022**, *2*, 738–747. [CrossRef]
13. Gaukel, K.; Pélerin, D.; Härtl, M.; Wachtmeister, G.; Burger, J.; Maus, W.; Jacob, E. *Der Kraftstoff OME2: Ein Beispiel für den Weg zu emissionsneutralen Fahrzeugen mit Verbrennungsmotor/The Fuel OME2: An Example to Pave the Way to Emission-Neutral Vehicles with Internal Combustion En…*; VDI Verlag: Duesseldorf, Germany, 2016; pp. II-193–II-223. [CrossRef]
14. ECN. Engine Combustion Network. Available online: https://ecn.sandia.gov/ (accessed on 4 April 2024).
15. Pastor, J.V.; García-Oliver, J.M.; Micó, C.; García-Carrero, A.A.; Gómez, A. Experimental Study of the Effect of Hydrotreated Vegetable Oil and Oxymethylene Ethers on Main Spray and Combustion Characteristics under Engine Combustion Network Spray A Conditions. *Appl. Sci.* **2020**, *10*, 5460. [CrossRef]
16. Strauß, L.; Rieß, S.; Wensing, M. Mixture formation of OME3-5 and 1-Octanol in comparison with diesel-like Dodecane under ECN Spray A conditions. *Front. Mech. Eng.* **2023**, *9*, 1083658. [CrossRef]
17. Wiesmann, F.; Strauß, L.; Rieß, S.; Manin, J.; Wan, K.; Lauer, T. Numerical and Experimental Investigations on the Ignition Behavior of OME. *Energies* **2022**, *15*, 6855. [CrossRef]
18. Wiesmann, F.; Bauer, E.; Kaiser, S.A.; Lauer, T. *Ignition and Combustion Characteristics of OME_{3-5} and N-Dodecane: A Comparison Based on CFD Engine Simulations and Optical Experiments*; SAE Technical Paper 2023-01-0305; SAE: Warrendale, PA, USA, 2023. [CrossRef]
19. García-Oliver, J.M.; Novella, R.; Micó, C.; De Leon-Ceriani, D. Numerical analysis of the combustion process of oxymethylene ethers as low-carbon fuels for compression ignition engines. *Int. J. Engine Res.* **2023**, *24*, 2175–2186. [CrossRef]
20. Pastor, J.V.; García-Oliver, J.M.; Micó, C.; Tejada, F.J. Characterization of the oxymethylene ether fuels flame structure for ECN Spray A and Spray D nozzles. *Appl. Energy* **2023**, *332*, 120475. [CrossRef]
21. Kaario, O.T.; Karimkashi, S.; Bhattacharya, A.; Vuorinen, V.; Larmi, M.; Bai, X.S. A comparative study on methanol and *N*-Dodecane Spray Flames Using Large-Eddy Simulation. *Combust. Flame* **2024**, *260*, 113277. [CrossRef]
22. Sim, H.S.; Maes, N.; Weiss, L.; Pickett, L.M.; Skeen, S.A. Detailed measurements of transient two-stage ignition and combustion processes in high-pressure spray flames using simultaneous high-speed formaldehyde PLIF and schlieren imaging. *Proc. Combust. Inst.* **2021**, *38*, 5713–5721. [CrossRef]
23. ASG. ASG Analytik-Service. Available online: https://asg-analytik.de/ (accessed on 4 April 2024).
24. Tagliante, F.; Nguyen, T.M.; Dhanji, M.P.; Sim, H.S.; Pickett, L.M.; Manin, J.; Kukkadapu, G.; Whitesides, R.; Wan, K. The role of cool-flame fluctuations in high-pressure spray flames, studied using high-speed optical diagnostics and Large-Eddy Simulations. *Proc. Combust. Inst.* **2023**, *39*, 4871–4879. [CrossRef]
25. Higgins, B.; Siebers, D.L.; Aradi, A. *Diesel-Spray Ignition and Premixed-Burn Behavior*; SAE Technical Paper 2000-01-0940; SAE: Warrendale, PA, USA, 2000; ISSN 0148-7191. [CrossRef]
26. Reitz, R.D.; Beale, J.C. Modeling Spray Atomization with the Kelvin-Helmholtz/Rayleigh-Taylor Hybrid Model. *At. Sprays* **1999**, *9*, 623–650. [CrossRef]
27. Manin, J.; Bardi, M.; Pickett, L.; Payri, R. Boundary condition and fuel composition effects on injection processes of high-pressure sprays at the microscopic level. *Int. J. Multiph. Flow* **2016**, *83*, 267–278. [CrossRef]
28. CMT. Virtual Injection Rate Generator. Available online: https://www.cmt.upv.es (accessed on 4 April 2024).
29. Liang, L.; Stevens, J.G.; Farrell, J.T. A Dynamic Multi-Zone Partitioning Scheme for Solving Detailed Chemical Kinetics in Reactive Flow Computations. *Combust. Sci. Technol.* **2009**, *181*, 1345–1371. [CrossRef]
30. Niu, B.; Jia, M.; Chang, Y.; Duan, H.; Dong, X.; Wang, P. Construction of reduced oxidation mechanisms of polyoxymethylene dimethyl ethers (PODE1–6) with consistent structure using decoupling methodology and reaction rate rule. *Combust. Flame* **2021**, *232*, 111534. [CrossRef]
31. Nguyen, T.M.; Dahms, R.N.; Pickett, L.M.; Tagliante, F. The Corrected Distortion model for Lagrangian spray simulation of transcritical fuel injection. *Int. J. Multiph. Flow* **2022**, *148*, 103927. [CrossRef]
32. Pope, S.B. Ten questions concerning the large-eddy simulation of turbulent flows. *New J. Phys.* **2004**, *6*, 35. [CrossRef]
33. Senecal, P.K.; Pomraning, E.; Richards, K.J.; Som, S. *An Investigation of Grid Convergence for Spray Simulations Using an Les Turbulence Model*; SAE Technical Paper 2013-01-1083; SAE: Warrendale, PA, USA, 2013. [CrossRef]
34. Kundu, P.; Ameen, M.M.; Som, S. Importance of turbulence-chemistry interactions at low temperature engine conditions. *Combust. Flame* **2017**, *183*, 283–298. [CrossRef]
35. Kahila, H.; Wehrfritz, A.; Kaario, O.; Ghaderi Masouleh, M.; Maes, N.; Somers, B.; Vuorinen, V. Large-eddy simulation on the influence of injection pressure in reacting Spray A. *Combust. Flame* **2018**, *191*, 142–159. [CrossRef]
36. Hanjalić, K.; Popovac, M.; Hadžiabdić, M. A robust near-wall elliptic-relaxation eddy-viscosity turbulence model for CFD. *Int. J. Heat Fluid Flow* **2004**, *25*, 1047–1051. [CrossRef]

37. Durbin, P.A. Near-wall turbulence closure modeling without "damping functions". *Theor. Comput. Fluid Dyn.* **1991**, *3*, 1–13. [CrossRef]
38. Patel, V.C.; Rodi, W.; Scheuerer, G. Turbulence models for near-wall and low Reynolds number flows—A review. *AIAA J.* **1985**, *23*, 1308–1319. [CrossRef]
39. Brenn, G.; Deviprasath, L.J.; Durst, F. Computations and experiments on the evaporation of multi-component droplets. In Proceedings of the ICLASS 2003, Sorrento, Italy, 13–17 July 2003.
40. Reitz, R.D. Modeling atomization processes in high-pressure vaporizing sprays. *At. Spray Technol.* **1987**, *3*, 309–337.
41. O'Rourke, P.J.; Bracco, F. Modelling of Drop Interactions in Thick Sprays and a Comparison with Experiments. *IMECHE* **1980**, *404*, 101–116.
42. Amsden, A.A.; Butler, T.D.; O'Rourke, P.J. *The KIVA-II Computer Program for Transient Multidimensional Chemically Reactive Flows with Sprays*; SAE Technical Paper 872072; SAE: Warrendale, PA, USA, 1987. [CrossRef]
43. Schiller, L.; Naumann, A.Z. A Drag Coefficient Correlation. *Zeit. Ver. Deutsch. Ing.* **1933**, *77*, 318–320.
44. Liu, A.B.; Mather, D.; Reitz, R.D. *Modeling the Effects of Drop Drag and Breakup on Fuel Sprays*; SAE Technical Paper 930072; SAE: Warrendale, PA, USA, 1993. [CrossRef]
45. Pomraning, E.; Rutland, C.J. Dynamic One-Equation Nonviscosity Large-Eddy Simulation Model. *AIAA J.* **2002**, *40*, 689–701. [CrossRef]
46. Idicheria, C.A.; Pickett, L.M. *Formaldehyde Visualization Near Lift-off Location in a Diesel Jet*; SAE Technical Paper 2006-01-3434; SAE: Warrendale, PA, USA, 2006. [CrossRef]
47. Mueller, C.J. *The Quantification of Mixture Stoichiometry When Fuel Molecules Contain Oxidizer Elements or Oxidizer Molecules Contain Fuel Elements*; SAE Technical Paper 2005-01-3705; SAE: Warrendale, PA, USA, 2005. [CrossRef]
48. Maes, N.; Meijer, M.; Dam, N.; Somers, B.; Baya Toda, H.; Bruneaux, G.; Skeen, S.A.; Pickett, L.M.; Manin, J. Characterization of Spray A flame structure for parametric variations in ECN constant-volume vessels using chemiluminescence and laser-induced fluorescence. *Combust. Flame* **2016**, *174*, 138–151. [CrossRef]
49. Dahms, R.N.; Paczko, G.A.; Skeen, S.A.; Pickett, L.M. Understanding the ignition mechanism of high-pressure spray flames. *Proc. Combust. Inst.* **2017**, *36*, 2615–2623. [CrossRef]